REVEALING ELECTRONIC STRUCTURE IN ATOMICALLY-ENGINEERED MANGANITE THIN FILMS

A Dissertation

Presented to the Faculty of the Graduate School

of Cornell University

in Partial Fulfillment of the Requirements for the Degree of

Doctor of Philosophy

by

Eric Justin Monkman

May 2014

REVEALING ELECTRONIC STRUCTURE IN ATOMICALLY-ENGINEERED MANGANITE THIN FILMS

Eric Justin Monkman, Ph.D.

Cornell University 2014

Semiconductor technology is based on tuning the properties of devices by manipulating thin films and interfaces. Recently, this approach has been extended to complex oxides, where quantum many-body interactions give rise to emergent ground states not present in the parent materials. Rationally controlling and engineering correlated electronic phases has the potential to revolutionize modern electronics, but is hindered by the inability of current theory to account for the effects of many-body interactions on the underlying electronic structure. Manganites provide a particularly model system for studying many-body effects due to their complex electronic and magnetic phase diagrams, which give rise to many potentially useful properties. Despite extensive work on manganite films demonstrating numerous electronic phase transitions, little is directly known about how the electronic structure responds to the 'control parameters' accessible in thin films. This dissertation presents direct measurements of the electronic structure in $La_{1-x}Sr_xMnO_3$ based thin films and interfaces through several phase transitions using a unique integrated oxide molecular-beam epitaxy and angle-resolved photoemission spectroscopy system.

We observe the full Fermi surface and near-E_F electronic structure of the ferromagnetic and A-type antiferromagnetic metallic phases, reconciling first-principles calculations with experiment for the first time. Furthermore, our results provide key insights into the polaronic nature of the metallic charge carriers. We then explore the mechanism underlying the insulating ground state for $La_{2/3}Sr_{1/3}MnO_3$ under strong tensile strain. Our measurements rule out the scenarios of bandwidth or localization-driven metal-insulator

transitions, and reveal an instability of the strongly interacting metal towards an ordered insulating phase that can be accessed through epitaxial strain. By next studying atomically precise interfaces in $(LaMnO_3)_{2n}/(SrMnO_3)_n$ superlattices, we directly see how the interplay between dimensionality and strong many-body interactions drives large period superlattices into a pseudogapped insulating phase. Our results provide new insights into the physics of perovskite manganites, and illustrate in detail the nature and importance of phase competition in controlling the electronic properties of correlated thin films. These results should be applicable to correlated materials in general, and can help develop predictive models capable of realizing the full potential of oxide electronics.

Biographical Sketch

Eric Monkman has shown a keen interest in the scientific and mechanical from an early age. His childhood room was a shrine to LEGO®, K'Nex®, and Meccano®, and he could be found on more than one occasion tearing electric motors and spare wires from his toys to build new gadgets. From a young age he focused his attention on understanding all he learned through thought, debate and occasional argument, to the frustration of some math and science teachers.

His developing love for the unknown led him to enroll in the Astrophysics program at McMaster in 2003, from which he graduate *magna cum laude* in 2007 with a Bachelor of Science Degree in Physics. During this time, he worked with Prof. Alison Sills to study collisions within clusters of millions of stars. This work lead to his first peer reviewed article, and reinforced his appetite for discovery. His passion for stars, the cosmos, and the unknown remains, but his focus has shifted to more terrestrial matters. Prof. Robin Marjoribanks at the University of Toronto exposed him to experimental physics in the summer of 2006, and encouraged him to enroll at Cornell. Shortly after arriving at Cornell in 2007, Eric joined Prof. Kyle Shen's newly formed research group and had the once-in-a-lifetime opportunity to construct an entire laboratory from the ground up. Work within this laboratory earned him a Master of Science Degree from the Cornell physics department in 2011. He has continued these experiments as his doctoral thesis topic, the results of which are presented here.

Eric has earned several academic and research based awards throughout his career, including being named *Outstanding Teaching Assistant* by the American Association of Physics Teachers, and receiving an *Alexander Graham Bell* Doctoral Scholarship from the Natural Sciences and Engineering Research Council of Canada.

To Katie.

For all the times you asked: “when will you be finished?”

I’m finished.

Acknowledgements

It is largely thanks to the support and mentorship of Prof. Alison Sills, who gave an unproven undergraduate his first research opportunity, and Prof. Robin Marjoribanks, who exposed me to the joys of experiment, that I pursued a PhD at Cornell. I am further grateful to Nate Ellis for teaching me nearly everything I know about metalworking and 'making stuff'. Rodney Bowman, Bob Tillotson, Stan McFall, Chris Cowulich, and Jeff Koski have continually amazed with their efficient handling of our frequent rush orders, but I am most thankful for the guidance and support they have provided for many of my less 'scientific' projects.

The best part about a world class institution like Cornell is the opportunity to work with a team of exceptionally talented and brilliant people, and I have been particularly blessed in this regard. I could not have asked for better colleagues than John Harter and Daniel Shai, who have been with me since the beginning. Both have a humility that belies their intellect, and working with them has been a constant source of personal motivation. Carolina Adamo has been my link to the Schlom group, providing nearly all of the films discussed in this dissertation and then teaching me to take over once she moved on. Despite her tremendous scientific contributions, I am most grateful for her continued friendship. Julia Mundy has been a joy to work with. Her TEM images provided key insights into my work, and I will sorely miss her frequent delicious cakes. Dawei Shen, Yuefeng Nie, and Phil King have provided guidance throughout my PhD, and each brought a new and valuable perspective to the group. It has also been a pleasure to work with Shouvik Chatterjee, Bulat Burganov, Ed Lochocki, Haofei Wei, Jacob Ruf, and Brendan Faeth, and to see them grow into scientists. I am reassured to know that I leave our lab in capable hands.

Of course, this dissertation would not exist but for our film growth collaborators. I am indebted to Prof. Darrell Schlom for introducing me to the many aspects of materials science that are foreign to physicists, and particularly for letting me operate his MBE. Tassilo

Heeg showed me what it really means to construct and run complex equipment. Maitri Warusawithana and Shaobo Zhu provided great company during our many late nights and early mornings working side-by-side. Darrell has put together an exceptional team whose friendship and advice made long-hours and failed experiments bearable. Alex Melville, Charles Brooks, Hanjong Paik, Rainer Held, Natalie Dawley, Jessica Burton, Hari Nair, and John Heron - I will miss you all.

Taryn Mattice has been a spiritual guide and a source of support during personal hardship, and for that I am thankful. My close friend, Matthew Farrar has grounded me spiritually and morally, and has remained someone I look up to in both a scientific and personal capacity.

I am immensely grateful to my advisor, Kyle Shen. Kyle puts tremendous effort into developing all aspects of his students, and has been a constant source of inspiration and advice in areas as diverse as technical design, writing and public speaking. Kyle has taught me to be a scientist, but in the process, has instilled a sense of confidence and personal character that I carry with me well beyond the lab.

Most of all, I am grateful to my family. My parents and brothers have been extremely supportive of my studies and have made every effort to learn about my work, even when the jargon becomes overwhelming. My beautiful wife Katie, to whom this thesis is dedicated, is a source of unending love and inspiration. Teaching, studying, and providing support during my PhD are more than most could handle, and I am grateful to be married to someone who can 'do it all'.

G. K. Chesterton wrote, "The poet only asks to get his head into the heavens. It is the logician who seeks to get the heavens into his head. And it is his head that splits" [1]. It is only through the support of these and many others, that after nearly seven years, my head remains intact.

Table of Contents

Chapter 1

Introduction

Strongly correlated materials form a central theme within condensed matter physics. These are materials in which conventional Fermi liquid and bandstructure considerations fail to account for their macroscopic properties due to strong Coulomb interactions between electrons or the many-body interactions of electrons with other degrees of freedom. This field can be traced back to work on electron-electron repulsion by Wigner in 1934 [2], leading to Mott's subsequent proposal [3] that the insulating nature of NiO is due to Coulomb interactions that prevent two electrons from sharing the same site - the *Mott insulator* now bears his name. Since then, a wide array of correlated materials have been discovered and share the common theme of extreme electrical and magnetic properties compared with conventional Fermi liquids. Just a few examples are superconductivity at temperatures above 130 K [4], up to 10^{11} fold changes in resistivity under the application magnetic fields [5], and many transitions between metallic and insulating phases caused by small perturbations [6]. The *many-body problem* of calculating the properties of a system of strongly interacting degrees of freedom presents an immense challenge to modern theoretical physics. For this reason, theoretical progress is based on creating accurate and

predictive approximation schemes, whose development relies extensively on exploratory experimental studies and discoveries of new materials with interesting behavior.

Despite these challenges, a great deal of progress has been made on treating and understanding correlated materials over the past six decades, and recent work has begun to focus on the possibility of using correlations to *rationally engineer* new useful physical properties [7]. The biggest motivation for this endeavor is to generate materials for the next generation of electronic devices that take advantage of correlated materials' extreme electronic and magnetic behaviors at the atomic scale [8]. As was the case for semiconductor microelectronics, much of the promise for this new field lies in thin film growth techniques. Several milestones have already been reached, including the generation of high mobility two-dimensional electron gases in complex oxide heterostructures [9] and the realization of a theoretically predicted multiferroic in a strained thin film [10]. Unfortunately, examples of successful theoretical predictions are rare due to the inherent complexity of many-body interactions, and the field still progresses largely through unexpected experimental discoveries. True rational engineering of many-body phases stands just beyond reach.

There thus remains a strong need to develop a more complete understanding of the microscopic physics underlying the macroscopic behavior of strongly correlated materials, and particularly how they respond to the tuning parameters accessible through thin film growth. In this dissertation, I present direct experimental measurements of the electronic structure of manganite thin films that provide new insight into the role played by many-body interactions in tuning their electronic properties through several phase transitions. The colossal magnetoresistive manganites are one of the most extensively studied families of correlated materials, and provide an ideal system for modifying the electronic and magnetic properties through thin film growth due to their many competing interactions and the presence of many accessible ground states [11]. In addition, mangan-

ite films play a central role in many potential spintronic and oxide electronics devices [12, 13, 14, 15]. The three most important "knobs" for engineering conventional semiconductor thin films are chemical doping, epitaxial strain, and interface engineering. This dissertation will explore the effect of all three on the underlying electronic structure of $La_{1-x}Sr_xMnO_3$ films using our unique combined oxide molecular-beam epitaxy (MBE) and in-situ angle-resolved photoemission spectroscopy (ARPES) system.

Chemical doping (e.g., varying x) is extensively used to tune the properties of bulk crystals, and as a result has been extensively studied by ARPES in many compounds [16, 17]. Nevertheless, due to experimental difficulties in measuring $La_{1-x}Sr_xMnO_3$ single crystals with ARPES, our results represent the first determination of how its entire Fermi surface and near-E_F electronic structure evolve with x. We reconcile the electronic structure of this canonical large-bandwidth manganite with theory and the heavily-studied Ruddlesden-Popper $(La,Sr)_{m+1}Mn_mO_{3m+1}$ compounds, provide measurements of the strength of many-body interactions within the metallic phase, and confirm our results for a wide range in x spanning the ferromagnetic to antiferromagnetic phase transition at $x = 0.5$.

Epitaxial strain, where films are grown on deliberately lattice mismatched substrates, has been used to dramatically alter the electronic phases of many complex oxides [18]. Here I present the first direct measurements of the near-E_F electronic structure through a strain driven metal-insulator transition, which allow us to determine the hitherto unknown underlying mechanism. Our results rule out band insulator or Anderson localized phases, and instead reveal how epitaxial strain drives $La_{2/3}Sr_{1/3}MnO_3$ between two drastically different regimes: the bulk-like strongly interacting metal and an insulator with static or fluctuating order.

Interface engineering has no bulk analogue. It corresponds to growing two or more distinct materials on top of each other, with the goal of generating new phases or phys-

ical properties at the atomic-scale interfaces between them. Exotic magnetism [19], high temperature superconductivity [20], and two-dimensional correlated electron systems [9, 21, 22] are only a few examples of novel states recently realized at complex oxide interfaces. Until now, such interfaces have remained inaccessible to ARPES. In this dissertation I present measurements of the electronic structure at the interfaces within $(LaMnO_3)_{2n}/(SrMnO_3)_n$ superlattices. Tuning the separation between neighboring interfaces via n drives the system between a bulk-$La_{2/3}Sr_{1/3}MnO_3$-like three dimensional polaronic metal to a strongly correlated pseudogapped insulator. We explain this behavior through the reduced dimensionality inherent to isolated interfaces, which enhances the effects of many-body interactions and makes the metallic phase unstable to fluctuations involving ordered insulating states.

Our results in all three cases demonstrate the central role played by quantum many-body interactions in controlling the physical properties of manganite thin films, and how the effects of those interactions can be rationally tuned through structure and interface engineering. These results can contribute to the formation of a general framework for treating many-body interactions in correlated thin films and heterostructures, providing a pathway for exploiting such effects in novel electronics.

Chapter 2

Photoemission spectroscopy and electronic structure

The central technique involved in this dissertation, photoelectron spectroscopy, was discovered in 1887 (ref. [23]) and predates the development of modern physics. The fact that photoelectron spectroscopy finds more use today than ever before is a testament to the profound insight that can be gained from such a fundamental process and the ingenuity with which scientists continue to develop its methodology and applications.

With our modern understanding of the quantized nature of light and the structure of the atom, the photoelectric effect is simple to comprehend. A material is illuminated with ultraviolet light or x-rays. An electron absorbs one of these photons, and is provided with enough energy to be ejected from the material (Fig. 2.1a). This picture was less clear in 1887, when the controversial *atom of electricity* had yet to be named the *electron* [24], and the concept of photons had been thoroughly trounced by Maxwell's wave theory of light.

In fact, the explanation of the photoelectric effect by Albert Einstein and subsequent

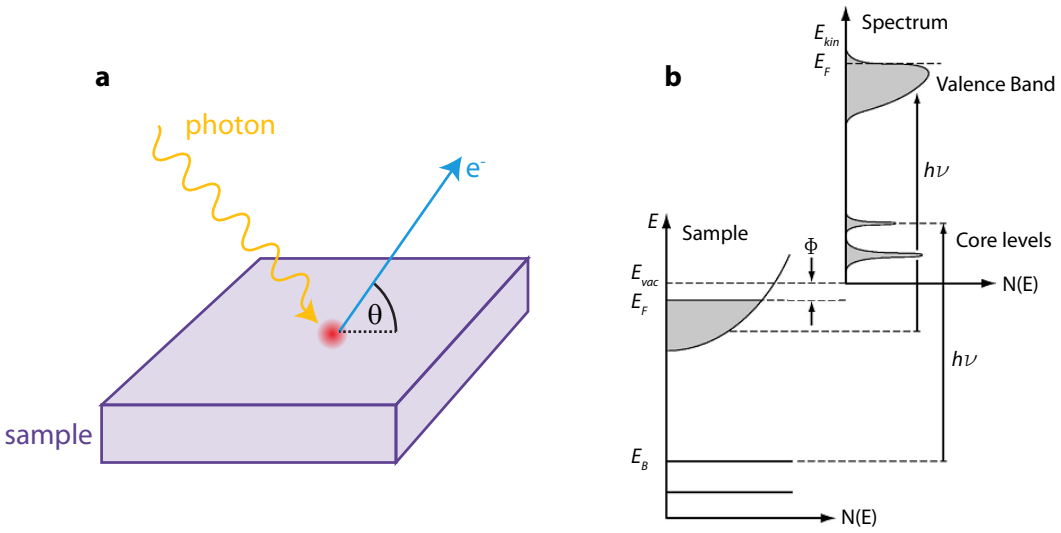

Figure 2.1: (**a**) A schematic illustration of the photoemission process. A single photon is absorbed, causing the emission of a single electron at an angle θ with respect to the surface. (**b**) The energetics of the photoemission process (Reprinted with permission from A. Damascelli, Z. Hussain & Z.-X. Shen (2003) [16]. Copyright 2003 by the American Physical Society). The photon of energy $h\nu$ excites an electron from the sample into the vacuum by overcoming the work function ϕ. The free electron's energy is detected, and via the known $h\nu$ is related directly to electron binding energies within the sample.

tests of his theory by Robert A. Millikan provided the essential proof of the photon's existence and spurred the development of quantum mechanics. Key to this discovery was the observation that the energy of photoemitted electrons is independent of the intensity of light used. In Maxwell's wave theory of light, electrons continuously absorb energy from the electromagnetic field. A more intense field generates higher energy electrons. Based on Planck's theory of black body radiation, Einstein realized instead that if light came in quantized units of energy $h\nu$, with ν the frequency, the energy of electrons would be proportional to and solely determined by ν [25]. This dependence was later verified in detail by Millikan [26]. It was this work that resulted in Einstein's Nobel prize (1921), and Millikan was subsequently awarded with the same for his contributions (1923).

In the 20th century, photoelectron spectroscopy became an important tool for studying the chemical makeup of a wide variety of materials, and led to a third Nobel prize for the photoelectric effect (Kai Siegbahn in 1981). In 1964, two essential steps were made in the development of photoelectron spectroscopy in back-to-back papers: Gobeli, Allen and Kane demonstrated the conservation of electron momentum in the photoemission process from crystalline solids, and Kane realized the implications for directly measuring bandstructure [27, 28]. This new technique, angle-resolved photoelectron spectroscopy (ARPES), has subsequently contributed extensively to our understanding of the electronic structure underlying the behavior of crystalline materials, and plays the central role within this dissertation.

2.1 X-ray photoelectron spectroscopy

First and foremost the photoemission process relies on energy conservation. A photon has energy $h\nu$ and the electric field at the surface of a material provides a work function (ϕ) that reduces the energy of escaping electrons. Then for an electron of binding energy E_B (with respect to the chemical potential), the photoemission process must satisfy:

$$E_{kin} = h\nu - \phi - E_B$$

Where E_{kin} is the kinetic energy of the emitted electron. Figure 2.1b illustrates this process. Work functions typically fall in the range of 3-5 eV, so we find that photoemission can precisely measure the electron energy levels within a material up to nearly $h\nu$. When the photons used are x-rays ($h\nu \gg 100$ eV), photoemission spectroscopy becomes a powerful technique for measuring the deeply bound atomic-like *core levels* that contain detailed information on sample stoichiometry and the chemical environment.

Because they are highly localized around an individual atom, the core levels measured

by X-ray photoelectron spectroscopy (XPS) occur at energies characteristic of the relevant element and are only weakly perturbed (typically $\Delta E \approx 1$ eV) due to details of the chemical environment. By identifying all of the core levels and measuring their intensities, the elemental composition of a sample can be determined to a typical accuracy of a few percent. Excluding instrumental factors that are the same for all peaks (photon intensity, detector efficiency, etc...), the photoemission intensity for core level i of element X with energy E is [29]:

$$I(i, X) = \sigma(h\nu, \alpha, E)T(i, X)\lambda_{mfp}(E)n(X)$$

Where σ is the cross section for photoemission, which generally depends on the angle between the incident photon and detected electron, α . These are ideally calibrated for the material of interested based on similar materials, but in many cases calculated cross sections for isolated atoms are used [30]. The factor $T(i, X)$ describes the probability of transmission through the surface, $\lambda_{mfp}(E)$ is the energy-dependent electron escape depth, and $n(X)$ is the desired elemental concentration. Typically, many core levels are measured and a comparison of the integrated intensities provides the relative atomic concentrations for each element.

In addition, XPS is routinely performed with sub-eV resolution, and can resolve small shifts induced by the chemical environment of each atom. Final state effects like exchange coupling to valence band states can also give rise to peak-splittings on the scale of ≈ 1 eV, which provide another sensitive indication of chemical environment. The calculation of this fine structure is more complex than that of atomic-like intensities, but by comparison to reference samples fine details of the bonding environment, such as oxidation states, can be determined.

The electron escape depth or mean-free-path, λ_{mfp}, is critical to the interpretation of photoemission results. Electrons are easily scattered, and so λ_{mfp} is extremely short. Escape depths have been measured for several materials and have been found to fall

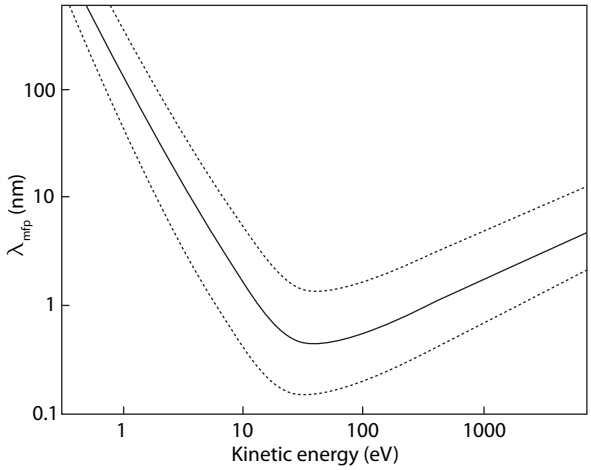

Figure 2.2: The universal curve of electron mean free path vs. kinetic energy. Adapted from ref. [31]. Dotted lines encompass the compiled data from many materials. Note that given the logarithmic scales, these bounds represent a large amount of variability.

roughly along a so-called *universal curve* (Fig. 2.2). Typical values are 1-5 nm for XPS, and can become considerably shorter for lower photon energies. On the one hand this places severe limitations on the ability of photoemission to determine the properties of bulk materials, and great care must be taken to measure pristine surfaces and avoid surface-related changes in composition and chemistry. On the other hand, this surface sensitivity has established photoemission as one of the most powerful surface analysis techniques available.

A particular technique that makes use of the intrinsically short λ_{mfp} is angle-resolved x-ray photoelectron spectroscopy (ARXPS) [32]. The electron mean-free-path is a material dependent quantity, but translating it into the depth of material probed by XPS (d_{probe}) requires consideration of the experimental geometry as well. In the simplest consideration, one notes that as the angle of electron propagation with respect to the sample surface increases, the electron must pass through more material before exiting the crystal (Fig. 2.3a). Thus, as the angle between electron detection and the surface normal (θ) is increased, the

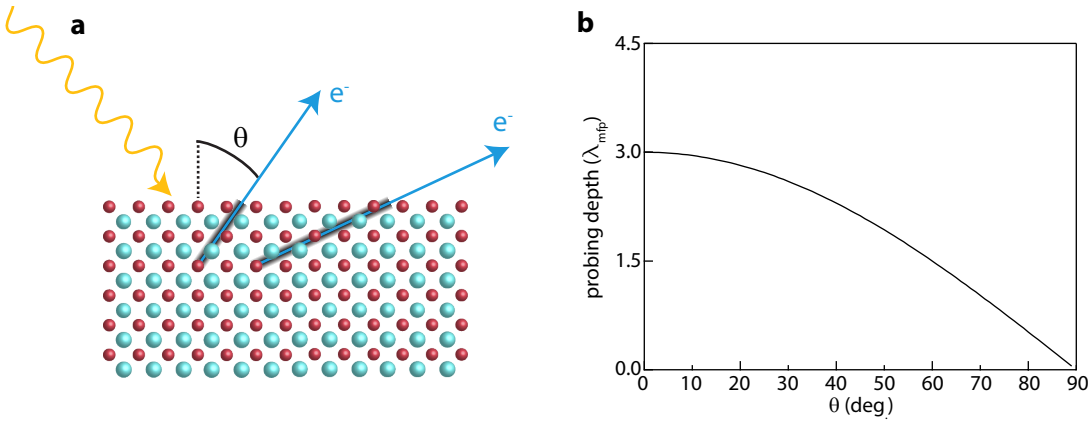

Figure 2.3: (**a**) The key principle behind ARXPS depth profiling. As the angle θ between the emitted electron and the surface normal increases, the electron must pass through more material before exiting the sample. This leads to a $\cos\theta$ dependence of the effective probing depth ($\approx$ triple the escape depth) on the emission angle (**b**).

volume probed by XPS decreases as $d_{probe} \propto \lambda_{mfp}\cos\theta$ (Figure 2.3b). Measuring atomic concentrations or chemical-induced spectral features as a function of emission angle thus allows for the precise determinations of depth profiles near the surface with sub-nm resolution.

2.2 Angle-resolved photoelectron spectroscopy and the three step model

In addition to energy conservation, the clean surface of a crystal preserves its periodicity along the in-plane (x, y) directions. An immediate consequence of Noether's theorem is the conservation of the in-plane components of electron momentum (k_x, k_y). This simple consideration highlights the most important principle of ARPES: by measuring the $E(\mathbf{k})$ relationship for the electrons photoemitted from a crystal, one can directly determine its

bandstructure.

That the electron momentum *vector* can be determined by ARPES is trivial: we measure both the energy of an electron and its propagation direction. The energy provides us with the magnitude of momentum via $E = p^2/2m_e$, and the direction is parallel to the measured free electron propagation direction (i.e., its angle with respect to the crystal surface). Due to the non-conservation of k_z, this component of momentum must be given special consideration. We discuss this further in section 5.2.1.

Due to the fact that we are no longer dealing with non-dispersive atomic-like core levels, we must be more careful with our formalism. The most common method of analysis for ARPES data relies on the *three-step model* [29]. In this approximation scheme we break down the photoemission process into three steps. First, the photon is absorbed and excites the electron from the initial Bloch state to a higher energy final Bloch state within the crystal. Second, the excited electron propagates to the crystal surface. Third, the electron escapes through the surface of the crystal into a free-electron vacuum state. In reality, all steps form a single coherent quantum process, but the separation into well defined and easier to compute quantities makes analysis of ARPES data more tractable.

The most complicated first step contains the information we wish to learn about the crystal's electronic structure. First, let us start by ignoring many-body effects and treating the crystal's states as a collection of independent electron energy levels. We can use Fermi's golden rule to calculate the photoemission intensity corresponding to transitions from an initial single-electron Bloch state ($\psi_i(\mathbf{k}_i)$) of energy $E_i(\mathbf{k}_i)$ to a final single-electron Bloch state ($\psi_f(\mathbf{k}_f)$) of energy $E_f(\mathbf{k}_f)$ (ref. [29]):

$$I(E_f, \mathbf{k}_f, h\nu) \propto \sum_i |\langle \psi_f(\mathbf{k}_f)|\mathbf{A}\cdot\mathbf{p}|\psi_i(\mathbf{k}_i)\rangle|^2 \delta(h\nu - (E_f(\mathbf{k}_f) - E_i(\mathbf{k}_i)))$$

The transition matrix element involves the vector potential ($\mathbf{A}$), and we have made use of the dipole approximation ($\nabla\mathbf{A} = 0$). This form illustrates two critical factors contribut-

ing to the photoemission intensity: first, the δ-function between terms of the form $E(\mathbf{k})$ demonstrates that the photoemission intensity directly tracks the bandstructure of the system. Second, the photoemission intensity is modulated by a dipole matrix element between the initial and final states. The consequences of this term are creatively called *matrix element effects* by the photoemission community. Varying the photon energy and polarization has a large effect on this term, and it can be used to isolate specific bands of interest in many-band systems [33], or to determine the symmetries and even spin arrangement of the observed states [34].

More generally, the electronic structure of crystals must be described as a many body system. In this context the δ-function in the above expression is replaced by the *spectral function* $A(\mathbf{k}, \omega)$, where ω is the electron energy with respect to E_F. In addition, since photoemission only measures occupied electronic states, the intensity is further multiplied by a Fermi function centered at E_F. The association between the ARPES intensity and $A(\mathbf{k}, \omega)$ requires the use of the so-called sudden approximation, wherein we assume that the initial electron was instantaneously removed from the crystal before the many-body system could relax. This is generally assumed valid at large photon energies, but must break down for small enough $h\nu$. Nevertheless, this approximation is in widespread use and has so far produced satisfactory results even for very low energy ARPES ($h\nu < 7$ eV).

In technical terms, A is the imaginary part of the one-electron removal Green's function that describes the propagation of one-hole excitations in the many-body ground state [16] and is given by:

$$A(\mathbf{k}, \omega) = \sum_m | < \psi_m^{N-1} | c_k | \psi_i^N > |^2 \delta(\omega - (E_m^{N-1} - E_i^N))$$

Here we see directly how it corresponds to the removal of a single electron (c_k) from an N particle state to form a new $N-1$ particle state with its energy reduced by ω, of which there are several possibilities each labeled by m. In a non-interacting system, this reduces to a delta-function peak that tracks the single-electron bandstructure (Fig. 2.4a). In the true

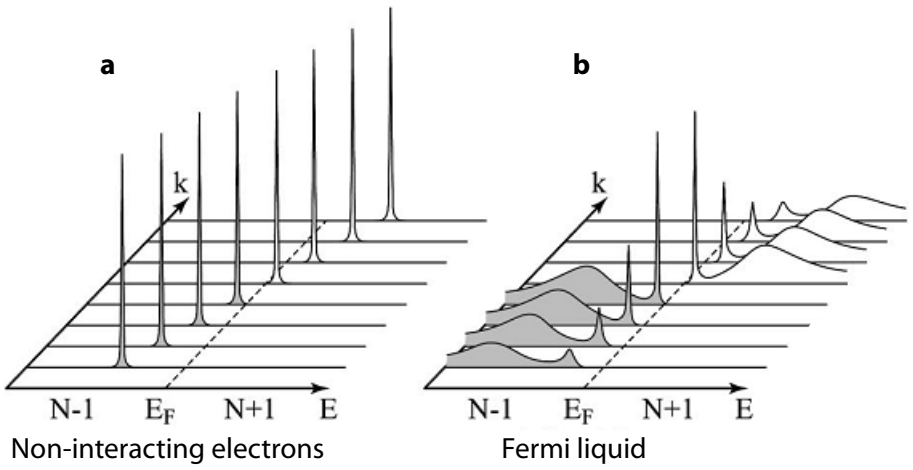

Figure 2.4: (**a**) Illustration of the spectral function vs. energy and momentum for a non-interacting system, which consists of a delta-function peak at each value of k. (**b**) The spectral function for a Fermi liquid still includes sharply defined quasiparticle peaks, but also now includes a broad incoherent background at higher binding energies. As the quasiparticle moves farther in energy from E_F its scattering rate increases and the peak broadens. (Both figures reprinted with permission from A. Damascelli, Z. Hussain & Z.-X. Shen (2003) [16]. Copyright 2003 by the American Physical Society).

many-body system, $A(\mathbf{k}, \omega)$ describes the probability of generating a hole with a given momentum and energy, starting from the ground state.

2.3 Incoherent spectral weight and bandstructure renormalization

With Fermi liquid theory as our guide, it would be desirable to cast the spectral function in a form where its connection to electron like quasiparticles is more transparent. With this aim in mind, it is convenient to discuss the effects of many-body interactions in terms of an electron self-energy Σ, whose real part (Σ') is related to the renormalization of quasiparticle energies and whose imaginary part (Σ'') gives the finite quasiparticle lifetime. We

write [16]:

$$A(\mathbf{k},\omega) = -\frac{1}{\pi}\frac{\Sigma''(\mathbf{k},\omega)}{(\omega - \epsilon_k - \Sigma'(\mathbf{k},\omega))^2 + (\Sigma''(\mathbf{k},\omega))^2}$$

Where ϵ_k is the non-interacting bandstructure. This form is quite suggestive, and one can see how for weak Σ that varies slowly as a function of $\mathbf{k}$ and ω the spectral function becomes a sharp peak at the renormalized energy $\epsilon_k - \Sigma'(\mathbf{k},\omega)$ and with width inversely proportional to $\Sigma''(\mathbf{k},\omega)$. In the case where Σ is large and does appreciably depend on energy or momentum, the concept of a Fermi liquid may break down entirely and the spectral function can assume a form without well defined peaks. In general, it is typical to discuss the spectral function as composed of two distinct terms: a coherent quasiparticle like Lorentzian peak and a broad so-called *incoherent* background, which describes more complex many-body processes. Figure 2.4b shows an example spectral function for a Fermi liquid with a non-negligible incoherent background.

At first pass one might assume that the incoherent spectral weight contains little useful information on the underlying bandstructure of correlated materials, since Fermi liquid theory focuses entirely on quasiparticles. Nevertheless, Fermi liquid theory breaks down in many correlated materials of interest, and the incoherent spectral weight provides important insights into the resultant many-body state. For example, in the Mott insulating state of the cuprates, it was shown that the dispersive lower Hubbard band features observed by ARPES consist of incoherent spectral weight arising from a strong electron-lattice coupling[35]. More generally, theoretical studies of systems with very strong electron-phonon coupling have demonstrated that the quasiparticle weight can become vanishingly small while the incoherent features track the underlying *bare* bandstructure in $\mathbf{k}$ and ω (refs. [36, 37]).

The case of a weaker electron-phonon coupling's effect on bandstructure is well established (see e.g., ref. [38, 39]), and provides an example where both coherent and incoherent parts of the spectral function play a central role in ARPES analysis (Fig. 2.5).

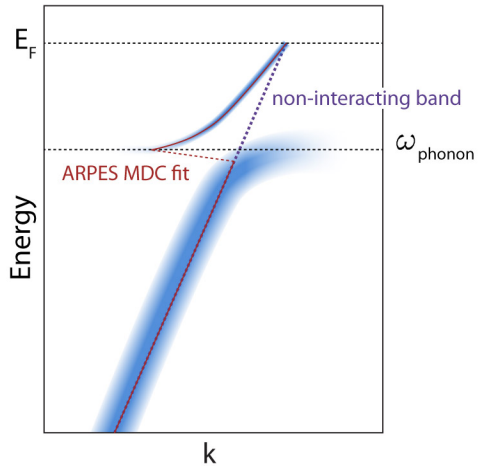

Figure 2.5: The 'kink' in the electronic structure near E_F induced by electron-phonon (or more generally any boson) coupling. The band is split into a low-energy coherent part, and a high energy incoherent part. MDC fits to ARPES data over this range will track both halves, resulting in a distinct kink at the phonon energy (ω_{phonon}).

Below the energy of the optical phonon mode, screening of the hole's charge by a coherent lattice distortion leads to a renormalization of the energies that increases the effective mass: the hole drags the lattice distortion with it as it moves through the crystal. Thus, the spectral function below the phonon energy consists of a sharp coherent quasiparticle. Above this threshold, the emission of phonons becomes possible, leading to rapid damping of any charged excitations and eliminating the possibility of coherent quasiparticle motion. Since the lattice is unable to coherently screen this excitation, the hole sees an effectively frozen lattice and tracks the unrenormalized bare dispersion that occurs in the absence of electron-phonon coupling. The presence of a low energy high-mass feature and a high-energy low-mass feature gives rise to the 'kink' seen in many ARPES measurements of systems with strong electron-phonon coupling (Fig. 2.5), and the degree of mass renormalization is routinely used to indicate the approximate electron-phonon coupling strength ($\lambda_{e\text{-}ph} = \frac{m_{low\text{-}energy}}{m_{high\text{-}energy}} - 1$ in a weak coupling treatment).

2.4 k_z effects in ARPES

Above we noted that, unlike k_x and k_y, k_z is not conserved during the photoemission process. ARPES is often used to study quasi-two-dimensional materials where k_z is irrelevant, but in the case of truly three-dimensional electronic structure, the determination of k_z becomes an important task. Unfortunately, there are no precise and generally applicable methods for the determination of k_z, which depends not only on material-specific properties but very sensitively on photon energy. On the other hand, the dependence on photon energy provides us with a handhold if we make the crude but somewhat reasonable assumption that the high-energy final state in the photoemission process can be described with a free electron parabolic dispersion whose only free parameter is an overall energy offset: the inner potential (V_0). Knowing the final-state dispersion is sufficient since the first step of the three step model, excitation from the initial to the final state, conserves *all three* components of **k**. Basic kinematic constraints provide us with (ref. [16]):

$$k_z = \sqrt{\frac{2m}{\hbar^2}(E_{kin} + V_0) - k_{\shortparallel}^2} \tag{2.1}$$

Where m is the electron mass, E_{kin} is the kinetic energy of a photoelectron, and $k_{\shortparallel}^2 = k_x^2 + k_y^2$. For electrons at the Fermi level that are typically of most interest to ARPES, we write Eq. 2.1 in terms of the photon energy and the work function:

$$k_z = \sqrt{\frac{2m}{\hbar^2}(h\nu + V_0 - \phi) - k_{\shortparallel}^2} \tag{2.2}$$

The determination of the inner potential requires ARPES data spanning a range in photon energies sufficient to cover more than one Brillouin zone along k_z. The periodicity of the ARPES data as a function of $h\nu$ is then used to determine an appropriate V_0.

In addition, k_z is susceptible to an additional complication related to the short electron mean-free-path [40]. We wish to precisely determine the electron's momentum, yet its wavefunction decays within $\approx$ 1 nm of the surface. Heisenberg's uncertainty principle tells us that our task is impossible, and that there must be an intrinsic broadening of

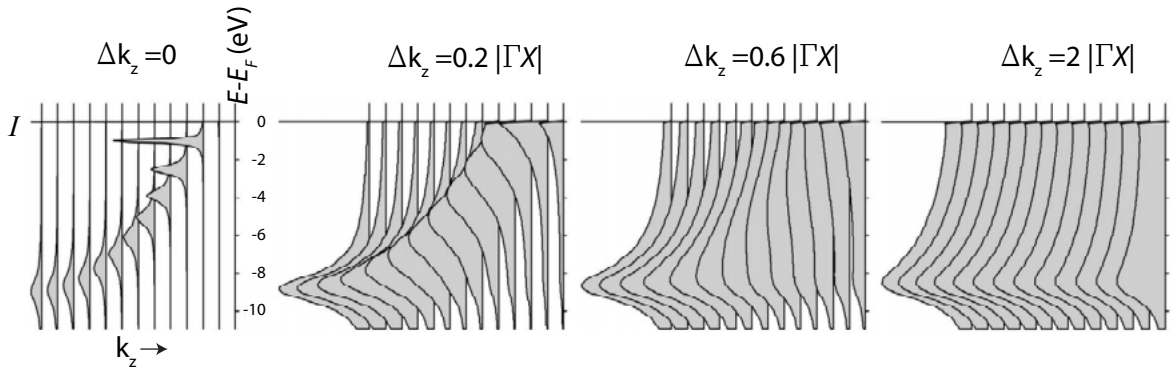

Figure 2.6: Simulations of normal-emission ARPES spectra from the copper sp band for varying electron mean free paths from very long (left panel) to very short (right panel). Long λ_{mfp} corresponds to a small amount of k_z broadening, allowing the intrinsic bandstructure to be observed. Short λ_{mfp} averages over all k_z, resulting in significantly broadened spectra and the loss of a well defined band. (Figure reprinted from V.N. Strocov (2003) [40], with permission from Elsevier).

k_z. For the particular form of wavefunction relevant to photoemission, a step function at the surface followed by an exponential decay, the Fourier transform is a Lorentzian with a full-width at half-maximum (FWHM) given by $\Delta k_z = 1/\lambda_{mfp}$. The measured photoemission intensity is proportional to a weighted average of the spectral function over this range. This can span a significant fraction of the Brillouin zone and must be carefully accounted for in the analysis of ARPES data from three-dimensional materials. Fig. 2.6 shows the simulated photoemission signal from a free-electron like band with different values for Δk_z. As can be clearly seen, when $\Delta k_z \ll \pi/c$ the photoemission intensity tracks the intrinsic three dimensional bandstructure. At the other limit, $\Delta k_z \gg \pi/c$, the spectra show a k_z independent one-dimensional density of states. ARPES studies of real materials often exists somewhere between these two regimes, where k_z final state effects can significantly impact the measured spectral function.

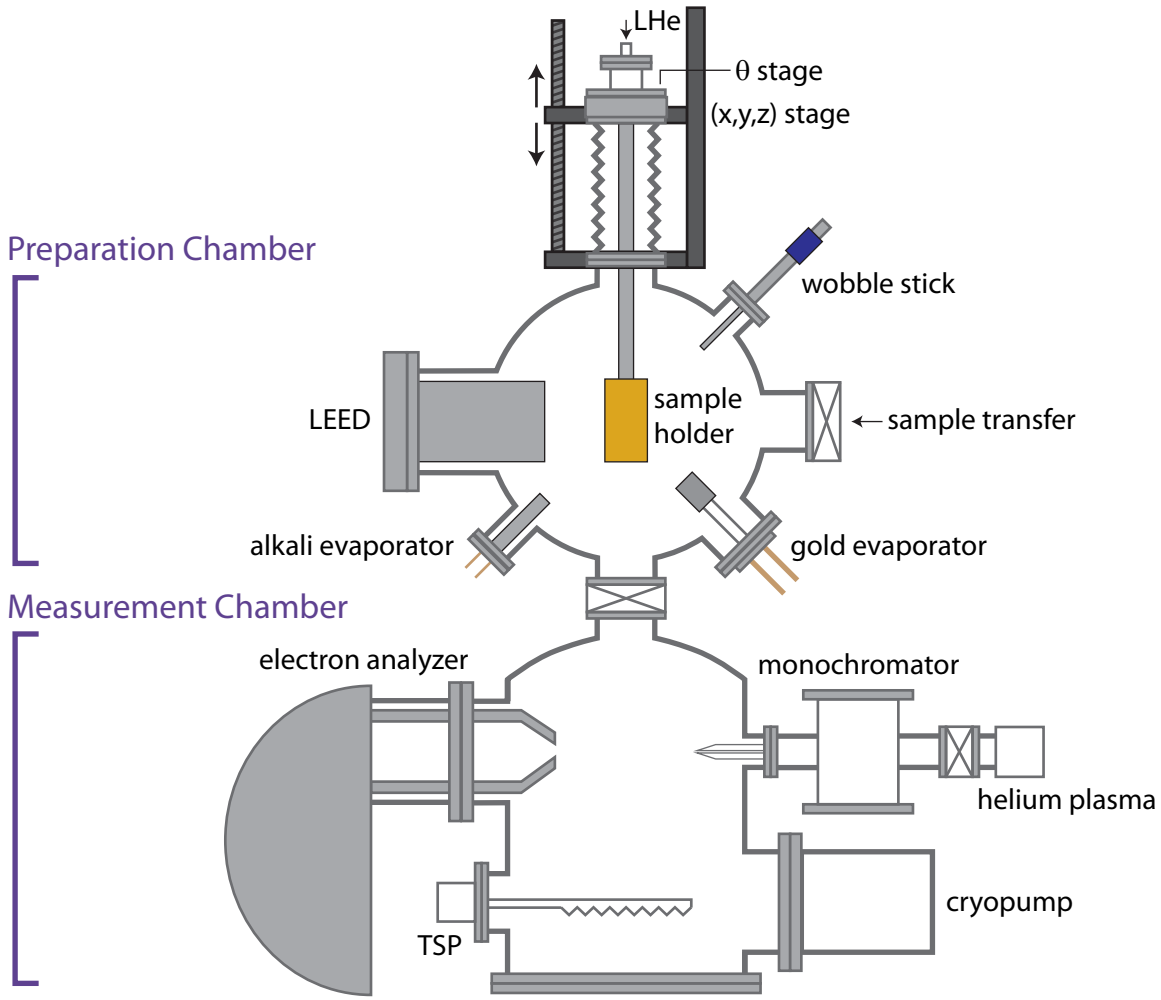

Figure 2.7: Schematic of our ARPES system highlighting key components (TSP short for titanium sublimation pump).

2.5 Experimental considerations for ARPES

Fig. 2.7 illustrates the basic layout of our ARPES system. It is both physically and conceptually separated into two parts, which we refer to as the *preparation* and *measurement* chambers. Samples are loaded into the preparation chamber via a connected ultra-high vacuum (UHV) transfer chamber (discussed further in section 3.3). This first chamber is equipped with several apparatus to prepare for and support photoemission measurements. A magnetically coupled wobble stick is used for in-vacuum manual manipulation

wherever required, and in particular for cleaving single-crystal samples to expose a fresh surface. A gold evaporator deposits thin films of gold onto our sample manipulator, which provides a clean reference spectra at an equal temperature to the sample for high precision photoemission measurements. An alkali-metal evaporator can be loaded with cesium, potassium, sodium, rubidium or lithium for doping the surface of samples in-situ. Finally, a low-energy electron diffraction system (LEED) is used to characterize the crystal structure of our sample surfaces in-situ [41].

On top of the upper chamber sits our (x, y, z, θ) stage. This consists of out-of-vacuum linear translators for the (x, y, z) axes that are coupled via a vacuum bellows to a liquid helium flow cryostat. In addition, the cryostat rests on a differentially pumped rotary stage to provide rotation about the z axis (θ). The cryostat is capable of reaching 4.2 K under normal flow conditions, and can reach 1.8 K by reducing the helium gas exhaust pressure via pumping. Our sample manipulator bolts to the cryostat cold finger, and by translating z can be transferred between the upper and lower chambers. This manipulator holds samples during preparation and measurement, and provides additional angular degrees of freedom to access larger windows of **k**-space with ARPES. Our first manipulator ("Mk-I") is capable of achieving a base temperature of $T < 3$ K at the sample, but provides no motorized degrees of freedom and only a single manually actuated rotation (ϕ which rotates about x). Our second manipulator ("Mk-II") has a base temperature of $T = 7$ K at the sample, and has a fully automated ϕ axis in addition to a manually operated ω axis (rotation about y). Both manipulators were designed and constructed by John Harter.

The chief purpose of the lower chamber is to perform high-resolution ARPES measurements. As such, the interior of the chamber is enclosed by two μ-metal magnetic shields that are integrated into the photoelectron analyzer's μ-metal shielding to minimize stray magnetic fields that interfere with ballistic electron trajectories. This chamber houses our electron analyzer and several light sources.

2.5.1 Light sources

ARPES typically requires a high intensity of monochromatic light in the 5-100 eV range. Low resolution ARPES requires <100 meV linewidths, and high resolution studies can approach 1 meV or better. Historically synchrotrons have been by far the most useful source of photons in this range, and have been used extensively for ARPES. Their advantages include not only high flux and excellent energy resolution, but tunable photon energies and polarizations, which can be used to reveal the orbital character and symmetry of electronic structure. More recently, lab based ARPES systems have become increasingly common, and their light sources have seen dramatic improvements.

Our lab makes extensive use of a VG Scienta VUV 5000 helium plasma lamp. This source provides high resolution ($\Delta E < 2$ meV) photons at several helium resonances, the most intense being He Iα at 21.2 eV and He IIα at 40.8 eV. Our system includes a grating monochromator and a retractable glass capillary. The entire path from helium plasma to the sample is windowless due to the high absorption of all materials within this photon energy range. For this reason, the path from plasma to sample contains several narrow apertures and is differentially pumped by three turbopumps in series. The glass capillary serves the obvious use of directing the beam at the sample to provide a reduced spot size (FWHM = 2mm), but serves the additional purpose of providing a final high-impedance aperture on the gas load within the lamp. Under our current differential pumping setup, we are able to maintain a helium plasma at $> 10^{-3}$ Torr in the lamp head while causing a rise in the lower chamber pressure of only 5×10^{-11} Torr. We also note that the increase in chamber pressure consists of high-purity helium, which is highly non-reactive and therefore is not expected to significantly reduce the lifetime of samples within our ARPES measurements. We measured the integrated flux exiting the capillary to be 8.8×10^{11} photons/sec at 21.2 eV and 3.0×10^{10} photons/sec at 40.8 eV using a calibrated photodiode from IRD Incorporated (now Opto Diode Corporation).

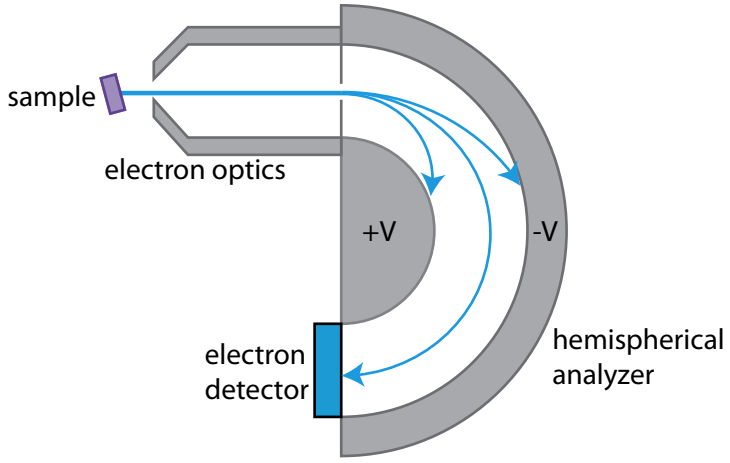

Figure 2.8: The mechanism for resolving electron energies with a hemispherical analyzer. Electrons that are too slow moving fall into the inner sphere. Electrons that are too fast hit the outer sphere. Only electrons within a narrow energy window can make it through the analyzer and reach the electron detector.

Several low photon energy (< 10 eV) sources have been recently developed [42, 43]. The chief advantage here is the increased momentum resolution obtained by using smaller overall photoelectron momentum, although there is a corresponding reduction in the accessible range of k-space. According to the universal curve (Fig. 2.2) these sources are also expected to provide a longer electron mean free path than deep-UV sources, resulting in less surface sensitivity. Our lower chamber includes a CaF_2 viewport to allow the use of out-of-vacuum photon sources with energies up to 10 eV. We operate a 5.5 eV quasi-CW laser from Photon Systems ($\Delta E < 10\,\mu$eV). In addition, we developed a high-resolution tunable photon source based on a monochromated Xe lamp that operates continuously up to 7 eV [44].

2.5.2 Electron analyzer

Initial ARPES studies operated using point-detectors of electrons. Angle-resolution was obtained by moving the sample or detector, and acquiring a single spectrum for each set of angles. Fortunately, those days are gone. All modern ARPES systems operate using area detectors that use electron optics to image a wide angular range simultaneously, a technique pioneered by VG Scienta. Our lab operates a Scienta R4000 electron spectrometer capable of simultaneously recording 600 spectra over an angular range of 30 degrees. In this system, electrostatic optics focus electrons to image them in angle along ϕ and reduce their kinetic energy to operate within the specified pass energy of the spectrometer. The electrons then pass through a narrow slit before entering the hemispherical portion of the spectrometer (Fig. 2.8). The energy analyzer consists of a positively charged inner hemisphere and a negatively charged outer hemisphere at an average radius of $r = 200$ mm. The bending radius of the electron trajectories depends on their kinetic energy, so when they impinge on the electron detector at the exit port they have been spread based on electron energy along one axis and ϕ (by the lens) along the perpendicular axis.

The theoretical energy resolution of the detector depends on the user selectable pass energy and entrance slit size as:

$$\Delta E \approx \frac{sE_P}{2r}$$

Where s is the slit width and E_P the pass energy of the analyzer. We can select slit widths of 0.1-2.0 mm and pass energies of 1-200 eV, resulting in a theoretical best energy resolution of $\Delta E \approx$0.25 meV. Factory resolution tests of our spectrometer were performed for a 2 eV pass energy and 0.2 mm slits and indicated a resolution of $\Delta E = 0.9$ meV, in excellent agreement with the calculated $\Delta E \approx 1$ meV for these settings. Larger slits and pass energies result in poorer resolution but higher intensities, since many more electrons are transmitted through the analyzer. The angular resolution is determined primarily by the electron optics and the emission spot size (smaller spots allow for higher angular reso-

lution), and can in principle reach an ultimate resolution of $\Delta\theta$ = 0.1 deg. Under typical operating conditions, we use an an angular range of 30 deg. and measure emission from a $\leq$ 3 mm spot, which results in an angular resolution of $\Delta\theta \approx 1$ deg.. A higher resolution of $\Delta\theta \approx 0.5$ deg. can be achieved under similar conditions by operating the lens within a more narrow angular range of 14 deg.

2.5.3 Ultra-high vacuum and surface preparation

Due to the surface sensitivity of ARPES, surface cleanliness if of the utmost importance. A fraction of a monolayer coverage can cause severe distortions of the photoemission spectra by modifying the electronic structure in the surface region, particularly for highly reactive materials. At atmospheric pressure, a monolayer of coverage can form within several nanoseconds. To maintain a pristine surface for the several hours to days that a typical ARPES experiment takes, experiments must be performed in a UHV environment with pressures $< 10^{-10}$ Torr. This places severe restrictions on the equipment, methods, and in some cases samples that may be used.

Our chamber achieves a base pressure of 4×10^{-11} Torr through a combination of UHV pumps. The upper chamber is pumped by a magnetically levitated turbo pump. This pump has a compression ratio for N_2 of 10^8, so to allow the upper chamber to reach 4×10^{-11} Torr the backing line must be at $< 4 \times 10^{-3}$ Torr. This is achieved via a second turbopump in series with the first that maintains a backing line pressure of $< 10^{-4}$ Torr. The lower chamber is pumped primarily by a cryogenic pump operating at $\approx$ 10 K and with a pumping speed of 4000 l/s for water and $>$ 1000 l/s for many other gases. In addition, the chamber contains three titanium filaments that are used to sublimate fresh titanium onto the walls of the bottom half. Titanium is highly reactive and forms an effective getter pump when used in this fashion.

The need for UHV also means that sample surfaces must be prepared in the photoemission vacuum chamber. It would do no good to have prepared an atomically clean surface only to expose it to atmosphere shortly thereafter. By far the most common approach is to obtain a pristine surface by cleaving a single crystal in the ARPES chamber. Many quasi-two-dimensional materials cleave well along a particular crystallographic plane, and this approach has directly lead to the extensive literature on cuprates and Ruddlesden-Popper transition metal oxides. Unfortunately, there is a vast array of compounds that do not readily cleave but are nonetheless physically interesting. Furthermore, recently great interest has been focused on the states forming at interfaces between complex materials, and cleaving does not provide a practical means for accessing these through ARPES. As described in the following chapter, we have developed in-situ sample synthesis capabilities so that high-quality crystals can be grown with pristine surfaces and transferred directly to our ARPES chamber without breaking vacuum.

Chapter 3

Molecular-beam epitaxy and in-situ ARPES

Molecular-beam epitaxy (MBE) is capable of producing extremely high quality crystalline films with record breaking carrier mobilities [45], but stripping away the (many) details can be thought of as nothing more complex than "atomic spray painting" [18]. Individual elements are thermally evaporated in a vacuum chamber. The resulting *molecular beams* converge on the surface of a suitable substrate and condense to form a thin film. By shuttering each molecular beam on and off, the composition of the film can be precisely controlled. Growth rates as low as a single atomic monolayer per minute can be easily achieved, allowing exquisite control over the film's composition and structure at the atomic scale.

This technique was initially developed in the 1960s by A.Y. Cho and J.R. Arthur and focused to a large extent on the growth of GaAs and (Al,Ga)As films and heterostructures on GaAs substrates [46]. Although this may seem like a great deal of trouble to go through

to end up with an ever-so-slightly thicker piece of GaAs, the results were groundbreaking. Films of unprecedented purity and crystalline perfection could be obtained and doped in a layer-by-layer fashion, resulting in greatly enhanced carrier mobilities over bulk crystals [47]. This has led directly to the development of new electrical and optical devices [48] and the discovery of new physics such as the fractional quantum Hall effect [49].

More recently, the 1986 discovery of high-temperature superconductivity in the cuprates [50] spurred the development of reactive oxide MBE systems capable of growing transition metal oxides in thin-film form [18]. These oxide MBEs opened the door to studying the wide array of complex properties associated with transition metal oxides in thin film form, leading to new multiferroics [51], interface-induced high-temperature superconductivity [20], and enhanced magnetic properties of layered structures [52] to name a few examples.

3.1 The power of perovskites

One of the core strengths of MBE is its ability to grow coherently strained epitaxial films, wherein the film inherits the lattice structure and in-plane lattice constants of the substrate. Biaxial strains higher than 3% are attainable using this technique, far beyond the point where bulk crystal would shatter [53]. Large biaxial strain allows us to tune hopping parameters and crystal-field splitting of the transition-metal *d* orbitals [54], as well as the interaction between the electrons and lattice. This can be used to achieve properties not attainable in bulk, such as multiferroicity of $EuTiO_3$ [10].

Unfortunately, not all films and substrates are compatible. The film must have a stable (or meta-stable) bulk crystal structure that is similar enough to the substrate for the accumulation of strain energy within the bulk of the film to be overwhelmed by the en-

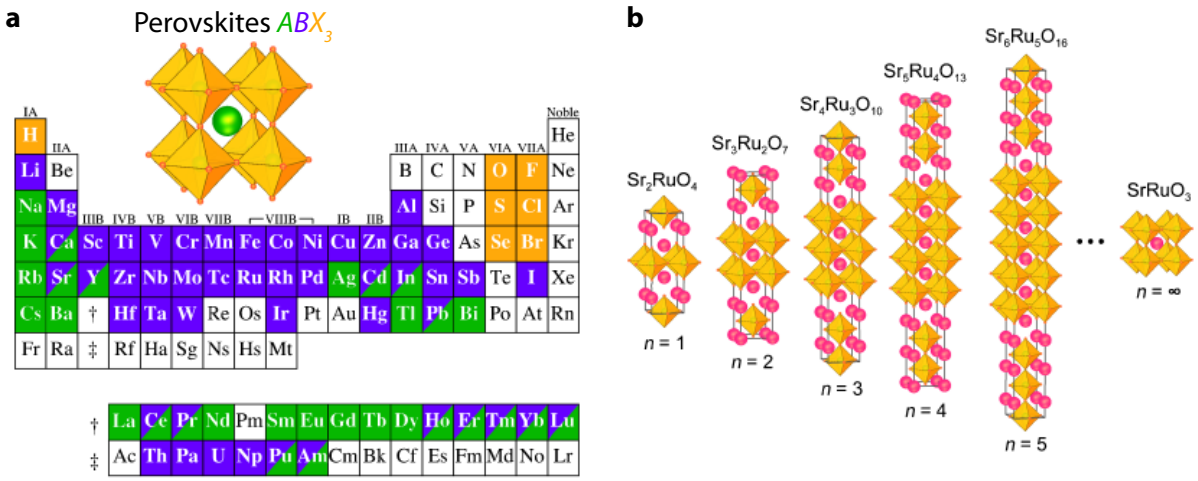

Figure 3.1: (**a**) The perovskite structure with A-site in green, B-site in blue, and the oxygen octahedra in yellow, along with a periodic table illustrating which sites can be occupied by various atoms. (**a**) The Ruddlesden-Popper series of layered perovskite based materials, here shown for $SrRuO_3$. The general form is $Sr_{n+1}Ru_nO_{3n+1}$. (Both figures reprinted from D.G. Schlom *et al.* (2008) [18], with permission from John Wiley and Sons).

ergy contribution from the film-substrate interface. This is where the perovskite structure comes to the rescue. In its ideal form, it has the formula ABX_3 and consists of a cube with an A atom at the center, a B atom at each corner, and an X atom at the center of each edge. For the oxides we are interested in, X is always oxygen. Figure 3.1a shows the structure along with a periodic table labeling each of the elements that can crystallize on one of the three sites. Remarkably, nearly all elements can form the perovskite structure. Furthermore, there are several families of related structures that, sharing a similar in-plane lattice structure, can be epitaxially grown on perovskite substrates, including the Ruddlesden-Popper family of layered materials (Fig. 3.1b).

Due to the vast array of perovskites, for a given compound of interest there exists a variety of suitable substrates with varying lattice constants. A summary of many commercially available perovskites substrates is provided in Fig. 3.2 in comparison to the

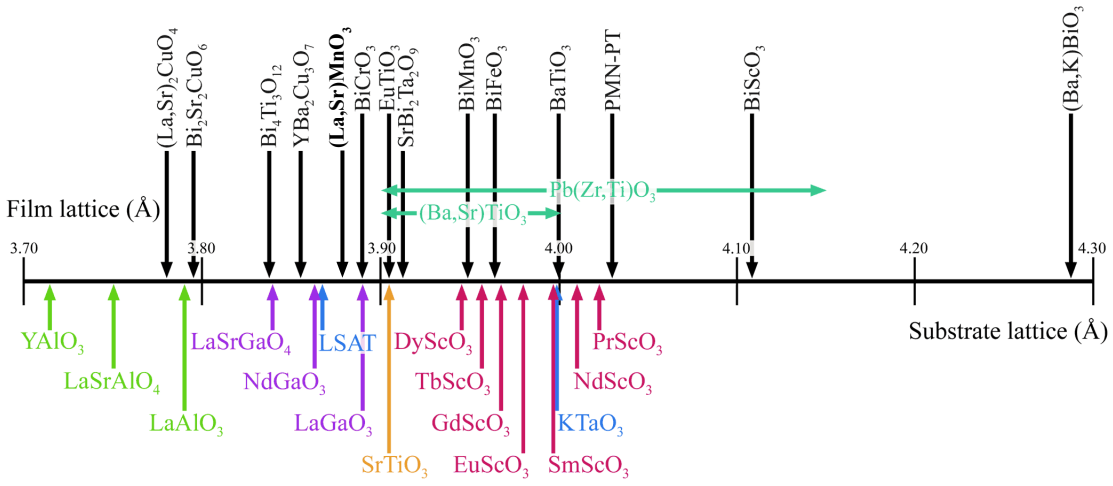

Figure 3.2: (**a**) Number line showing the pseudocubic lattice constants of several single crystal perovskite and perovskite related substrates (bottom) along with many thin films of interest (top). (Reprinted from L.W. Martin & D.G. Schlom (2012) [51], with permission from Elsevier).

bulk lattice constants of many films. For $La_{1-x}Sr_xMnO_3$ in particular, there exist many suitable substrates that give rise to films with dramatically different physical properties despite their identical chemical composition (chapter 6). A similar 'strain game' can be played with any perovskite compound of interest.

Many of these structures do not assume the full cubic symmetry of the ideal perovskite lattice, and tetragonal and orthorhombic forms are common. In particular, the oxygen octahedra are often rotated away from the line joining neighboring *B* atoms. The transition metal occupies the *B* site, and the oxygen-mediated hopping of the relevant *d* electrons depends sensitively on the angle of the *B*-O-*B* bond (section 4.2). This provides us with an additional means of controlling the properties of each film, since they not only depend on the *a* and *b* axis lattice constants, but also on the detailed oxygen rotation pattern, both of which can be inherited from the substrate.

In addition, the plethora of possibilities for chemically and structurally compatible

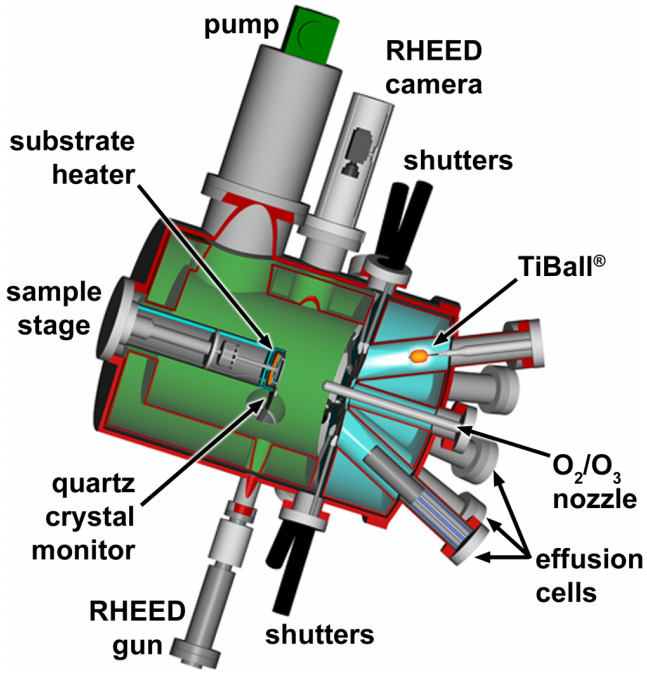

Figure 3.3: An MBE growth chamber with several key components labeled. (Reprinted from D.G. Schlom *et al.* (2008) [18], with permission from John Wiley and Sons).

compounds gives rise to the possibility of creating more complex *heterostructures*. The precision of MBE allows for the growth of films with atomic precision along the growth direction, so that one can grow structures consisting of stacks of many dissimilar materials and stabilize new electronic phases of matter at the interfaces [7]. Prominent examples include coupled magnetic and superconducting behavior at manganite-cuprate interfaces [55] and the strongly correlated electron liquid at the $LaMnO_3/SrMnO_3$ interface (chapter 7).

3.2 Experimental considerations

All of our films were grown using two different MBE systems: a dual-chamber Veeco 930 MBE and a dual-chamber Veeco GEN10 MBE. Figure 3.3 shows a schematic of one

growth chamber from the 930 MBE system, highlighting the key components. The sample stage can accept substrates of up to 3" diameter, although 10×10 mm substrates are more commonly used, and rotates during growth to ensures film uniformity. A heater holds the substrate at growth temperatures of up to 1000 °C. A quartz crystal microbalance (QCM) on a retractable arm allows for initial flux calibration, and reflection high-energy electron diffraction (RHEED) is used for finer flux calibration and monitoring film quality during growth. The GEN10 growth modules are each equipped with two RHEED systems at 45° to each other so that both the [100] and [110] directions can be simultaneously monitored. Oxygen and ozone are supplied via a nozzle focused on the substrate position to provide a locally high oxidant flux. Finally, automatically shuttered elemental sources provide a controllable, stable, and high purity atomic flux.

The 930 MBE is the older of the two and involves the manual transfer of samples into and out of the growth chambers using an in-vacuum *train* system. The GEN10 MBE is a state-of-the-art research MBE system, and includes a fully automated robotic sample transfer procedure.

3.2.1 Ultra-high vacuum

With growth rates routinely in the range of one unit cell per minute, the background pressure of unwanted vapors in the growth chamber must be very low to prevent their incorporation into the film. Our growth and transfer chambers typically operate with a background pressure of 10^{-9} Torr. In the transfer chamber, this pressure is maintained by the combination of an ion pump and a cryopump, and to preserve good vacuum samples are introduced through an additional load-lock chamber (pressure $< 5 \times 10^{-7}$ Torr). Both growth chambers are also equipped with cryopumps in addition to large (1800 l/s) turbopumps. During the growth of films requiring a high pressure of ozone in the cham-

ber, the cryopumps must be gated off to prevent them from becoming saturated with this dangerous substance, and the growth module is pumped solely by turbopump. In addition, a fortuitous side-effect of MBE growth is the evaporation of highly reactive metals over the walls of the vacuum chamber. This coating chemically reacts with and captures unwanted gases within the vacuum system, acting as an efficient getter pump.

Although introducing additional complexity into the design and operation of the MBE chamber, the requirement for UHV is the key reason for the compatibility of MBE with ARPES. Films grown by MBE typically have smooth, atomically pristine surfaces, and the UHV environment allows that surface to be preserved while the film is transferred to the ARPES measurement chamber.

3.2.2 Elemental sources

Any functional *oxide* MBE must have a source of oxygen. This is achieved by introducing gaseous oxygen into the growth chamber via a nozzle directed at the surface of the substrate. Obtaining a sufficiently high oxygen pressure to fully oxidize our films is often a source of difficulty, since the total oxygen pressure in our chamber is limited to $< 10^{-6}$ Torr by the requirement that we do not begin oxidizing the elemental sources.[1] Higher oxidation power can be obtained by replacing some or all of the O_2 with more reactive ozone (O_3). A 90% O_2 - 10% O_3 mix is obtained using a commercial ozone generator. Higher proportions of O_3 can be generated via a custom built ozone still. This uses a liquid nitrogen cooled porous silica gel to accumulate liquified O_3 over a period of several hours, which is then boiled off in a controlled fashion to supply O_3 for film growth. The use of O_3 is not for the faint of heart: if sufficiently high pressures are reached the accumulated O_3 will exothermically decompose to O_2 (i.e., explode). For this reason, many

[1] Recently, a new generation of differentially pumped sources has allowed us to grow at up to 10^{-5} Torr of 100% O_3 (ref. [56]).

safety precautions are taken including housing the ozone still within a steel blast cabinet.

The remaining elements are most commonly supplied from commercial Knudsen effusion cells. These consist of a crucible containing the desired element in high-purity form. The crucible is typically composed of alumina, tungsten, or pyrolytic boron nitride, chosen so as not to react with the source element at the evaporation temperature. The crucible is surrounded by coiled tungsten heating filaments and thermally shielded by a tungsten sheet metal enclosure. Combined with an internal thermocouple and PID temperature controller, a temperature stability of ±0.1°C can be maintained at source temperatures as high as 2000 °C, providing a uniform flux that drifts by << 1% per hour. The case of titanium is special due to its requirements for a high source temperature and its high reactivity. In this case, a Varian *Ti-ball* is used: a tungsten heating element enclosed within a thin-walled ball of titanium. The surface of the ball effuses as the source is used and provides a sufficiently stable flux for precision MBE growth.

Each source is initially calibrated using a QCM that can be placed directly in front of the substrate position. Mass accumulated on an oscillating quartz crystal induces a proportional change in the resonant frequency, as expressed by the Sauerbrey equation $\Delta f = -C\Delta m$, where C is a sensitivity factor derived from the quartz crystal dimensions [57]. The QCM takes advantage of this relationship by measuring Δf for an oscillating quartz crystal at the substrate position and converting this to a mass accumulation rate. With the known element atomic mass, an accurate flux is easily determined. This procedure gives a typical error of ±5% in the flux.

Blocking each effusion cell is a computer controlled programmable shutter, capable of opening and closing in ≈ 0.1 s. Once the sources have been accurately calibrated, the shutters are used to deposit the desired film in a layer-by-layer fashion, either one element at a time or by co-depositing several simultaneously.

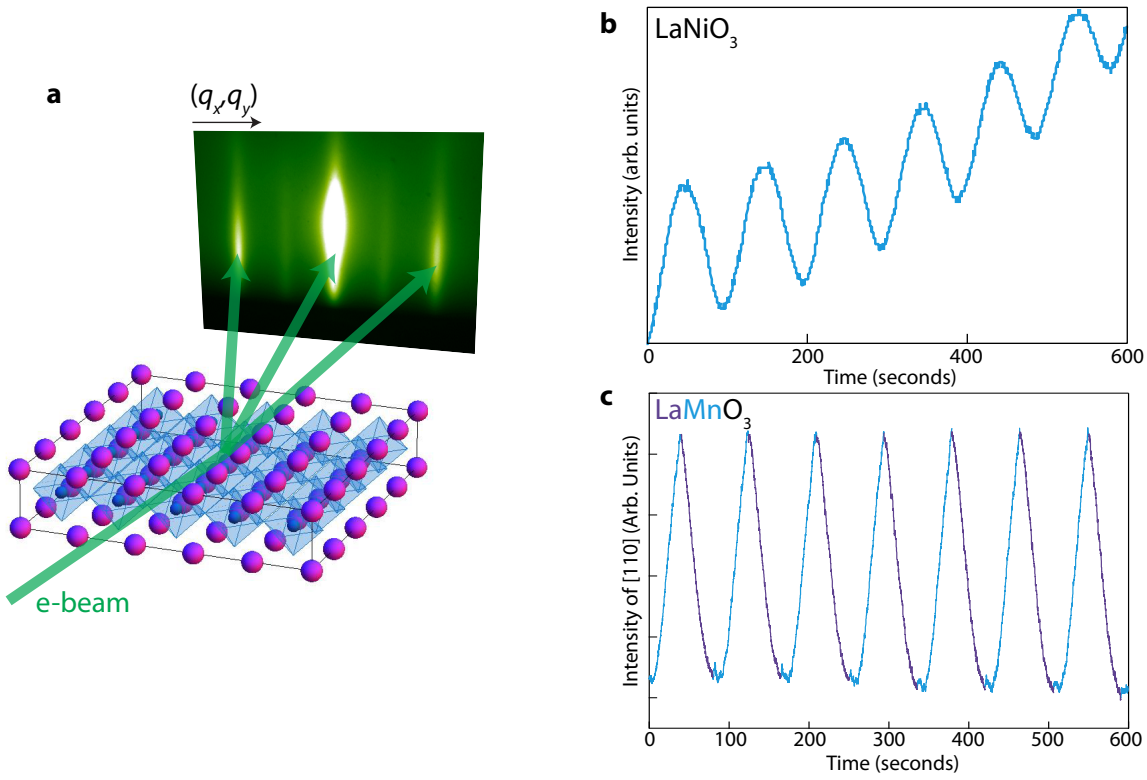

Figure 3.4: (**a**) Illustration of the RHEED process. High energy electrons at grazing incidence (green line) are reflected from the surface of a thin film producing a two-dimensional diffraction pattern. (**b**) Oscillations in RHEED intensity during the co-deposition growth of $LaNiO_3$ [56]. Each oscillation period corresponds to one monolayer of $LaNiO_3$. (**c**) Shuttered oscillations of the [110] peak intensity during the growth of $LaMnO_3$. The intensity increases when the Mn shutter is open and decreases when the La shutter is open.

3.2.3 Reflection high-energy electron diffraction

The MBE chamber is equipped with RHEED to monitor film quality during growth, and to assist in calibrating source fluxes [58]. Figure 3.4a illustrates the process. A beam of high energy (10 keV) electrons is directed at the sample surface at a grazing angle ($< 3°$). The diffraction pattern in the reflected beam is then measured by a phosphor screen on the opposite side of the vacuum chamber. The grazing angle results in a high degree

of surface sensitivity, so that RHEED represents an excellent means of characterizing the crystal structure at the surface of a thin film. RHEED patterns are typically acquired with the incident beam along a well-defined in-plane crystallographic direction ([100] or [110]).

Since RHEED measures a diffraction pattern from the film surface, there is no diffraction along the q_z direction and one might expect to see features that are sharply resolved in (q_x, q_y) but that form long streaks along q_z. Nevertheless, for diffraction from a perfect crystal the RHEED pattern will still show sharp points along the out-of-plane direction due to kinematic constraints on the electrons: (q_x, q_y) are determined by the surface diffraction pattern, and $|\mathbf{q}|$ must be equal to that of the incident beam. In a real material the diffraction peaks have finite width in (q_x, q_y), and correspondingly the spots along q_z are converted into streaks whose intensity profile is related to the crystalline perfection of the surface.

RHEED diffraction patterns play a key role in the accurate calibration of source fluxes. If one monitors the intensity of a RHEED diffraction peak during film growth, one often sees a characteristic oscillation in its intensity. As the deposition of a new monolayer begins, the film surface roughens and the RHEED intensity correspondingly decreases. As the layer approaches completion the RHEED intensity recovers (Fig. 3.4b). These *co-deposition* oscillations provide a precise measure of the source flux via the amount of time required to deposit one full monolayer, and can be used to determine an absolute calibration of the total flux to within 1% (ref. [59]). In a perovskite, we must calibrate two or more elements (the A and B sites), and so in addition we need a means for determining the relative $A : B$ stoichiometry.

The *shuttered* oscillation technique was developed for this purpose [59], and relies upon the fact that the RHEED intensity is sensitive to the surface termination of the film (Fig. 3.4c). Taking $LaMnO_3$ as an example case: the intensity of the RHEED pattern is highest for the MnO_2 surface. Opening the Mn shutter thus causes the RHEED inten-

sity to increase. After depositing approximately one monolayer of MnO_2, the Mn shutter is closed and the La shutter is opened. When the RHEED intensity reaches the starting point, equal amounts of Mn and La have been deposited. Fine-tuning the shutter times for each cycle allows calibration of the relative fluxes to within 1%. In practice, this step is performed before co-deposition oscillations are measured (to ensure they represent the growth of a stoichiometric film).

3.3 In-situ ARPES

We are not the first group to use in-situ ARPES to study the electronic structure of thin films, and several ARPES studies of thin films have been published to date. In this regard one must mention the pioneering work of Tai-Chang Chiang on the electronic structure of metallic quantum wells [60] that dates back to 1986. On the other hand, the growth of transition metal oxides with atomically pristine surfaces requires complex growth techniques like MBE or pulsed-laser deposition (PLD), and has only recently been achieved. Beginning in 2003 three synchrotron ARPES systems with oxide PLD capabilities came online at: (1) BL-1C of the Photon Factory at the High Energy Accelerator Research Organization (KEK) [61], (2) the Surface and Interface Spectroscopy beamline at the Swiss Light Source [62], and (3) BL17SU at SPring-8 (ref. [63]). All three have generated a considerable body of work and greatly improved our understanding of correlated transition metal oxides.

Nevertheless, in 2007 our group undertook the construction of the first in-situ oxide MBE-ARPES system. We pursued this course because of several important advantages of MBE over other growth techniques. First, MBE is a low energy growth mode involving thermal atoms and has the ability to independently control individual elemental fluxes. This enables unprecedented fine-tuning of growth parameters and minimizes damage

due to high-energy particles, resulting in extremely high quality films that are essential for our work on, for example, $SrRuO_3$ [64] and $La_{2/3}Sr_{1/3}MnO_3$ films (chapter 5). In addition, control of film structure at the monolayer-scale is readily achieved due to the individual-element shuttered growth inherent to the MBE process. This enables the growth of complex multi-layered heterostructures, essential to our work on $(LaMnO_3)_{2n}/(SrMnO_3)_n$ superlattices (chapter 7). Of course our chief advantage has been our expert collaborators in the form of Darrell Schlom and his team. Thin film growth is a complex field, and producing the highest quality films requires extensive experience and know-how. From the spectroscopist's perspective, in-situ MBE means unprecedented control over material composition, structure, and physical properties, while maintaining the atomically pristine surfaces required for ARPES measurement. This approach has been highly successful, and has garnered international recognition [65].

3.3.1 Experimental considerations

Figure 3.5 shows a simplified model of our in-situ MBE and ARPES system. The experiment starts by preparation of a substrate for film growth, which must be mounted to a sample holder compatible with the ARPES system. Our system can accommodate substrates of any size up to 10×10 mm, and sample holders with suitably sized pedestals are fabricated for each. Nevertheless, thermal performance at low temperature is significantly improved for smaller samples, and so we most often use 3×3 mm substrates. Substrates 10×10 mm in size are typically reserved for in-situ XPS measurements or when anticipated ex-situ characterization requires it.

The substrates are fastened to the sample holder using silver paint, which is found effective for substrate growth temperatures up to $\approx 900\,^{\circ}$C. Above this temperature, carbon based paint is used to mechanically secure the substrate, and gold paint is used to

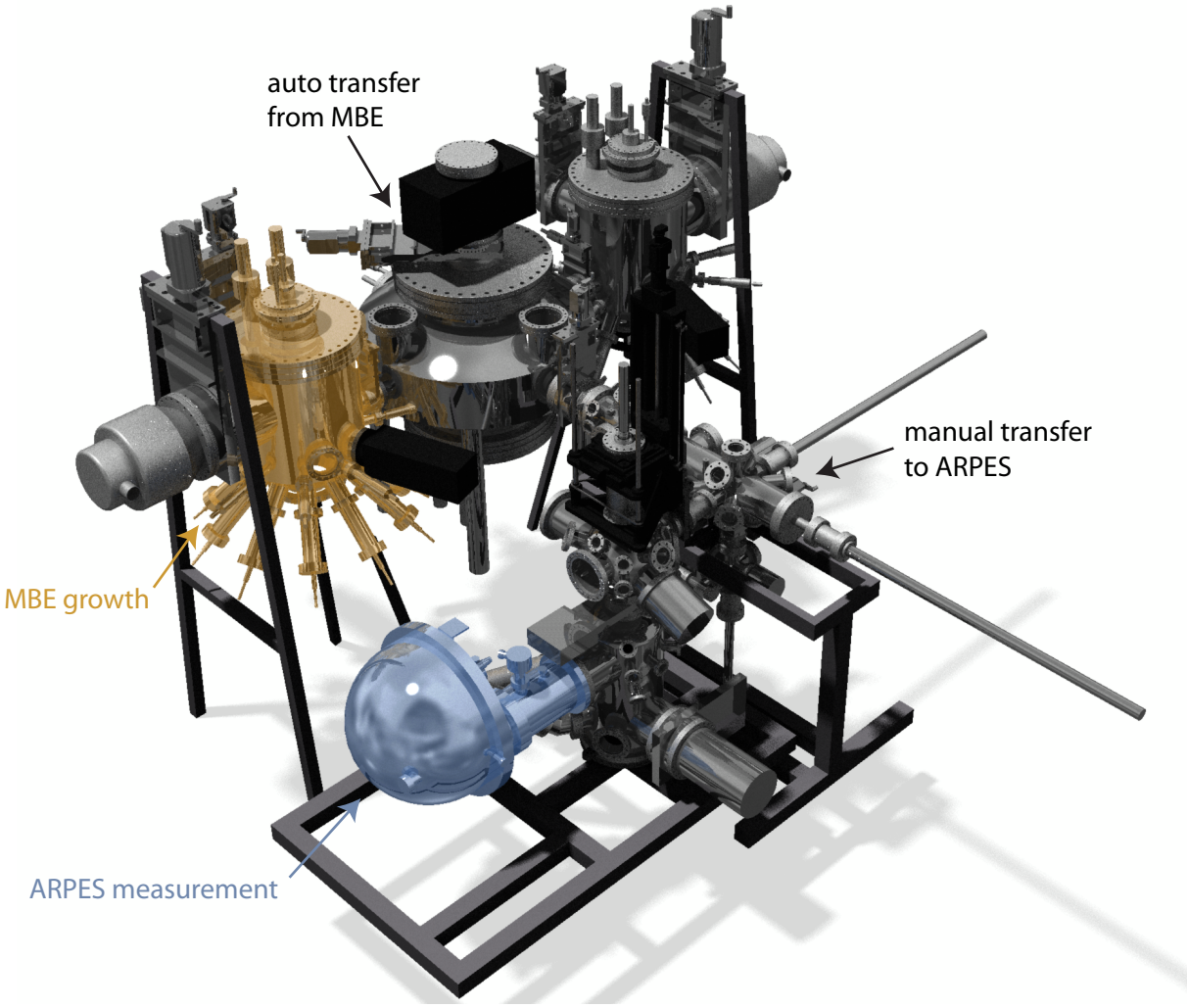

Figure 3.5: Rendered model of our combined oxide MBE-ARPES system. One of the two growth chambers is highlighted in gold, the ARPES analyzer is highlighted in blue, and the automatic and manual transfer stages are indicated.

electrically ground its surface. The ARPES sample holder is then loaded into a 3″ diameter wafer compatible with the MBE chamber made out of a corrosion resistant high nickel-content alloy, *Haynes 214*. Most films are grown using copper sample holders with an integral titanium screw due to copper's excellent thermal performance at low and high temperatures. Due to a Cu-Ti eutectic at 883 °C (ref. [66]), however, copper sample holders are unsuitable for growths above this temperature. In this case, Niobium sample

holders are used and have been found effective for growth temperatures up to 1000 °C. Niobium has a high thermal conductivity down to $T < 9$ K and provides adequate thermal performance for most ARPES measurements [67].

The Haynes wafer with its ARPES sample holder is then introduced to the MBE through its standard load lock and wafer transferring procedure, and growth proceeds as normal. After growth, the sample is kept deliberately warm ($\approx$ 200°C) to minimize surface contamination during the subsequent UHV transfer. Transferring from the growth chamber to the ARPES measurement chamber takes <5 minutes. First, the in-vacuum robotic arm removes the sample from the growth chamber and moves it to a manual-hand off point within the ARPES transfer chamber (pressure $\approx 10^{-10}$ Torr). Manually actuated transfer arms remove the ARPES sample holder with its attached film from the Haynes wafer and load it into the ARPES manipulator. The film is then cooled to measurement temperature, and the ARPES experiment begins.

Our system also contains an additional load lock, stemming off of the ARPES transfer chamber, which is used to bypass the MBE for bulk single-crystal studies, and to unload films after measurement.

Chapter 4

Physics of the manganites

Experimental studies of perovskites with the composition $RE_{1-x}AE_xMnO_3$ stretch back as far as 1950, when early work by Jonker and Santen on compositions with La as the rare earth (RE) and Ca, Sr or Ba as the alkaline earth (AE) discovered a stable ferromagnetic metallic phase over a wide range in x. Subsequent neutron scattering studies of the manganites began to unravel a complex phase diagram in temperature and x, including antiferromagnetism and signatures of possible charge ordering [68], and unusual magneto-transport was observed [69]. The intense current interest in manganites, however, arose as a consequence of the more recent discovery of *colossal magnetoresistance* in the early 1990s.

Magnetoresistance describes a change in resistance (R) under the application of a magnetic field (H), and is typically given by $(R(0) - R(H)/R(H)$ measured in percent. It is very small in ordinary metals, on the order of 1%. The realization that cleverly designed heterostructures could achieve a "giant" magnetoresistance exceeding 100% earned Albert Fert and Peter Grünberg the 2007 Nobel prize in physics and led directly to vast improvements in magnetic hard drive and sensor technology. Thus, when Jin et al. [70] observed

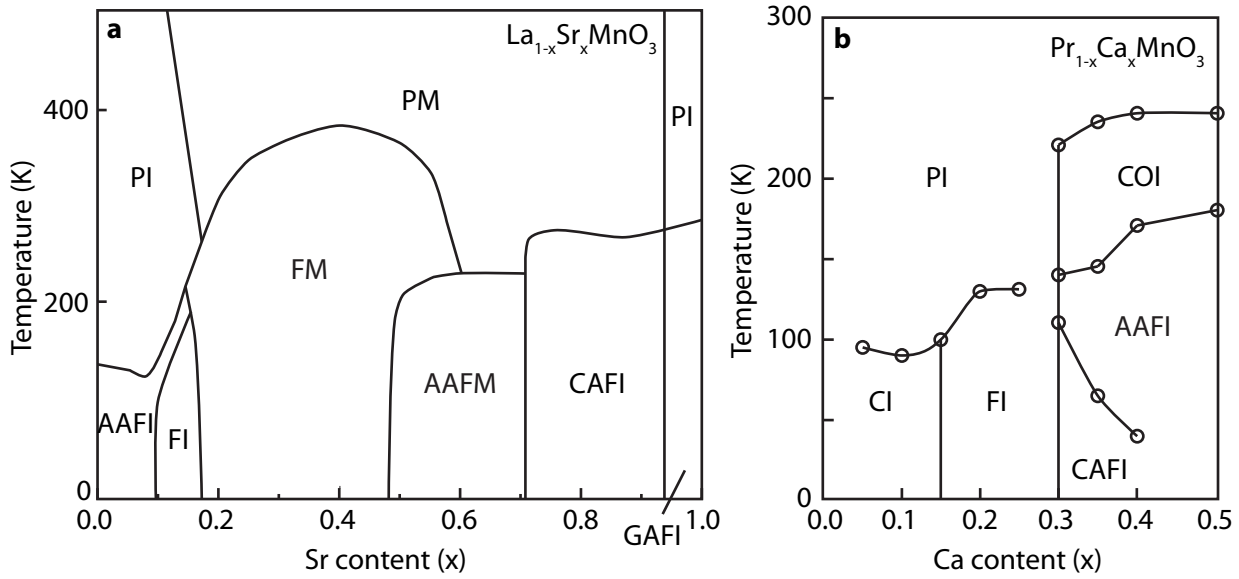

Figure 4.1: (**a**) Phase diagram for $La_{1-x}Sr_xMnO_3$ based on ref. [72]. (**b**) Phase diagram for $Pr_{1-x}Ca_xMnO_3$ (adapted with permission from Y. Tomioka, A. Asamitsu, H. Kuwahara, Y. Moritomo & Y. Tokura (1996) [73]. Copyright 1996 by the American Physical Society). Phases are: P = paramagnetic, F = ferromagnetic, AAF = A-type antiferromagnetic, CAF=C-type antiferromagnetic, C=charge ordered, CO = charge and orbital ordered. The last letter for each phase indicates whether it is metallic (M) or insulating (I).

$\delta R/R = 127,000\%$ in $La_{0.67}Ca_{0.33}MnO_3$ films in 1994, interest in the manganites exploded. Magnetoresistances as high as 10^{13} % were rapidly achieved [5]. Soon after, Millis et al. [71] demonstrated that simple electronic bandstructure considerations alone could not explain the magnitude of the observed effects, and that they must be tied to more complex many body interactions. Further theoretical work by Dagotto emphasized the important role played by the close competition between insulating and metallic ground states and the real-space phase separation between them [11]. The focus of manganite research has thus shifted toward achieving a more fundamental understanding of the complex phase diagrams underlying their astonishing electric and magnetic properties.

Figure 4.1 provides example phase diagrams for the cases of $La_{1-x}Sr_xMnO_3$ and

$Pr_{1-x}Ca_xMnO_3$. We will return to discuss these diagrams in more detail below, but of particular note is the large ferromagnetic metallic phase seen for $La_{1-x}Sr_xMnO_3$ near $x = 1/3$, whereas the isovalent compound $Pr_{1-x}Ca_xMnO_3$ shows no metallic phases whatsoever. That such a dramatic change in behavior can occur for a relatively small change in the lattice already indicates the complex physics underlying the properties of the manganites. The colossal magnetoresistance effect that sparked such interest to begin with is also closely tied to the many possible phases: it is strongest at the boundaries between the ferromagnetic and antiferromagnetic phases, and is most dramatic when a charge or orbital ordered insulator competes with the ferromagnet.

4.1 Electronic degrees of freedom

What is so special about manganites? The combination of many competing interactions and a degenerate electronic structure is a recipe for complexity, and it turns out that manganites fall precisely within this regime. The electronic properties of transition metal oxides are controlled by the transition metal $3d$ electrons, which are well known to support a close competition between the on-site Coulomb interaction and hoping to neighboring atoms. Furthermore, manganites have 3 to 4 d electrons per manganese atom, which results in a degenerate ground state that is highly sensitive to perturbations. The resulting electronic phase is highly sensitive to a variety of lattice, spin, charge and orbital effects.

4.1.1 Orbital effects

Orbital effects are intimately coupled to all other degrees of freedom within the manganites. We start with simple ionic considerations of $RE_{1-x}AE_xMnO_3$. The oxygen atom is highly electronegative, and forms O^{2-}. The rare earths assume a 3+ state, and the alkaline

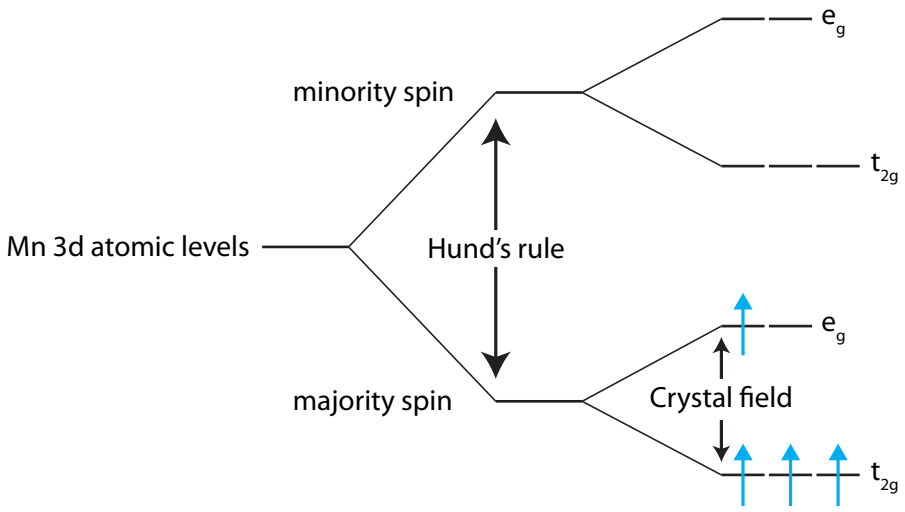

Figure 4.2: An energy diagram showing the degeneracy within the manganese 3*d* orbitals due to Hund's rule and crystal field splitting.

earths assume a 2+ state. Thus, we expect to find manganese in a valence of 3+ (4 *d* electrons) to 4+ (3 *d* electrons), depending on x. More precisely, the number of *d* electrons per Mn atom is given by $4-x$. This picture is more complex in practice, and it has been shown that for $0 < x < 0.3$ there is considerable charge transfer to the oxygen atom so that the true orbitals near E_F have strong Mn-O hybridization [74]. Nevertheless, first-principles calculations [75] and ARPES experiments on a variety of compounds (see e.g., ref. [76] and chapter 5) have demonstrated that the hybridized bands respect the symmetry of pure manganese *d* states, so that this remains a useful way of thinking about and modeling these compounds. This is directly related to the Zhang Rice singlet concept employed in the cuprates [77], whereby the itinerant hole on the oxygen sites surrounding a copper atom takes up the symmetry of the copper e_g orbital.

Hund's rule

Figure 4.2 shows a schematic diagram of the energy levels derived from manganese d orbitals in the manganites. From atomic physics, there are 10 degenerate d orbitals. Thus, our occupancy of $4 - x$ represents a less than half-filled shell. Hund's rule dictates that in this scenario the spins of the d electrons must all align. This splits the d manifold into five partially occupied states of one spin, and five unoccupied states of the other, and is the reason for the magnetic behavior of the manganese ion. Notably, this implies that E_F must fall within a 100% spin-polarized band for metallic manganites. Full spin polarization could result in a number of useful spintronic applications and is supported by several experiments [78, 79, 80].

Crystal field effects

The degeneracy of the remaining five d orbitals is then further reduced due to *crystal field effects* from the surrounding atoms within the crystalline environment (Fig. 4.2). The manganites discussed here all have perovskite or perovskite based (i.e., Ruddlesden-Popper) lattices. The ideal cubic perovskite structure surrounds each manganese atom with an octahedral arrangement of oxygen atoms (Fig. 3.1). This cubic crystal field splits the d manifold into a set of three t_{2g} and two e_g orbitals, as shown in Fig. 4.3. The hybridization between the manganese d orbitals and oxygen $2p$ orbitals is of an anti-bonding character, so orbitals that approach closest to the oxygen atoms, the e_g states, have the highest energies. Thus, we arrive at a state containing three electrons in the three t_{2g} orbitals and $1 - x$ electrons in the two e_g orbitals, all of which are aligned in spin. The spin-polarized t_{2g} electrons form an important magnetic background, but it is the partially occupied e_g states that reside closest to E_F and are ultimately responsible for the electronic properties.

The shape of the e_g orbitals plays an important role in electron transport. It is trivial

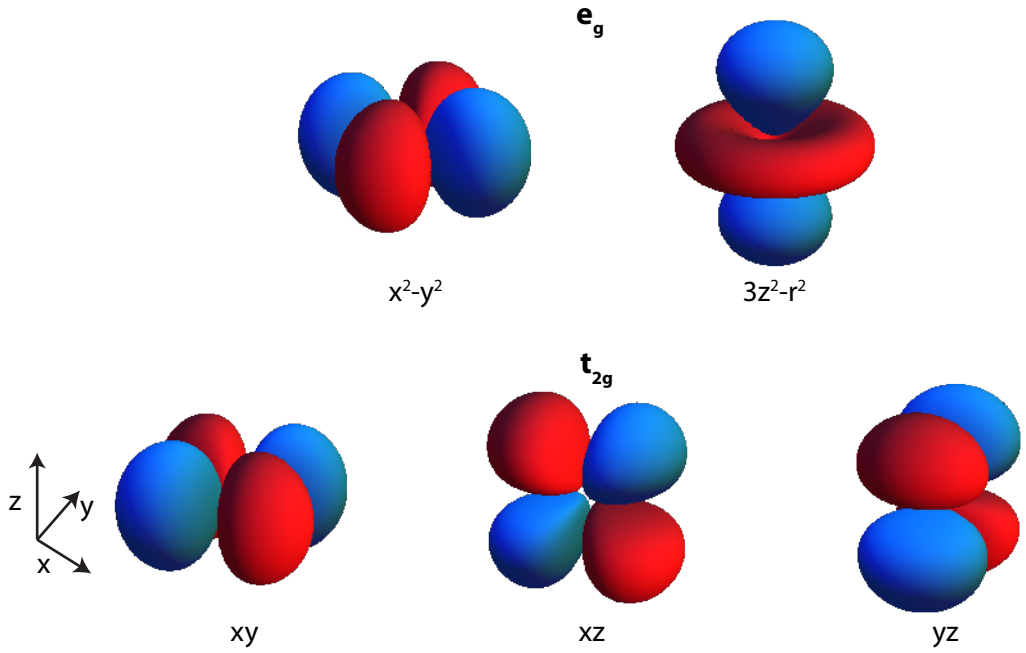

Figure 4.3: The five d-orbitals that are eigenstates of the cubic crystal field. Color indicates the sign of the wavefunction. For perovskites, the t_{2g} orbitals are lower in energy than the e_g orbitals.

to show by symmetry alone, for instance, that the $d_{x^2-y^2}$ orbital has an overlap integral of zero with the neighboring O $2p$ states along the z direction. Therefore, the z direction hopping vanishes for $d_{x^2-y^2}$ electrons. Conversely, the $d_{3z^2-r^2}$ orbital has its hopping within the (x, y) plane reduced by a factor of four with respect to the z direction [81]. Thus, states exhibiting varying amounts of orbital polarization[1] will also show a corresponding anisotropy in electron transport and any other effects that derive from electron hopping.

It is worth noting here that a loss of cubic symmetry can further break the degeneracies within the t_{2g} and e_g manifolds. This is less important for t_{2g} states, which are always fully occupied, but is critical for the partially occupied e_g. For example, the tetragonal crystal

[1] In the manganite literature, the phrase orbital *order* is used in an inconsistent manner and often interchangeably with orbital *polarization*. I exclusively reserve the phrase orbital *order* for states that consist of a non-trivial real space pattern that breaks the translational symmetry of the ideal crystal lattice (e.g., the checkerboard alternation between $d_{3x^2-r^2}$ and $d_{3y^2-r^2}$ found in $LaMnO_3$ (Fig. 4.6)). I use orbital *polarization* to refer to phases in which there is a uniform preferential occupation of one e_g orbital at the expense of the orthogonal orbital.

field of the Ruddlesden-Popper manganites drives a lowering of the $d_{x^2-y^2}$ with respect to the $d_{3z^2-r^2}$ orbital, resulting in a strongly orbital polarized state [82]. A similar effect plays a central role in epitaxially strained manganites, where the relative occupancies of the two e_g orbitals are tuned by the sign and degree of tetragonal strain [83].

4.1.2 On-site Coulomb interactions

Due to its small spatial extent, the $3d$ orbital generally has a strong on-site Coulomb interaction that associates a large energy cost with double occupancy of the same orbital (i.e., the Hubbard U). This is of course closely related to the Hund's rule discussed above: both stem from the same underlying Coulomb interactions, and both effectively prevent double-occupancy of d orbitals. The chief difference being that the Hubbard U works to prevent double occupancy of a single orbital regardless of the direction of spin, whereas Hund's rule enforces the alignment of spin between different orbitals. Also of relevance is the on-site coupling between the two distinct e_g orbitals (often denoted U'). This term works to prevent the simultaneous occupation of both e_g orbitals on the same manganese site.

4.1.3 Jahn-Teller electron-phonon coupling

In Fig. 4.4 we consider the case of a manganese atom with occupied $d_{3z^2-r^2}$ orbital. Following our discussion of the crystal field effect, it is clear that by extending the Mn-O bond length along the z direction we could lower the energy of the $d_{3z^2-r^2}$ orbital at the expense of raising the $d_{x^2-y^2}$ energy. Since $d_{3z^2-r^2}$ is occupied and $d_{x^2-y^2}$ is not, this corresponds to a net lowering of the total energy of this ion. Such a breaking of an orbital degeneracy due to a lattice (or molecular) distortion is generally referred to as the Jahn-Teller effect. The

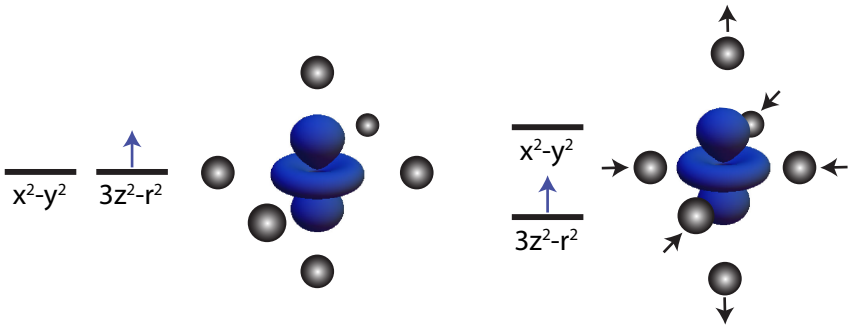

Figure 4.4: The Jahn-Teller effect on the $d_{3z^2-r^2}$ orbital. By breaking the cubic degeneracy of the surrounding oxygen atoms through a bond-stretching distortion, the energy of the occupied state is lowered.

same argument applies to the case of an occupied $d_{x^2-y^2}$, which couples to an analogous distortion. This Jahn-Teller effect gives rise to a strong electron-lattice coupling between oxygen octahedron distortions and the e_g electrons. Furthermore, this effect cooperates with the U' discussed in the previous section by also preventing the simultaneous occupation of both e_g orbitals on the same ion. The reason is clear: with both e_g orbitals occupied, the d manifold is half filled and hence spherically symmetric. There is no energy gain from anisotropic octahedron distortions in this case, since any energy gained by $d_{3z^2-r^2}$ is lost by $d_{x^2-y^2}$.

The Jahn-Teller interaction differs from the other interactions discussed so far in that it intrinsically couples neighboring manganese ions. A local extension of one Mn-O bond reduces the length of the neighboring O-Mn bond, since both share the same oxygen atom. This can be advantageous in cooperatively distorted phases, wherein the occupied e_g orbital alternates from site-to-site to take advantage of the alternating lengthening and shortening of Mn-O bonds. In addition, uniformly distorted states can occur where, for example, the crystal c axis globally expands, the a and b axes shrink, and a uniform $d_{3z^2-r^2}$ orbital polarization is established. Nevertheless, the case of a local distortion around a single electron in the orbital disordered phase is an important one since it is responsible

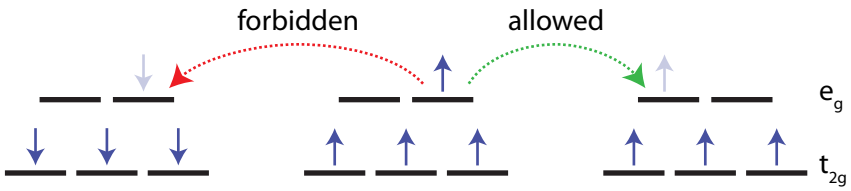

Figure 4.5: The double exchange effect. Due to the Hund's rule coupling between e_g and t_{2g} states, hopping is forbidden between neighboring manganese atoms whose t_{2g} spins are antiferromagnetically aligned.

for the formation of lattice polarons, in which the electron travels with or in the extreme case is localized by a surrounding lattice distortion [84, 85]. Scattering, transport, optical and photoemission experiments, including those discussed in this dissertation, all see pronounced effects of the electron-lattice interaction on the charge carriers that indicate their strongly-coupled polaronic nature [86, 87, 88, 89, 90, 91, 92].

4.1.4 Double exchange

So far I have discussed the mechanisms that enforce a local spin polarization of the manganese atoms, but I have yet to address the mechanisms that couple the spins of neighboring atoms and give rise to macroscopic magnetic order. The most important of these is the *double exchange* interaction, a consequence of the combination of strong Hund's rule with itinerant e_g states [93]. Figure 4.5 schematically illustrates the relevant processes. Hund's rule only allows hopping of the e_g electron to sites with an aligned t_{2g} spin, and thus the kinetic energy of the system strongly favors the ferromagnetic state. In the opposite extreme, a state with antiferromagnetic alignment between all neighboring manganese sites experiences a large kinetic energy cost. More generally, by treating the t_{2g} spins classically, Anderson and Hasegawa [94] showed that the effective hopping between manganese atoms scales as $t_{eff} = t \cos\theta_{spin}/2$, where θ_{spin} is the angle between spins

on the two sites. This mechanism depends strongly on the carrier concentration, and so it is weakest for $x \approx 0$ and $x \approx 1$.

4.1.5 Direct exchange

At $x = 1$ the double exchange interaction is irrelevant and the manganites assume an antiferromagnetic order. This state arises due to the direct exchange interaction between neighboring t_{2g} orbitals. The virtual hopping responsible for the exchange interaction is excluded by the Pauli principle when neighboring spins are aligned. Thus, this term is exclusively antiferromagnetic and competes with the ferromagnetic double exchange. Since it relies on direct hopping between manganese sites, rather than the much stronger Mn-O-Mn hopping contributing to the double exchange and kinetic energy, it is very weak. Nevertheless, direct exchange plays an important role in the manganite phase diagram due to the close competition between all other interactions. Even a small effect can tip the scales and stabilize a new ground state.

4.1.6 Constructing a general Hamiltonian

From the above considerations, one can construct an approximate Hamiltonian to describe the physics of the manganites (the *two orbital model* [11]):

$$H = -\sum_{\mathbf{i}\mathbf{a}\gamma\gamma'} t^{\mathbf{a}}_{\gamma\gamma'} c^{\dagger}_{\mathbf{i}\gamma} c_{\mathbf{i}+\mathbf{a}\gamma'} - J_H \sum_{\mathbf{i}} \mathbf{s_i} \cdot \mathbf{S_i} + J_{AF} \sum_{<\mathbf{i},\mathbf{j}>} \mathbf{S_i} \cdot \mathbf{S_j} + H_{JT}$$

The operator ($c^{\dagger}_{\mathbf{i}\gamma\sigma}$) creates an electron in an e_g orbital at site $\mathbf{i}$ with spin σ, and γ differentiates between the two orthogonal orbitals. We use $\mathbf{s_i}$ and $\mathbf{S_i}$ to represent the e_g and t_{2g} spins, respectively, and $\mathbf{a}$ denotes a nearest-neighbor translation. The effect of the cubic crystal field is incorporated implicitly by our assumption that only the e_g orbitals change

occupancy. The only degree of freedom for the t_{2g} manifold is the direction of its spin, whose magnitude remains fixed at $|\mathbf{S}| = 3/2$. Also of note is the absence of a Hubbard U term. As previously discussed, U becomes irrelevant for a strong Hund's rule coupling. This amounts to a great simplification of the Hamiltonian, and thus is typically assumed to be the case. I have left out the explicit form of the Jahn-Teller electron phonon interaction (H_{JT}). This couples distortions of the oxygen octahedron to the e_g occupancy of each site, and as usual is parametrized by a dimensionless constant λ.

Optical conductivity and photoemission experiments have been used to estimate the rough magnitudes of each of these parameters, and are summarized in ref. [11]. The hopping parameter $t \approx 0.5$ eV is small compared to the Hund's rule coupling $J_H \approx 2$ eV that enforces the spin-polarized bandstructure and underlies the double exchange interaction. The Jahn-Teller coupling is very strong with $\lambda \geq 1$. The smallest parameter is the direct t_{2g} exchange interaction $J_{AF} \approx 0.05$ eV, which is nevertheless critical for differentiating between various magnetic phases that can lie close in energy.

The presence of this multitude of competing interactions coupled with the e_g orbital degeneracy gives rise to the complex phase diagrams of the manganites and their high sensitivity to nearly any form of external perturbation.

4.2 Important electronic phases

Figure 4.1 shows phase diagrams for $La_{1-x}Sr_xMnO_3$ and $Pr_{1-x}Ca_xMnO_3$ as a function of x and temperature, but due to the strong difference between the two it is clear that there must be an additional important parameter controlling the macroscopic properties. The two compounds are isovalent; the difference arises due to the difference in ionic radii (r_A)

between (La,Sr) and (Pr,Ca), which can be described by the tolerance factor:

$$\Gamma = \frac{r_{\mathrm{A}}}{\sqrt{2} r_{\mathrm{Mn}}}$$

$\Gamma = 1$ in the ideal cubic structure, but the perovskite lattice can accommodate an enormous range of atoms on the A-site (Fig. 3.1) that cannot all precisely match the Mn ionic radius. Thus, the ideal cubic condition is usually not satisfied and we typically have $\Gamma < 1$. In such a case, the A-site is too small and the oxygen atoms shift toward this position, distorting the Mn-O-Mn bond angle away from the ideal $\theta = 180°$. The Mn-O-Mn overlap integrals responsible for hopping are largest when the Mn e_g and O $2p$ orbitals are aligned, but fall off as $\cos\theta$ when the bond is distorted (by the symmetry of the O $2p$ orbital, it is trivial to see that the overlap vanishes when $\theta = 90°$) [11]. Thus, we see that the key parameter for driving electron itinerancy is highly sensitive to the radius of rare earth and alkaline earth elements used for the perovskite A-site. Manganites with $\Gamma \geq 0.93$ are referred to as *large bandwidth* compounds. Conversely, when $\Gamma \leq 0.91$ the compounds have *small bandwidth* and the electrons should exhibit a greater tendency towards localized or insulating phases.

We see the role of the tolerance factor directly in the phase diagrams of $La_{1-x}Sr_xMnO_3$ and $Pr_{1-x}Ca_xMnO_3$, typically considered as canonical large and small bandwidth compounds. $La_{1-x}Sr_xMnO_3$ has a tolerance factor of 0.93 at $x = 0.3$ (ref. [95]), and exhibits a robust metallic phase spanning a wide region in x and T. On the other hand, $Pr_{1-x}Ca_xMnO_3$ has a tolerance factor of 0.91 at $x = 0.3$ (ref. [95]), and shows strong tendencies towards the formation of charge and orbital ordered insulating phases.

The phase diagrams are complex and show many different magnetic, charge, and orbital ordered phases. Several magnetic order patterns were discovered in the very early days of manganite research, and have since followed the alphabetical naming convention used by ref. [68]. We discuss several examples in what follows, but note that new phases of the manganites are still being actively discovered, and there remain many open ques-

tions about the nature of the different charge and orbital ordered phases and even the many-body physics relevant to metallic states.

Ferromagnetic metal

The ferromagnetic metallic phase occurs when the kinetic energy dominates over other terms in the Hamiltonian. The magnetic moments are ferromagnetically aligned and the e_g orbitals typically show negligible or small polarization. Nevertheless, fluctuations [96] or phase separation [11] involving other insulating phases play an important role, and the metallic charge carriers show indications of a strongly polaronic nature [85].

G-type antiferromagnetism

The ground state for $x = 1$ is the G-type antiferromagnet [97]. This composition has no e_g electrons, and thus no ferromagnetic double exchange interaction. In this case, the antiferromagnetic direct exchange (J_{AF}) dominates and all manganese atoms are antiferromagnetically coupled to their neighbors. This phase is insulating even for $x < 1$, since the antiferromagnetic coupling along all directions prevents e_g hopping.

A-type antiferromagnetism

The A-type antiferromagnetic phase consists of two-dimensional ferromagnetic sheets that are coupled antiferromagnetically along the z direction. Due to double exchange, this tends to promote a state with itinerancy in the (x, y) plane but insulating behavior along z. This magnetic order is tied to two different orbital states. For $x \geq 0.5$, an

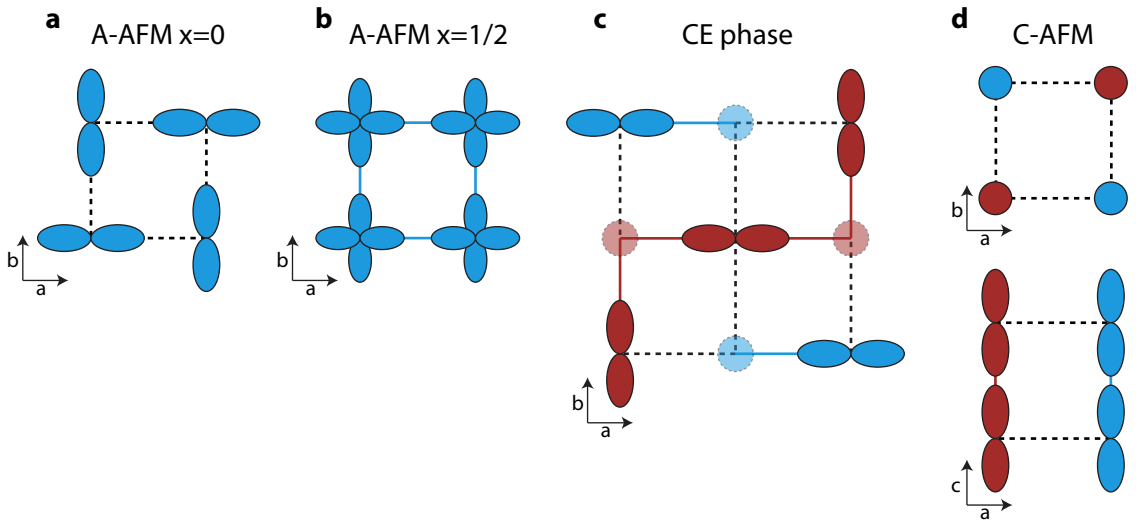

Figure 4.6: The magnetic (blue & maroon) and orbital order in several manganite phases. Colored lines indicate double exchange permitted hopping paths, whereas black dashed lines allow no hopping in the simplest 'cartoon' picture. Only the basal plane is shown for the first three, which have antiferromagnetic stacking along the c axis. (**a**) The orbital ordered A-AF phase at $x = 0$. (**b**) The orbital polarized A-AF phase at $x = 0.5$. (**c**) The CE phase at $x = 0.5$. Translucent circles indicate Mn 4+ sites (i.e., no e_g electrons). Note that there is still a well defined magnetic moment at these sites due to the t_{2g} electrons. (**d**) The C-AF phase found at large x, shown in both the basal plane and out-of-plane directions.

A-type antiferromagnetic metallic phase is common in large bandwidth manganite and goes hand-in-hand with $d_{x^2-y^2}$ orbital polarization (Fig. 4.6b). This form of orbital polarization reinforces the anisotropic hopping of e_g electrons, resulting in strongly anisotropic resistivity for some compounds [98].

A-type antiferromagnetism is also the ground state for the $x = 0$ manganites, but here the phase includes a checkerboard $d_{3x^2-r^2}/d_{3y^2-r^2}$ orbital order [99] (Fig. 4.6a). The e_g orbitals are half-filled for $x = 0$, so the doubling of the unit cell caused by the checkerboard order is sufficient to open a bandgap and causes this phase to be insulating. Alternating Jahn-Teller distortions cooperate with the alternating orbital order and play an important

role in stabilizing this state [100].

CE-type order

Many compounds exhibit an exotic charge, orbital and spin ordered state at $x = 1/2$ termed CE-order (Fig. 4.6c) and first proposed by Goodenough [101]. This strongly insulating phase competes with the metallic A-type phase, and dominates in small bandwidth compounds. The conventional model of this phase consists of a checkerboard charge order of alternating Mn3+/Mn4+ ions within the (x, y) plane. On the Mn3+ sites lies a $d_{3x^2-r^2}/d_{3y^2-r^2}$ orbital order. Double exchange effects from this unusual orbital order pattern then give rise to ferromagnetic zig-zag chains that are antiferromagnetically coupled to each other in the (x, y) plane. There is antiferromagnetic coupling along the z direction, while the charge and orbital order is stacked. This phase quadruples the in-plane unit cell, and is thus able to open a bandgap in the quarter-filled e_g manifold.

C-type antiferromagnetism

Another commonly occurring phase, C-type antiferromagnetism, occurs for $0.75 < x < 0.85$ (Fig. 4.6d) [68, 11]. This phase consists of a uniform $d_{3z^2-r^2}$ orbital polarization, which induces ferromagnetic coupling along the z direction but allows for antiferromagnetic coupling within the (x, y) plane. Thus, a magnetic order is formed wherein ferromagnetic chains along z are coupled antiferromagnetically to neighboring chains. Both the orbital order and double exchange interaction indicate that electron hopping is allowed only along the z direction, and thus we would expect to observe a one-dimensional conducting state. Nevertheless, in reality all C-type antiferromagnetic compositions are insulating, likely due to the effects of many-body interactions within the one-dimensional state (for

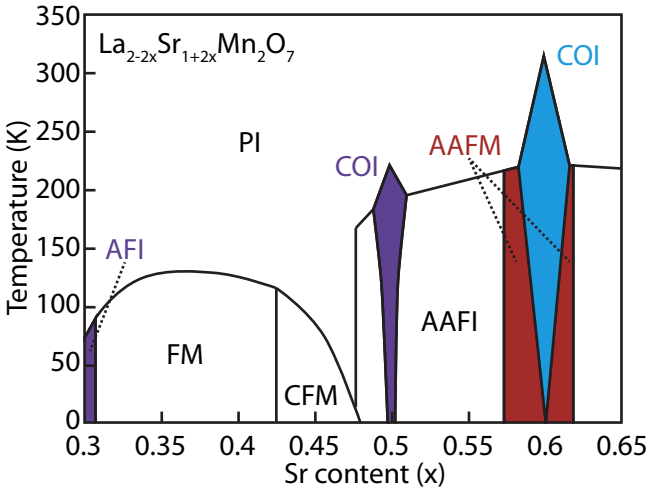

Figure 4.7: The phase diagram for $La_{2-2x}Sr_{1+2x}Mn_2O_7$. Phases are: P = paramagnetic, F = ferromagnetic, AAF = A-type antiferromagnetic, CF = canted ferromagnetic, CO = charge and orbital ordered. The last letter for each phase indicates whether it is metallic (M) or insulating (I). (Figure adapted with permission from H. Zheng, L. Qing'An, K.E. Gray & J.F. Mitchell (2008) [103]. Copyright 2008 by the American Physical Society).

which the Fermi liquid is unstable [102]).

4.3 Role of dimensionality

So far our discussion of manganites has focused on the three-dimensional perovskite structure, but several perovskite related Ruddlesden-Popper compounds can also be produced. These structures, of general form $(RE,AE)_{m+1}Mn_mO_{3m+1}$, consist of m perovskite layers separated from each other by a double (RE,AE)O layer (Fig. 3.1b). Electron hopping between manganese atoms is strongly confined to the connected MnO_2 networks, and thus these materials approach a quasi-two dimensional state as m is decreased. In addition, the Ruddlesden-Popper structure easily cleaves at the double (RE,AE)O layers making it highly favorable for conventional ARPES studies [104, 105, 106].

Fig. 4.7 shows the phase diagram for the $m = 2$ layered analogue of $La_{1-x}Sr_xMnO_3$. On comparing it with Fig. 4.1a, we see that the metallic phase is strongly suppressed, and multiple charge-ordered phases have appeared. Furthermore, metallic phases are completely absent in the quasi-two dimensional $m = 1$ compound [107, 108]. This illustrates the important role played by dimensionality in tuning the delicate balance between the many insulating and metallic states within the manganites, a topic we explore further in chapter 7.

4.4 Concluding remarks

The colossal magnetoresistive manganites are a complex and exciting system, where the interplay between lattice, charge, magnetic, and orbital degrees of freedom gives rise to a host of closely competing unusual electronic phases. These materials have stimulated new ideas and approaches for treating strongly correlated systems, and their highly tunable nature has also made them attractive for many potential applications. Thin films of manganites have been particularly valuable on both fronts. Fundamental scientific work has used atomically structured superlattices to increase magnetic transition temperatures and search for new magnetic ground states [52, 19], and epitaxial strain has been used as a control parameter for reaching new parts of the phase diagram [83]. Applied work has demonstrated an extremely high spin-polarization in manganites for spintronic applications [78, 79], and their ability to serve as key components within a wide array of potential electronic devices [12, 13, 14, 15]. Nevertheless, the strong many-body interactions that give rise to these striking properties are beyond the reach of conventional theoretical approaches, and many questions about the underlying electronic structure and fundamental physics of the manganites remain unresolved.

Chapter 5

Electronic structure of $La_{1-x}Sr_xMnO_3$

$La_{1-x}Sr_xMnO_3$ is the canonical large bandwidth manganite; at optimal doping ($x \approx 1/3$) it has a Curie temperature of $T_c = 370$ K in excess of room temperature and excellent conductivity [109]. These unique electronic and magnetic properties have driven its use in a variety of potential devices, including magnetic memories, tunnel junctions, and oxide-based transistors [12, 110, 79, 13, 14, 111, 15]. Additionally, $La_{1-x}Sr_xMnO_3$ has played an important role in the developing field of oxide interfaces through cation-ordered heterostructures, where layers of $LaMnO_3$ are alternately stacked with layers of $SrMnO_3$ [112]. Such heterostructures have shown new and dramatic metal-insulator transitions [113], increased magnetic ordering temperatures [52], and have been proposed to form spin-polarized two-dimensional electron gases at their interfaces [114].

As discussed in the previous chapter, manganites are complex materials where many-body interactions and several competing degrees of freedom give rise to many competing phases and non-trivial electronic behavior. In ferromagnetic $La_{1-x}Sr_xMnO_3$, this is evident

Some of the work discussed in this chapter has been submitted in a manuscript to *Physical Review Letters*.

in the polaronic behavior seen in optical conductivity [89] and scattering measurements [96]. Nevertheless, as the canonical large bandwidth system, much faith is placed in the ability of DFT to account for the basic electronic and magnetic behavior of $La_{1-x}Sr_xMnO_3$, or at least form a valid foundation for more complex many-body treatments [75, 115]. For example, DFT calculations have been used to propose numerous potential $La_{1-x}Sr_xMnO_3$-based devices [12, 110, 114].

Nevertheless, extensive ARPES measurements of pulsed-laser deposition grown $La_{1-x}Sr_xMnO_3$ films [62, 80, 116, 117, 118, 119, 120, 121, 122] have exhibited clear discrepancies with DFT-based approaches, casting doubt on its validity for descriptions of this material's underlying electronic structure. In particular, the experimental picture that has emerged is a single electron pocket at Γ, in contrast to the predicted two-sheet Fermi surface, and is at odds with bulk-sensitive electron-positron annihilation results [123] and the bandstructure measured in ultrathin films [124]. It has been postulated that a nesting instability of the cubic holelike Fermi surfaces may open a gap on these sheets [121], or that an electronic reconstruction or a modification in the surface chemistry or structure radically alters the electronic and magnetic properties within the probing depth of ARPES [125, 122]. It is also possible, however, that other experimental difficulties related to film growth or surface preparation have prevented the observation of the full electronic structure by ARPES.

Here, we measure the full two-sheet Fermi surface and corresponding band dispersion of pristine MBE-grown $La_{1-x}Sr_xMnO_3$ films for the first time. Our results provide the first consistent understanding of both theory and experiment and resolve outstanding questions regarding the accuracy of theoretical approaches and the nature of the electronic structure of $La_{1-x}Sr_xMnO_3$. Furthermore, we find several signatures of strong many-body interactions that renormalize the electronic structure and give rise to polaronic charge carriers.

5.1 Experiment methods and film characterization

5.1.1 Film growth and structural characterization

$La_{1-x}Sr_xMnO_3$ films were grown on buffered-HF treated (001) $SrTiO_3$ (STO) single crystal substrates [126] using shuttered layer-by-layer deposition in two different reactive MBE systems: a dual-chamber Veeco 930 MBE and a dual-chamber Veeco GEN10 MBE. ARPES and characterization results from both systems were indistinguishable. Nearly all films discussed in this dissertation were grown by Carolina Adamo, with growth parameters based on her extensive experience in manganite growth [127] and optimized for each growth chamber. I grew the remaining $La_{1-x}Sr_xMnO_3$ films using identical conditions.

Within the ferromagnetic metallic phase covering $0.15 < x < 0.5$, bulk $La_{x-1}Sr_xMnO_3$ has a rhombohedral lattice structure (space group $R\bar{3}c$). The rhombohedral lattice constants at $x = 0.3$ are $a = 5.509$ Å and $c = 13.372$ Å, corresponding to a pseudocubic lattice parameter of 3.88 Å (ref. [128]). This is closely matched to $SrTiO_3$ ($a = 3.905$ Å), so $La_{x-1}Sr_xMnO_3$ /$SrTiO_3$ films within this part of the phase diagram are under only a small amount of strain (i.e., 0.6% for $x = 0.3$). In the remainder of the dissertation, I will refer to the pseudocubic lattice of $La_{x-1}Sr_xMnO_3$ rather than the more complex rhombohedral unit cell.

Films were grown at 700 °C in 5×10^{-7} Torr of oxidant (O_2+10% O_3), and individual element fluxes are chosen so that monolayer coverage takes about 30 seconds ($\approx 2 \times 10^{13}$ atoms/cm^2 sec). ARPES films are typically grown on 3×3 mm substrates, whereas films exclusively for characterization are grown on 10×10 mm substrates. On several occasions, 10×10 mm films and ARPES 3×3 mm films were grown simultaneously on the same dual-substrate holder to provide an additional film for characterization measurements that is as similar to the ARPES film as possible. I refer to 10×10 mm films

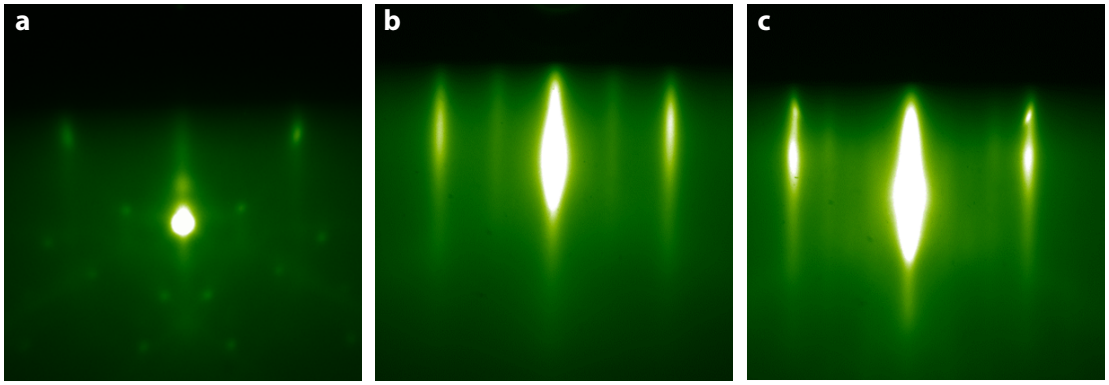

Figure 5.1: RHEED patterns from the substrate and film surface. (**a**) Along the [110] azimuth of the bare (001) $SrTiO_3$ substrate at 350 °C, before the deposition. (**b**) During the growth of a 20 nm thick $La_{0.7}Sr_{0.3}MnO_3$ film following the completion of the (La,Sr)O layer. Note the 2× surface reconstructions. (**c**) During the growth of the same 20 nm thick $La_{0.7}Sr_{0.3}MnO_3$ film following the completion of the MnO_2 layer. Note the 3× surface reconstructions.

from such growths as "companions" to the corresponding ARPES film. Furthermore, the ARPES films themselves are routinely subjected to many of the same characterization measurements performed on 10×10 mm films after being removed from the ARPES chamber.

Growth proceeds as follows: beginning with the TiO_2 terminated STO surface, we open the lanthanum and strontium shutters simultaneously to deposit one (La,Sr)O monolayer. We then close lanthanum and strontium, and open the manganese shutter to deposit a single MnO_2 monolayer. We have now deposited one unit cell of $La_{1-x}Sr_xMnO_3$, and can repeat this procedure the desired number of times. This requires a careful calibration of absolute fluxes for each source, which occurs in a multi-step procedure. First, the fluxes of the individual molecular beams are determined to ±5% using a QCM placed in front of the substrate. The source temperatures for La and Sr are carefully adjusted to obtain the desired doping level (x) at this stage. We then use RHEED intensity oscilla-

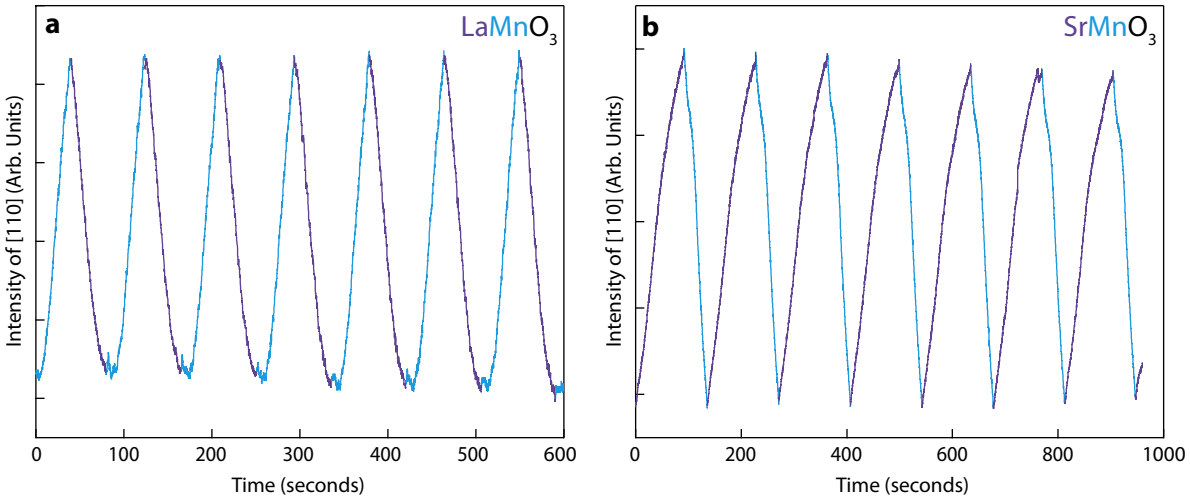

Figure 5.2: RHEED oscillations in the intensity of the [110] diffraction peak during shuttered growth of $LaMnO_3$ (**a**) and $SrMnO_3$ (**b**). During $LaMnO_3$ growth, the intensity rises during Mn deposition and falls during La deposition. In contrast, during $SrMnO_3$ growth, the intensity rises during Sr deposition and falls during Mn deposition. This behavior is generally seen for A-sites with 3+ and 2+ valence states, respectively [129].

tions of the first-order diffraction spot along the [110] direction to achieve better control of film composition [59]. First, $LaMnO_3$ is grown on STO using the QCM determined flux as a starting point. The individual shutter times for La and Mn are then fine-tuned to obtain a stable RHEED oscillation pattern (Fig. 5.2a) indicating 1:1 La:Mn stoichiometry (to within $\approx 1\%$) and monolayer coverage per each cycle. The final shutter times for $La_{1-x}Sr_xMnO_3$ can then be calculated assuming that the La:Sr ratio determined by QCM is correct. This gives an empirically determined, by our XPS and ARPES measurements, error in x of ± 0.05. More accurate calibration can be obtained using additional RHEED oscillations of $SrMnO_3$ (Fig. 5.2b), but this is not typically performed for random alloy growth due to time considerations. As a final verification of our film stoichiometry, a test $La_{1-x}Sr_xMnO_3$ film is grown and RHEED oscillations are again monitored to ensure that monolayer coverage and 1:1 (La+Sr):Mn stoichiometry is preserved.

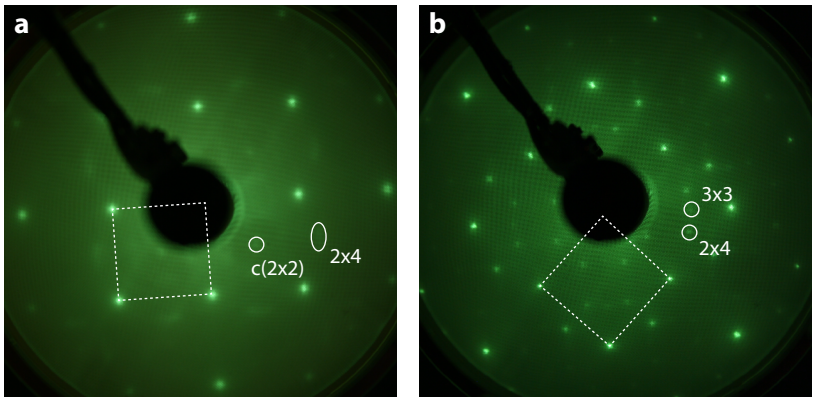

Figure 5.3: LEED pattern taken with 100 eV electrons from a $La_{0.7}Sr_{0.3}MnO_3$ film (**a**) and a $SrMnO_3$ film (**b**), both with MnO_2 surface terminations. Diffraction peaks corresponding to the unreconstructed surface and several reconstructions are indicated. Note that the $SrMnO_3$ LEED pattern is rotated by 45 degrees.

We monitor phase purity during growth using RHEED along the [110] pseudocubic direction. Example RHEED patterns are shown in Fig. 5.1 for a TiO_2 terminated STO substrate and a $La_{0.7}Sr_{0.3}MnO_3$ film during growth with both (La,Sr)O and MnO_2 surface terminations. Two-fold and four-fold surface reconstructions are visible for (La,Sr)O surfaces, and a three-fold reconstruction appears for the MnO_2 surface. Films are cooled to 200 °C in oxidant after growth and then immediately transferred through UHV to the ARPES chamber where they are cooled to the desired measurement temperature.

Several ARPES samples were measured using low-energy electron diffraction (LEED) to further resolve the symmetry of surface reconstructions and to verify their presence at the lower temperatures relevant to our photoemission experiments. All surfaces showed sharp diffraction peaks, demonstrating the high crystallinity of the surface of our films and proving that the pristine surface from growth is maintained throughout the transfer to our ARPES chamber and subsequent measurement that can last as long as eight days. Example LEED spectra are shown in Fig. 5.3a for a 20 nm MnO_2 terminated

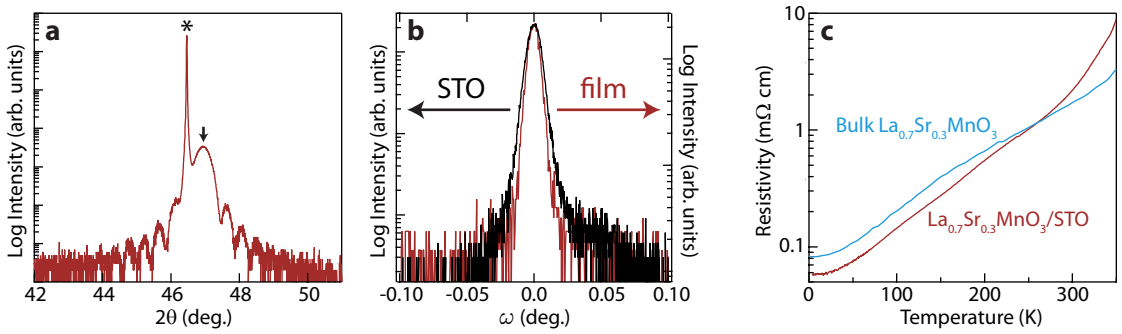

Figure 5.4: (**a**) $\theta - 2\theta$ x-ray diffraction patterns in the vicinity of the out-of-plane 002 pseudocubic $La_{0.7}Sr_{0.3}MnO_3$ reflection from a 20 nm thick $La_{0.7}Sr_{0.3}MnO_3$/STO film grown under the same conditions as ARPES samples. The film is coherently strained and shows clear thickness fringes. The sharp 002 pseudocubic substrate peak is labeled with an asterisk, and a black arrow indicates the 002 pseudocubic film peak. (**b**) Rocking curves of the 002 pseudocubic peaks from the same film and substrate demonstrate substrate-limited crystallinity with FWHM of 0.01°. (**c**) Resistivity of a 20 nm thick $La_{0.7}Sr_{0.3}MnO_3$/STO film that was measured by ARPES compared with the resistivity of a bulk $La_{0.7}Sr_{0.3}MnO_3$ single crystal from ref. [109].

$La_{0.7}Sr_{0.3}MnO_3$/STO film as well as an 8 unit cell thick $SrMnO_3$ film on Nb-doped STO (to prevent charging). All measured samples showed a $\sqrt{2} \times \sqrt{2}\,R45°$ reconstruction relative to the pseudocubic unit cell (hereafter called $c(2 \times 2)$) of varying strength. MnO_2 surfaces also show weaker 4×2 reconstructions, visible in Fig. 5.3a and b, and occasionally a 3×3 reconstruction corresponding to the reconstruction seen by RHEED, visible in Fig. 5.3b. Similar reconstructions have also been observed in LEED studies of PLD grown $La_{1-x}Sr_xMnO_3$ films [61, 122]. The origin of these surface reconstructions are not yet entirely understood, but they appear to have little effect on the electronic structure measured by ARPES aside from weak shadow bands appearing in some samples that correspond to the $c(2 \times 2)$ reconstruction.

After removal from the UHV chamber, structural quality of the films was verified using $\theta - 2\theta$ scans from a PANalytical X'pert Pro MRD and a high resolution four-circle

Rigaku SmartLab x-ray diffractometer with Cu $K_{\alpha 1}$ radiation and a hybrid monochromator (4-bounce 220 reflection germanium crystals) on the incident side. Rocking curves of the 002 pseudocubic peaks were measured with an additional 220 germanium monochromator on the diffracted beam. Examples of both measurements for a 100 nm $La_{0.7}Sr_{0.3}MnO_3$/STO film are shown in Fig. 5.4. The $\theta - 2\theta$ scans show pronounced thickness fringes, indicating a high quality surface. Rocking curves of all films were found to have the same FWHM as their substrates, indicating that crystallinity of the films are substrate limited.

5.1.2 Resistivity

Fig. 5.4c shows the resistivity of a 20 nm thick $La_{0.7}Sr_{0.3}MnO_3$/STO film that was measured by ARPES compared with the resistivity of a bulk $La_{0.7}Sr_{0.3}MnO_3$ single crystal from ref. [109]. Both show similar metallic resistivities and resistive anomalies indicative of the Curie temperature well above room temperature. Both features further indicate the high quality of our films.

5.1.3 Angle-resolved X-ray photoelectron spectroscopy

I performed x-ray photoelectron spectroscopy (XPS) measurements with a Surface Science Instruments model SSX-100 electron analyzer with a monochromated Al K_α x-ray source (1486.6 eV). Samples were measured after exposure to air, and measurements were preferentially performed at normal emission to minimize the effect of surface contamination. Fig. 5.5a shows the La 4*d* and Sr 3*d* core levels from a 20 nm $La_{0.7}Sr_{0.3}MnO_3$/STO sample, measured with an energy resolution of 1.8 eV. The area of each peak is proportional to the elemental concentration in our sample and is used to determine the La:Sr stoichiom-

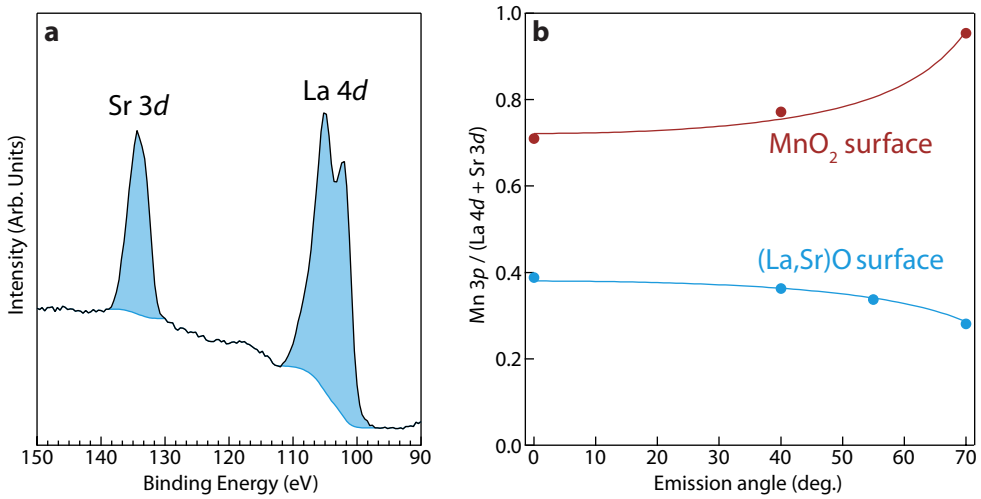

Figure 5.5: (**a**) XPS data for the La 4*d* and Sr 3*d* peaks from a $La_{0.7}Sr_{0.3}MnO_3$/STO film. The area of each peak is calculated after fitting the background with a Shirley function, as illustrated, and is used to determine x. (**b**) Ratio of the Mn 3*p* XPS intensity to the sum of the La 4*d* and Sr 3*d* core levels, after accounting for atomic sensitivity factors [30]. The points show data for a $La_{0.6}Sr_{0.4}MnO_3$ film with MnO_2 surface termination (maroon) and a $La_{0.8}Sr_{0.2}MnO_3$ film with (La,Sr)O surface termination (blue). The lines are fits to $Ae^{\pm c/(2\lambda\cos\theta)}$ with λ = 1.3 nm, c = 0.39 nm and A an arbitrary constant.

etry (i.e., x). The electron escape depth in metals is typically 1-2 nm in this energy range, so XPS provides a surface sensitive measurement of the doping of each sample that is directly applicable to our ARPES measurements. I extracted peak areas after fitting the background with a Shirley function for each peak, as shown in Fig. 5.5a. I then corrected for the relative sensitivity factors of La and Sr using calculated photoemission cross sections [30].

The surface sensitivity of XPS allows for the determination of the surface termination of our films by measuring the La:Sr ratio as a function of emission angle. The XPS signal is a weighted average over each layer along the [001] direction. For the specific case of MnO_2 terminated $La_{1-x}Sr_xMnO_3$, we start by computing the intensity for Mn-derived core

levels (I_{Mn}):

$$I_{Mn} = C\epsilon_{Mn} \sum_{j=0}^{\infty} e^{-jc/\lambda \cos\theta}$$

Where C is a constant that will divide out when we take ratios of core level intensities, ϵ_{Mn} is the core level's sensitivity factor (from ref. [30]), c is the perovskite pseudocubic lattice constant, λ is the electron mean free path, and θ is the emission angle. This geometric series is easily evaluated to:

$$I_{Mn} = C\epsilon_{Mn}(1 - e^{-c/\lambda \cos\theta})^{-1}$$

Similar considerations for the La core levels gives:

$$I_{La} = C\epsilon_{La}e^{-c/2\lambda \cos\theta}(1 - e^{-c/\lambda \cos\theta})^{-1}$$

The ratio of intensities is then seen to follow a simple form, which for MnO_2 terminations is:

$$I_{Mn}/I_{La} = \frac{\epsilon_{Mn}}{\epsilon_{La}} e^{c/2\lambda \cos\theta}$$

Similarly, LaO terminations give:

$$I_{Mn}/I_{La} = \frac{\epsilon_{Mn}}{\epsilon_{La}} e^{-c/2\lambda \cos\theta}$$

This can be trivially generalized to $La_{1-x}Sr_xMnO_3$ (non-zero x). We measured ARXPS on several manganite films and show two examples from $La_{1-x}Sr_xMnO_3$/STO that provided spectra consistent with singly-terminated surfaces (i.e., either purely MnO_2 or (La,Sr)O) in Fig. 5.5b. Here we have plotted the ratio of Mn to Sr+La (adjusted for relative sensitivity factors ϵ) as a function of electron emission angle. The downward sloping curve for the $x = 0.2$ film indicates a (La,Sr)O surface, whereas the $x = 0.4$ curve indicates a MnO_2 surface termination. Both films are fit well by the same electron escape depth of $\lambda = 1.3$ nm. This is smaller than the $\lambda = 2.4$ nm estimated from the TPP-2M formula [130], but consistent with the expected range of escape depths at this photon

energy. As discussed below, based on these results I developed a technique for determining the surface termination in-situ using angle-integrated photoemission spectra from our helium plasma lamp. We find that the film surface termination occasionally does not agree with the nominal termination chosen during film growth. A likely cause is a slight-off-stoichiometry during the film growth that accumulates over the span of tens of monolayers. Overcoming such small stoichiometry errors to preserve well defined surfaces and interfaces over the full film thickness requires a more extensive calibration than undertaken for our random alloy films, and is performed for the superlattices discussed in chapter 7.

An additional complication can arise from surface segregation of strontium, which has been observed in measurements of $La_{1-x}Sr_xMnO_3$ films grown by pulsed-laser deposition [131, 132], and depends sensitively on growth conditions. This can be measured through the angle-dependence of the Sr/La ratio, which is constant for an ideal film since strontium and lanthanum reside in the same layers. In the case of our films, our ARXPS measurements occasionally find evidence for a small amount of surface segregation that is likely related to film degradation after removal from the UHV chamber. All films that were stored in a high-vacuum environment or immediately measured after removal from the UHV chamber showed no detectable strontium surface segregation. Furthermore, in-situ ARPES measurements allowed us to determine a carrier concentration of $x = 0.29 \pm 0.04$ for the film with the largest observed strontium surface segregation (measured by XPS after 3 months of air exposure), a result consistent with $x = 0.29 \pm 0.2$ determined by normal-emission XPS and inconsistent with $x = 0.42 \pm 0.2$ from emission at 70° to the surface normal. ARPES with He II photons should be more surface sensitive than XPS [31], and thus this result suggests the strontium segregation occurred after removing the film from the measurement chamber.

5.2 Electronic structure calculations

Density functional theory calculations of the non-interacting electronic structure were performed following the work of refs. [80, 133, 134]. I used the PBE GGA functional [135], which was found to describe $La_{1-x}Sr_xMnO_3$ better than LDA in previous work [133]. Introducing a non-zero interaction parameter (U) onto the Mn d electrons is necessary to generate the half-metallic state often discussed at $x = 1/3$. On a more empirical basis, it was found that matching the position of the Mn t_{2g} valence band states observed in photoemission studies of $La_{1-x}Sr_xMnO_3$ required $U = 2$ eV [80]. Our photoemission studies also find good agreement with $U = 2$ eV in this regard. Calculations start with a cubic or tetragonal $LaMnO_3$ unit cell with ferromagnetic order. Note that bulk undoped $LaMnO_3$ has strong Jahn-Teller distortions and A-AF magnetic order that make it insulating, but neither of those are present in our calculation. Under these conditions, $LaMnO_3$ is a metal. The cubic unit cell uses $a = 3.89$ Å from bulk $La_{0.7}Sr_{0.3}MnO_3$, and the tetragonal unit cell uses $a = b = 3.905$ Å and $c = 3.86$ Å to simulate coherent strain from an STO substrate.

Calculations are run using the Wien2k package [136] to a convergence in energy and charge of 1.4 meV and $0.001e^-$ per unit cell, respectively. A k-mesh of 3000 points (before symmetry-related reduction) and *rkmax* of 8, which determines the size of the plane wave basis set, were found to provide sufficiently converged results. In particular, calculations with 3000 and 6000 k-points produced an energy difference per unit cell of only 0.7 meV, indicating that convergence has occurred already by 3000 k-points. I ran tests of *rkmax* from 7 to 11, and in this case found slower energy convergence. To reach a convergence of 2 meV per unit cell, a large $rkmax = 10$ was required. Nevertheless, no significant differences in bandstructure or DOS were observed on going from $rkmax = 7$ up to $rkmax = 11$. This is sensible: *rkmax* expands the basis set and thus lowers the energy of all states, so we can expect larger total energy changes without meaningful changes to electronic structure. A larger *rkmax* dramatically increases calculation time (time scales

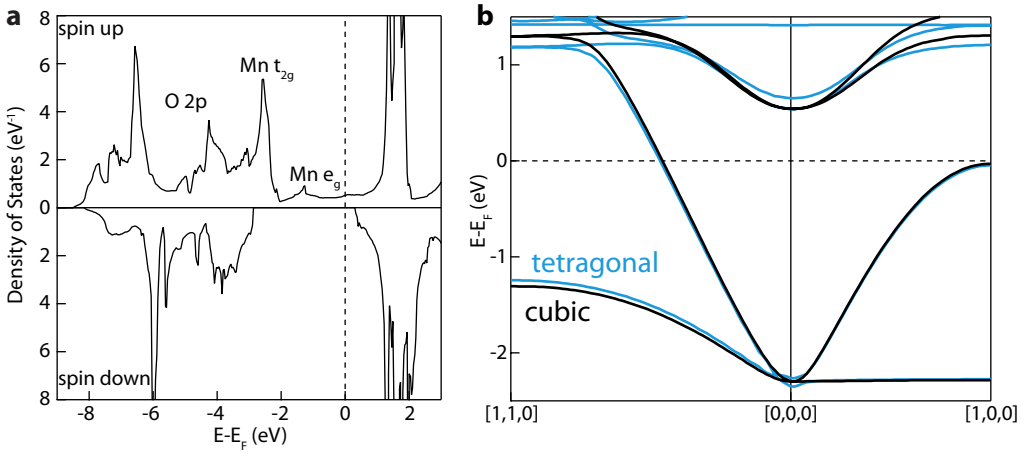

Figure 5.6: (**a**) Majority spin (positive) and minority spin (negative) density of states for a cubic ferromagnetic $LaMnO_3$ DFT calculation. The dominant orbital character of the majority spin bands are illustrated. Of particular note is the spin polarized e_g band spanning -2 eV up to E_F. (**b**) Majority-spin bandstructure for DFT calculations of cubic (black) and a tetragonal (blue) ferromagnetic $LaMnO_3$ show very little difference.

as *rkmax*[9]) and makes the calculation less stable, so a value of 8 was chosen to provide accurate bandstructure within reasonable calculation times.

In addition, there is a commonly occurring error for manganite calculations involving Wien2k's *QTL-B values*. This occurs when Mn 3*s* levels are included in the valence band calculation, since the limited number of s-wave spherical harmonics within the LAPW and APW+lo basis sets must be divided between the occupied Mn 3*s* and unoccupied 4*s* orbitals. Expanding the Mn *muffin tin* at the expense of La and O slightly increases calculation time, but allows the 3*s* states to be treated as core levels and leads to more stable calculations.

Results from calculations for ferromagnetic $LaMnO_3$ are shown in Fig. 5.6. The density of states in panel a shows the locations of O 2*p*, Mn t_{2g} and Mn e_g states, with a large region where majority spin Mn e_g states exist with zero density of minority spin states. Hole-

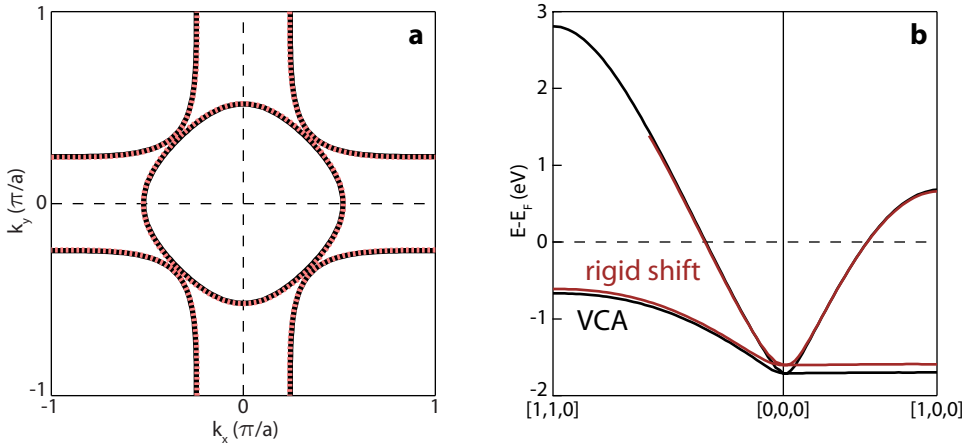

Figure 5.7: The Fermi surface (**a**) and bandstructure of the majority spin e_g bands (**b**) calculated for cubic $La_{0.7}Sr_{0.3}MnO_3$ by a rigid shift (maroon) and VCA (black). The Fermi surface electron pocket contour is at $k_z = 0$ and the hole pocket contour is at $k_z = \pi/c$. The rigidly shifted bandstructure is only shown up to 1.3 eV. Above this energy the Mn e_g band intersects the La $4f$ levels in the rigidly shifted calculation but not in the VCA. Both approximations are inappropriate for treating the La states, so the position of the $4f$ levels in both cases is not meaningful, nor does it effect the states at and below E_F that we measure with ARPES.

doping into this part of the bandstructure gives rise to the 100% spin-polarized metallic phase discussed for bulk $La_{1-x}Sr_xMnO_3$ [78]. Panel b compares the near-E_F majority-spin bandstructure for cubic (a = 3.89 Å) and tetragonal ($a = b$ = 3.905 Å, c = 3.86 Å) calculations. Here we see the two Mn e_g bands that make up the metallic Fermi surface, and that they change very little under the weak tensile strain induced by an STO substrate.

The effect of hole doping (x) is accounted for by either a rigid-shift of the chemical potential or the virtual crystal approximation (VCA). To obtain a non-zero doping within the rigid shift approximation, we lower E_F until the number of valence electrons per unit cell has been reduced by x. For VCA, we replace each La atom with a fictional atom of nuclear charge $(57 - x)$ while simultaneously reducing the number of valence electrons by x. Although both approximations ignore the effects of the random distribution of dopants

throughout the material, VCA should be a more accurate approach than a rigid shift since it accounts for the position of the dopant atoms within the unit cell in an averaged way. Nevertheless, we have found the differences between both approaches to be insignificant for the Mn e_g states in $La_{1-x}Sr_xMnO_3$. We compare the Fermi surfaces and bandstructure obtained by both approaches at $x = 0.3$ in Fig. 5.7. We find only small differences in the bandwidth (< 7%) and negligible changes in the Fermi surface. Such differences are inconsequential for the comparisons with ARPES data presented below. On the other hand, the rigid shift has a significant advantage over VCA: all values of x can be studied via a single calculation. For this reason, DFT results discussed below are taken from rigidly shifted calculations unless otherwise stated.

5.2.1 Analysis of three-dimensional DFT calculations

Detailed analysis of DFT is performed in a purpose-written set of macros in *IGOR Pro* titled *Hypercube*. I designed this software to extract bandstructure and Fermi surfaces from Wien2k, as well as account for the final-state k_z broadening that becomes important for materials with significant k_z dispersion (section 2.4).

A typical workflow for using the Hypercube macros starts by running a DFT calculation to convergence in Wien2k using standard procedures. Then, a three-dimensional user specified k-mesh is generated by Hypercube and imported into the Wien2k software, which calculates the eigenvalue spectrum at each k-point. The result is a four-dimensional data file with (k_x, k_y, k_z) and band index as the dimensions, and band energy as the value at each point. This file is imported back into Hypercube, and its functions can now operate independently of Wien2k. Hypercube uses IGOR's three-dimensional interpolation algorithm to determine eigenvalues that do not fall directly on the specified k-grid, and so grids of 30-60 points per edge produce very high-quality bandstructures and Fermi

surfaces, and in many cases courser grids are sufficient.

Basic analysis functions involve determining all bands that cross E_F, generating three-dimensional Fermi surface plots and two-dimensional Fermi surface slices, and generating bandstructure along arbitrary k-space cuts with variable k_z. In addition, Hypercube is capable of simulating ARPES spectra by accounting for k_z broadening and a user-specified energy-dependent quasiparticle lifetime ($\Sigma''(E - E_F)$). Following Krempasky et al. [80], the spectral function is written:

$$A(E, \mathbf{k}) = \sum_i \frac{C f(E - E_F)}{(E - \epsilon_i(\mathbf{k}))^2 + (\Sigma''(E - E_F))^2}$$

Where C is an arbitrary constant, $f(E-E_F)$ is the zero-temperature Fermi function, and $\epsilon_i(\mathbf{k})$ is the DFT calculated eigenvalue at $\mathbf{k}$ for band i. We compute the simulated ARPES intensity ($I(E, k_x, k_y)$) by averaging over k_z using a Lorentzian with a FWHM given by $\Delta k_z = 1/\lambda_{mfp}$ [80], where λ_{mfp} is the photoelectron mean free path:

$$I(E, k_x, k_y) = \int_{k_z} \frac{A(E, \mathbf{k})}{(k_z - k_z^o)^2 + (\Delta k_z/2)^2}$$

Where k_z^o is the nominal k_z probed by photoemission at the specified photon energy. With this formalism, Hypercube can simulate a two-dimensional projected Fermi surface and projected bandstructure for direct comparison with ARPES data. Examples of output from several of these functions can be seen in the following section.

DFT results for $La_{1-x}Sr_xMnO_3$

Fig. 5.8a shows the calculated Fermi surface for cubic $La_{1-x}Sr_xMnO_3$ at $x = 1/3$. It consists of a roughly spherical electron pocket at the center of the Brillouin zone and a roughly cubic hole pocket at the zone corner. ARPES measurements probe a two-dimensional slice through momentum space, so we must take a projection of this three-dimensional calculation at an appropriate k_z for comparison to experiment. As a starting point, I use the

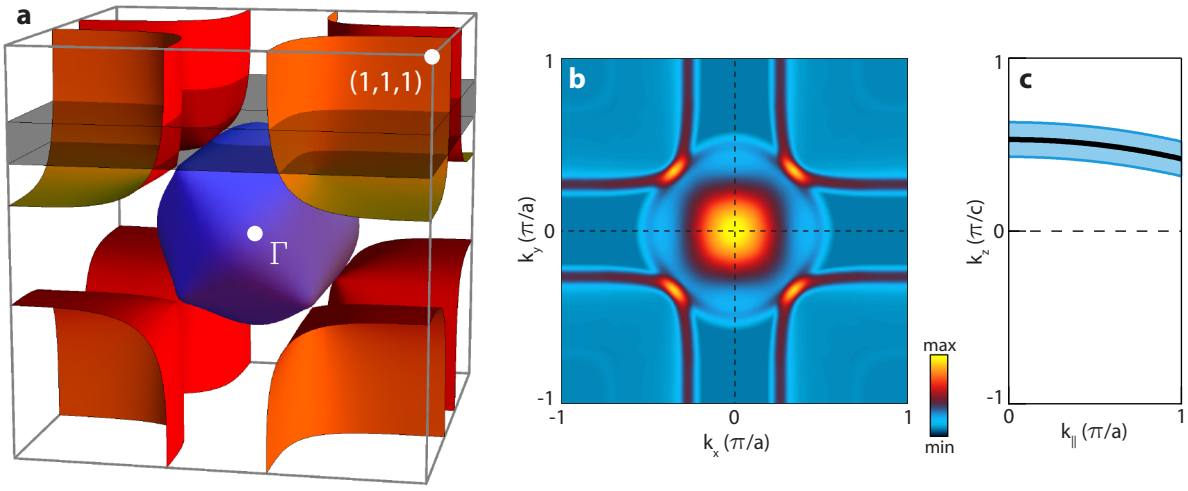

Figure 5.8: (**a**) Three dimensional plot of the DFT predicted bulk Fermi surface with the hole pocket shown in orange and the electron pocket in purple. The shaded box denotes the region measured by ARPES. (**b**) Projected Fermi surface accounting for k_z broadening and instrumental resolution. To mimic the observed photoelectron cross section, the theoretical electron pocket intensity is multiplied by a factor of five. (**c**) Calculated k_z for varying $k_{\parallel}$ using an inner potential $(V_0 - \phi) = 10.16$ eV and a photon energy $E_{ph} = 40.8$ eV. k_z has been translated by $-4\frac{\pi}{c}$ to bring it into the first Brillouin zone. Also shown in blue is the FWHM of the k_z broadening caused by the surface sensitivity of ARPES.

inner potential of $(V_0 - \phi) = 10.16eV$ determined for $La_{0.66}Sr_{0.34}MnO_3$/STO by synchrotron ARPES measurements of the electron pocket [62]. The result of this inner potential for the photon energy used by us (40.8 eV) is shown in Fig. 5.8c. We find $k_z^o = 0.53\frac{\pi}{c}$ at normal emission ($k_x = k_y = 0$), which varies slightly over the range of our ARPES data in k.

Projecting k_z out of the Fermi surface and bandstructure also requires consideration of final state k_z broadening induced by the short photoelectron escape depth as discussed above. I estimated $\lambda_{mfp} = 6$ Å by comparing with our ARPES data, but found that changing λ_{mfp} by a factor of 2 does not qualitatively affect our conclusions. Due to the large k_z broadening, which follows a Lorentzian distribution and thus has large 'tails', we neglect

the small variation in k_z with (k_x, k_y) when projecting our DFT results and use $k_z^o = 0.53\frac{\pi}{c}$ everywhere. The region encompassed by $k_z^o \pm \Delta k_z$ is illustrated by a shaded box in Fig. 5.8a, but this region accounts for only half of the total ARPES signal.

The k_z projected Fermi surface in Fig. 5.8b again shows both Fermi surface pockets, but now we see the dramatic effect of final state k_z smearing. The electron pocket is dominated by states around the zone center that make up the top and bottom of the spherical feature. These states are strongly k_z dispersive, being of primarily $d_{3z^2-r^2}$ character, and as a result are broadened to such a degree as to obscure any meaningful features within the underlying dispersion. On the other hand, the hole pockets have large vertical-running sections of $d_{x^2-y^2}$ character that show very little k_z-dispersion, resulting in sharp and well resolved Fermi surface contours. Furthermore, the weak k_z dispersion of these features causes the projected Fermi surface and related bandstructure to be insensitive to the precise values of k_z and escape depth used in our modeling. To further illustrate this point, in Fig. 5.9a I show bandstructure *spaghetti* plots for varying k_z. Figure 5.9b-d shows the results of projecting out k_z using varying λ_{mfp} by following a similar procedure used for the Fermi surface map presented above. In all cases the hole pocket presents well-defined sharply dispersive features that are dominated by the most weakly k_z-dispersive sections of the bands (Fig. 5.9b-d). In contrast, the electron pocket is more sensitive to λ_{mfp}. It always contributes significant indistinct intensity at $(0, 0)$, and only shows sharp features for very small escape depths arising from the outer edges of the electron pocket.

5.3 ARPES results

ARPES measurements were performed with a VG Scienta R4000 electron analyzer and a VUV5000 helium plasma discharge lamp and monochromator using He II photons ($h\nu = 40.8$ eV). The base pressure of the ARPES system was $5{\times}10^{-11}$ Torr and the sam-

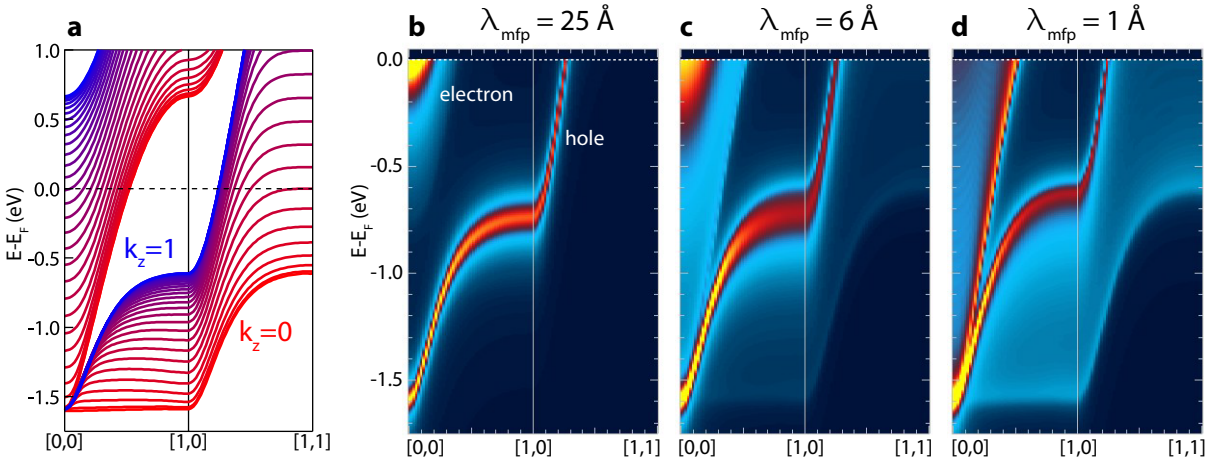

Figure 5.9: (**a**) DFT calculated bandstructure as a function of (k_x, k_y) for varying k_z. (**b-d**) Simulated ARPES spectra generated by integrating the DFT calculation from panel a over k_z using varying λ_{mfp}. λ_{mfp} = 6 Å is a realistic value, whereas the other two are extreme cases significantly beyond values expected for ARPES with 40.8 eV photons.

ple temperature was held at 20 K or lower. Spectra were taken with an energy resolution of 40 meV unless specified otherwise.

5.3.1 Angle-integrated valence band spectra

Angle-integrated valence band spectra show the O 2p and Mn t_{2g} states at 1-8 eV as well as the more deeply bound La 5p, Sr 4p, and O 2s states in the 15 – 21eV range. Fig. 5.10a shows example spectra for films with MnO_2 and (La,Sr)O surface terminations, as well as a film with mixed surface termination. Films with (La,Sr)O surface termination show a strong enhancement of the La 5p and Sr 4p levels with respect to the MnO_2 termination, as well as a modified multi-peak shape that we attribute to surface-related core-level shifts due to the change in coordination for surface atoms [29]. We confirmed this relationship by comparing valence band spectra of several $La_{1-x}Sr_xMnO_3$ films and $LaMnO_3/SrMnO_3$

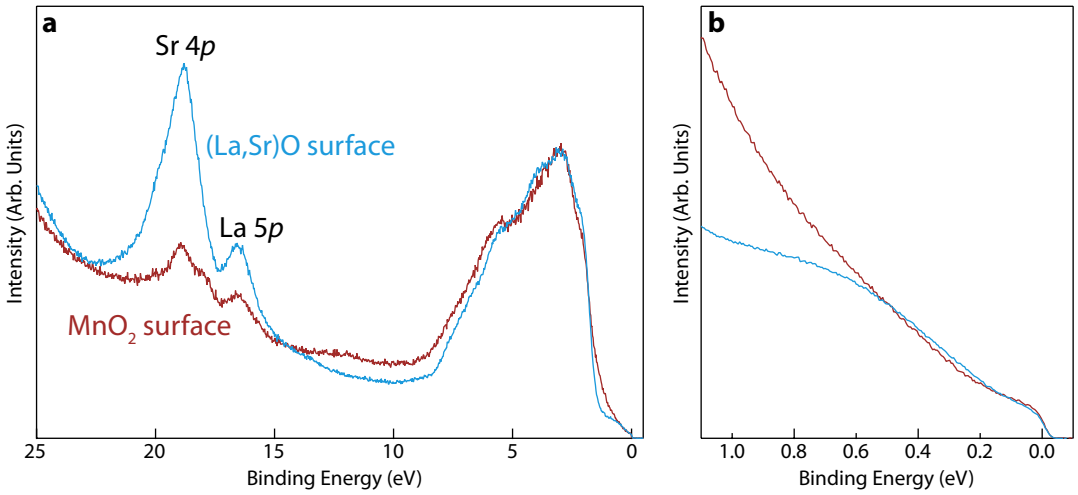

Figure 5.10: (**a**) Angle-integrated valence band of two $La_{0.7}Sr_{0.3}MnO_3$/STO samples, one (La,Sr)O terminated (blue) and the other MnO_2 terminated (maroon), normalized to the peak at 3 eV. The Sr 4*p* and La 5*p* peaks are indicated. The 15-21 eV region also has strong overlap with O 2*s* states. Films terminated with (La,Sr)O show a strong enhancement of these deeply bound La and Sr peaks. (**b**) The near-E_F intensity (shown here for the hole pocket k_F and normalized as in panel a) has a strong tail from the valence band for MnO_2 terminations that is absent for (La,Sr)O terminated films.

superlattices to ARXPS measurements of the surface termination on the same films (section 5.1.3).

In addition to the clear changes at 15 – 21eV, we also observe changes in the angle-integrated valence band closer to E_F. In particular, Fig. 5.10b shows spectra for MnO_2 and (La,Sr)O terminated films within 1.1 eV of E_F. In this region, we find a strong non-dispersive tail from the valence band for the MnO_2 surface termination that is much weaker for (La,Sr)O terminated films, and which we thus attribute to states from the surface MnO_2 layer itself. Surface states could arise from the change in Mn coordination at the surface or a surface reconstruction driven by a polar catastrophe associated with the polar (La,Sr)O and MnO_2 layers [137]. A DFT slab calculation that we performed predicts

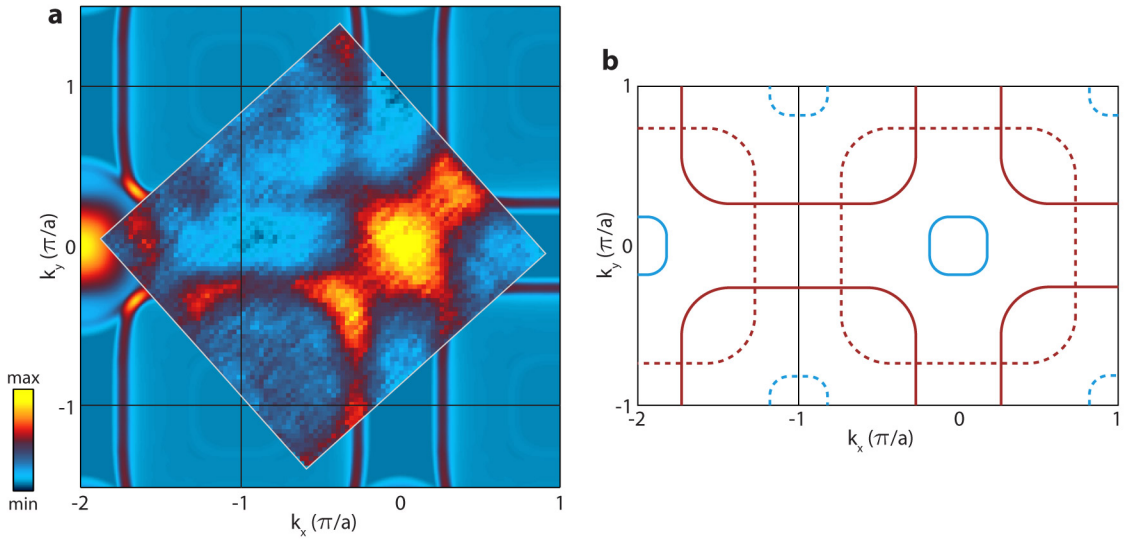

Figure 5.11: (**a**) The experimental Fermi surface of $La_{0.7}Sr_{0.3}MnO_3$ (inside the gray box) overlaid onto the DFT simulation from Fig. 5.8b. Both the hole and electron pockets are clearly visible. (**b**) An illustration of the shadow bands (dotted lines) induced by a $c(2 \times 2)$ surface reconstruction of the primary bands (solid lines).

these surface states to be metallic (Appendix B), but their non-dispersive character and lack of weight at E_F in our ARPES measurements indicate that they are insulating, similar to findings in layered manganites of an electrically and magnetically inactive surface [138]. Most importantly, films with both surface terminations show no significant differences in the dispersive bandstructure used for our analysis of the $La_{1-x}Sr_xMnO_3$ electronic structure below.

5.3.2 Fermi surface of $La_{0.7}Sr_{0.3}MnO_3$

Figure 5.11a shows the experimental Fermi surface from ARPES, which can be compared with the calculated projected Fermi surface in Fig. 5.8 and used as a backdrop here. The experimental Fermi surface was obtained by integrating over 9000 spectra taken as a func-

tion of k_x and k_y in the first two Brillouin zones within ±50meV of E_F, and normalizing by dividing by the valence band between 17.7-17.8 eV binding energies. The experimental data and simulation are remarkably similar, and both the electron pocket at $(0,0)$ and the cubic hole pockets centered at $(\pi/a, \pi/a)$ are clearly observed. The absence of this hole like Fermi surface sheet in earlier experiments was the source of an apparent inconsistency between theory and experiment [80, 119, 121], and was attributed to the opening of a gap due to a possible nesting instability [121] or surface reconstruction [122]. In contrast, our measurements clearly resolve both features, in agreement with bulk-sensitive electron-positron annihilation measurements [123] and ARPES measurements of ultrathin films [124]. The observation of these features is central to the content of this dissertation, as the presence of well defined bands enables us to perform a quantitative study of the near E_F electronic structure responsible for the macroscopic electronic properties of manganite films.

Figure 5.11a also shows weak *shadow bands* that stem from the c(2x2) reconstruction seen in our LEED measurements, which we schematically illustrate in Fig. 5.11b. In this film these features are most prominent crossing the hole pocket at $k_x \approx -1.25\pi/a$, but weak diffuse intensity within the hole pockets can also be attributed to this reconstruction. Similar reconstructions are seen in Fermi surface measurements from many of the manganite films discussed in this dissertation, and vary both in intensity and sharpness of the reconstructed features. In all cases, the reconstruction does not appear to otherwise affect the measured electronic structure.

5.3.3 Dispersive states in $La_{0.7}Sr_{0.3}MnO_3$

Figure 5.12 shows ARPES spectra along three k-space cuts for an $La_{0.7}Sr_{0.3}MnO_3$/STO film. Previous ARPES studies have focused on the dispersion of the central electron

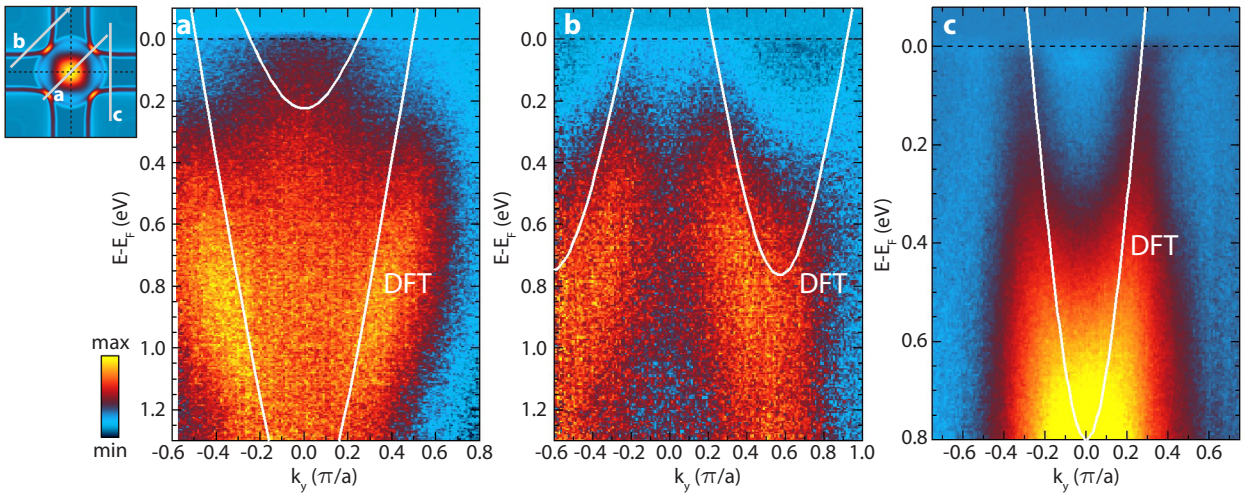

Figure 5.12: (**a-c**) Dispersion measured by ARPES for $La_{0.7}Sr_{0.3}MnO_3$ along the three **k**-space cuts shown in the upper left panel, after subtraction of a non-dispersive background (Fig. 5.13). The DFT calculated bands are overlayed as guides to the eye for $k_z = 0.53\pi/c$ for panels b and c, and $k_z = 0.45\pi/c$ in panel a to better illustrate the electron pocket.

pocket, seen in Fig. 5.12a. Unfortunately, this feature is intrinsically broad and ill-defined in ARPES measurements due to final-state k_z smearing effects (ref. [80] and section 5.2.1), inhibiting their use for detailed quantitative analysis of the $La_{0.7}Sr_{0.3}MnO_3$ electronic structure. Furthermore, we note that $La_{0.7}Sr_{0.3}MnO_3$ is a hole doped material with hole like Hall conductivity [139], and thus measurements of the hole like bands are essential to develop an understanding of its electronic properties.

As shown in Fig. 5.11, our measurements clearly resolve the hole pocket Fermi surface sheets of $La_{0.7}Sr_{0.3}MnO_3$, and ARPES spectra in Fig. 5.12b,c show that they form sharply resolved highly dispersive features over a wide range in energy. The spectra have well-defined Fermi steps at the Fermi wavevectors, consistent with the film's metallic resistivity. A smooth, k-integrated monotonic background was subtracted from the data in order to clearly visualize the band over the entire energy window. Fig. 5.13 shows the data from Fig. 5.12c prior to this background subtraction. Along with the dispersive band crossing

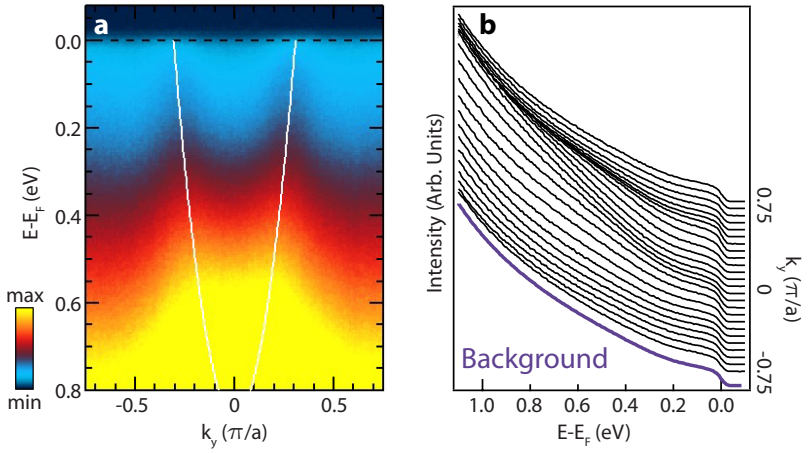

Figure 5.13: (**a**) ARPES spectra for $La_{0.7}Sr_{0.3}MnO_3$ from Fig. 5.12c, before subtracting the non-dispersive background and overlaid with a parabolic fit to the experimental bandstructure. (**b**) EDCs from the same ARPES data showing the non-dispersive background used to produce Fig. 5.12c.

the Fermi level, a large background growing toward higher binding energies is evident. We accounted for this large background by integrating over momenta that are not crossed by the dispersive band to generate a momentum-independent background curve, plotted in Fig. 5.13b. Subtracting this integrated background for all momenta allows us to arrive at the data presented in Fig. 5.12c. An analogous process is followed for other *k*-space cuts.

In addition to the background introduced by MnO_2 surface terminations (section 5.3.1), we also observe non-dispersive spectral weight that tracks the intensity distribution of dispersive states, indicating that it arises from elastic scattering that may be due to crystal imperfections within the film or at the surface. The magnitude of this contribution varies between samples, but is comparable to the MDC peak height of dispersive states in all films. We do not find significant correlations with film thickness, surface termination, or temperature, and it does not appear to otherwise adversely affect our measurements of the dispersive electronic structure.

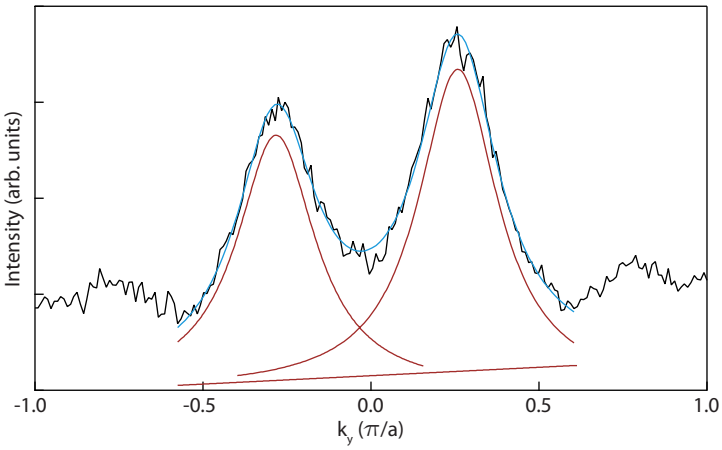

Figure 5.14: MDC at $E = 0.20 \pm 0.01$ eV from the data in Fig. 5.12c. A two-Lorentzian fit (blue) and the individual components (maroon) are shown. Note the two additional weaker peaks outside of the fitted region. These are artifacts due to $c(2 \times 2)$ shadow bands.

A DFT calculation for the band structure of $La_{0.7}Sr_{0.3}MnO_3$ is overlaid onto the ARPES spectra in Fig. 5.12c, exhibiting excellent agreement between the measured and calculated dispersion. This is particularly surprising given the strong electron-electron interactions expected for $3d$ transition metal oxides, although ostensibly incoherent features with similar total bandwidth to the DFT dispersion have also been observed in the layered manganites [140].

I extract the hole pocket bandstructure from our ARPES data on $La_{0.7}Sr_{0.3}MnO_3$ using standard MDC analysis techniques. Depending on the number of bands intersecting the momentum window to be analyzed, I fit the MDC to a function of the form:

$$a + bk + \sum_{i=1}^{n} \frac{A_i}{(k - k_i)^2 + (\Delta k_i/2)^2}$$

Where a and b specify a linear background, and we include n Lorentzians of height $4A_i/\Delta k_i$ and full width at half maximum (FWHM) Δk_i at positions k_i. Figure 5.14 shows an example fit to an MDC at $E = 0.20 \pm 0.01$ eV from the data in Fig. 5.12c.

Our sharpest features have MDC widths of 0.12 Å^{-1}. This is significantly broader than the quasiparticle peaks observed in some layered manganites [141, 142, 106], and indeed we do not observe EDCs anywhere in momentum space that satisfy the conventional definition of a quasiparticle ($\Delta E < E$). Nevertheless, the origin of quasiparticles that have been observed in manganites is controversial [106], and many studies of layered manganites find features that are similarly broad to ours [140, 104, 105]. The lack of sharply defined quasiparticles is a possible indication of the strongly interacting and incoherent nature of these states. Broadening of the spectra can also arise, however, from scattering at imperfections within the crystal structure or at the polar surface of our films. Furthermore, the quasiparticle peak at E_F could be suppressed by the ARPES matrix elements of our fixed photon energy. For these reasons, we do not take our lack of observation of sharp quasiparticles to indicate that they do not exist, and it remains likely that the intrinsic width of the observed features is narrower than our spectra indicate.

Nonetheless, it is well established that in strongly coupled materials the incoherent dispersion can track the unrenormalized *bare* bandstructure [36, 37]. The microscopic details of the Mott insulating state and its relation to the *t*-*J* model in the cuprates are determined from an analysis of the incoherent dispersion making up the lower Hubbard band [36, 37]. Similarly in the layered manganites, gaps due to ordered phases [104, 140], the broadening of bands due to localization [143], and the effects of Fermi surface nesting [105] have all been measured through broad dispersive states without sharply resolved quasiparticles. Thus, despite their possibly incoherent nature, the measured dispersive features in $La_{1-x}Sr_xMnO_3$ films should accurately represent the underlying electronic structure.

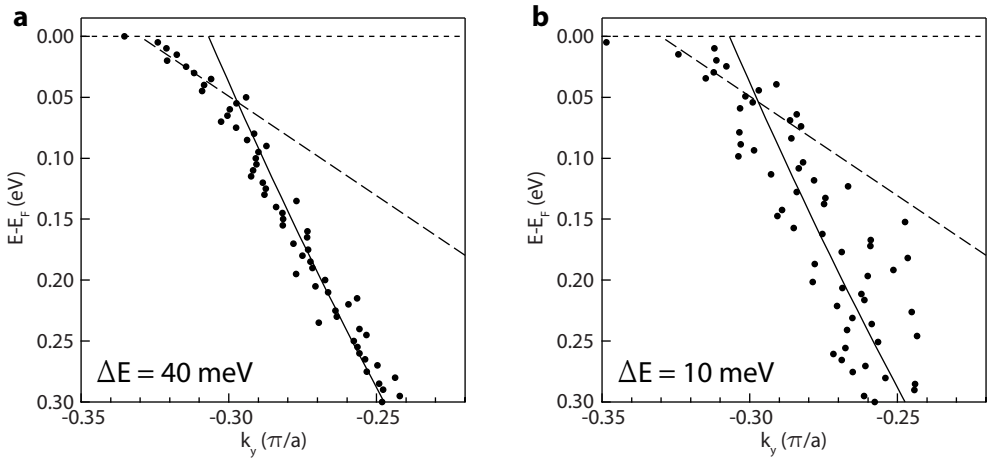

Figure 5.15: (**a**) The experimental dispersion for $La_{0.7}Sr_{0.3}MnO_3$ at $k_x = 0.6\pi/a$ showing a kink near E_F. Also shown are a parabolic fit to the high-energy dispersion (solid line) and a linear fit to the low energy dispersion (< 50 meV, dashed line). This data was taken with an energy resolution of 40 meV. (**b**) The same dispersion measured with 10 meV resolution. The solid and dashed lines are identical to those from panel a. Despite the greater noise in the data, we still resolve the low-energy kink.

5.3.4 Electron-boson coupling strength

As shown in Fig. 5.12c, the experimental band dispersion corresponds remarkably well to predictions from DFT. The close agreement of the band velocity at high energies ($v_{HE} = 5.9 \pm 0.1$ eV Å) with the DFT velocity ($v_{DFT} = 5.3$ eV Å) suggests that electron correlations alone do not strongly renormalize the effective mass. Upon closer inspection of the ARPES data, we observe a sudden deviation in the band velocity at 40 ± 10 meV, which we have also confirmed with an improved energy resolution of 10 meV (Fig. 5.15). This feature is a classic consequence of the coupling to a bosonic mode at an energy of 40 meV (section 2.3). Fitting the band velocity at low (v_F) and high (v_{band}) energies gives $v_{\text{band}}/v_F = 2.7 \pm 0.5$. This is similar in both energy and magnitude to the strong electron-phonon coupling found in bilayer $La_{2-2x}Sr_{1+2x}Mn_2O_7$ (ref. [142]), and indicates

that $La_{1-x}Sr_xMnO_3$ falls within a strong coupling regime. A Fermi liquid theory based analysis gives an enhancement in the effective mass (m^*) over the bare mass (m^{band}) of $m^*/m_{\text{band}} = 2.7$, which is in good agreement with $m^*/m^{\text{band}} = 2.5$ determined by specific heat measurements of bulk $La_{0.7}Sr_{0.3}MnO_3$ (ref. [144]), despite the strong coupling nature of this material.

5.4 Variation with x

5.4.1 Fermi surfaces for $0.2 \leq x \leq 0.6$

In addition to $La_{1-x}Sr_xMnO_3$/STO films at $x = 0.3$, we also measured films at $x = 0.2$, $x = 0.4$, and $x = 0.6$ to observe the changes in electronic structure over a wide range of doping. First we examined the Fermi surface shape and volume for each film by extracting Fermi wavevectors from our ARPES data covering a wide range in k-space. Due to differences in the photoemission intensity at the various x values [119], we used different energy integration windows for each film: $E_F \pm$ 200 meV for $x = 0.2$, $E_F \pm$ 50 meV for $x = 0.3$, $E_F \pm$ 60 meV for $x = 0.4$, and $E_F \pm$ 50 meV for $x = 0.6$. Hole pocket Fermi wavevectors were extracted from the ARPES data by fitting the resulting Fermi surface maps to Lorentzian line shapes and extracting the peak positions. The symmetry operations of the 2D-projected BZ were then applied to the data. The central electron pocket does not provide well-defined Fermi surface crossings in ARPES data, as discussed above. To extract an estimate for the size of this feature, we extracted contours from our Fermi surface maps at 30% and 70% of the electron pocket's peak intensity. Due to strong matrix element effects for the $x = 0.4$ Fermi surface, we did not extract a 70% contour. The resulting Fermi surface contours are plotted in Fig. 5.16, where the hole pocket data are shown as blue points and the electron pocket contours as shaded regions.

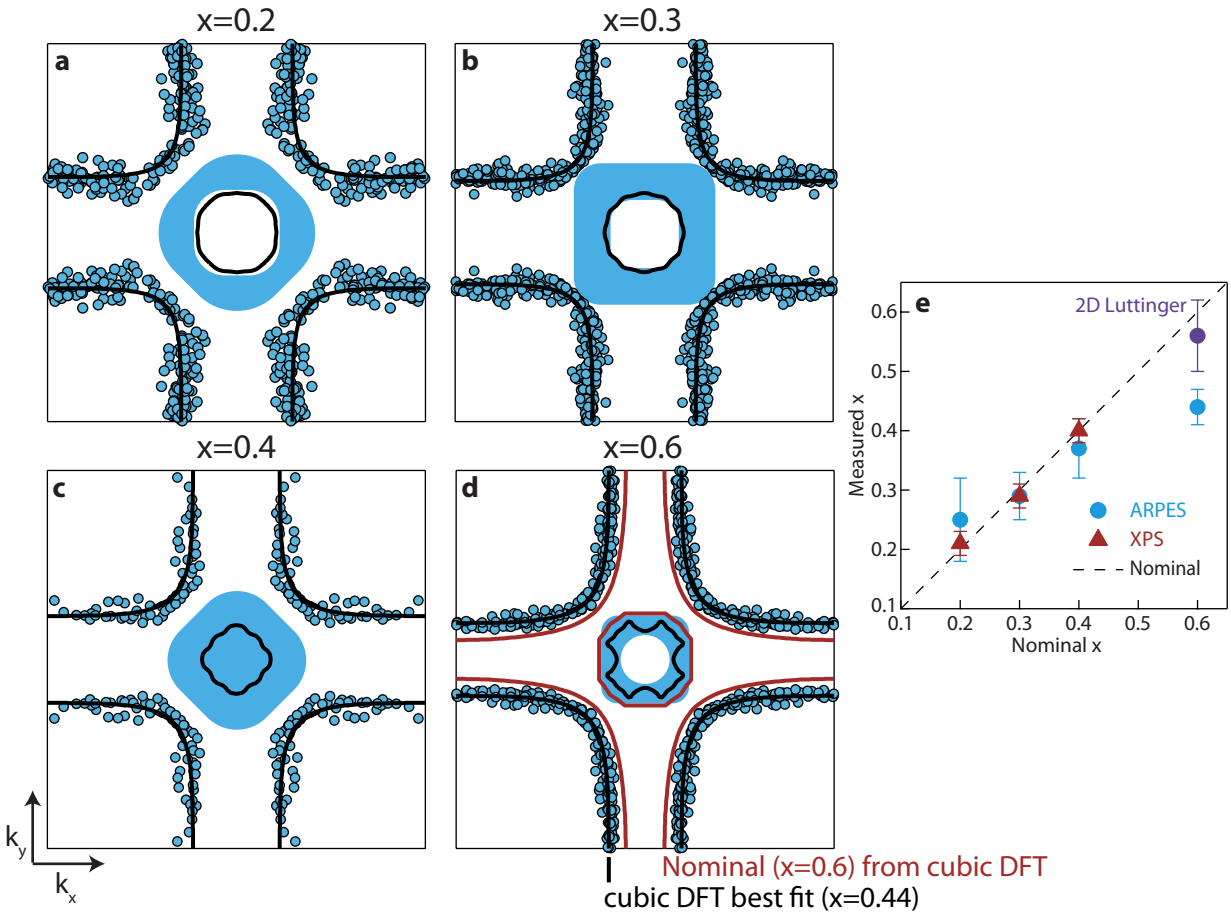

Figure 5.16: (**a**) Experimental Fermi wavevectors (blue points and shaded regions) for $x = 0.2$ (**a**), $x = 0.3$ (**b**), $x = 0.4$ (**c**) and $x = 0.6$ (**d**) compared to the DFT calculated Fermi surface contours at best-fit values for x (within the ferromagnetic phase and for a cubic structure). The electron pocket does not present sharp Fermi surface crossings, so here we have compared constant spectral intensity contours with the DFT predictions (see main text). The nominal ($x = 0.6$) DFT contour is also shown for the $x = 0.6$ film. (**e**) Doping for these four samples determined by ARPES and XPS. In addition, we show the two-dimensional Luttinger count for $x = 0.6$. Error bars for XPS are taken as a typical value of ±0.02. Error bars for ARPES represent an increase in the χ^2 of the fit to 150% of the best-fit value.

In addition, Fig. 5.16 overlays contours extracted from our tetragonally strained DFT calculation for $La_{1-x}Sr_xMnO_3$/STO at x values that best fit the experimentally measured Fermi surfaces. These contours were generated by first projecting out the DFT calculation along the k_z direction as described in section 5.2.1, and exemplified in Fig. 5.8c. Then, hole pockets were extracted following the same procedure used on actual ARPES data and electron pockets were drawn from the 50% intensity contour of the central feature. We then used the extracted DFT hole pockets to perform Luttinger counts of the three dimensional Fermi surface using the two-dimensional contours measured by ARPES. This was done by varying the chemical potential within the calculation to obtain the best fit to the experimentally measured hole pocket contours for each film. The volume of the three-dimensional calculated Fermi surface corresponding to each two dimensional ARPES measurement provides the mobile carrier concentration for each film. To account for the fact that in experiment we do not resolve states above E_F, the DFT integration window uses only the occupied portion of the spectrum. For example: the $x = 0.2$ experimental data was integrated over $E_F \pm 200$ meV, and the corresponding DFT calculation was integrated over $E_F - 200$ meV up to E_F. This shift of 0.1 eV in the center of the integration window corresponds to a change in x of 0.04. For the smaller integration windows used in other samples (0.05-0.06 eV), the corresponding change in x is 0.01.

The results are reported in Fig. 5.16e alongside XPS measurements of the La:Sr stoichiometry for the same $x = 0.2$-0.4 films. The close agreement between the mobile carrier concentration, nominal x, and experimentally determined x suggests that all of the Sr dopants contribute to itinerant carriers throughout the ferromagnetic metallic phase. Furthermore, the good agreement between DFT and ARPES data for both Fermi surface sheets at $x = 0.2$-0.4 suggests that a simple rigid band model accurately describes the underlying single electron band structure of the ferromagnetic metallic state in a wide range around $x = 0.3$, and provides further support that our results are representative of the intrinsic electronic structure of bulk $La_{1-x}Sr_xMnO_3$. Of course, this treatment does not ac-

count for the many-body effects such as incoherence and suppression of spectral weight that can interfere with quasiparticle-like metallic conduction despite the large carrier concentration. Nevertheless, these results constitute the first direct demonstration that DFT calculations correctly account for the shape and underlying bandstructure within the ferromagnetic metallic phase of $La_{1-x}Sr_xMnO_3$, and thus form a meaningful foundation for more sophisticated many-body treatments.

5.4.2 The A-type antiferromagnetic state at $x = 0.6$

In contrast to x = 0.2-0.4, we see clear disagreement between the nominal and ARPES determined carrier concentrations for the x = 0.6 film. This is further highlighted in Fig. 5.16d by the maroon contours showing the DFT calculated Fermi surface for a nominal value of x = 0.6. This indicates a fundamental change in the underlying electronic structure on passing from x = 0.4 to x = 0.6, a result that is in excellent agreement with the established $La_{1-x}Sr_xMnO_3$ phase diagram (Fig. 4.1a). Upon increasing x to above $\approx$ 0.5, the ground state of bulk $La_{1-x}Sr_xMnO_3$ transitions from the ferromagnetic to an A-type antiferromagnetic phase (A-AF). This phase is distinct from the highly insulating A-AF phase in undoped $LaMnO_3$, which has a staggered $d_{3x^2-r^2}/d_{3y^2-r^2}$ orbital order with unit occupancy at each site [99]. Instead, near x = 0.5 we expect $d_{x^2-y^2}$ polarized fractionally occupied orbitals [145]. Consistent with this expectation, it is found that the transition into the A-AF phase is accompanied by a tetragonal structural distortion [146]. In addition, the resistivity increases by an order of magnitude over the FM metallic phase and becomes fairly independent of temperature [72]. The $d_{x^2-y^2}$ orbital order and A-AF spin arrangement is expected to give rise to a quasi-two-dimensional metal with strongly anisotropic resistivity. Although resistivity anisotropy has been observed in the much more insulating $Nd_{0.45}Sr_{0.55}MnO_3$ (ref. [147]), a similar observation has not been reported for $La_{1-x}Sr_xMnO_3$.

In comparing to the bulk phase diagram, it is important to note that the lattice constant of $La_{1-x}Sr_xMnO_3$ decreases as the Sr content is increased, and as a result the in-plane tensile strain for $La_{0.4}Sr_{0.6}MnO_3$/STO is quite large (1.4%) [72]. Tensile strain from the substrate breaks the symmetry between the *a*-*b* plane and the *c*-axis, which leads to an out-of-plane orientation for the A-type antiferromagnetic coupling and an in-plane orientation for $d_{x^2-y^2}$ orbital polarization [83]. Equally thick $La_{0.45}Sr_{0.55}MnO_3$ films in the literature were found to be either coherently strained [148] or heavily relaxed [149], presumably depending on growth conditions, so it is possible that some degree of relaxation has occurred in our film. Nevertheless, tensile strain acts to stabilize the A-AF phase found in bulk $La_{0.4}Sr_{0.6}MnO_3$, so we expect similar magnetic and electronic structure for both coherently strained and partially relaxed films. In fact, both of the aforementioned studies find similar Néel temperatures of $T_N \approx 220$K with similar bad-metallic conductivity [148, 149].

Sun et al. [17] have performed extensive measurements of the electronic structure in the A-AF metallic phase of the bilayer Ruddlesden-Popper $La_{0.82}Sr_{2.18}Mn_2O_7$. They reported a very weak coupling between bilayers resulting in a lack of bilayer splitting of the bandstructure, and the absence of the $d_{3z^2-r^2}$ electron pocket from the Fermi surface. Both results are consistent with DFT calculations of the $d_{x^2-y^2}$ polarized A-AF state. No ARPES studies of the perovskite A-AF phase have been reported, however. In perovskites we might expect the effect of A-AF on the c-axis hopping parameters and orbital polarization to be significantly reduced relative to the layered materials, where the crystal structure already provides a degree of $d_{x^2-y^2}$ polarization and reduced c-axis hopping. Nevertheless, our results in Fig. 5.16d already show that the electronic structure has a dramatic response to this phase transition.

Figure 5.17 shows the raw Fermi surfaces measured by ARPES for $x = 0.6$ and $x = 0.3$. Although qualitatively similar, the hole pockets for $x = 0.6$ are noticeably larger and

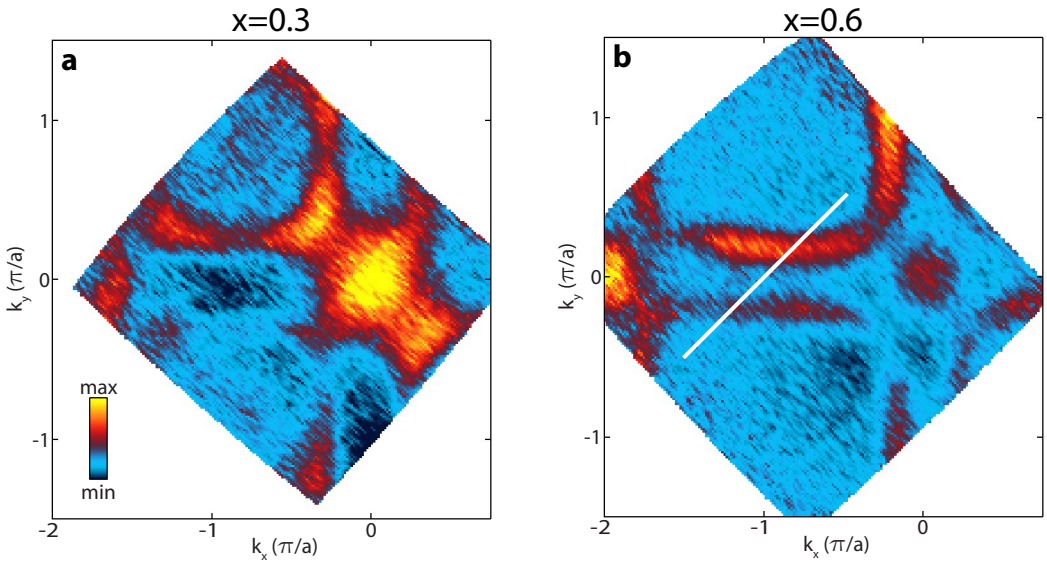

Figure 5.17: The Fermi surface (integrated over $E_F \pm 50$ meV) from $x = 0.3$ (**a**) and $x = 0.6$ (**b**) films. The larger hole pockets and smaller electron pocket for $x = 0.6$ are indicative not only of the increased hole doping for this film, but also of a strongly reduced k_z dispersion. The white line indicates the **k**-space cut used in Fig. 5.19.

the electron pocket smaller than the corresponding features at $x = 0.3$. This is partly a consequence of the increased hole doping of this compound, but as we showed in Fig. 5.16d, doping alone is unable to account for the measured $x = 0.6$ Fermi surface. On the other hand, the electronic structure of an anisotropic $d_{x^2-y^2}$ polarized state in A-AF $La_{1-x}Sr_xMnO_3$ should exhibit a strongly reduced k_z dispersion. To explore this issue quantitatively, I calculated the Luttinger volume of each Fermi surface sheet for the $x = 0.3$ and $x = 0.6$ films. Assuming a purely two-dimensional bandstructure results in an experimentally determined x of 0.42 ± 0.05 and 0.56 ± 0.06 for $x = 0.3$ and $x = 0.6$ films, respectively, where the error is dominated by the difficulty in precisely determining k_F for the electron pockets. On the other hand, our three-dimensional Luttinger counts indicated 0.29 ± 0.04 and 0.44 ± 0.03 for $x = 0.3$ and $x = 0.6$ films (Fig. 5.16e). A two-dimensional electronic structure clearly provides a much better estimate for the hole concentration of the $x = 0.6$

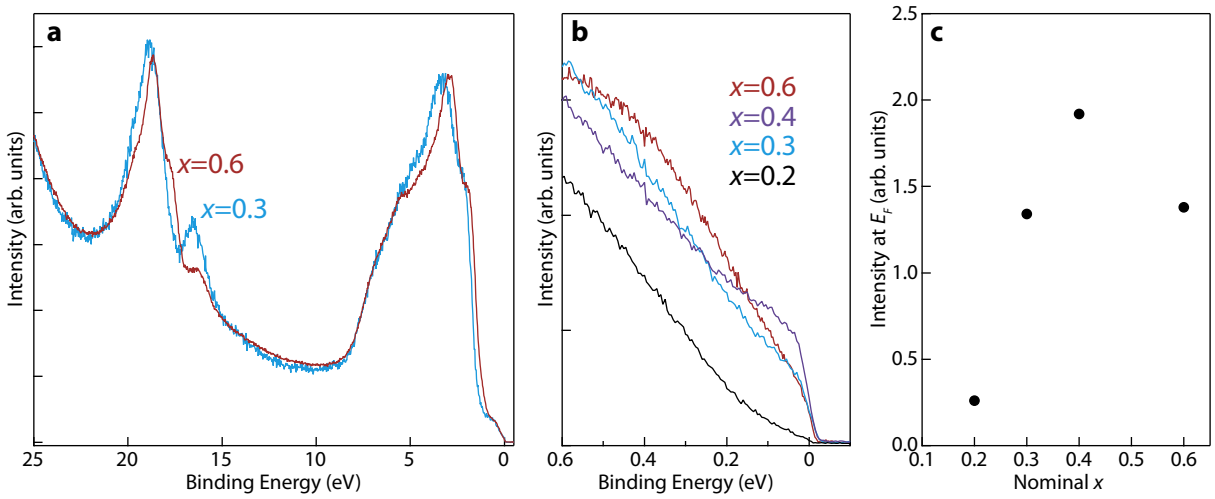

Figure 5.18: (**a**) The angle-integrated valence band from $x = 0.3$ and $x = 0.6$ films. (**b**) EDCs at the hole pocket k_F for the same two films in addition to films at $x = 0.2$ and $x = 0.4$, all normalized to the valence band peak at $E \approx 3.2$ eV. (**c**) The spectral weight integrated within 100 meV of E_F for each film. We find a strong reduction in intensity at E_F for $x = 0.2$ relative to the films at larger x.

sample, whereas the $x = 0.3$ film agrees with the expected three-dimensional model. Our ARPES results therefore demonstrate a crossover from the three-dimensional electronic structure of the ferromagnetic phase, to a strongly anisotropic electronic structure within the $d_{x^2-y^2}$ polarized A-AF.

5.4.3 Energy dependent electronic structure for varying x

Fig. 5.18a shows the measured angle-integrated valence band for the $x = 0.6$ film compared to an otherwise identically grown $x = 0.3$ film. The high-binding energy features demonstrate the (La,Sr)O termination of this film (section 5.3.1), which is consistent with the nominal surface termination from growth. The La $5p$ derived peak has become weaker for the $x = 0.6$ film, consistent with its smaller La content. Furthermore, the

$x = 0.6$ valence band shows a general shift to lower binding energies. Hole-doping shifts the chemical potential deeper into the occupied bands. Since the location of the chemical potential defines our zero position in energy, this is reflected in a lower binding energy for all other features in the photoemission spectrum of the $x = 0.6$ film. The Sr $4p$ peak shifts by 0.16 ± 0.05 eV. This is much less than the rigid-band shift from our FM DFT calculation (0.5 eV), but this discrepancy is not surprising given the over-simplicity of the rigid-shift model and the phase transition occurring at $x \approx 0.5$. XPS measurements of the chemical potential in $La_{1-x}Sr_xMnO_3$ find a shift of 0.26 ± 0.1 eV on increasing x from 0.3 to 0.6, within error of our results [150].

Fig. 5.18b and c show a comparison for $x = 0.2$-0.6 at the hole-pocket k_F and within a narrow energy window around E_F. We observe little change in the spectral weight at E_F for $x = 0.3$-0.6, indicating that our $x = 0.6$ film remains within a metallic phase, consistent with both the bulk $La_{1-x}Sr_xMnO_3$ phase diagram and transport measurements on $x = 0.55$ $La_{1-x}Sr_xMnO_3$/STO films [72, 148]. On the other hand, there is a dramatic decrease in weight at E_F for $x = 0.2$. A similar suppression of spectral weight at E_F was observed in angle-integrated studies of of pulsed-laser deposition grown $La_{1-x}Sr_xMnO_3$ films [151], and further explored in detail by in-situ ARPES measurements of the electron pocket at the Brillouin zone center [119]. $La_{1-x}Sr_xMnO_3$ transitions into a ferromagnetic insulating phase for $x < 0.15$, at which point the spectral weight at E_F vanishes. The suppression of weight on approaching this transition from the metallic side was interpreted as evidence that this transition is of the Mott type, and that spectral weight from the Mn e_g band is transferred to a higher binding energy *lower Hubbard band* that is obscured by the intense O $2p$ and Mn t_{2g} valence band. Our results are consistent with this interpretation, but now verify that this model holds for both the electron and hole pockets that make up the Fermi surface.

High resolution ARPES measurements of the hole pocket, shown in Fig. 5.19a, allow

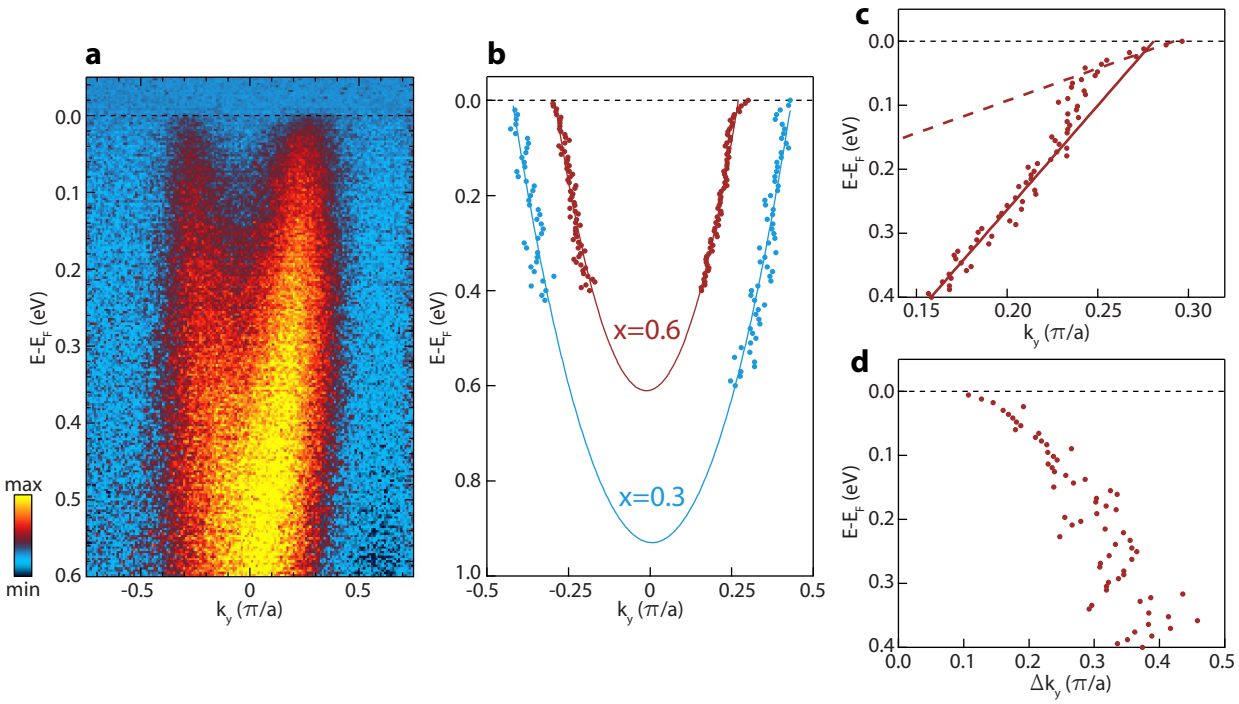

Figure 5.19: (**a**) $x = 0.6$ ARPES spectra along the **k**-space cut indicated by the white line in Fig. 5.17b taken with an energy resolution of 10 meV, after subtraction of a non-dispersive background. (**b**) Points correspond to MDC fitted experimental dispersion for $x = 0.3$ and $x = 0.6$ data along the same **k**-space cut as in panel a. Lines show quadratic fits to the experimental data. (**c**) Dispersion extracted from MDC fits to the $x = 0.6$ electronic structure in panel a showing a clear low energy kink. Linear fits to the high energy and low energy dispersion are shown as a solid and dashed line, respectively. (**d**) FWHM of the Lorentzian MDC fits showing a slight change in energy-dependence below 0.1 eV.

us to examine the electronic structure of A-AF $La_{1-x}Sr_xMnO_3$ in more detail. We observe well-defined dispersive features with k-widths comparable to our narrowest measured ferromagnetic $La_{1-x}Sr_xMnO_3$ features (Δk as small as 0.1 Å^{-1}). Figure 5.19b shows the results of MDC fits to the experimental dispersion for $x = 0.6$ compared to the dispersion along the same **k**-space cut for $x = 0.3$. Due to the larger hole-doping, the $x = 0.6$ band bottom lies closer to E_F. Nevertheless, fits to the high energy dispersion (0.4-0.1 eV) indi-

cate a 25% lower effective mass for $x = 0.6$ than the ferromagnetic phase at $x = 0.3$. This indicates that carriers at $x = 0.6$ have comparable or slightly higher in-plane hopping coefficients. This is reasonable to expect; the *in-plane* MnO_2 network is ferromagnetically coupled in both the A-AF and ferromagnetic states, and tight-binding parametrizations of first-principles calculations find similar hopping parameters for both [75, 152]. As emphasized by our Fermi surface measurements, the key change in the electronic structure is the dramatic reduction in hopping along the k_z direction due to the combination of antiferromagnetic coupling and the strong Hund's rule interaction [152].

Figure 5.19c and d show the extracted bandstructure and k-widths for the band at $k \approx 0.25\,\pi/a$ within a narrow window around E_F. We observe a clearly resolved kink deviating from the high-energy dispersion at 110 meV and crossing over into a low-velocity dispersion at 60 meV. This feature is a classic signature of electron-boson coupling, and equating the ratio of high-energy (> 150 meV) to low-energy (< 60 meV) velocities with the enhancement of the hole band's effective mass gives $m^*/m = 3$. This value is in excellent agreement with the renormalization observed in A-AF Ruddlesden-Popper manganites [17] and by us in ferromagnetic $La_{1-x}Sr_xMnO_3$ (section 5.3.4), indicating an electron-phonon source for the renormalization and a similar strength in the three-dimensional and quasi-two dimensional cases for both layered and cubic manganites.

5.5 Conclusions

In this chapter we have shown extensive measurements of the electronic structure of the canonical large-bandwidth manganite. These represent the first measurements of the entire Fermi surface and near E_F electronic structure in $La_{1-x}Sr_xMnO_3$, and allowed us to establish that first-principles calculations accurately describe the underlying Fermi surface shape and band dispersion over a wide range in x. Nevertheless, our measurements

showed substantial departures from a simple Fermi liquid scenario, including a dramatic suppression of spectral weight at E_F for $x = 0.2$ and a strong renormalization of the dispersion near E_F. The sharply resolved hole pockets enabled direct comparisons between our data on perovskite $La_{1-x}Sr_xMnO_3$ and the extensive literature on the bilayer Ruddlesden-Popper manganites. Both share a similar strong electron-lattice coupling within the ferromagnetic and A-AF metallic phases, suggesting that the charge carriers of $La_{1-x}Sr_xMnO_3$ have a strongly polaronic nature. The close agreement between layered and perovskite manganites is particularly surprising given the two-order of magnitude difference in resistivity between them.

Further ARPES measurements of A-AF $La_{0.4}Sr_{0.6}MnO_3$ demonstrated a similar spectral weight at the Fermi level and comparable in-plane hopping parameters to the ferromagnetic phase. Nevertheless, our Fermi surface measurements ruled out an isotropic three-dimensional electronic structure, indicating instead a strongly anisotropic state that is consistent with the expected $d_{x^2-y^2}$ polarized A-AF. As discussed in chapter 7, a growing body of evidence from Ruddlesden-Popper manganites as well as our experiments on manganite superlattices have demonstrated the important role played by the c-axis dispersion in stabilizing the fragile metallic state of the manganites. It is thus natural that as the dispersion in perovskite $La_{1-x}Sr_xMnO_3$ becomes more anisotropic, the A-AF phase should experience the measured order-of-magnitude jump in resistivity over the FM. The A-AF phase alone is insufficient to promote a truly insulating two-dimensional state though, as transport measurements and our ARPES results demonstrate that it remains on the verge of metallic behavior.

Working from $La_{1-x}Sr_xMnO_3$/STO as a starting point, in the following chapters we will use epitaxial strain and atomically engineered heterostructures to disrupt the ferromagnetic metallic phase at $x = 1/3$ while directly measuring the corresponding changes in the underlying electronic structure.

Chapter 6

Epitaxial strain control of electronic structure through the metal-insulator transition in $La_{2/3}Sr_{1/3}MnO_3$

Pressure has played a key role in modifying the physical properties of correlated materials and has been demonstrated, for instance, to enhance high temperature superconductivity in cuprates and drive quantum phase transitions in organic and heavy fermion materials [153, 154, 155]. Nevertheless, experimental probes such as ARPES and scanning tunneling spectroscopy that have played a key role in understanding the electronic structure of cuprates [16, 156], topological insulators [157] and many other complex electronic phases remain incompatible with typical high pressure apparatus, due to the need for accessible surfaces and ultra-high vacuum conditions. The epitaxial growth of films on deliberately lattice mismatched substrates provides a clean and accessible analogue to external pres-

Much of the work discussed in this chapter has been submitted as a manuscript to *Physical Review Letters*.

sure, and is capable of attaining biaxial strain (typically $\Delta a/a < 3\%$) far beyond the $\approx 0.1\%$ shattering point of typical bulk ceramic crystals [53].

Due to these advantages, epitaxial strain has been used extensively to enhance carrier mobilities in semiconductor devices, for example [158]. Nevertheless, some of the most exciting applications of epitaxial strain involve dramatically altering the electronic phases of complex oxide films. This includes controlling phase separation at the nanoscale [159], enhancing high-temperature superconducting and ferromagnetic transition temperatures [160, 161], and engineering new powerful multiferroics [10, 162]. Our ability to access the electronic structure underlying such strain-driven phase transitions presents us with the opportunity to develop a detailed understanding of the many-body interactions that give rise to complex strain based phase diagrams, essential to the use of strain for rationally engineering new and useful correlated electron states.

The role of epitaxial strain in tuning the properties of $La_{1-x}Sr_xMnO_3$ was first studied by the Tokura group in 1999 [83]. Under compressive strain, the ferromagnetic phase became unstable to the C-type antiferromagnet. On the other hand, tensile strain was found to preferentially favor the A-type antiferromagnet. Theoretical calculations in this and subsequent work [163, 164, 165, 166] uncovered the origin of the magnetic phase transitions. Compressive strain favors a $d_{3z^2-r^2}$ orbital polarization which encourages ferromagnetic coupling along the z direction and in-plane antiferromagnetic coupling, naturally leading to a C-type antiferromagnetic phase. This polarization is consistent with the x-ray linear dichroism found in compressively strained films [54]. Conversely, tensile strain favors $d_{x^2-y^2}$ polarization, with ferromagnetic in-plane coupling and antiferromagnetic out-of-plane coupling that gives rise to A-type antiferromagnetism. Figure 6.1a shows the first-principles *magnetic* phase diagram from ref. [163].

Nevertheless, the excellent agreement between first-principles calculations and magnetic behavior obscures an essential remaining puzzle: all of these treatments predict a

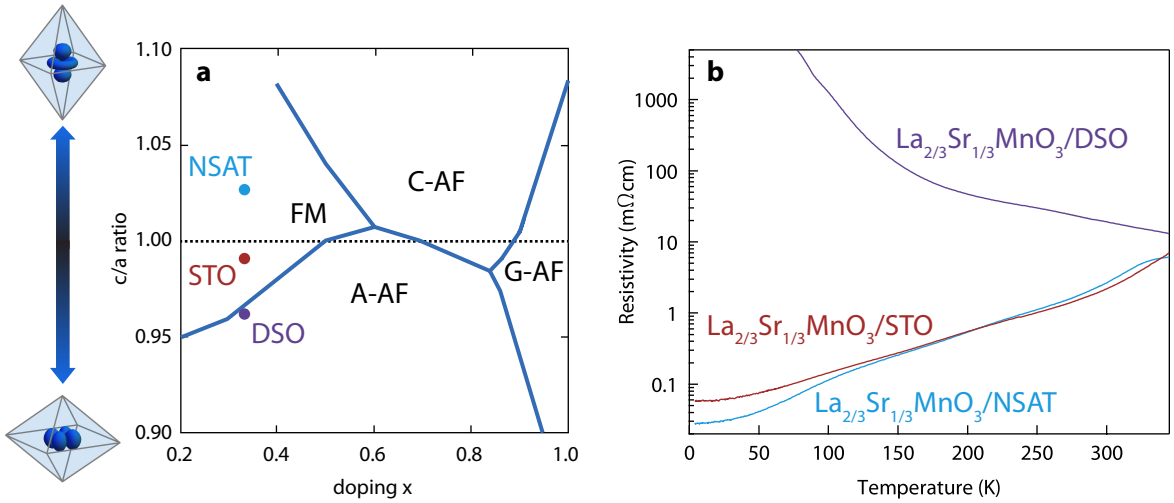

Figure 6.1: (**a**) The *magnetic* phase diagram for epitaxial strain (c and a are the out-of-plane and in-plane pseudocubic lattice constants) and x predicted by DFT in ref. [163]. We schematically show exaggerated distorted oxygen octahedra and the corresponding Mn e_g polarizations. Points corresponding to $x = 1/3$ films on the substrates used in this chapter (see main text) are also shown. (**b**) Resistivity of three strained $La_{2/3}Sr_{1/3}MnO_3$ films that were measured by ARPES showing the insulating behavior of the film on DSO.

metallic electronic structure that is at odds with the insulating behavior observed under strong tensile and compressive strain [83, 167, 127]. The quasi-one-dimensional C-type phase realized under strong biaxial compressive strain is insulating in bulk manganites, but particularly mysterious is the metal-insulator transition under biaxial tensile strain, which should favor the A-type phase. Bulk crystal transport measurements [72] and our ARPES measurements of $La_{0.4}Sr_{0.6}MnO_3$ films in the previous chapter demonstrate the typically metallic nature of this phase.

Here, we use in-situ ARPES to directly measure the electronic structure of biaxially strained $La_{2/3}Sr_{1/3}MnO_3$ thin films[2] under compressive and tensile strain (Fig. 6.1a,b).

[2]As discussed below, our characterization and ARPES measurements indicate that all of the films presented in this chapter fall within $x = 0.33 \pm 0.05$. Over this entire range, unstrained $La_{1-x}Sr_xMnO_3$ is well inside of the ferromagnetic metallic phase and our ARPES measurements of the previous chapter demonstrate that the near-E_F electronic structure shows little variation. For convenience, all films will henceforth

Our measurements show a strong suppression of spectral weight near the Fermi level (E_F) for the insulating phase under tensile strain, despite the fact that the global bandwidth and width in momentum space (Δk) are comparable to the metallic samples. These results rule out the scenarios of bandwidth or localization-driven metal-insulator transitions, and reveal an instability of the ferromagnetic metal towards an ordered insulating phase which can be accessed through epitaxial strain.

6.1 Film growth and characterization

We synthesized coherently strained films of (001) $La_{2/3}Sr_{1/3}MnO_3$ on $(NdAlO_3)_{0.39}$–$(SrAl_{1/2}Ta_{1/2}O_3)_{0.61}$ (NSAT, a = 3.84 Å) [168] and $DyScO_3$ (DSO, a = 3.95 Å) substrates, which have lattice mismatches of -1.2% and 1.7% with bulk $La_{2/3}Sr_{1/3}MnO_3$, respectively (a referred to pseudocubic unit cells). Films were grown in a dual-chamber Veeco GEN10 MBE equipped with reflection high-energy electron diffraction at a substrate temperature of 700 °C and with a background oxidant (O_2+10% O_3) partial pressure of 5×10^{-7} Torr. Samples were cooled in the oxidant to below 200 °C, and then immediately transferred to the ARPES cryostat for measurement. The $La_{2/3}Sr_{1/3}MnO_3$/STO films discussed in the previous chapter and further discussed here were grown using identical conditions, and have a smaller lattice mismatch of 0.6%. Further details on film growth are provided in section 5.1. Weakly strained $La_{2/3}Sr_{1/3}MnO_3$/STO films were either 100 nm or 20 nm thick, and ARPES spectra for both thicknesses showed no significant differences. The more heavily strained films on DSO and NSAT were 20 nm thick, which was previously found to preserve coherent epitaxial strain [127].

We measured resistivities of the same samples measured by ARPES in a four-point probe linear geometry after removing the films from our vacuum chamber

be referred to as $La_{2/3}Sr_{1/3}MnO_3$, including when comparing to x = 0.3 data from the previous chapter.

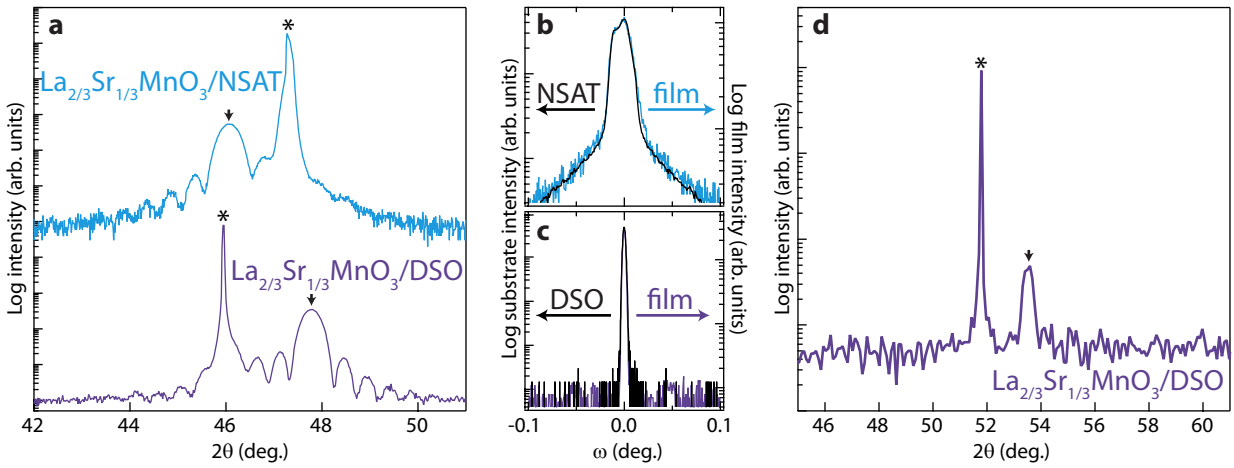

Figure 6.2: (**a**) θ-2θ x-ray diffraction patterns around the out-of-plane 002 pseudocubic $La_{2/3}Sr_{1/3}MnO_3$ reflection from 20 nm thick $La_{2/3}Sr_{1/3}MnO_3$/DSO and $La_{2/3}Sr_{1/3}MnO_3$/NSAT films grown under the same conditions as ARPES samples. All films are coherently strained and show clear thickness fringes. Asterisks and black arrows identify the 002 pseudocubic substrate and film peaks, respectively. (**b,c**) X-ray rocking curves of the 002 pseudocubic peaks from the same films, demonstrating substrate-limited crystallinity in both cases. FWHM values for both the films and substrates are 0.02° for $La_{2/3}Sr_{1/3}MnO_3$/NSAT and 0.003° for $La_{2/3}Sr_{1/3}MnO_3$/DSO. (**d**) X-ray diffraction scan along the [101] pseudocubic direction for the same $La_{2/3}Sr_{1/3}MnO_3$/DSO film showing the [101] pseudocubic substrate and film peaks used for determining the in-plane lattice constant.

(Fig. 6.1b). Our $La_{2/3}Sr_{1/3}MnO_3$/NSAT and $La_{2/3}Sr_{1/3}MnO_3$/STO films have resistivities characteristic of the ferromagnetic metallic ground state in bulk samples, whereas $La_{2/3}Sr_{1/3}MnO_3$/DSO films are more than five orders of magnitude more insulating at low temperature (Fig. 6.1b).

We verified the structural quality of our films using high-resolution $\theta-2\theta$ x-ray diffraction with monochromated Cu $K_{\alpha 1}$ radiation and a four-circle Rigaku SmartLab x-ray diffractometer. In addition, we acquired rocking curves of the 002 pseudocubic peaks of both the films and substrates using an additional 220 germanium monochromator on the

diffracted beam. Fig. 6.2 shows example diffraction patterns for films on each substrate, grown under identical conditions to our ARPES films. The $\theta - 2\theta$ scans show strong film peaks with an absence of any undesired intergrowth phases, in addition to well developed thickness fringes indicating smooth high quality film surfaces. In all cases, rocking curves for the films had the same FWHM as the corresponding substrates, which indicates that film crystallinity is substrate limited and provides further support for the high quality of our growths.

To directly confirm that our heavily strained $La_{2/3}Sr_{1/3}MnO_3$/DSO films are coherently lattice matched to the substrate, we measured several in-plane diffraction patterns for a 20 nm thick $La_{2/3}Sr_{1/3}MnO_3$/DSO film (Fig. 6.2c). First, we used the $\theta - 2\theta$ peak positions to calculate the out-of-plane lattice constant ($c = 3.805 \pm 0.005$ Å) using a Nelson-Riley plot [169]. We then used the position of the [101] pseudocubic film peak along with the known c axis lattice constant to determine an in-plane lattice constant of $a = 3.95 \pm 0.01$ Å. This value is in excellent agreement with the pseudocubic DSO lattice constant ($a = 3.95$ Å), indicating that this film is indeed coherently strained.

Film stoichiometry was characterized by ex-situ XPS measurements of the La 4*d* and Sr 3*d* core levels using a monochromated Al K_α source (1486.6 eV), as discussed in section 5.1.3. In addition, three samples were sent to Jürgen Schubert at Forschungszentrum Jülich GmbH for Rutherford backscattering spectrometry measurements to provide an additional measure of film stoichiometry and cross check for our XPS results. The samples were 10×5 mm of nominal composition $La_{2/3}Sr_{1/3}MnO_3$, and were on DSO, NSAT, and $LaAlO_3$ substrates. The films on DSO and NSAT were 20 nm thick, and the film on $LaAlO_3$ was 9 nm thick. Due to the very thin film thicknesses and the use of substrates that contain heavy elements, the signal from these RBS measurements is intrinsically much lower than is typical. Nevertheless, our collaborators were able to measure and analyze the spectra from each film, and we report these results in table 6.1 alongside

Substrate	RBS x	XPS x
NSAT	0.32 ± 0.03	0.35 ± 0.02
DSO	$0.35^{+0.05}_{-0.03}$	0.36 ± 0.02
LAO	$0.35^{+0.05}_{-0.03}$	0.40 ± 0.02

Table 6.1: Experimentally determined x for $La_{1-x}Sr_xMnO_3$ films on NSAT, LAO, and DSO substrates by RBS and XPS.

XPS measurements from the same films. Due to the aforementioned experimental difficulties, the estimated error bars are large, and may be particularly so for the very thin film on $LaAlO_3$ whose spectra showed additional surface-derived features that could not be accounted for. Nevertheless, the main point is that within the admittedly large error bars, our XPS results are consistent with RBS from these films and that our XPS measurements are thus not subject to large systematic errors.

An additional concern regarding the stoichiometry of manganite films is the possibility of a large concentration of oxygen vacancies [170]. We are unable to directly obtain accurate measurements of the oxygen concentration of our films from our ex-situ XPS measurements, since they are surface sensitive and will be affected by contamination due to air exposure, and Rutherford backscattering spectrometry is unable to accurately determine the concentration of such light elements. On the other hand, we are able to indirectly approach this problem through several means. First, the highly metallic resistivities of films on STO and NSAT substrates provide strong evidence against the formation of a large concentration of oxygen vacancies, which would dope the films away from $x = 1/3$ and thus increase their resistivity. More cause for concern exists in the insulating $La_{2/3}Sr_{1/3}MnO_3$/DSO films, though, since we must ensure that the metal insulator transition is intrinsic to $La_{2/3}Sr_{1/3}MnO_3$ and not an artifact of poor stoichiometry.

To address this, I measured the Mn $3s$ splitting by XPS for the same film measured by ARPES. As shown in Fig. 6.3a using data from Galakhov et al. [74], the energy splitting of the Mn $3s$ doublet depends sensitively on the Mn valence due to an exchange coupling be-

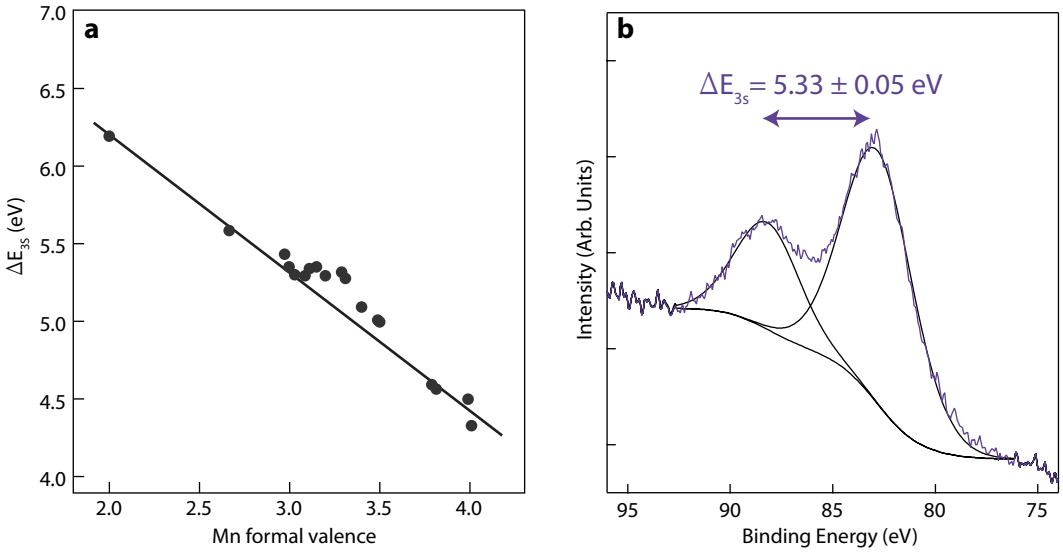

Figure 6.3: (**a**) The Mn 3*s* core level splitting for many compounds as a function of the formal Mn valence (adapted with permission from Galakhov *et al.* (2002) [74]. Copyright 2002 by the American Physical Society). (**b**) Mn 3*s* XPS spectrum from the $La_{2/3}Sr_{1/3}MnO_3$/DSO film measured by ARPES. The XPS data is shown in purple, and the fit peaks and background are shown in black. The observed splitting is consistent with the nominal Mn valence.

tween the core hole and the Mn 3*d* valence electrons. For a composition $La_{1-x}Sr_xMnO_{3-y}$, the nominal Mn valence is given by $V_{\mathrm{Mn}} = 3 + x - 2y$, so that V_{Mn} is sensitive to the concentration of oxygen vacancies. Unfortunately, due to charge transfer between O and Mn, $x = 1/3$ lies in a region where the actual charge on the Mn site is relatively constant with x leading to a plateau in the Mn 3*s* splitting. We measured a splitting of $\Delta E_{3s} = 5.33 \pm 0.05$ eV for the $La_{2/3}Sr_{1/3}MnO_3$/DSO film, putting us within this plateau and indicating a Mn valence between 3+ to the ideal 3.3+. This provides an upper bound of $y < 0.19$ given the XPS determined Sr concentration ($x = 0.38$).

As an additional check, we note that the lattice parameters of our $La_{2/3}Sr_{1/3}MnO_3$/DSO film closely agree with published values in earlier work [127], indicating no measurable lattice expansion due to oxygen vacancies. Furthermore, our ARPES measurements of

Substrate	Nominal x	XPS x	ARPES x
NSAT	0.3	0.37 ± 0.02	0.37 ± 0.04
STO	0.3	0.29 ± 0.02	0.29 ± 0.04
DSO	0.3	0.38 ± 0.02	0.30 ± 0.05
STO	0.2	0.21 ± 0.02	0.25 ± 0.07
STO	0.4	0.40 ± 0.02	0.37 ± 0.05

Table 6.2: Experimentally determined x for $La_{1-x}Sr_xMnO_3$ films that were measured by ARPES. The uncertainty for XPS is taken as a typical value of ±0.02. Uncertainties for ARPES represent an increase in the χ^2 of the fit to 150% of the best-fit value.

iso-energy contours in $La_{2/3}Sr_{1/3}MnO_3$ films can be used to estimate the carrier concentrations following the procedure outlined in section 5.4.1. Table 6.2 shows results for films on STO, NSAT, and DSO. The mobile carrier concentration for each metallic sample from ARPES closely agrees with the La/Sr ratio as measured by XPS, demonstrating a lack of a measurable concentrations of oxygen vacancies. Due to the insulating nature of this sample, which is not captured by DFT calculations, we do not expect this procedure to be as precise as for metallic films. Nevertheless, we estimate a charge concentration in the Mn e_g states corresponding to $x = 0.3 \pm 0.05$ that is well within the ferromagnetic metallic phase for unstrained $La_{1-x}Sr_xMnO_3$, and indicating at most only a small concentration of oxygen vacancies $y < 0.07$.

6.2 ARPES results

ARPES and angle-integrated valence band measurements were performed with a VUV5000 helium plasma discharge lamp and monochromator using He II photons ($h\nu$ = 40.8 eV) and a VG Scienta R4000 electron analyzer. The sample temperature was kept below 20 K for films on NSAT and STO substrates. Measurements were performed at 70 K for films on DSO substrates to avoid charging, as discussed below. We used an energy

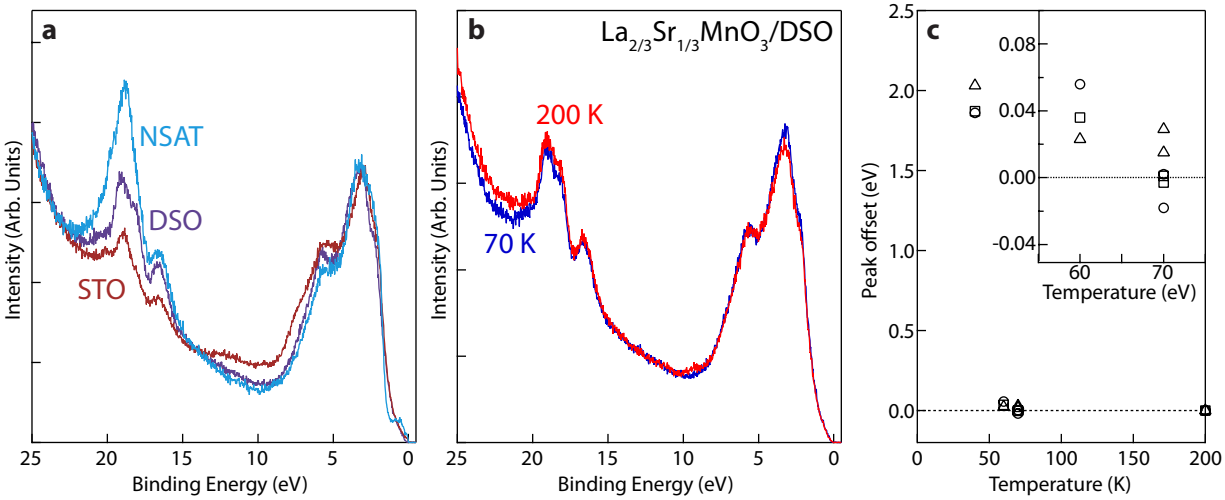

Figure 6.4: (**a**) Angle-integrated valence band spectra from $La_{2/3}Sr_{1/3}MnO_3$ films on all three substrates. (**b**) Valence band spectra for $La_{2/3}Sr_{1/3}MnO_3$/DSO taken at 70 K and 200 K, showing the absence of any shift due to charging. (**c**) Extracted positions for the peaks at 17.4 eV (circles), 18.4 eV (squares), and 19.9 eV (triangles) as a function of temperature, relative to the 200 K data ($E_{offset} = E_T - E_{200K}$). Charging is large at 40 K, but negligible by 70 K.

resolution of 40 meV.

6.2.1 Angle-integrated valence band

Figure 6.4a shows angle-integrated valence band spectra for 20nm thick $La_{2/3}Sr_{1/3}MnO_3$ films on NSAT, STO, and DSO substrates. As discussed in section 5.3.1, the deeply bound Sr4p and La5p states at 15 – 21 eV allow us to determine (La,Sr)O, MnO_2, and mixed surface terminations for the films on NSAT, STO, and DSO respectively. Our extensive studies of $La_{2/3}Sr_{1/3}MnO_3$/STO films have demonstrated that this does not have a significant effect on the dispersion of the near-E_F states that will be the subject of analysis below.

The photoelectrons measured during our experiments constitute a current flowing out of the sample surface that must be replenished by transport through the film in order to prevent the buildup of a large electrostatic charge within the measured volume. This charge would appear in our measurements as a shift of the photoemission spectra to deeper binding energies (i.e., higher voltage). Metallic films are easily grounded through their edges, but the appearance of charging is a common problem with insulating films or bulk crystals and is seen in our $La_{2/3}Sr_{1/3}MnO_3$/DSO at low temperatures. At 20 K, the valence band spectra were severely distorted and shifted by > 19 eV due to charging. By $T = 70$ K, however, charging has become negligible due to the decreased film resistance (Fig. 6.1b). This is seen clearly in the spectra of Fig. 6.4b at 70 K and 200 K, where no relative shift of the spectra is apparent despite the greater than two order of magnitude change in the film's resistivity. In Fig. 6.4c we show the result of fits to each of the three peaks that appear between 15-21 eV, comparing their position to the spectrum at 200 K. Significant charging is observed below 40 K but by 70 K the peaks are shifted by a negligible small amount (4±20meV). For this reason, we chose to perform ARPES measurements on $La_{2/3}Sr_{1/3}MnO_3$/DSO at T = 70 K.

6.2.2 Momentum resolved maps of electronic structure

Figure 6.5 shows momentum-resolved maps of spectral intensity for $La_{2/3}Sr_{1/3}MnO_3$ on NSAT, STO, and DSO substrates. At $E = E_F$ (top panels) these represent the films' Fermi surfaces, discussed extensively for $La_{2/3}Sr_{1/3}MnO_3$/STO in the previous chapter. Similarly, in $La_{2/3}Sr_{1/3}MnO_3$/NSAT we observe a two-sheet Fermi surface with sharply resolved hole pocket sheets and a broad central electron pocket despite its large compressive strain (−1.2%), but consistent with its metallic resistivity.

In sharp contrast to the metallic films, Fig. 6.5c shows that $La_{2/3}Sr_{1/3}MnO_3$/DSO lacks

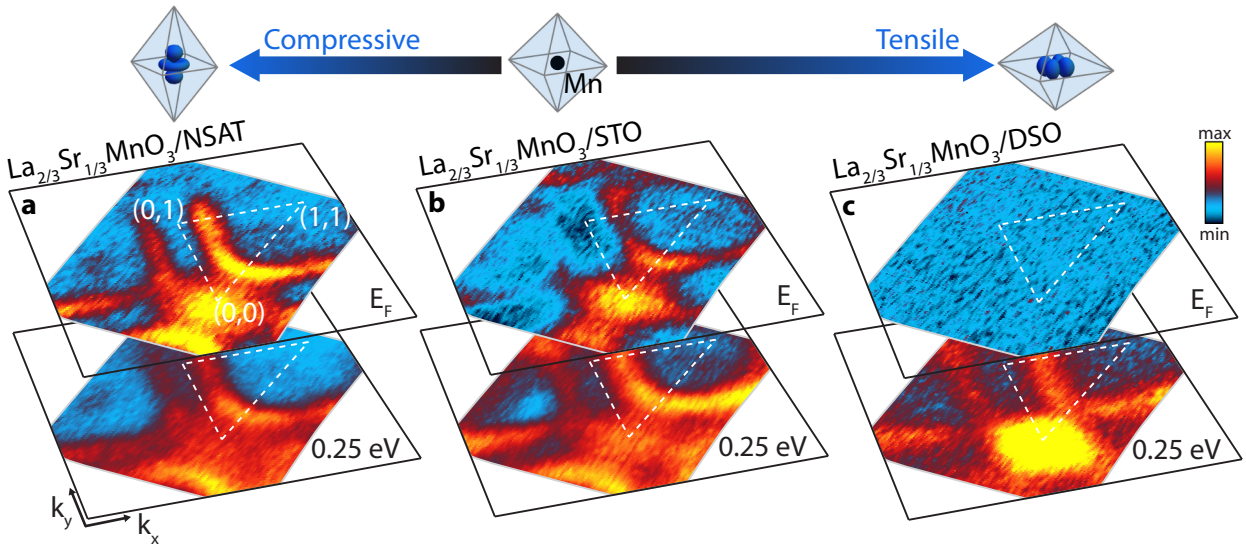

Figure 6.5: (**a-c**) k-resolved maps of photoemission spectral weight for $La_{2/3}Sr_{1/3}MnO_3$ films on NSAT, STO and DSO, respectively, at E_F and 0.25 eV (integrated over ±50 meV). Dashed lines indicate high-symmetry lines of the pseudocubic projected Brillouin zone. Data from each film are normalized to provide similar intensity at 0.25 eV, and maps at E_F are enhanced by an additional factor of 2 so all can be plotted on comparable color scales. Top: exaggerated illustration of the distorted oxygen octahedron around the Mn ion due to epitaxial strain and its expected effect on occupied e_g orbitals.

a Fermi surface and has no measurable spectral weight at E_F. This is, of course, consistent with the insulating nature of this film. Nevertheless, we observe a remnant Fermi surface for $E \geq 250$ meV that is strikingly similar to that of metallic $La_{2/3}Sr_{1/3}MnO_3$. This is unexpected, since a conventional band insulator involves reconstruction of the entire bandstructure close to E_F as the gap is opened. Instead, this is strong evidence for the unconventional nature of the insulating phase in tensile strained films.

ARPES spectra of the hole pockets taken along $k_x = 0.6\,\pi/a$ are shown for each film in Fig 6.6. These spectra have had a non-dispersive background subtracted to better display the dispersive features near E_F; the corresponding raw data is shown in Fig.

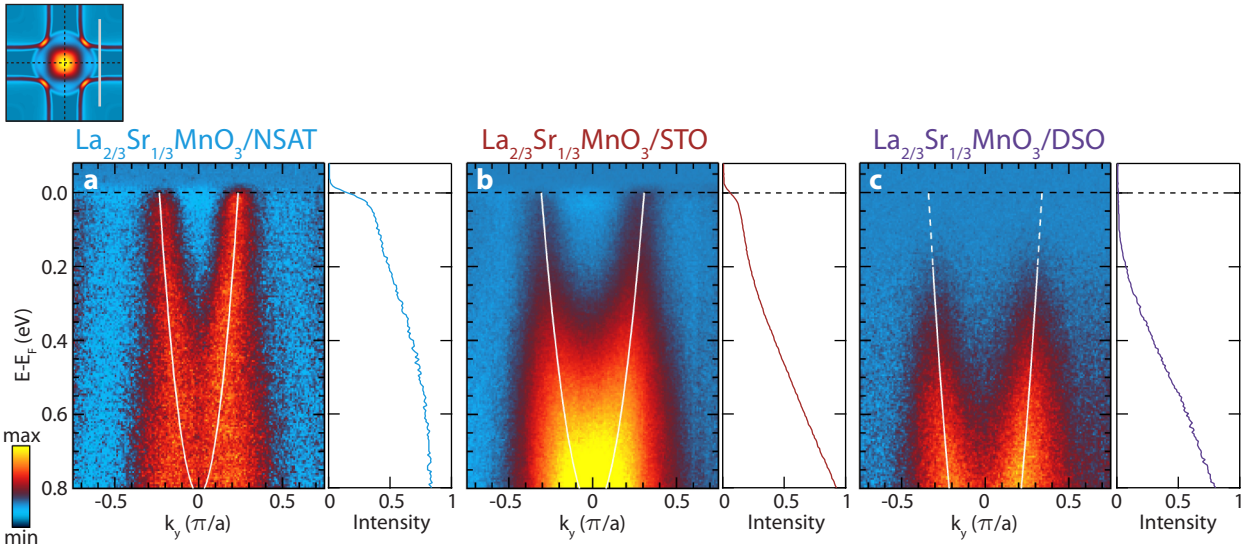

Figure 6.6: (**a-c**) ARPES spectra along $k_x = 0.6\ \pi/a$ (gray line in top left panel) for $La_{2/3}Sr_{1/3}MnO_3$ films on NSAT (a), STO (b) and DSO (c), after subtraction of a non-dispersive background and overlaid with parabolic fits to the experimental bandstructure. Right panels show energy distribution curves at k_F for each film without background subtraction and normalized to the valence band.

6.7. $La_{2/3}Sr_{1/3}MnO_3$/NSAT and $La_{2/3}Sr_{1/3}MnO_3$/STO have distinct bands with a well-defined Fermi step at k_F. On the other hand, $La_{2/3}Sr_{1/3}MnO_3$/DSO has highly dispersive bands that appear to vanish several hundred meV below E_F with a gap in intensity of $E_g = 0.10 \pm 0.01$ eV at the extrapolated k_F. This is consistent with the energy gap of $E_g = 0.10 \pm 0.02$ eV extracted from fitting the resistivity to the form $\rho(T) \propto e^{E_g/2k_BT}$, further indicating that our results reflect the bulk properties of this film.

Fig. 6.8 shows the results of MDC fits to the experimental dispersion for each film. Despite a large downward shift of the $La_{2/3}Sr_{1/3}MnO_3$/DSO hole pocket band and a smaller upward shift for $La_{2/3}Sr_{1/3}MnO_3$/NSAT, all three bands surprisingly exhibit curvatures that are in close agreement. All fall within $0.22 \pm 0.05\ m_e$ showing no clear relationship to resistivity, and are in good agreement with the cubic (unstrained) DFT calculation of $0.21\, m_e$ (Fig. 6.8c). This indicates that the hopping integrals and underlying bandwidth do

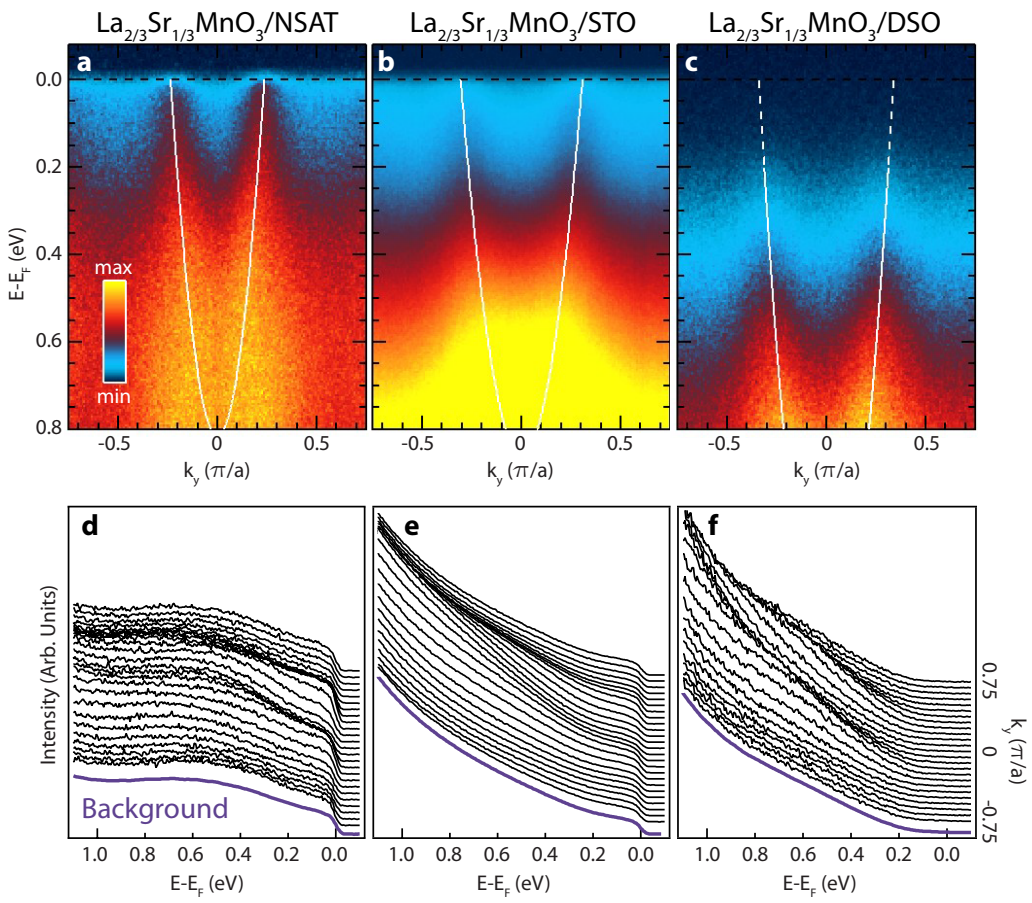

Figure 6.7: (**a-c**) ARPES data from Fig. 6.6 prior to background subtraction. (**d-f**) Energy distribution curves (EDCs) corresponding to panels a-c. The non-dispersive backgrounds used to generate Fig. 6.6 are shown by the purple lines.

not change significantly through the metal-insulator transition. Furthermore, Fig. 6.8b,c show that we find similarly broad MDCs for all three films. Thus, our results indicate that the electronic structure of metallic and insulating films are surprisingly similar, with the key difference being a strong suppression in intensity throughout the Brillouin zone on approaching E_F.

Due to the surface sensitivity of ARPES, care must be taken to ensure that our results are representative of the 'bulk' behavior of the films. In our earlier discussion of $La_{2/3}Sr_{1/3}MnO_3$/STO this was self-apparent due to the excellent agreement between the

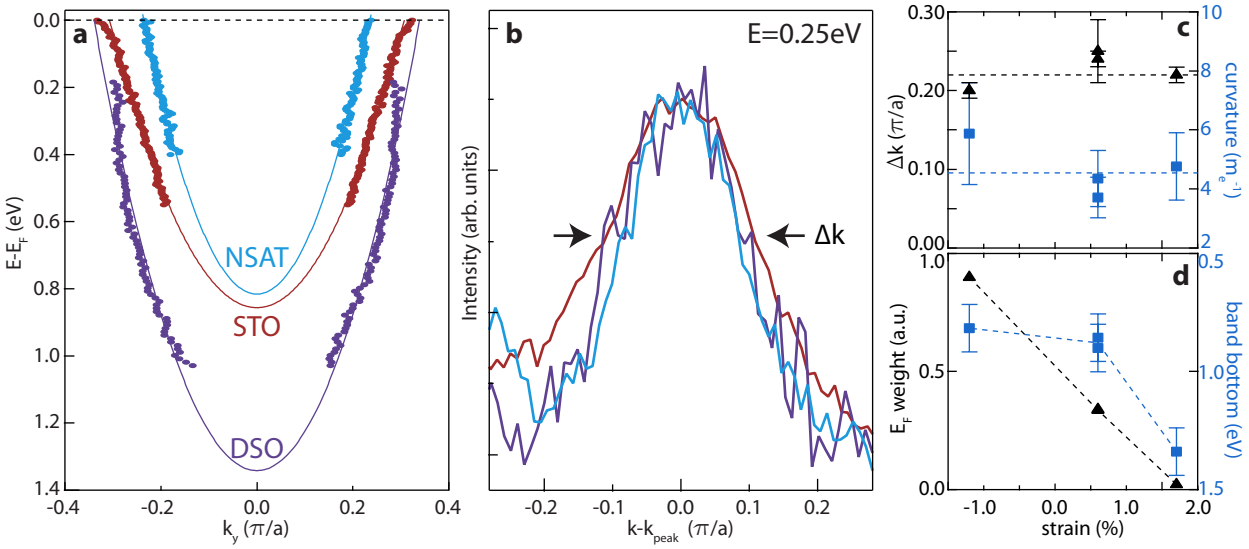

Figure 6.8: (**a**) The experimental dispersion extracted from MDCs for $La_{2/3}Sr_{1/3}MnO_3$ films on each substrate overlaid with parabolic fits. (**b**) MDCs at $E = 0.25 \pm 0.025$ eV from the data in Fig. 6.6. For these bands, k_z broadening accounts for only $\Delta k < 0.03\ \pi/a$ due to their strongly $d_{x^2\text{-}y^2}$ character. Curves are normalized to the peak height and offset in k by the peak position. (**c**) Experimentally determined Δk and band curvature, which remain constant with strain. (**d**) The weight at E_F and position of the band bottom, on the other hand, correlate strongly with the metal-insulator transition. Lines in (c,d) are guides-to-the-eye. Error bars in (c) are estimates based on variation in these parameters when varying our function fitting methodology. Error in the band bottom represents both the uncertainty in the fit to the MDCs as well as the uncertainty in x, which shifts the chemical potential and causes an apparent shift of the band-structure.

ARPES measurements, experimentally measured bulk physical properties, and the calculated bulk electronic structure. On the other hand, in the present chapter we are probing the strain induced metal-insulator transition that is not captured by first-principles calculations and has been difficult to directly address by other means. By comparing the $La_{2/3}Sr_{1/3}MnO_3$/STO Fermi surface with our DFT calculation in the previous chapter, we determined a carrier concentration in the film of 0.29 ± 0.03 holes/Mn atom that

is in close agreement with the Sr concentration measured by XPS of 0.29 ± 0.02. To perform a similar analysis for the film on NSAT, I performed a DFT calculation using the experimentally determined film lattice constants and then fit to the experimentally determined Fermi surface using a similar procedure (varying the chemical potential of the calculated bandstructure). This results in a carrier concentration of 0.37 ± 0.04 holes/Mn atom, again consistent with our XPS determined Sr concentration of 0.37 ± 0.04. The $La_{2/3}Sr_{1/3}MnO_3$/NSAT Fermi surface shows similar $c(2 \times 2)$ reconstructions to those seen in films on STO, most visible here at $(\pm 3/4, 3/4)\ \pi/a$ in Fig. 6.5a, which we attribute to structural reconstructions of the topmost atomic layer. Nevertheless, these appear to otherwise have little effect on the measured electronic structure. Recent x-ray linear dichroism measurements found that the loss of octahedral Mn coordination at MnO_2 surface terminations induced a strong orbital polarization [171]. Our ARPES measurements of both (La,Sr)O and MnO_2 terminated films on STO substrates showed no significant differences in the dispersive states, suggesting that these states originate from below the top monolayer of our films and represent the bulk electronic structure. The main effect of surface termination is a momentum-independent background (section 6.2.1) that could be due to an electronically inactive or disordered surface dead layer [172]. In all samples we find excellent agreement between ARPES measurements and the expected Fermi surface shape, carrier concentration, and transport behavior. We can therefore be confident that our ARPES measurements through the strain induced metal-insulator transition reflect the bulk electronic structure of $La_{2/3}Sr_{1/3}MnO_3$ films.

6.3 Why is $La_{2/3}Sr_{1/3}MnO_3$/DSO insulating?

Perhaps the most famous example of a metal-insulator transition in correlated materials is the Mott transition that occurs near half filling. The transition from a kinetic-energy

dominated Fermi liquid to an insulator occurs when the bandwidth becomes smaller than the local Coulomb repulsion, and electrons are thus prevented from hopping to neighboring occupied sites. The Mott transition cannot explain the insulating behavior of $La_{2/3}Sr_{1/3}MnO_3$/DSO since it is not close to half filling, and furthermore we see no evidence for the presence of a lower Hubbard band in our spectra[3]. Nevertheless, bandwidth driven metal-insulator transitions can occur through a variety of many-body interactions, such as self trapping due to polaronic effects [173]. Our ARPES measurements that find similar bandwidths for both insulating and metallic films, however, are strong evidence that a reduction in bandwidth does not play a key role in the strain driven metal-insulator transition for $La_{2/3}Sr_{1/3}MnO_3$.

Another possibility is that the insulating behavior of this film is a result of Anderson localization of the charge carriers, which is believed to occur in general at the Mott-Ioffe-Regel limit ($k_F L \approx 1$), where L is the carrier's mean free path [174]. The high carrier density in $La_{2/3}Sr_{1/3}MnO_3$ implies a localization length of only a few unit cells, which via the uncertainty principle implies a significant broadening in k space (Fig. 6.9b). Such an effect was seen, for example, in ARPES studies of a temperature driven metal-insulator transition in $La_{0.82}Sr_{2.18}Mn_2O_7$ [143]. Our data strongly refute this mechanism for the case of strained $La_{2/3}Sr_{1/3}MnO_3$ as we do not observe any significant difference in momentum widths between metallic and insulating films. If we alternately consider the possibility that the observed momentum widths are dominated by extrinsic effects by using $L > 1/\Delta k$, we obtain $k_F L > 3.5$, still well above the Mott-Ioffe-Regel limit for localization.

Theories of correlated materials provide us with one additional scenario: the formation of a competing electronically ordered phase (Fig. 6.9c), known to occur in several layered manganite compounds [140, 104]. This mechanism causes the opening of a gap at E_F

[3]This is not to say that Coulomb interactions are not important in the insulation phase. They may, for example, play an important role in stabilizing the ordered insulation phase discussed later in this chapter. We only claim here that an unreconstructed unit cell containing one Mn site should not be made insulating by Coulomb interactions.

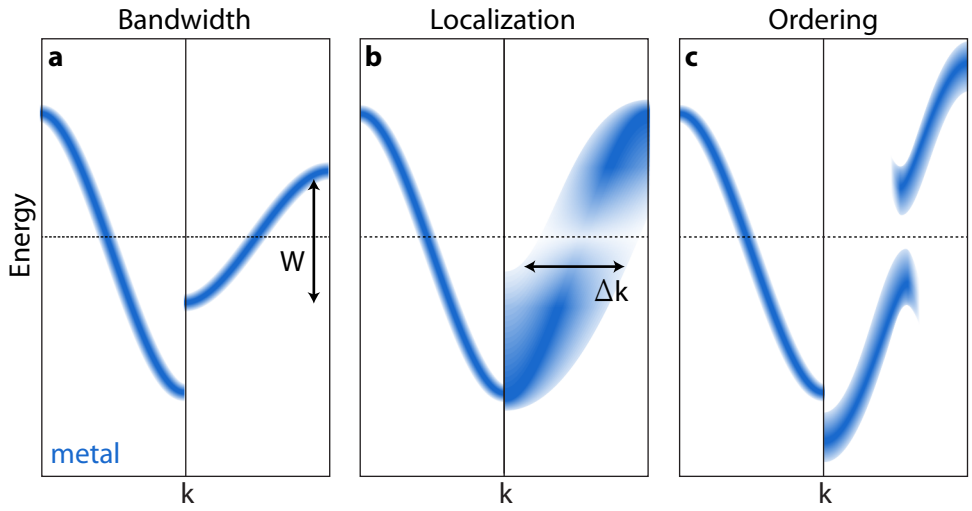

Figure 6.9: Schematic illustrations of the metallic bandstructure and its change through the metal-insulator transition for each mechanism are shown in the left and right panels, respectively. (**a**) A reduction in bandwidth (W) reduces the importance of kinetic energy and can promote an insulating state. (**b**) Localization of itinerant charge carriers broadens the electronic structure in momentum (Δk). (**c**) Instability of the metallic phase to an ordered insulator opens a gap at E_F with a corresponding downward shift of the band from the non-interacting dispersion. The bandstructure around the gap contains back-bending portions for $k > k_F$ with rapidly diminishing intensity.

with spectral weight that rapidly decays beyond the non-interacting k_F. In addition, the entire gapped band shifts down in energy [140]. Figure 6.6c clearly shows the presence of bands with a gap at E_F and vanishing intensity for $k > k_F$ in $La_{2/3}Sr_{1/3}MnO_3$/DSO, comparable to spectra from charge-orbital ordered $Pr_{0.5}Sr_{0.5}MnO_3$ and $La_{0.5}Sr_{1.5}MnO_4$ (refs. [175, 104]). Figure 6.8a,d highlights the band's 0.5 eV downward shift with respect to $La_{2/3}Sr_{1/3}MnO_3$/STO.

The downward shift might in principle be partially ascribed to a crystal field effect. The hole bands measured by ARPES have mostly x^2-y^2 orbital character, and these bands are expected to be lowered in energy by the tetragonal crystal field imposed by the 1.7% tensile biaxial strain [163, 54]. Nevertheless, a similar opposing effect should also occur in

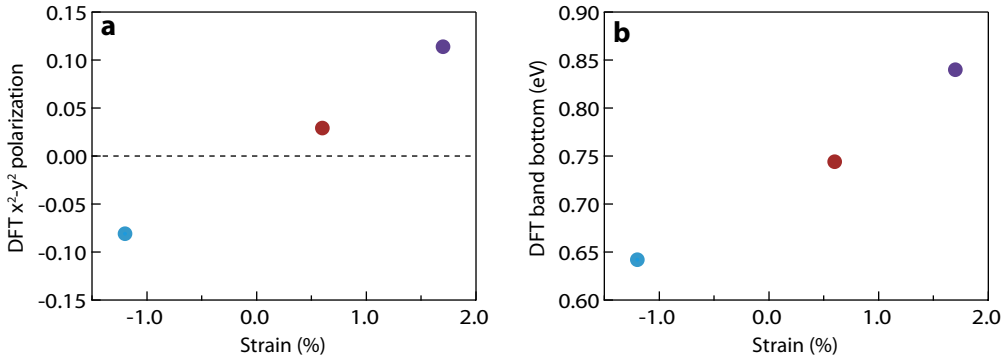

Figure 6.10: (**a**) The orbital polarization from VCA DFT calculations corresponding to $x = 0.33$ for the experimentally measured film lattice constants on each substrate. We define the polarization as $P = (N_{(x^2-y^2)} - N_{(3z^2-r^2)})/(N_{(x^2-y^2)} + N_{(3z^2-r^2)})$, where N is the integral of the Mn e_g partial density of states up to E_F. (**b**) The calculated position of the hole pocket band bottom (predominantly $d_{x^2-y^2}$ character) along the **k**-space cut corresponding to the ARPES data in Fig. 6.6. The calculated band shifts by ±0.1 eV due to the strain-induced orbital polarization.

the film on NSAT due to its large compressive strain of -1.2%. In addition, the shift of the film on NSAT should be further accentuated by our choice of STO as the reference point, whose weak tensile strain of 0.6% places it closer to DSO than NSAT. On the contrary, whereas we see a very large (0.5 ± 0.1 eV) downward shift for $La_{2/3}Sr_{1/3}MnO_3$/DSO, we see a much smaller upward shift (0.1 ± 0.1 eV) for $La_{2/3}Sr_{1/3}MnO_3$/NSAT, indicating that crystal field effects alone are insufficient to explain the shift under tensile strain. Our virtual crystal approximation DFT calculations for each film using the experimentally determined lattice constants indicate the expected degree of orbital polarization due to strain, and provide corresponding shifts of -0.10 eV for $La_{2/3}Sr_{1/3}MnO_3$/NSAT and +0.10 eV for $La_{2/3}Sr_{1/3}MnO_3$/DSO with respect to $La_{2/3}Sr_{1/3}MnO_3$/STO for the hole pocket band (Fig. 6.10). This agrees well with the film on NSAT, but is far too small to explain the large shift that occurs under large tensile strain.

6.3.1 Weak coupling model of an ordered phase

The effects of the formation of an electronically ordered phase on the spectral function measured by ARPES can be computed within first-order perturbation theory (i.e., assuming weak coupling), following for example the work of ref. [176]. Given an underlying band dispersion, ϵ_k, with wave functions $|k\rangle$, and an ordering at wave vector q, the new eigenstates are:

$$|\psi_k\rangle = u_{k-q}|k-q\rangle + u_k|k\rangle + u_{k+q}|k+q\rangle$$

The coefficients (u) describe the mixing of states at k, $k+q$, and $k-q$ and, along with the new eigenenergies, are found by solving the matrix:

$$\begin{pmatrix} \epsilon_{k-q} & V & 0 \\ V & \epsilon_k & V \\ 0 & V & \epsilon_{k+q} \end{pmatrix}$$

The bare dispersion is taken as the DFT calculated hole pocket bandstructure, using the virtual crystal approximation and the experimentally determined DSO lattice constants.

For illustrative purposes, I take $q = 1/3\ 2\pi/a$ along $\hat{k}_y$, corresponding to a 3×1 reconstruction. Choosing $V = 0.65$ eV provides the best fit to our ARPES measurements, but other combinations of q and V can also provide qualitatively similar spectra. Figure 6.11a shows the results of this calculation for the band dispersion in the non-interacting (black solid line) and ordered (maroon circles) phases. The ARPES intensity can be computed in a straightforward manner from the wavefunction coefficients (u_k^2), and is shown in Fig. 6.11b with the addition of a Lorentzian energy broadening of 0.6 eV full width at half maximum (a typical value extracted from our ARPES spectra). The resemblance to our ARPES data for $La_{2/3}Sr_{1/3}MnO_3$/DSO is immediately apparent, despite the qualitative nature of the selection of parameters. Nevertheless, despite this simple model's ability to capture the main features of the insulating spectral function - the opening of a

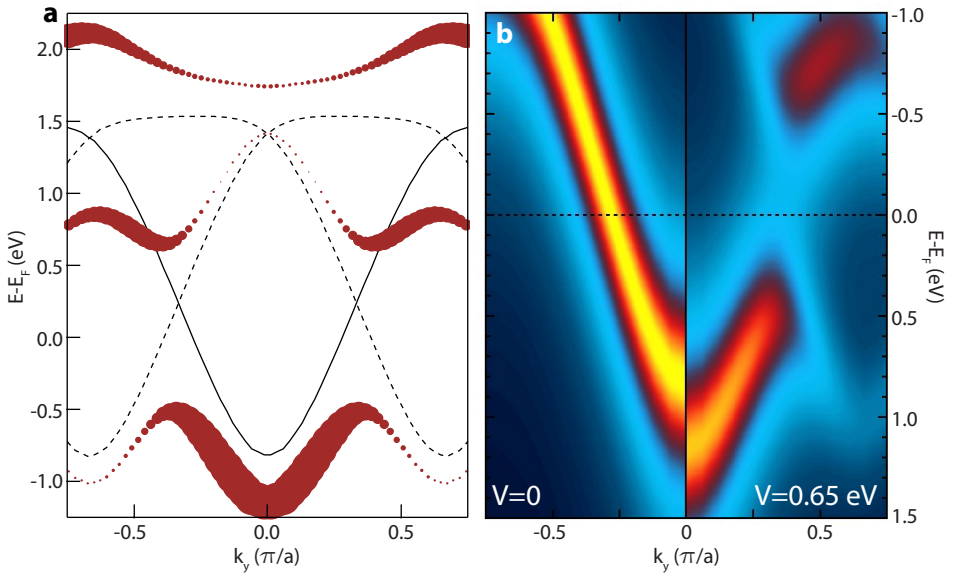

Figure 6.11: (**a**) The calculated dispersion for an ordered phase with $q = 2/3\,\pi/a$ along $\hat{k}_y$ and $V = 0.65$ eV. The maroon points track the reconstructed dispersion with a point size proportional to u_k^2. The solid line shows ϵ_k and dashed lines show ϵ_{k+q} and ϵ_{k-q}. (**b**) The right half shows simulated ARPES spectra from the weak coupling model. The left half shows the metallic state ($V = 0$) for reference.

gap, downward shifting of the bands, and rapid decay of intensity at $k > k_F$ - first-order perturbation theory should not be trusted at a quantitative level for coupling strengths that are of the same order as the bandwidth.

6.3.2 Strong coupling nature of the insulating phase

The drawbacks of a weak coupling treatment of the electronic ordering can also be seen more directly from our ARPES data. In the case of a nesting driven ordered phase, we expect to see band back-folding and a momentum dependent gap that are strongest around nested regions of the Fermi surface [176], but neither are apparent in our data. Nevertheless, our data bear a strong resemblance to ARPES measurements of bulk layered

manganites with long range or fluctuating order. In particular, these materials also show a gap or pseudogap spanning the full Fermi surface, dispersive states that vanish within several hundred meV of E_F, and weak or absent momentum-space reconstructions and band back folding [104, 105, 140]. Furthermore, a comparison of the typical transition temperatures and energy gaps in the layered manganites indicates that they fall within a strong coupling regime ($\Delta/k_BT_c >> 1.76$), as noted by Ref. [105]. The similarity between the layered manganites and our measurements of $La_{2/3}Sr_{1/3}MnO_3$/DSO provides further evidence that the insulating phase of strained $La_{2/3}Sr_{1/3}MnO_3$ is driven by strong many-body interactions, and that a complete description requires a strong coupling many-body calculation that goes well beyond the simple perturbation theory described in the previous section. In this regime, the role of Fermi surface nesting becomes less important as stable ordered phases can be tied to local and real-space effects such as structural distortions and commensurate ordering vectors. Our $La_{2/3}Sr_{1/3}MnO_3$/DSO Fermi surface indicates a nesting vector of $q_{\text{nest}} = 0.29 \pm 0.01\ 2\pi/a$. However, it is just as likely that the actual ordering pattern locks into a $q_x = q_y = 0.25\ 2\pi/a$ pattern, commonly observed in many manganites included layered manganites with nesting vectors similar to that of $La_{2/3}Sr_{1/3}MnO_3$/DSO [105].

6.4 Conclusion

Competition between metallic and charge-ordered insulating phases is central to the complex phase diagram of the manganites, and forms the basis for colossal-magnetoresistance [177, 178]. Theory has shown how biaxial strain can stabilize charge ordered phases at $x = 1/2$ (ref. [179]), and experiments demonstrated a high sensitivity of charge and orbital ordered phases to epitaxial strain in small-bandwidth manganites [180]. Our measurements of $La_{2/3}Sr_{1/3}MnO_3$ films have revealed how the electronic structure responds

as epitaxial strain tunes this competition, giving rise to a state with strong fluctuations [140] or static order under tensile strain. These results demonstrate the ability to control and understand the effects of strain on electronic structure, providing essential guidance for the development of new theoretical techniques aimed at a deeper understanding of correlated electronic materials.

Chapter 7

Interplay of dimensionality and many-body interactions in $(LaMnO_3)_{2n}/(SrMnO_3)_n$ superlattices

Controlling the electronic properties of interfaces has enormous scientific and technological importance. Modern digital technology is based on the electron gases formed at semiconductor interfaces and our ability to control their properties with tunable structures and electric fields [182]. Furthermore, interfaces in GaAs heterostructures have given us new insight into the physics of correlated electrons through the discovery of the fractional quantum Hall effect [49]. This approach to generating new materials and electronic systems has been recently extended from semiconductors to complex oxides. Due to strong many-body interactions, these interfaces can host emergent ground states not present in the parent materials [8], including exotic magnetic phases [19, 55], high-T_c supercon-

Much of the work discussed in this chapter was published in E.J. Monkman *et al.*, *Nat. Mater.* 11, 855 (2012) [181].

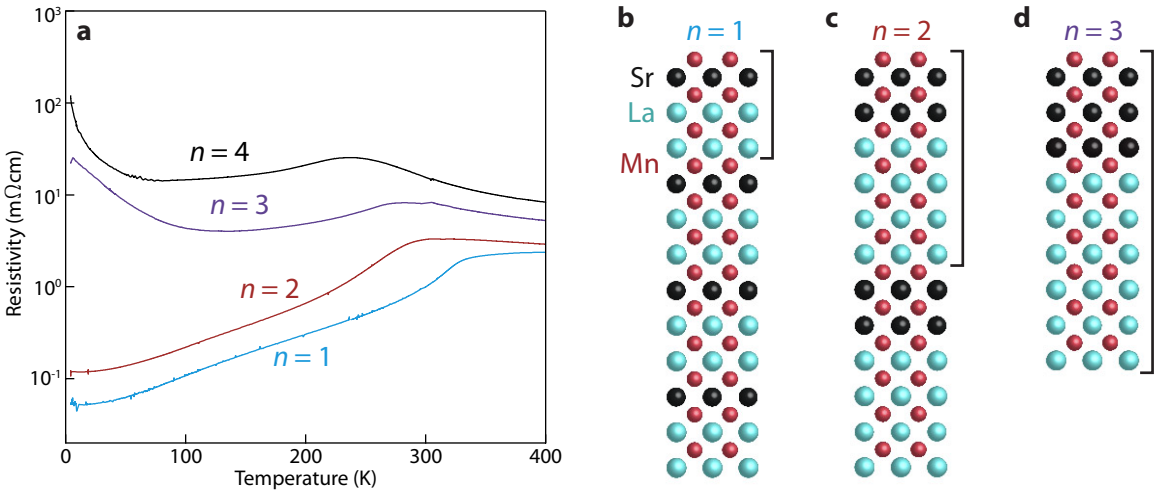

Figure 7.1: (**a**) Resistivity of $(LaMnO_3)_{2n}/(SrMnO_3)_n$ superlattices as a function of n and temperature showing the crossover to insulating behavior for $n \geq 3$ (data from ref. [113]). (**b-c**) Schematic illustration of the $(LaMnO_3)_{2n}/(SrMnO_3)_n$ structure for $n = 1-3$.

ductivity [20], and two-dimensional correlated electron systems [9, 21, 22] . Thus, these oxide interfaces present a fundamentally new opportunity where instead of conventional bandgap engineering, the electronic and magnetic properties can be optimized by engineering quantum many-body interactions [22, 7, 183].

Although the electronic properties of conventional semiconductor heterostructures can be described by one-electron theories, performing such calculations for correlated materials is far more challenging. Understanding these correlated interfaces has been complicated by the inability to probe their underlying electronic structure [7, 183]. Our in-situ combined MBE and ARPES system is equipped with the capability to both synthesize extremely high-quality oxide interfaces, and image their electronic structure. In this chapter, we use these capabilities to provide the first direct measurements of the electronic structure at a complex oxide interface.

$La_{1-x}Sr_xMnO_3$ presents an ideal case for modifying electronic and magnetic proper-

ties through interfacial engineering due to its competing interactions and wide variety of ground states, as discussed extensively in previous chapters. In this chapter we study its heterostructure analog: $(LaMnO_3)_{2n}/(SrMnO_3)_n$ superlattices (Fig. 7.1b-d). Bulk $LaMnO_3$ is an A-type antiferromagnetic Mott insulator and $SrMnO_3$ is a G-type antiferromagnetic band insulator [97, 99]. Increasing the separation between the $LaMnO_3$ and $SrMnO_3$ layers with integer n has been shown to drive a crossover from a $La_{2/3}Sr_{1/3}MnO_3$ like ferromagnetic metallic ($n < 3$) to ferromagnetic insulating ground state ($n \geq 3$) (Fig. 7.1a) [112, 113, 184, 185]. The origin of this transition was hitherto not understood, as theoretical studies predicted metallic interfaces for large n [134, 186]. Furthermore, the expected competition between ferromagnetic interfaces and antiferromagnetic $LaMnO_3$ and $SrMnO_3$ gives rise to complex magnetic states. All superlattices show signs of ferromagnetism [113], but neutron scattering measurements have shown that the magnetism is strongly modulated throughout the superlattice unit cell in insulating films [184, 187].

In this chapter, we first examine the magnetic order in $n = 4$ superlattices using resonant soft x-ray scattering. Our measurements reveal an unexpected strongly modulated magnetic state with a period twice as large as the structural unit cell. We then turn our focus to the n driven metal insulator transition. The tunability of oxide heterostructures can arise from either controlling the single-electron bandstructure as done in conventional semiconductors, or by taking advantage of the strong many-body interactions that are uniquely accessible in correlated materials. Our in-situ ARPES data reveal that while the band structure remains largely unchanged with interfacial separation, a large pseudogap is opened within 800 meV of E_F for $n = 3$, and closes either upon warming into the paramagnetic state or reducing the interfacial separation ($n \leq 2$). This work provides the first direct observation of how quantum many-body interactions can be engineered in artificial materials constructed with atomic-layer precision to control the electronic ground state.

7.1 Growth technique and characterization

7.1.1 Film growth and x-ray diffraction

Carolina Adamo performed the very demanding growth of all films presented in this chapter. In consultation with her, I have since grown several films for follow-up experiments. The need to maintain sharply defined interfaces with a roughness much less than one atomic layer throughout the $(LaMnO_3)_{2n}/(SrMnO_3)_n$ superlattices places stringent requirements on the flux calibration used for film growth. For example, an error in the La flux of 1 % will accumulate to 1/3 of a monolayer over the growth of a 20 nm thick film - an unacceptable amount if sharp interfaces are to be maintained. This is particularly important for ARPES studies of our films, since ARPES is only sensitive to the topmost interface where the accumulation of flux errors is largest. For this reason, sub-percent-level calibrations are required. To achieve such high precision, we resort to a more stringent procedure than that used for random alloy films. We begin with the QCM and RHEED calibration procedures discussed for $La_{1-x}Sr_xMnO_3$ in section 5.1. In particular, we used buffered-HF treated (100)-$SrTiO_3$ substrates [126] and grew in an oxidant (O_2+10% O_3) background partial pressure of 5×10^{-7} Torr at a substrate temperature of 750 °C. Individual elemental fluxes were calibrated by QCM and then shuttered RHEED oscillations [59], including a RHEED oscillation calibration of the Sr flux using $SrMnO_3$ that we forgo for $La_{1-x}Sr_xMnO_3$ films.

Following this initial calibration, we rely on ex-situ XRD to further tune element fluxes. First we grow a $(SrMnO_3)_8/(LaMnO_3)_1$ superlattice, ten repetitions thick. This structure is chosen because it provides superlattice reflections at positions and with strengths that are highly sensitive to errors in our $SrMnO_3$ calibration but relatively unaffected by errors in $LaMnO_3$. Using the peak positions, we estimate the thickness of the

$SrMnO_3$ layers, adjust the flux accordingly, and grow additional characterization superlattices until a satisfactory XRD pattern is obtained. Next, we perform a corresponding calibration of the $LaMnO_3$ flux using $(LaMnO_3)_8/(SrMnO_3)_1$ superlattices. We then verify our precise calibration and confirm that the individual sources have not drifted significantly over the several hours required by growing a final test $(LaMnO_3)_{2n}/(SrMnO_3)_n$ superlattice and measuring its XRD pattern.

We found that ARPES is extremely sensitive to film quality - more so than detectable by bulk probes such as XRD or resistivity. This likely results from the accumulation of flux errors, which have the largest effect at the topmost surface. In addition, the extended nature of the fragile electronic states that are the focus of our ARPES measurements should cause them to be sensitive to scattering from roughness present at a non-ideal interface. Thus, the final calibration step for superlattice growth incorporates ARPES directly. The $n = 2$ superlattice presents sharply defined bandstructure that becomes broadened and weakened by a non-ideal flux calibration. We grew and briefly measured by ARPES several $n = 2$ superlattices to fine-tune film stoichiometry before the final growth of our most critical superlattices to ensure that they are of the highest possible quality. This precaution was particularly important to ensure that the measurements of a pseudogap in $n = 3$ superlattices presented below are intrinsic to the ideal $(LaMnO_3)/(SrMnO_3)$ interface.

Pure $LaMnO_3$ has a Jahn-Teller distorted orthorhombic structure (space group *Pbnm*) with a pseudocubic lattice constant of $a_{LMO} = 3.94$ Å (ref. [100]). On the other hand, $SrMnO_3$ is cubic (space group $Pm\bar{3}m$) with $a_{SMO} = 3.81$ Å. The average ($\frac{2a_{LMO}+a_{SMO}}{3} = 3.90$ Å) is closely matched to the $SrTiO_3$ substrate ($a = 3.905$ Å) and should lead to little average strain, although individual layers of either $LaMnO_3$ or $SrMnO_3$ within the superlattices may experience significant internal strain (-0.9% and +2.5%, respectively). From XRD we find an average out-of-plane pseudocubic lattice constant of $c = 3.87 \pm 0.01$ Å for all measured films, consistent with earlier work [185] and further indicating a small average

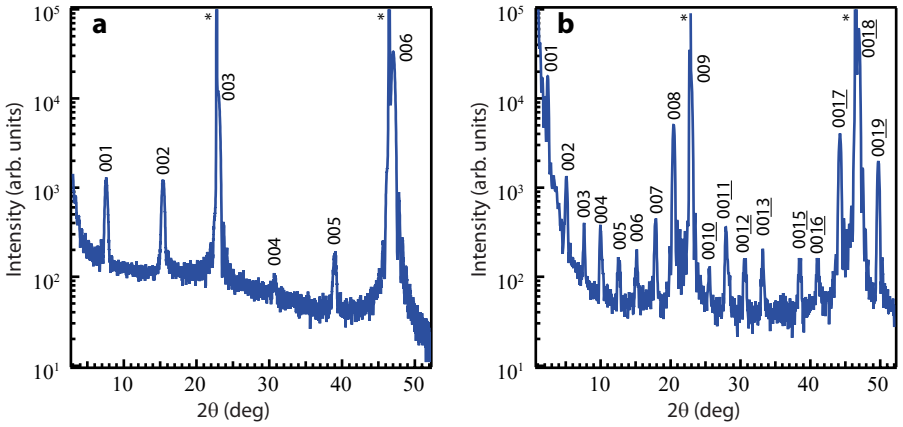

Figure 7.2: X-ray diffraction curves of the (**a**) $n = 1$ and (**b**) $n = 3$ superlattices measured by ARPES. Diffraction peak indices are indicated for the films; substrate peaks are denoted by the *.

lattice mismatch with $SrTiO_3$. Figure 7.2 presents example XRD data for $n = 1$ and $n = 3$ superlattices measured by ARPES. In addition to the standard perovskite peaks, we observe all anticipated superlattice reflections at the correct locations, consistent with the high structural quality and precise stoichiometry of our films.

7.1.2 Transmission electron microscopy

Nevertheless, as mentioned above XRD is insufficient to distinguish small defects in film growth that can affect ARPES data. To directly measure our film structure at the atomic scale, Julia Mundy of David Muller's group measured high quality Electron energy loss spectroscopic images (EELS-SI) from three of the films measured by ARPES using Cornell's 100 keV NION UltraSTEM. Figure 7.3 shows high angle annular dark field scanning transmission electron microscopy (HAADF-STEM) images from each film, demonstrating a coherent interface between the film and substrate that is free of defects, and providing a direct view of the $(LaMnO_3)_{2n}/(SrMnO_3)_n$ layered structures. Spectroscopic images were then recorded, two examples of which are shown in Figs. 7.4 and 7.5. We note that Fig. 7.5

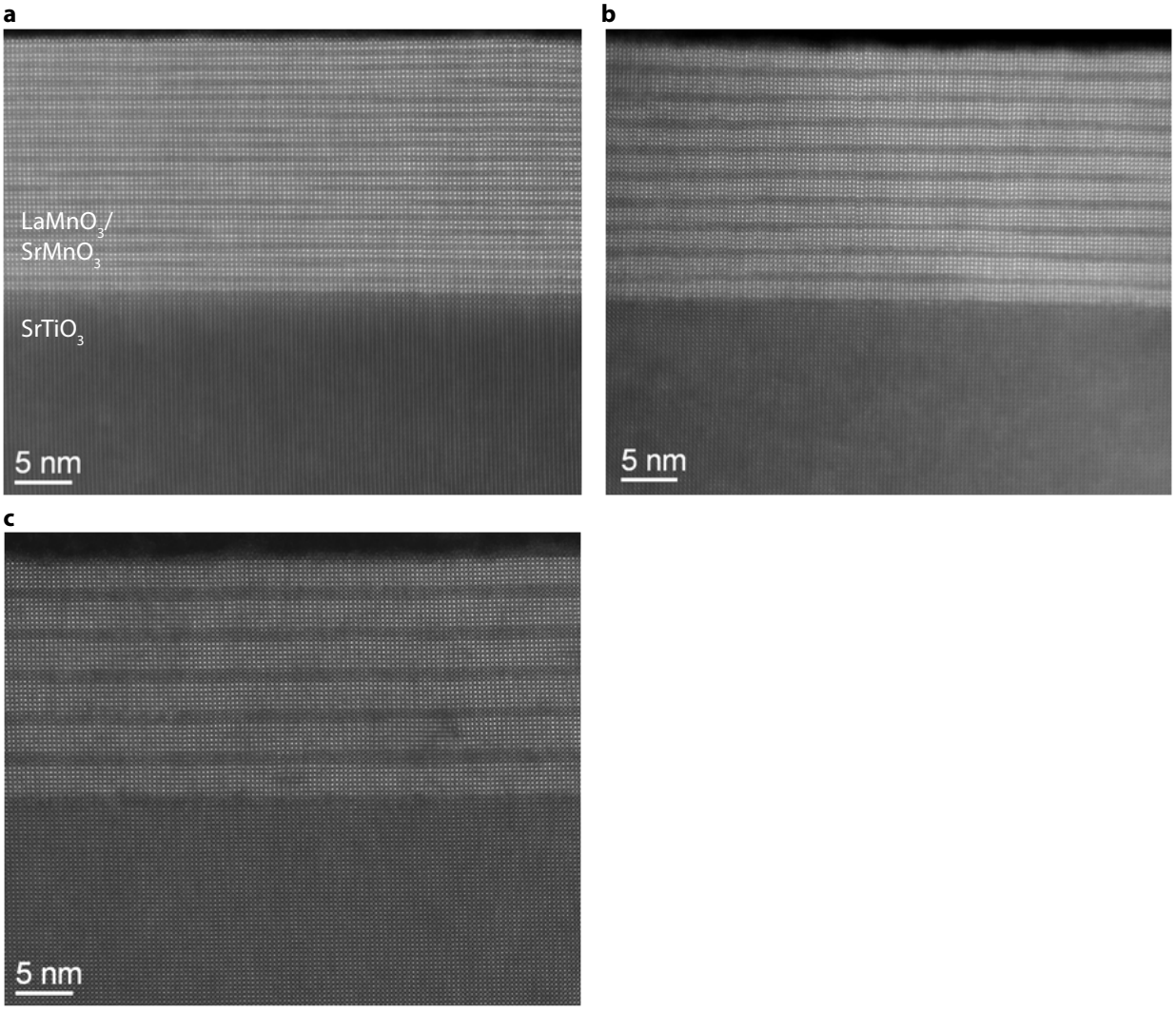

Figure 7.3: HAADF-STEM images of the same (**a**) $n = 1$, (**b**) $n = 2$, and (**c**) $n = 3$ $(LaMnO_3)_{2n}/(SrMnO_3)_n$ films measured by ARPES. The films show a coherent interface between the film and the substrate free of observable defects and a clear repetition of the $LaMnO_3$ and $SrMnO_3$ layering to form the desired superlattices.

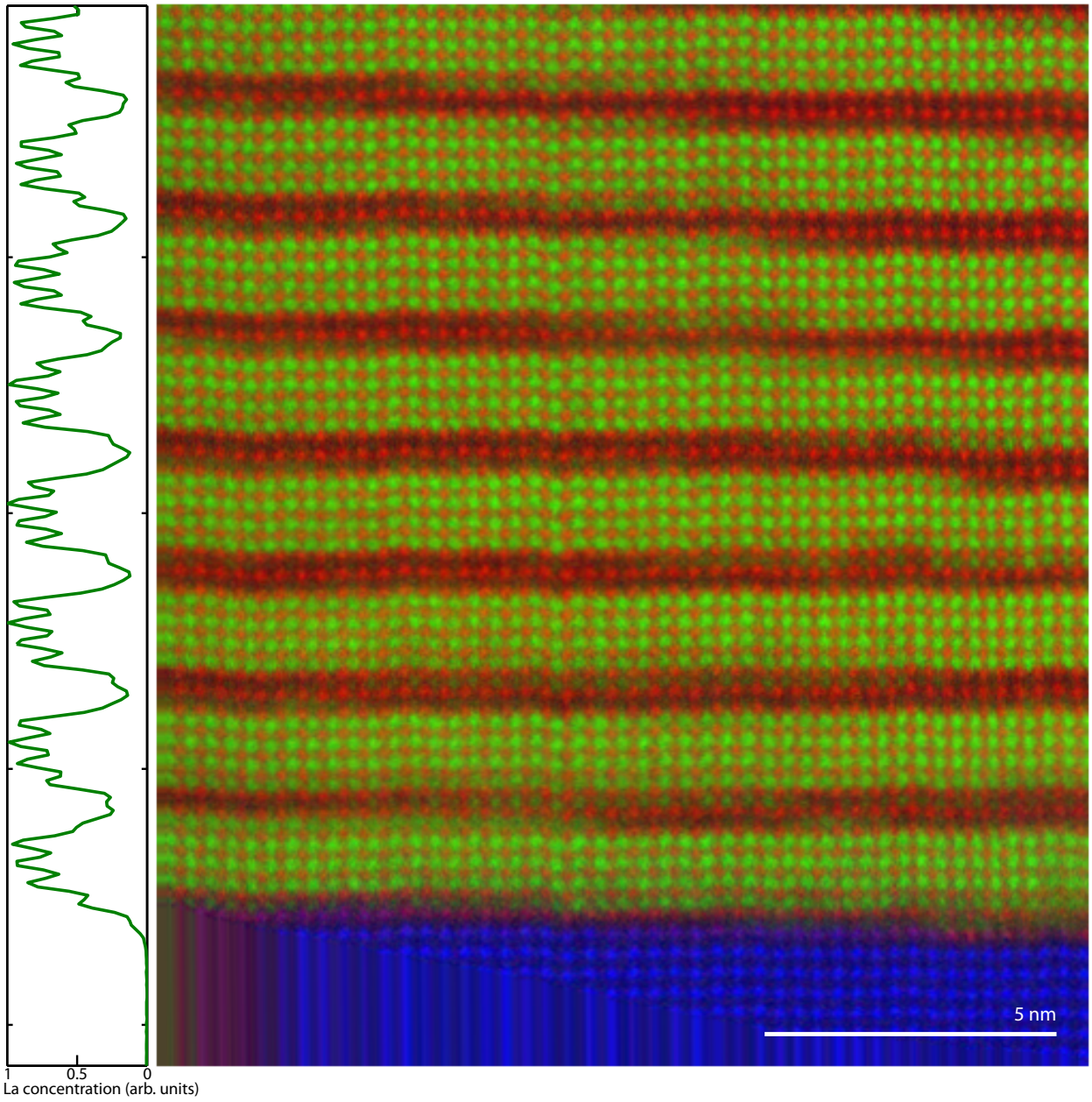

Figure 7.4: EELS map over a wide field of view from an $n = 2$ $(LaMnO_3)_{2n}/(SrMnO_3)_n$ film measured by ARPES, showing La in green, Mn in red, and Ti (from $SrTiO_3$ substrate) in blue. Steps in the $LaMnO_3/SrMnO_3$ interfaces follow the terraces of the $SrTiO_3$ substrate. Left: the La concentration along the growth direction of the film (obtained by integrating the La-$M_{4,5}$ intensity across the image) showing sharp interfaces between $LaMnO_3$ and $SrMnO_3$ lacking any systematic asymmetry. Streaks in the bottom left corner of the EELS map are an artifact of post-acquisition drift correction.

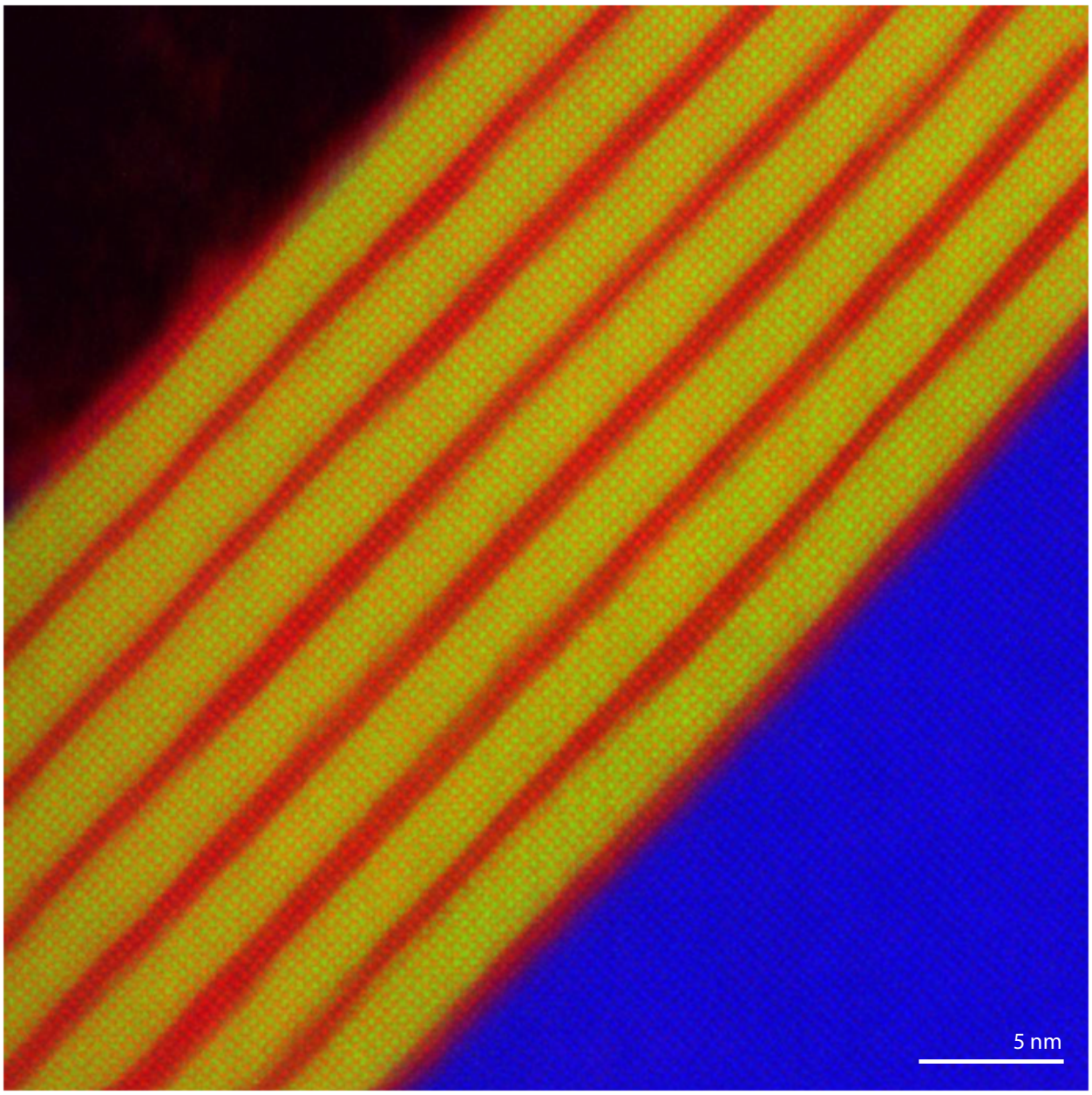

Figure 7.5: EELS map over a wide field of view from an $n = 3$ $(LaMnO_3)_{2n}/(SrMnO_3)_n$ film measured by ARPES, showing La in green, Mn in red, and Ti (from $SrTiO_3$ substrate) in blue. The irregularity of the topmost surface in this image is an artifact of the preparation procedure for EELS and HAADF-STEM measurements, and does not reflect the topmost surface of the as-grown film.

constitutes the largest atomically resolved EELS map ever measured and thus represents an extremely demanding measure of the interface quality. The Mn, La, and Ti concentrations are determined from the integrated Mn-$L_{2,3}$, La-$M_{4,5}$, and Ti-$L_{2,3}$ edges, respectively. In all cases, we find that ARPES films show a clear repetition of the $LaMnO_3$ and $SrMnO_3$ layers following the desired superlattice structure throughout the large imaged region with very few defects.

Note that an apparent slight modulation of the interfaces observable in EELS images is an artifact of sample drift during acquisition, and is absent in the more quickly acquired HAADF-STEM images. May et al. [187] found a strong structural asymmetry between $LaMnO_3/SrMnO_3$ and $SrMnO_3/LaMnO_3$ interfaces in $(LaMnO_3)_{11.8}/(SrMnO_3)_{4.4}$ superlattices, which was found to significantly affect the superlattice's magnetic properties. We note that in our extensive EELS investigations, we observed no signatures of such an asymmetry for $n = 1$ and $n = 2$ superlattices (Fig. 7.4), and only a very weak asymmetry for $n = 3$ when examined over very wide regions (Fig. 7.5). Thus, we do not expect that the asymmetry reported in ref. [187] adversely affects the properties of the films reported in our study. Although we do not understand the difference between our samples and those of May et al., the asymmetric roughening trend would be consistent with a Stranski-Krastanov growth mode for the $LaMnO_3$ layer, with the onset for island formation somewhere between 6 (ours) and 11 layers (May's).

7.1.3 Electron diffraction

The high structural quality of the film surface was verified after ARPES measurements with in-situ LEED. In Fig. 7.6a we present a LEED image taken from an $n = 3$ superlattice after remaining in the ARPES chamber for 8 days. We observe sharp diffraction peaks, a 2×4 surface reconstruction, and a 3×3 surface reconstruction also seen by RHEED dur-

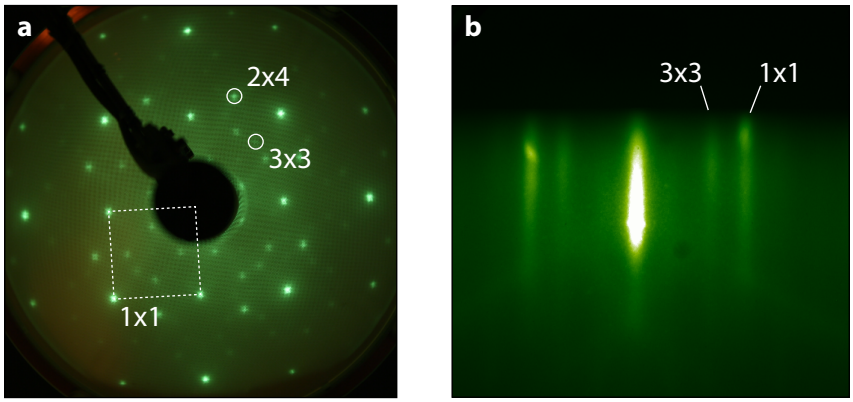

Figure 7.6: (**a**) LEED pattern taken with 100 eV electrons from an $n = 3$ superlattice with MnO_2 surface termination. Diffraction peaks corresponding to the unreconstructed surface and two reconstructions are indicated. (**b**) RHEED pattern from the MnO_2 surface of the same $n = 3$ film during growth.

ing growth (Fig. 7.6b). This demonstrates the high crystallinity of the surface of our films, and proves that the pristine surface from growth is maintained throughout the transfer to our ARPES chamber and subsequent measurement. The origin of these surface reconstructions are not yet entirely understood, but we find that they are generic to the MnO_2 surface of the perovskite manganites, and not unique to our superlattices. Both the 2×4 and 3×3 reconstructions are observed on undoped $SrMnO_3$ and $La_{1-x}Sr_xMnO_3$ random alloy films with MnO_2 surface termination (section 5.1). The 3×3 reconstruction is also routinely observed on the MnO_2 surface by RHEED during MBE growth of both the superlattices and $La_{1-x}Sr_xMnO_3$ films. We do not observe signatures of these reconstructions in our ARPES data, and since they are present for both insulating and metallic films of widely varying composition and structure, they cannot be responsible for the spectra that we report. On the other hand, we do observe a $c(2\times2)$ reconstruction in our ARPES Fermi surface maps from superlattices. This reconstruction is expected to exist throughout the superlattice due to its stability in $LaMnO_3$ [134], and so in this case it may not be solely a surface effect.

7.2 Resonant soft x-ray scattering

We commonly use non-resonant x-ray scattering, i.e. $\theta - 2\theta$ diffraction, to probe the structural quality of our thin films. In this case, the x-ray scattering amplitude is determined by the total electron density at each atom, and the locations of Bragg peaks provide us with information about the structure of the film at the atomic scale. At synchrotron beamlines, however, the energy of x-rays can be tuned to specific atomic absorption resonances. At precise resonant energies, the scattering amplitude for a single electronic transition can become comparable to the combined scattering from all other electrons in the crystal. This is a powerful technique for tracking magnetic, structural, and chemical order within crystalline materials, and has been used for decades with hard x-rays [188, 189, 190, 191]. Recently, resonant *soft x-ray* scattering (RSXS) has seen tremendous growth in the study of electronic reconstructions occurring in oxide superlattices [192, 193, 194, 195]. Periodic superlattices provide long wavelength modulations ideally suited to the q-space accessible to soft x-rays, and many transition metal oxides have transitions in this energy range that are highly sensitive to the relevant d orbitals.

In the case of the manganites, the two relevant resonances are the O K-edge and the Mn L-edge. The O K-edge at 570 eV consists of a transition from the occupied $1s$ level to unoccupied $2p$ states. In an ionic picture, the O $2p$ states are fully occupied and this transition would be forbidden. In reality, however, there is strong hybridization between the O $2p$ and Mn $3d$ states, so that the O K-edge acts as a probe of the unoccupied Mn $3d$ states. The Mn L-edge consists of two lines occurring at 640 eV and 650 eV for the so-called L_3 and L_2 edges, respectively. These correspond to transitions out of the spin-orbit split Mn $2p$ core levels into unoccupied Mn $3d$ states. Thus, both the O K-edge and Mn L-edge provide us with the means to directly probe the Mn $3d$ orbitals, which are the driving force for the complex magnetic and electronic properties of the manganites.

Smadici et al. [192] exploited this sensitivity in a RSXS study of $n = 4$ and $n = 5$ $(LaMnO_3)_{2n}/(SrMnO_3)_n$ superlattices. They observed strong diffraction at a structurally forbidden peak for both the O K and Mn L edges corresponding to an interface-confined electronic state close to E_F in energy. Furthermore, the intensity of this feature closely tracked the temperature dependence of the conductivity and magnetization, suggesting these electrons play a key role in driving the electronic and magnetic behavior of this system. An additional study of the $n = 2$ superlattice observed the development of a ferromagnetic moment at the interface and modulations of the effective hole-doping with the superlattice period [196].

To probe the detailed properties of both the interface confined states and states throughout the rest of the superlattice structure, we have performed extensive *polarization dependent* RSXS measurements on $(LaMnO_3)_{2n}/(SrMnO_3)_n$ superlattices with $n = 1-4$. Measuring resonant processes while varying the linear polarization of the x-rays allows the direct study of any electronic mechanisms that break the fourfold rotation symmetry of the lattice. In particular, orbital polarization or orbital order leads to strong linear dichroism signals, and recent work has demonstrated its use in x-ray resonant scattering to determine atomically-resolved orbital polarization profiles in $LaNiO_3/LaAlO_3$ superlattices [194]. In addition, the electron spin can break this symmetry in both ferromagnetic and antiferromagnetic states, giving rise to linear dichroic scattering [188].

Further information about the magnetic order can be obtained through circular dichroism. The photon momentum generally couples to the orbital angular momentum of the excited electron in the absorption process. For spin-orbit split core levels like the Mn L-edge, this results in sensitivity to the spin-polarization of the unoccupied $3d$ states. Since the photon angular momentum is along the propagation direction, circular dichroism provides a means of directly measuring the magnetic moment along the beam direction [188].

Both linear and circular dichroism at the Mn L-edge were used by Aruta et al. [197] in a non-scattering measurement to determine the average magnetization and orbital order within a series of $(LaMnO_3)_{2n}/(SrMnO_3)_n$ superlattices. By using the same processes in a scattering geometry, one can probe the spatial structure of both the orbital and magnetic orders at the atomic scale.

7.2.1 The REIXS beamline at the Canadian Light Source

Our resonant scattering experiments were performed at the Resonant Elastic and Inelastic X-ray Scattering (REIXS) beamline of the Canadian Light Source (CLS) in Saskatoon, Saskatchewan. The beamline undulator provides full control of beam polarization over 80-2000 eV, with a resolving power of $\Delta E/E \approx 1 \times 10^{-4}$. The RSXS endstation consists of an in-vacuum four-circle diffractometer with additional (x, y, z) translation for the sample and a base pressure of 2×10^{-10} Torr (Fig. 7.7a and ref. [198]). Several photon detectors are available and can be changed on-the-fly via in-vacuum motors. Here we use a high-sensitivity photodiode capable of accessing the greater than six order of magnitude dynamic range required for reflectivity measurements. Total electron yield is simultaneously measured by a picoammeter in series with the sample ground. Magnetic fields can be applied by mounting samples onto a permanent magnet. In our case, we used out-of-plane oriented magnets. This provides us with a high-sensitivity to the ferromagnetic component of the film for large q, i.e. when the photon propagation direction is close to the sample normal. Fig. 7.7b illustrates the scattering and magnetic field geometry used for our measurements.

These experiments were performed with considerable support from our many collaborators: Feizhou He and Ronny Sutarto of the CLS; Andrew Achkar and David Hawthorn of the University of Waterloo; and Sebastian Macke and George Sawatzky of the Univer-

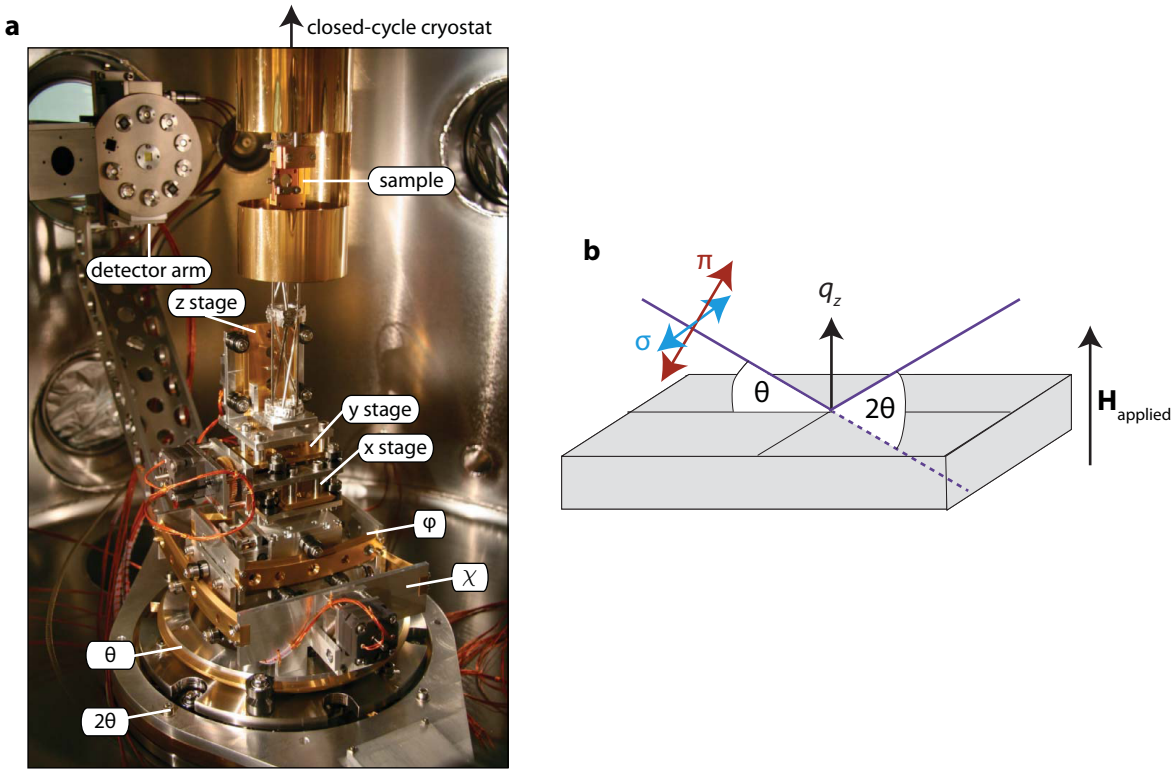

Figure 7.7: (**a**) An annotated image of the in-vacuum diffractometer at the CLS (Reprinted with permission from D.G. Hawthorn *et al.* (2011) [198]. Copyright 2011, AIP Publishing LLC). (**b**) Illustration of the scattering geometry used in this study (Adapted by permission from Macmillan Publishers Ltd: Benckiser *et al.* (2011) [194]). The scattering q vector is in the out-of-plane direction and along the applied magnetic field ($\mathbf{H}_{applied}$). Also shown are the orientations for the two linear polarizations, σ and π.

sity of British Columbia. We have acquired a vast dataset encompassing the energy, linear polarization, and circular polarization dependence of diffraction at both the O K-edge and the Mn L-edge for $(LaMnO_3)_{2n}/(SrMnO_3)_n$ superlattices with $n = 1 - 4$. The subsequent and ongoing analysis of this complex dataset has been spearheaded by Sebastian Macke and Bulat Burganov (of Cornell), and makes use of the ReMagX software package [199]. In this section, I highlight the primary conclusion drawn so far: our discovery of a new and exotic magnetic structure within the $n = 4$ film.

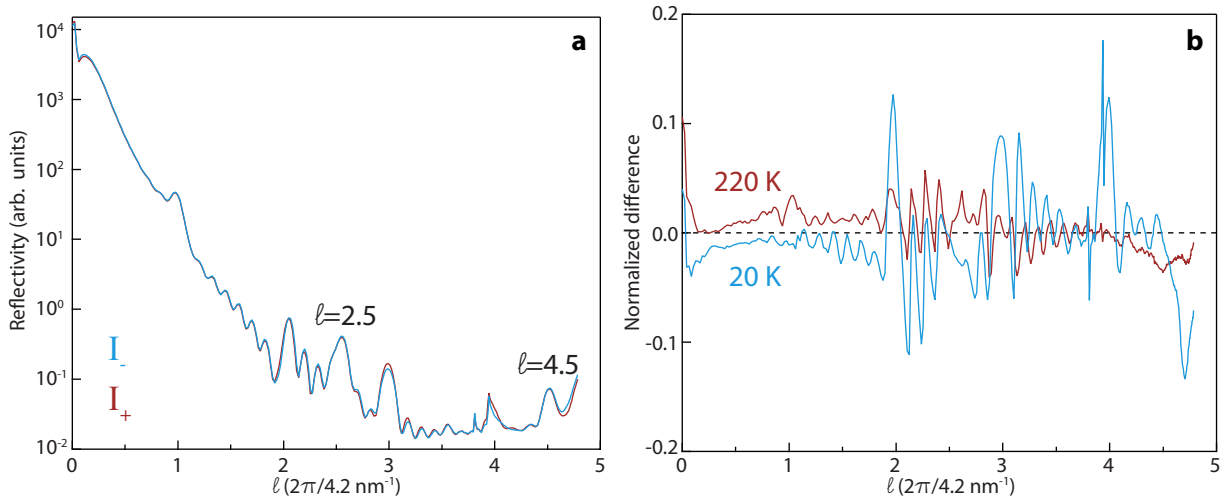

Figure 7.8: (**a**) Resonant reflectivity at the Mn L_3-edge (E = 640.4 eV) for the n = 4 superlattice with right-circular (I_+) and left-circular (I_-) polarized x-rays. The unexpected half-order peaks are indicated. (**b**) The normalized difference (*asymmetry*= $(I_+ - I_-)/(I_+ + I_-)$) for the reflectivity at T = 20 K and T = 220 K, above the Curie temperature. None of the superlattice peaks are visible in the high temperature data as expected, but even in low temperature data, there is no enhanced magnetic asymmetry at the half-order peaks.

7.2.2 Results

Figure 7.8a shows reflectivity data from the n = 4 superlattice taken with E = 640.4 eV at the Mn L_3- edge for circularly polarized x-rays at T = 20 K. We see several diffraction peaks corresponding to the superlattice structure, but in addition find unexpected half-order peaks at ℓ = 2.5 and ℓ = 4.5. Such features correspond to a signal with periodicity of twice the n = 4 structural unit cell, an extremely long length scale of 9.4 nm. By taking a normalized difference between right and left polarized data, we can extract the component corresponding to the magnetization along the beam direction (Fig. 7.8b). The integer-order peaks show strong magnetic scattering that vanishes above the Curie temperature, and thus provide direct evidence for strongly modulated ferromagnetism arising due to the $LaMnO_3/SrMnO_3$ interfaces. On the other hand, we see that both half-

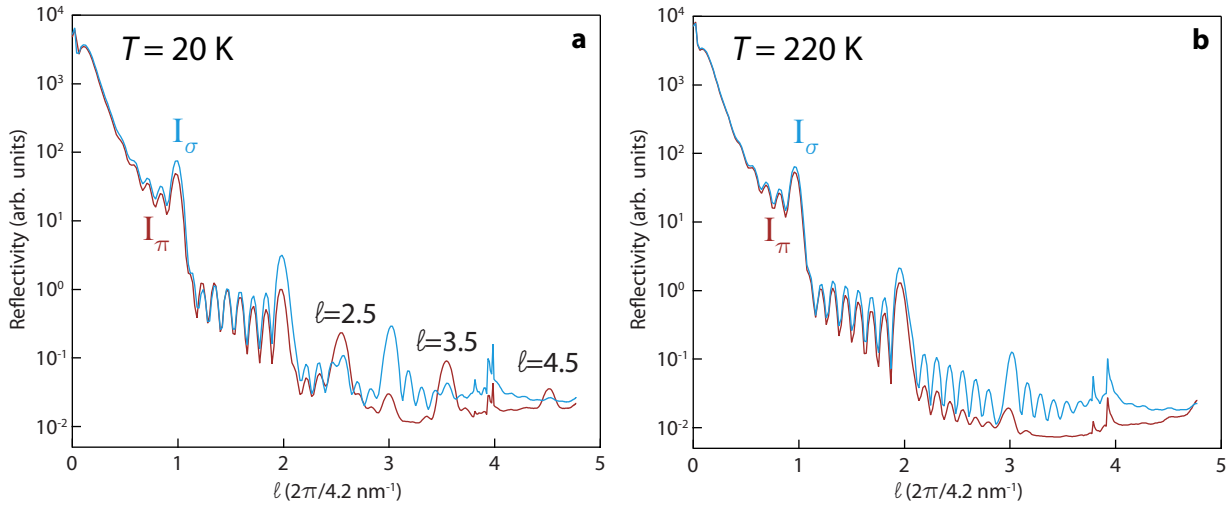

Figure 7.9: (**a**) Resonant reflectivity at the Mn L_3-edge ($E = 638.8$ eV) for the $n = 4$ superlattice with linear polarized x-rays at $T = 20$ K. The unexpected half-order peaks are indicated, and all show strong linear dichroism. (**b**) Reflectivity at $T = 220$ K, where we still see the structural derived integer-order peaks, but no longer see the half-order reflections. Note that in data from both temperatures the π reflectivity shows a strong suppression at $\ell \approx 3.4$, which corresponds to Brewster's angle ($\approx 45°$ for x-rays).

order peaks show no circular dichroism and vanish in the normalized difference, indicating that the order giving rise to this scattering has no net magnetic moment. Nevertheless, this leaves many possible origins including charge, orbital or antiferromagnetic order.

To uncover the origin of these unexpected features, we also measured the scattering with linear polarization (Fig. 7.9). Again we observe strong half-order peaks including an additional peak at $\ell = 3.5$, and all show strong linear dichroism that is clearly visible within the raw data. Furthermore, data at $T > T_c$ in Fig. 7.9b show that all half order peaks vanish. The strong dichroism rules out a purely charge-order mechanism, and the temperature dependence rules out orbital-order, which survives to much higher temperatures [197]. Our data thus indicate a purely antiferromagnetic origin for the half-order peaks. Further temperature dependent measurements of the $\ell = 3.5$ resonant peak shown

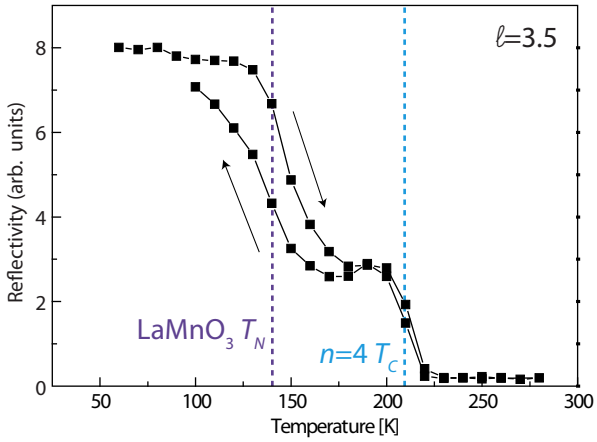

Figure 7.10: Temperature dependence of the $\ell = 3.5$ resonant peak on heating and cooling, as indicated. We observe an initial onset at the $n = 4$ Curie temperature ($T_C \approx 210$ K) [185] and an additional increase at the bulk $LaMnO_3$ Neel temperature ($T_N = 140$ K) [99].

in Fig. 7.10 confirm its magnetic origin: its initial onset occurs at the $n = 4$ Curie temperature ($T_C \approx 210$ K) [185] and an additional increase occurs close to the bulk $LaMnO_3$ Neel temperature ($T_N = 140$ K).

7.2.3 Long-wavelength magnetic structure for $n = 4$

How can we understand the extremely long period antiferromagnetism arising in the $n = 4$ superlattice? We propose that the half-order peaks arise from a combination of the A-type antiferromagnetic state within $LaMnO_3$ layers and their coupling across the interface and subsequent $SrMnO_3$ layers. In bulk, $LaMnO_3$ has a layered A-type antiferromagnetic structure consisting of alternating ferromagnetic planes, whereas $SrMnO_3$ has a G-type antiferromagnetic structure with a magnetic moment that cancels in each layer. For long period superlattices, we expect the magnetic order within the $LaMnO_3$ and $SrMnO_3$ blocks to approach the bulk structure and ferromagnetism to be confined to

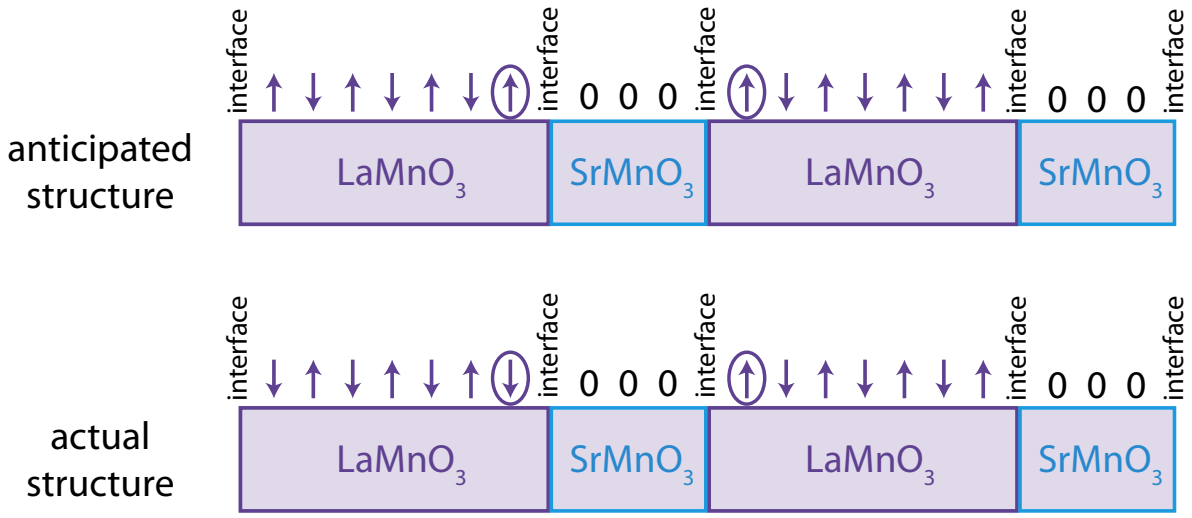

Figure 7.11: The top panel illustrates the anticipated magnetic structure in the $n = 4$ superlattice, which has the same periodicity as the structural lattice. Arrows represent the spin for each MnO_2 layer. The bottom panel illustrates the magnetic structure suggested by our observation of half-order resonant diffraction peaks. The $LaMnO_3$ A-type antiferromagnetic order has a 180° phase change between neighboring superlattice unit cells, illustrated for example by the highlighted spins for the two structures. The magnetic order at the interface is not yet known, but will be determined by future analysis.

the interface region [134]. This leads to an antiferromagnetic order along the out-of-plane direction that has the same period as the structural superlattice unit cell (Fig. 7.11a), and that gives rise only to integer-order scattering peaks. The central result of our observations is that, contrary to this expectation, the interface and $SrMnO_3$ layers provide an additional antiferromagnetic coupling that causes a 180° phase change for the $LaMnO_3$ magnetism in neighboring unit cells. The resultant magnetic structure is illustrated in Fig. 7.11b. This unusual magnetic order has twice the period of the structural unit cell and gives rise to the observed half-order peaks. In addition the structure factors of the half-order peaks depend sensitively on the magnetic order at the $LaMnO_3/SrMnO_3$ interfaces, and our ongoing analysis is aimed at resolving this additional component of the

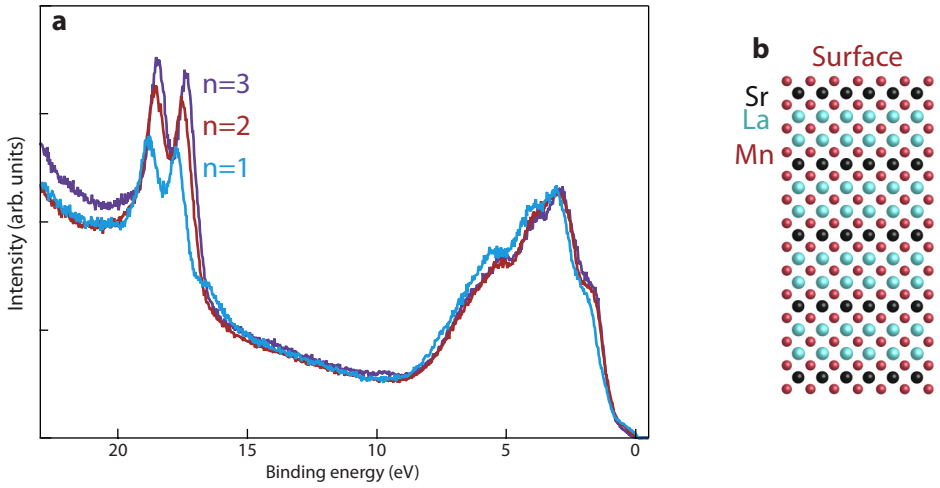

Figure 7.12: (**a**) The valence bands of the three superlattices are nearly identical over a wide energy range, except for the increasing intensity of the Sr 4*p* core states around 18 eV due to the termination of each superlattice by *n* unit cells of $SrMnO_3$ (**b**) A schematic illustration of the MnO_2 surface termination of our films, shown here for $n = 1$.

superlattice magnetic structure. The lack of comparable half-order peaks at the Mn *L*-edge for smaller *n* indicates that this phenomena occurs exclusively for the large-period insulating systems, and is consistent with our requirement for bulk-like $LaMnO_3$ layers, which should be suppressed in short-period metallic superlattices. Our observation of an unexpected 9.4 nm period magnetic structure indicates the power of resonant scattering for determining the unusual electronic and magnetic reconstructions that occur in complex oxide superlattices, and demonstrates that despite intense study, manganite superlattices still have many surprises in store.

7.3 ARPES results

Films measured by ARPES were 20 nm to 25 nm thick, and were terminated with *n* layers of $SrMnO_3$, where a layer corresponds to a formula-unit-thick layer along the growth

direction (Fig. 7.12b). To avoid surface effects arising from the polarity of the $LaMnO_3$ layers, our thin films were also made to be inversion symmetric by initiating growth on the $SrTiO_3$ substrates with n $SrMnO_3$ layers. The additional $SrMnO_3$ layers introduce a very slight change of the global average doping of the entire film by at most $\Delta x \leq 0.03$ away from $x = 1/3$. ARPES measurements were performed with a VG Scienta R4000 electron analyzer and a VUV5000 helium plasma discharge lamp and monochromator using 40.8 eV photons. The base pressure of the ARPES system was $4{\times}10^{-11}$ Torr, and data were taken at below 20 K unless specified otherwise. Constant-energy maps consist of 2×10^4 spectra integrated within ±30 meV of the specified energy and taken with an energy resolution of 40 meV. Measurements of the band dispersion were taken with a resolution of 10 meV.

We show the angle-integrated valence bands for $n = 1$, 2 and 3 superlattices in Fig. 7.12a. These closely resemble the valence band spectra of $La_{1-x}Sr_xMnO_3$ random alloy films (section 5.3.1), although we see progressively stronger Sr $4p$ and weaker La $5p$ intensities with increasing n due to the termination of each superlattice by n unit cells of $SrMnO_3$. In addition, the valence band for all superlattices are characteristic of a well defined MnO_2 surface termination, as should be present for the ideal structure from growth.

7.3.1 k-resolved electronic structure

In Fig. 7.13, I show **k**-resolved spectral weight maps for the n = 1, 2, and 3 samples of $(LaMnO_3)_{2n}/(SrMnO_3)_n$. In Fig. 7.13a and b, the Fermi surfaces of the metallic n = 1 and 2 materials are apparent. These are quite similar to the Fermi surface of $La_{2/3}Sr_{1/3}MnO_3$ (Fig. 5.11) but appear sharper and more distinct, likely due to the elimination of the dopant-induced random potential that is a source of scattering in the random alloy. Similar to that case, the relevant bands have Mn e_g character and consist of a hole pocket

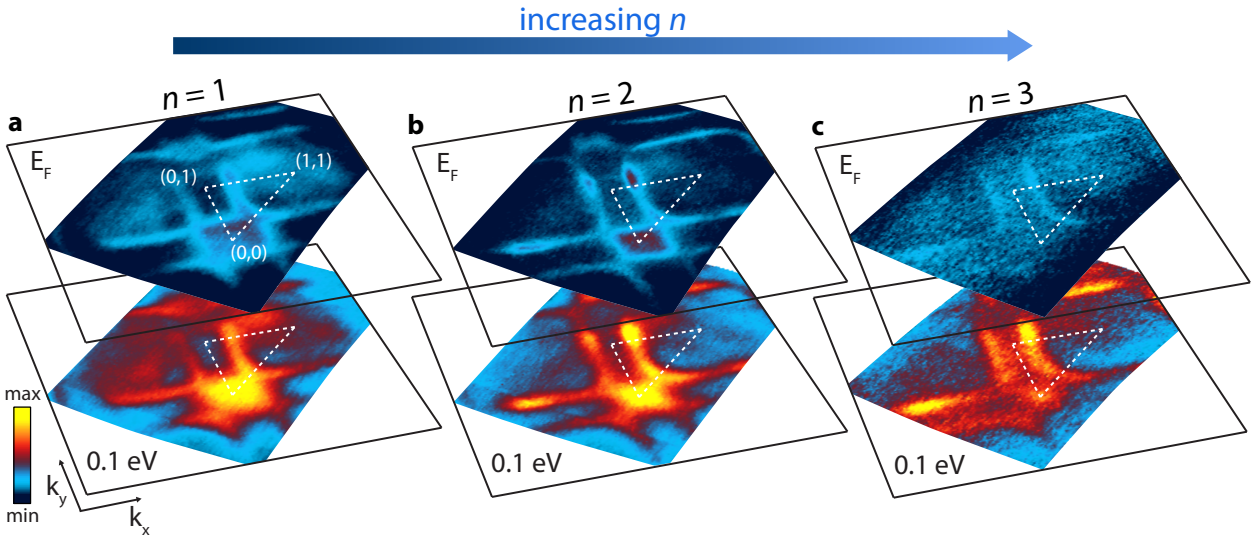

Figure 7.13: (**a-c**) **k**-resolved maps of photoemission spectral weight for $(LaMnO_3)_{2n}/(SrMnO_3)_n$ with n = 1, 2, and 3 respectively, at T = 10 K. Maps are at E_F and 0.1 eV binding energy as indicated.

with primarily $d_{x^2-y^2}$ character around the Brillouin zone corner, and a smaller electron pocket with primarily $d_{3z^2-r^2}$ character around the zone center. Spectral weight at E_F is suppressed for the insulating n = 3 sample, but clear states are still observed below E_F that roughly track the dispersion seen in metallic films.

The electron pocket decreases in size as n increases in Fig. 7.13, indicating the preferential filling of $d_{x^2-y^2}$ orbitals as well as a possible change in carrier concentration, which suggests an approach towards an interfacial two-dimensional electronic structure. Estimating the carrier density from counting the Luttinger volume of the Fermi surfaces gives higher hole concentrations ($x \approx 0.50 \pm 0.1$) than would be expected from a random alloy ($x = 0.33$), as expected from a $LaMnO_3/SrMnO_3$ interface.

To further quantify these changes, we fit the measured Fermi surfaces and dispersions to a tight-binding parametrization. The $(LaMnO_3)_{2n}/(SrMnO_3)_n$ superlattice contains $3n$ inequivalent Mn sites, and a full tight-binding parametrization would contain $6n$ e_g or-

bitals and many free parameters. In the interest of using the simplest possible model to represent our data, and noting that we only wish to parametrize the bandstructure at the interface, we expect a model containing one $d_{3z^2-r^2}$ and one $d_{x^2-y^2}$ state to be adequate. Thus, we use a modified version of the model defined in Ref. [75] for $LaMnO_3$;

$$t_{\pm a\hat{x}} = \frac{t_1}{4}\begin{pmatrix} 1 & -\sqrt{3} \\ -\sqrt{3} & 3 \end{pmatrix} \qquad t_{\pm a\hat{y}} = \frac{t_1}{4}\begin{pmatrix} 1 & \sqrt{3} \\ \sqrt{3} & 3 \end{pmatrix} \qquad t_{\pm a\hat{z}} = \alpha t_1 \begin{pmatrix} 1 & 0 \\ 0 & 0 \end{pmatrix}$$

$$t_{\pm a\hat{x}\pm a\hat{y}} = \frac{t_2}{2}\begin{pmatrix} 1 & 0 \\ 0 & -3 \end{pmatrix} \qquad t_{\pm a\hat{x}\pm a\hat{z}} = \frac{\alpha t_2}{2}\begin{pmatrix} -2 & \sqrt{3} \\ \sqrt{3} & 0 \end{pmatrix} \quad t_{\pm a\hat{y}\pm a\hat{z}} = \frac{\alpha t_2}{2}\begin{pmatrix} -2 & -\sqrt{3} \\ -\sqrt{3} & 0 \end{pmatrix}$$

With $d_{3z^2-r^2} = [\ 1 \quad 0\ ]$, $d_{x^2-y^2} = [\ 0 \quad 1\ ]$, and with a chemical potential μ. The key parameter for describing the anisotropy of the electron liquid at the $LaMnO_3/SrMnO_3$ interface is $0 \leq \alpha \leq 1$, which represents the suppression of hopping in the z direction caused by the superlattice and is assumed to affect nearest neighbor and next-nearest neighbor hopping equally.

This model was fit to our ARPES data for each superlattice and for data from the random alloy $La_{2/3}Sr_{1/3}MnO_3$ (chapter 5) as follows. First, we use the sharply-resolved hole pocket at E_F to determine t_2/t_1 and μ/t_1. This feature is dominated by segments of the hole pocket near $k_z = \pi/c$, which are essentially independent of α. With the values of t_2/t_1 and μ/t_1 now determined by the hole pocket data, we then determine α by fitting data from the electron pocket, which is very sensitive to the value of α. We find that this two-step approach produces more reliable fit parameters than an unconstrained fit where both Fermi surface sheets are fit simultaneously by allowing t_2/t_1, μ/t_1, and α to vary freely. The determination of the size of the electron pocket is the dominant source of uncertainty in determining α and hence the orbital polarization, which is made more complicated by

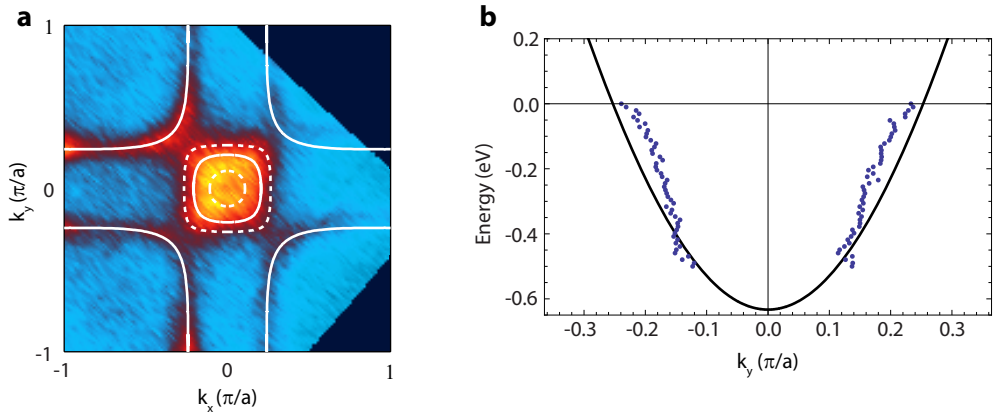

Figure 7.14: An example of the tight-binding fit to experimental data, this data taken from the $n = 2$ superlattice. (**a**) The Fermi surface overlaid with the hole pocket and electron pocket fits, which are used to determine t_2, μ, and α. The dotted-line shows the upper and lower bounds for the size of the electron pocket. (**b**) The dispersion of the hole pocket at $k_x = 0.55\pi/a$, which is used to determine t_1. Black lines are the tight-binding fit.

k_z-smearing that results in an electron pocket with a combination of sharp peaks and a broader background (section 5.2.1). Therefore, we estimate the uncertainty in the size of the electron pocket by taking as an upper bound the FWHM of the intensity around Γ, and as a lower bound, the separation between two peak maxima around Γ, as shown in Fig. 7.14a. For the $n = 3$ superlattice, where no electron pocket Fermi surface is resolved, we provide only an upper bound for α that lifts the electron pocket completely above E_F. We then use the uncertainty in the size of our electron pockets to obtain uncertainty estimates for α shown in Table 7.1. The remaining parameter, t_1, is then fit to the dispersion of the hole pocket away from E_F. Note that the value of t_1 has no effect on the calculated Fermi surfaces, band fillings and orbital polarizations, since it only results in an overall scaling of the energy units. Our extracted tight-binding parameters for all four samples are displayed in Table 7.1.

The resulting bandstructure, Fermi surfaces, and orbital polarization from our tight-binding fits are shown in Fig. 7.15 as well as directly overlaid onto experimental data

Sample	t_1	t_2	μ	α
alloy	0.87	$0.13t_1$	$-1.13t_1$	1
$n = 1$	1.1	$0.15t_1$	$-1.33t_1$	0.45±0.25
$n = 2$	0.97	$0.10t_1$	$-1.31t_1$	0.22±0.09
$n = 3$	1.2	$0.08t_1$	$-1.38t_1$	≤0.16

Table 7.1: The tight-binding parameters that best fit our experimental data. Error bars for α are estimated from the uncertainty in fits of the electron-pocket Fermi surface.

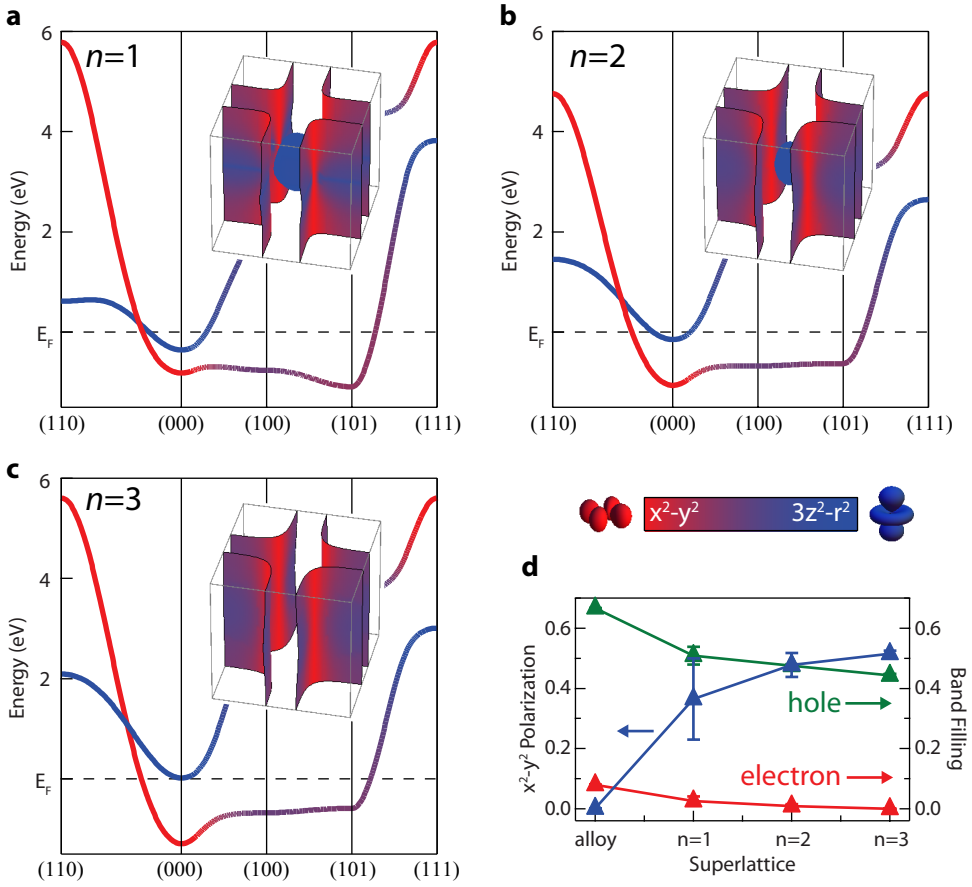

Figure 7.15: (**a-c**) Tight-binding bandstructures and Fermi surfaces extracted from our ARPES data for the n = 1, 2, and 3 superlattices. Orbital character throughout the Brillouin zone is indicated by each band's color. (**d**) Orbital polarization and filling of the electron and hole pockets from the tight-binding model for the three superlattices and the random alloy. Error bars are determined from the maximum and minimum estimated size of the electron pocket from our ARPES data, which dominates the uncertainty of the model.

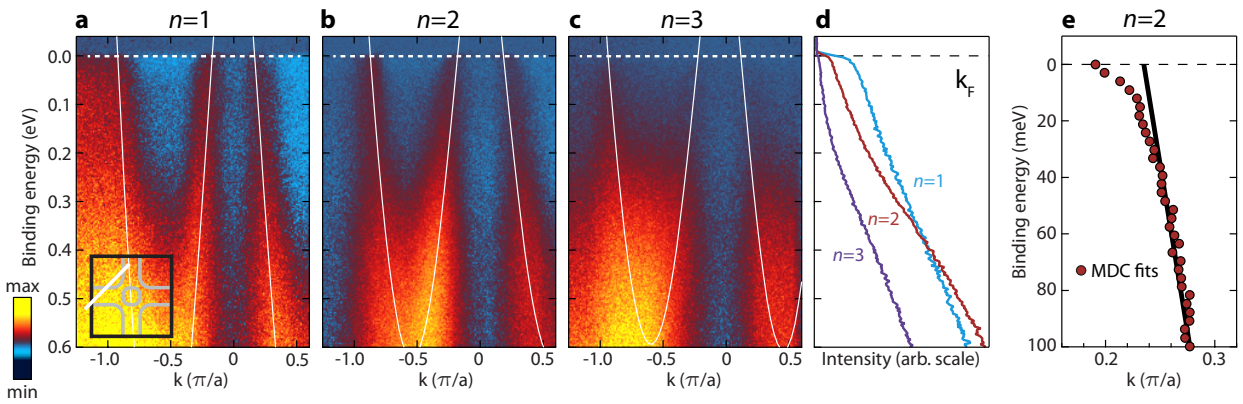

Figure 7.16: (**a-c,**) ARPES spectra along the **k**-path illustrated by the inset of panel a, showing the hole-pocket band crossing E_F at three points. Tight-binding fits are overlaid in white as guides to the eye. A non-dispersive background has been subtracted from the ARPES data to more clearly illustrate the bandstructure. (**d**) Energy-dependent photoemission intensity (EDCs) at $\mathbf{k_F}$ of the hole pocket. (**e**) ARPES band dispersion for $n = 2$ compared to the linear extrapolation of the dispersion for $E > 0.075$ eV, showing a kink at 35 meV.

in Figs. 7.16 and 7.17. We define the orbital polarization as $(N_{(x^2-y^2)} - N_{(3z^2-r^2)})/(N_{(x^2-y^2)} + N_{(3z^2-r^2)})$, where N is the integral of the indicated partial density of states up to E_F. The orbital polarization increases from 0% for cubic $La_{2/3}Sr_{1/3}MnO_3$ to approximately 50% for $n = 3$, consistent with x-ray absorption measurements that find $d_{x^2-y^2}$ polarization at the interfaces [197]. This polarization is dominated by the $d_{x^2-y^2}$ character of the hole-like sheets, although our orbital polarization never approaches 100% because their tight-binding wavefunctions still retain non-negligible $d_{3z^2-r^2}$ character. Our tight-binding model provides a qualitative description of the change in orbital polarization with n, but more sophisticated density functional or dynamical mean field theory calculations would be necessary to obtain more accurate wavefunctions.

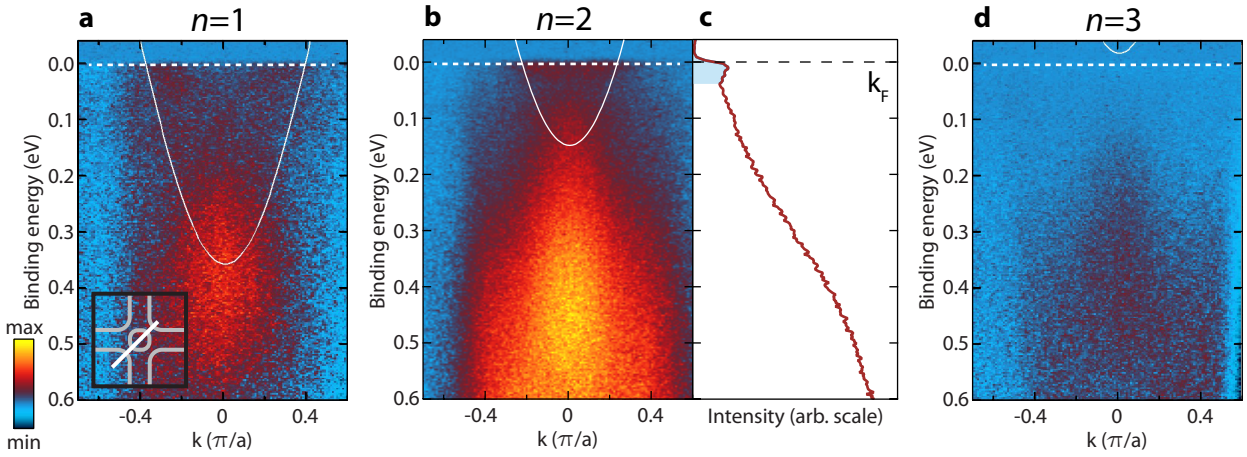

Figure 7.17: (**a,b,d**) ARPES spectra along the **k**-path illustrated by the inset of panel a for the n = 1, 2, and 3 superlattices. The tight-binding bands for the electron pocket are shown by the white lines. A non-dispersive background has been subtracted from the ARPES data to more clearly illustrate the bandstructure. (**c**) EDC at $\mathbf{k_F}$ of the electron pocket for n = 2. The quasiparticle peak is schematically illustrated by the blue shaded area.

7.3.2 High-resolution ARPES spectra

In Figs. 7.16 and 7.17, we show the spectra as a function of energy and momentum along cuts shown in the insets of Figs. 7.16a and 7.17. The n = 1 and 2 samples exhibit well-defined and dispersive hole like bands (Fig. 7.16a,b). In addition, a sharp quasiparticle-like peak can be observed for the n = 2 electron pocket (Fig. 7.17). Due to photoelectron final state effects (section 5.2.1), the highly k_z dispersive electron pocket typically appears as an indistinct broad feature in photoemission measurements. Thus, the sharply resolved feature for n = 2 can likely be attributed to the interfacial states' increasing confinement to two-dimensions with n, which reduces the k_z dispersion. The peak-dip-hump structure, where the coherent quasiparticle peak is dominated by a broad hump of incoherent spectral weight, is a signature of strong many-body interactions and has been observed in the cuprates [16] and other manganites [141].

Fig. 7.16e shows a kink in the dispersion for the $n = 2$ hole pocket band within 35 meV of E_F. The ratio of band velocities at high and low energy gives $v_{F,\mathrm{high}}/v_{F,\mathrm{low}} = 3.7 \pm 0.6$. Within a weak-coupling scenario, this would correspond to a mass renormalization $m^*/m_{\mathrm{band}} = 3.7$, although this falls well into the strong coupling regime. In addition to our measurements of $La_{2/3}Sr_{1/3}MnO_3$ (chapter 5), similar features have been observed in other correlated systems which exhibit strong electron-boson interactions, such as the cuprates [16], and some bilayer manganites, where a similar velocity renormalization was observed at nearly the same energy ($v_{F,\mathrm{high}}/v_{F,\mathrm{low}} = 5.6$) and was attributed to strong electron-phonon coupling [141]. The observed peak-dip-hump EDC shape and large kink indicate that the metallic state experiences strong many-body interactions that renormalize the bandstructure and push this system far from a conventional Fermi liquid.

Unlike the metallic superlattices, $n = 3$ exhibits only pseudogapped intensity at E_F (Fig. 7.16d and 7.18a,b), similar to some polaronic systems with strong electron-phonon coupling [76, 106]. Despite the pseudogap, the $n = 3$ sample still exhibits the underlying hole-like $d_{x^2-y^2}$ dispersion at higher binding energies with a comparable bandwidth and similar remnant Fermi surface to the $n = 1$ and 2 samples, as shown in Fig. 7.13c. The similar dispersion of $n = 3$ to $n = 1$ and 2 demonstrates that the insulating behavior is not caused by the opening of a conventional bandgap as might be the case in semiconductor interfaces, and is consistent with the observation of interface derived states near E_F in recent resonant scattering measurements on the insulating $n = 4$ superlattice [192]. This suggests that the pseudogap is the origin of the n-driven metal-insulator crossover.

Further support that the pseudogap underlies the insulating behavior is obtained from temperature dependent measurements of the spectral weight (Fig. 7.18c). The metallic $n = 2$ superlattice shows a reduction in weight near E_F with increasing temperature, consistent with a loss of coherent quasiparticles in the paramagnetic state. On the other hand, the spectral weight of the $n = 3$ film increases above T_c as the pseudogap fills in,

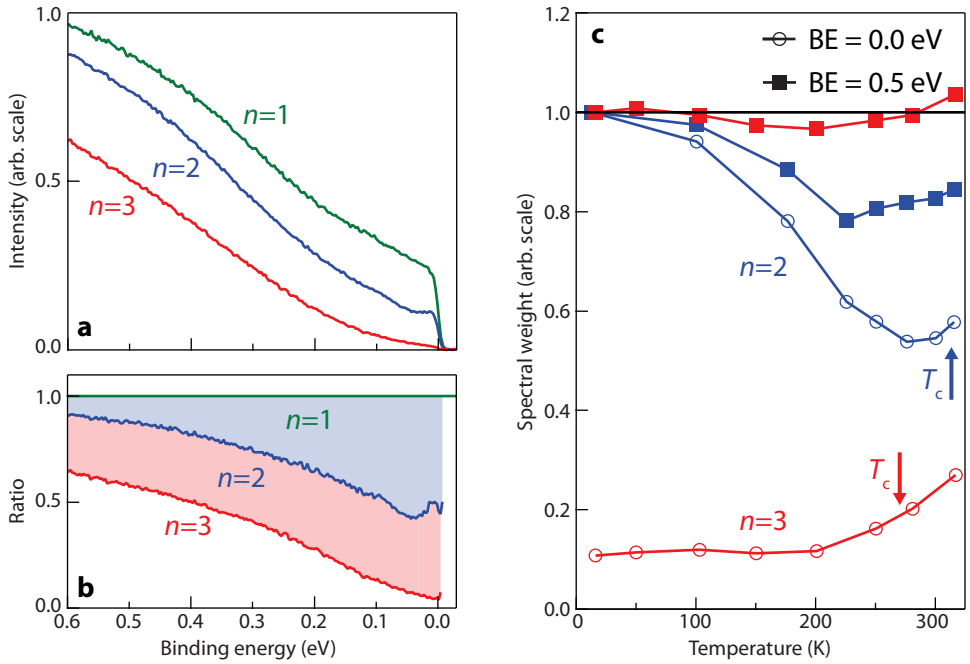

Figure 7.18: (**a**) The angle-integrated spectral weight for the $n = 1$, 2, and 3 superlattices, showing pseudogap behavior in the $n = 3$ film. (**b**) The data from panel a normalized to the spectral weight of the $n = 1$ superlattice, highlighting the strong energy-dependence of the pseudogap. (**c**) Temperature dependence of the spectral weight at the Brillouin zone center for the $n = 2$ and 3 superlattices. Open circles show the spectral weight within 50 meV of E_F, closed squares show the spectral weight at a binding energy of 400 to 550 meV. Also indicated in c are the Curie temperatures (T_c) of each material. Data in c are normalized to unity at 20 K, except for the $n = 3$ open circles. Here, $n = 3$ data are normalized such that the integrated weight over E_F to 8.4 eV is equal to the $n = 2$ integral over the same window, allowing for a meaningful comparison between the two films.

consistent with its resistivity approaching the metallic superlattices in the paramagnetic state.

It is important to ensure that our ARPES measurements of the surface region are representative of the properties of the entire film. There are several reasons that we believe this to be the case. First, our observations of states at E_F for the $n = 1$ and 2 superlattices and a pseudogap for the $n = 3$ superlattice are consistent with macroscopic resistivity measurements. Second, this near-E_F suppression of spectral weight is highly energy dependent close to E_F (Fig. 7.18a,b), suggesting that this effect is not due to surface sensitivity, since the electron escape depth is effectively energy-independent in such a narrow range. Third, we observe a correspondence between the temperature dependence of our spectra and the films' Curie temperatures. Fourth, our LEED and RHEED patterns show 2×4 and 3×3 reconstructions associated with the $SrMnO_3$ termination (Fig. 7.6), but the ARPES data do not exhibit any evidence of such a periodicity, suggesting that the near-E_F states arise from the buried interface and are not unduly influenced by surface related effects.

As a final confirmation that the measured near-E_F electronic structure arises from the buried $LaMnO_3/SrMnO_3$ interface rather than the $SrMnO_3$ surface, we ran ARPES measurements of $SrMnO_3$ and $LaMnO_3$ films. Specifically, we have performed ARPES experiments on a 10 unit cell thick $LaMnO_3$ film with MnO_2 surface termination, an 8 unit cell thick $SrMnO_3$ film with SrO termination, an 8 unit cell thick $SrMnO_3$ film with MnO_2 termination, and a 6 unit cell thick $SrMnO_3$ film with MnO_2 termination. To avoid charging effects due to the insulating nature of these films, all samples were grown on 0.5% Nb-doped $SrTiO_3$ substrates and measured at room temperature. Samples were chosen to be thin enough to avoid charging while being thick enough to minimize any signal from the $SrTiO_3$ interface.

In all cases, we observe dispersive valence band spectra and sharp LEED patterns, indicative of the high quality of the films. As expected, we did not observe any appreciable

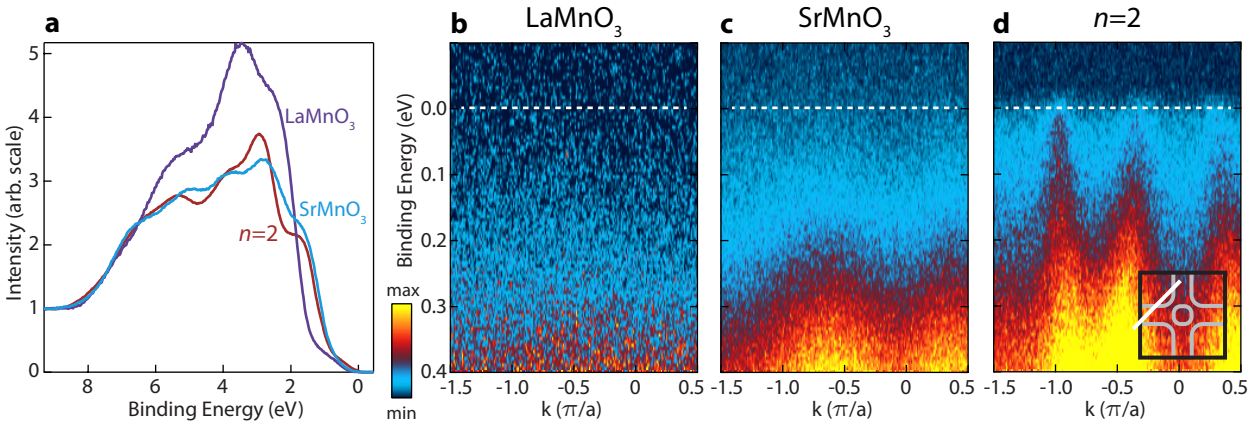

Figure 7.19: (**a**) Valence bands of $LaMnO_3$ and $SrMnO_3$ films (10 and 8 u.c. thick respectively, MnO_2 terminated), compared with the n = 2 superlattice. (**b,c**) ARPES data for the $LaMnO_3$ and $SrMnO_3$ films showing a lack of dispersive features within 0.4 eV of E_F. (**d**) ARPES data for the n = 2 superlattice showing the dispersive e_g-derived bands responsible for this film's metallic behavior.

or dispersive spectral weight within 0.4 eV of E_F for any of the control samples, as shown in Fig. 7.19. Therefore, we can safely conclude that the dispersive states near E_F arise from the $LaMnO_3/SrMnO_3$ interface. The angle-integrated valence band of the MnO_2 terminated $SrMnO_3$ films qualitatively resemble those of the superlattices at higher binding energies due to the $SrMnO_3$ termination of the superlattices. As expected, we also observe the tail of the $SrMnO_3$ valence band (occupied Mn t_{2g} and O $2p$ states) at approximately 0.3 eV binding energy in both the $SrMnO_3$ and superlattices (Figs. 7.19c,d). Nevertheless, only the superlattices exhibit the well-defined near E_F bands that are the focus of our manuscript.

7.4 Discussion

It has been suggested that reduced dimensionality could drive the $n \geq 3$ superlattices insulating via Anderson localization [186], where a Coulomb gap could form due to inter-

actions between localized electrons. Localized states should be broad in **k** due to a short mean free path (L), and from the Mott-Ioffe-Regel limit are expected to satisfy ($k_F L \approx 1$) [174]. Despite their suppressed intensity, we observe well-defined bands for $n = 3$ with $k_F L > 5$ (taking $L = 1/\Delta k$), significantly exceeding the expected criteria for Anderson localization. Our density of states near E_F (which follows $\approx (E - E_F)^2$) also deviates from the linear dependence expected for a Coulomb gap due to localization in two-dimensions [200], and our TEM measurements demonstrate a nearly disorder-free structure. In addition, a change in the hole concentration does not explain the crossover to insulating behavior at higher n, since $La_{1-x}Sr_xMnO_3$ has no ferromagnetic insulating state at large x.

It is then natural to consider the quantum many-body interactions that are inherent to the manganites as the origin of the metal-insulator crossover observed with n. These interactions are known to give rise to insulating ordered states, as the effective dimensionality (i.e. coupling along the c-axis) is lowered in the Ruddlesden-Popper series of manganites, $(La,Sr)_{m+1}Mn_mO_{3m+1}$, where m is the number of MnO_2 planes per unit cell [107]. Bilayer $m = 2$ $La_{2-2x}Sr_{1+2x}Mn_2O_7$ around $x = 1/3$ is a pseudogapped ferromagnetic bad metal with a low temperature resistivity two orders of magnitude higher than the metallic three-dimensional perovskite ($m = \infty$). The quasi two-dimensional $m = 1$ compound $La_{1-x}Sr_{1+x}MnO_4$ is insulating for all Sr concentrations [107, 11] due to the formation of charge, spin, or orbital order [201, 107], and exhibits fully gapped spectral weight at E_F and a remnant Fermi surface observed by ARPES in $La_{0.5}Sr_{1.5}MnO_4$ [104].

Our measurements demonstrate that dimensionality also plays a similar role in the superlattices (Fig. 7.20). The partially occupied interfacial states become progressively separated from neighboring interfaces with increasing n . As the effective hopping between interfaces is reduced, the states become increasingly two-dimensional. The similarities between spectral features in superlattices and bulk compounds indicate that the many-body interactions responsible for the properties of the single and bilayer manganites are

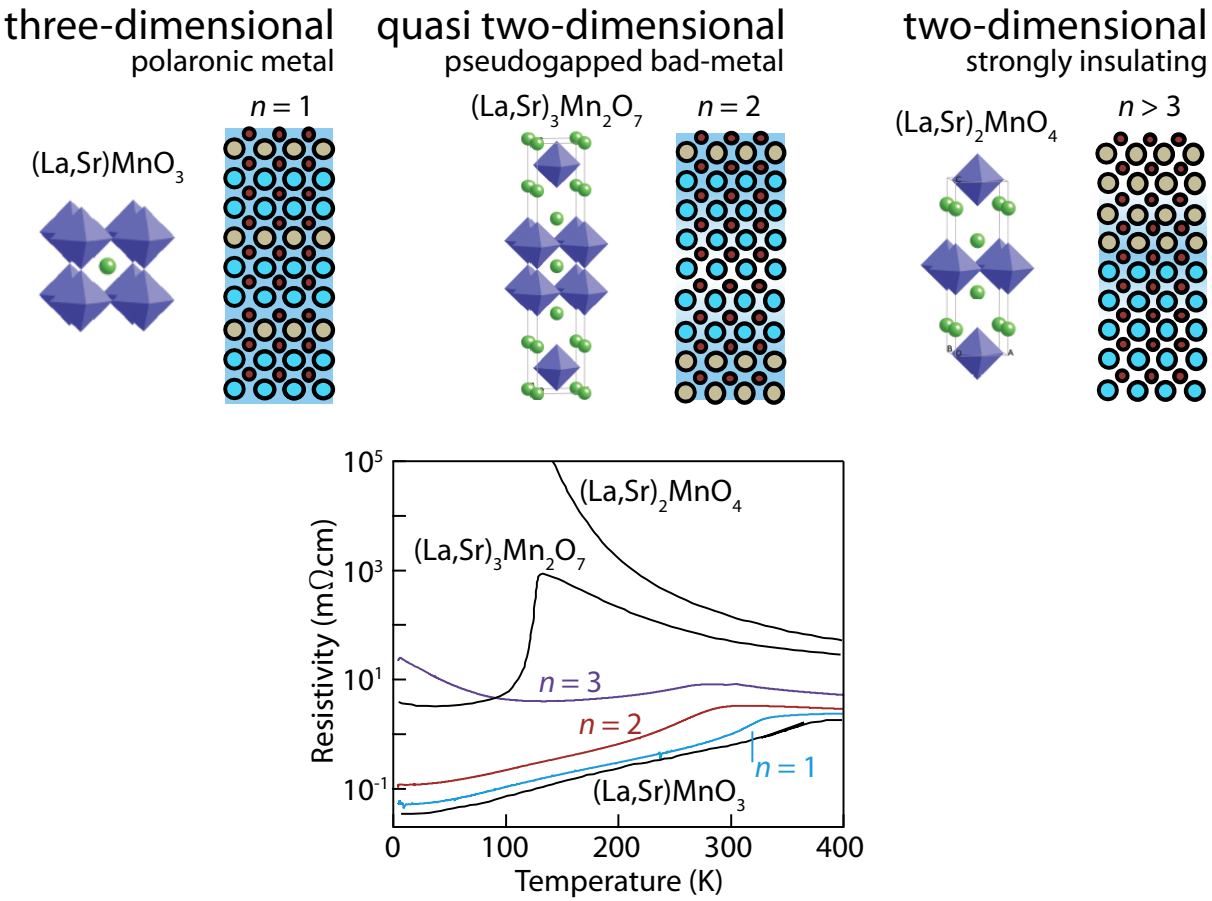

Figure 7.20: A schematic illustration of the link between dimensionality and metal-insulator transitions in the manganites, highlighting the commonalities between the layered Ruddlesden-Popper manganites and the $(LaMnO_3)_{2n}/(SrMnO_3)_n$ superlattices studied here. In the superlattices, as we increase n the interfaces become increasingly separated and decoupled from each other. Our ARPES measurements indicate that this enhances the effects of many-body interactions and stabilizes an unconventional insulating state. The bottom panel shows resistivity for the $n = 1 - 3$ superlattices (from ref. [113]) compared to the resistivity for $x = 0.4$ Ruddlesden-Popper compounds (from ref. [107]).

also central to the superlattice electronic structure. Furthermore, the small quasiparticle weight and kink observed in the $n = 2$ superlattice suggests a metallic state comprised of coherent polarons which are strongly coupled to the lattice, orbital, and/or magnetic degrees of freedom [76, 141, 16]. Recent calculations also suggest that electron-lattice coupling should strongly influence the properties of manganite superlattices and interfaces [202, 203]. Reducing the dimensionality from $n = 2$ to 3 results in a situation where the lowered dimensionality and possibly increased nesting in two-dimensions may enhance quantum fluctuations towards the insulating charge, spin, and orbital ordered states, such as those observed in the single layer $m = 1$ manganites [76, 140] or recently predicted for the $LaMnO_3$-$SrMnO_3$ interface [204]. These quantum fluctuations can disrupt the coherence of the fragile polaronic metallic state, giving rise to the weakly insulating / bad metal state observed in the bilayer manganites, as proposed by Massee *et al.* and Salafranca *et al.* [106, 205], thereby resulting in the pseudogap and loss of coherent QP weight in the $n = 3$ superlattice.

7.5 Conclusion

In this chapter we presented spectroscopic measurements of $(LaMnO_3)_{2n}/(SrMnO_3)_n$ superlattices aimed at uncovering the underlying electronic and magnetic structure driving its phase diagram. RSXS results in the insulating $n = 4$ system demonstrated the existence of a magnetic state with an unexpected antiferromagnetic component whose wavelength is twice the structural unit cell. We then illustrated how this is a natural consequence of the A-type antiferromagnetism in $LaMnO_3$ layers when combined with an antiferromagnetic coupling across the $SrMnO_3$ part of the structure. The remainder of the chapter then focused on our extensive ARPES measurements of the $n = 1 - 3$ superlattices. Our results showed that by decoupling the $LaMnO_3$-$SrMnO_3$ interfaces with increasing n, we

are able to reduce the effective dimensionality, and drive the polaronic metal at small n into a pseudogapped insulator for $n \geq 3$. More generally, our measurements demonstrate how the interplay of interactions and dimensionality can be used to control the properties of correlated oxide interfaces, and should be a key step towards the rational manipulation and optimization of their functionality for potential applications.

Chapter 8

Conclusions

In this dissertation, I explored the response of the electronic structure in manganite thin films to the effects of chemical, structural, and interface engineering. The starting point was a series of measurements of the electronic structure of the "parent" compound, $La_{2/3}Sr_{1/3}MnO_3$. Our clear observation of highly dispersive hole pocket features that track the unrenormalized bare bands predicted by DFT reconciled first-principles calculations with experiment in this compound for the first time. Furthermore, these features allowed us to perform quantitative comparisons with the extensive literature on the electronic structure of layered $(La,Sr)_3Mn_2O_7$. We established that both share a similar and very strong electron-lattice coupling within the ferromagnetic metallic phase, and that the charge carriers of $La_{2/3}Sr_{1/3}MnO_3$ should therefore be polaronic. This is particularly surprising since $La_{2/3}Sr_{1/3}MnO_3$ is two orders of magnitude more conducting than optimally doped $(La,Sr)_3Mn_2O_7$. Our studies of $La_{1-x}Sr_xMnO_3$ for $x = 0.2 - 0.4$ demonstrated the validity of our conclusions throughout the ferromagnetic metallic phase. We then observed a similar electronic structure within the A-type antiferromagnetic $d_{x^2-y^2}$ orbital polarized phase at $x = 0.6$, which remains robustly metallic despite its reduced k_z dispersion and

shows a similarly strong electron-lattice coupling.

With our understanding of bulk like $La_{1-x}Sr_xMnO_3$ established, we explored the mechanism underlying its epitaxial-strain controlled metal-insulator transition at $x = 1/3$. This transition occurs under large (1.7%) tensile strain, but we also measured the corresponding electronic structure for large (−1.2%) compressive strain. In both cases, we found that the underlying bandstructure is only weakly affected by epitaxial strain and maintains a similar effective mass at large (> 100 meV) energy scales. These results ruled out the scenarios of bandwidth or localization driven metal-insulator transitions. On the other hand, we observed a dramatic suppression of spectral weight at E_F in insulating $La_{2/3}Sr_{1/3}MnO_3$ and a large downward shift of the entire bandstructure. These results revealed an instability of the ferromagnetic metal to the formation of an ordered insulating phase, and the several hundred meV magnitude of the gap indicated the central role played by strong many-body interactions.

Replacing the random alloy with atomically-precise $(LaMnO_3)_{2n}/(SrMnO_3)_n$ superlattices then allowed us to eliminate the random potential from dopant atoms and provided us with an experimental 'dimensionality knob', shown by prior work to allow tuning between metallic and insulating ground states. We were able to directly measure a progression from a three-dimensional alloy-like electronic structure for $n = 1$ to a quasi-two-dimensional electronic structure for $n = 3$ due to the increasing separation between $LaMnO_3/SrMnO_3$ interfaces with increasing n. Nevertheless, the metal-insulator transition is not caused by the underlying bandstructure itself, since this shows clear dispersion towards E_F in all cases. Instead, the insulator is characterized by a wide pseudogap that suppresses the spectral weight within 800 meV of E_F. This feature is a clear indication of strong many-body interactions, which are effectively enhanced in reduced dimensions due to the decreased importance of electron kinetic energy and increased strength of Fermi surface nesting. These interactions enhance quantum fluctuations towards the

insulating charge, spin, and orbital ordered states ubiquitous in manganites and disrupt the fragile polaronic metal.

Throughout this dissertation, our results illustrate the central role played by the close competition between the fragile polaronic metal of bulk $La_{1-x}Sr_xMnO_3$ and the strong ordering tendencies of charge, orbital, and lattice degrees of freedom. By tuning anisotropy (through strain) and dimensionality (through interfaces), we can control this competition and the resulting electronic and magnetic properties. The competition between a variety of distinct phases is a hallmark of strongly correlated systems. Our results should thus be generally applicable to a wide array of transition metal oxides beyond the manganites, and can provide guidance to rationally engineering their physical properties for the next generation of electronic devices.

8.1 Future work and open questions

Our measurements of the electronic structure of manganite thin films established the importance of competing electronically ordered phases in controlling their physical properties. Due to the strong coupling nature of these transitions, however, Fermi surface nesting may not play a dominant role and ARPES results alone are thus insufficient to determine the precise ordering pattern underlying each insulating phase. Several additional experiments are capable of shedding light on this important issue. X-ray and resonant x-ray scattering measurements are often used to determine ordering patterns in bulk manganites [86, 206]. Thin films provide very weak diffraction signals due to their small volume, but measuring superlattice peaks due to an ordered phase may still be feasible [207]. We have pursued this experiment on 20 nm thick tensile strained $La_{2/3}Sr_{1/3}MnO_3$/DSO films at the Cornell High Energy Synchrotron Source (CHESS) using non-resonant 15 keV x-rays and a Pilatus area detector, but were unable to resolve the weak diffraction peaks

expected from the ordered phase. Resonant diffraction at the manganese $L_{2,3}$-edge (640 eV) will be particularly sensitive to charge or orbital order [206], and one might expect a more successful result in this case. This photon energy is large enough to reach several of the peaks expected from an ordered phase (with $|\mathbf{q}| = 0.25 - 0.35\ 2\pi/a$). In addition, further theoretical work using dynamical mean-field theory [115, 202] or model Hamiltonians [205] could make important contributions to determining the microscopic details of the ordered or fluctuating phases. In this endeavor, our measurements of the spectral function of the insulating and metallic phases provide an important test for theoretical models. More extensive DFT calculations can also contribute to our understanding of the ordered phases that are most stable within a single-electron approximation, and which might play an important role in the ultimate many-body ground state. Toward this goal, a recent calculation demonstrated the stability of checkerboard charge order at the interfaces in $(LaMnO_3)_{2n}/(SrMnO_3)_n$ (ref. [204]).

We were unable to directly address the existence of quasiparticles within bulk-like $La_{1-x}Sr_xMnO_3$, but whether their absence in our spectra is due to intrinsic or extrinsic effects is an important issue. A recent controversy has arisen in the bulk layered manganites regarding the existence of quasiparticles and the role they play in determining the macroscopic properties of $(La,Sr)_3Mn_2O_7$ [141, 106]. A clear observation of quasiparticles in $La_{1-x}Sr_xMnO_3$ could lend strong support to the hypothesis that quasiparticles are weakest in quasi-two-dimensional materials and only develop for large m layered manganites ($(La,Sr)_{m+1}Mn_mO_{3m+1}$). It is unlikely that improvements to sample quality will significantly reduce our ARPES momentum-widths, since spectra from extremely high-quality superlattices were only marginally sharper. Nevertheless, the use of newer low energy photon sources may allow for the resolution of quasiparticles (if present) due to reduced surface sensitivity. This can have the double effect of reducing k_z smearing effects in the photoemission spectra and reducing scattering from the possible surface dead layer. In addition, MBE is capable of growing the high m Ruddlesden-Popper structures

that cannot be grown as bulk single crystals. ARPES measurements on these could directly address the evolution of quasiparticles with m in the manganites, although such a study will be complicated by the inevitable presence of different-m intergrowths [106].

There are many other aspects of the manganites where in-situ ARPES could make important contributions. One particular example would be to reveal the intrinsic electronic structure underlying the C-type antiferromagnetic phase at $0.65 < x < 0.95$. This phase remains largely unexplored by ARPES, in part due to its strongly insulating nature. With thin film growth, however, this problem might be circumvented by growing a suitably thin film on a metallic substrate or buffer layer. Within the C-type phase, we expect one-dimensional dispersion through chains along the c-axis, which could be oriented along an in-plane direction by a suitable tensile strain. An orthorhombic substrate could further break the twofold symmetry so that the potentially one-dimensional states could be directly measured by ARPES. $La_{1-x}Sr_xMnO_3$ with x = 0.65-0.95 has a pseudocubic lattice constant of $\approx$ 3.83 Å (ref. [72]), ideally suited to weak and asymmetric tensile strain from orthorhombic [001] $NdGaO_3$.

Appendices

Appendix A

Formation of Mn 2+ due to air exposure

The colossal magnetoresistive manganites ideally have an intermediate valence between Mn 3+ and Mn 4+. Nevertheless, several studies of manganite thin films have found the existence of unwanted Mn 2+ ions. De Jong et al. [208, 209] used x-ray absorption spectroscopy (XAS) at the Mn *L*-edge and XPS of the Mn 3*s* core level to demonstrate the formation of magnetically inactive Mn 2+ at the surface of $La_{0.7}Sr_{0.3}MnO_3$/STO films due to oxygen vacancies. These vacancies could, however, be easily cured by a post-growth oxygen anneal, eliminating the Mn 2+ signal.

On the other hand, Valencia et al. [210, 211] have documented the seemingly paradoxical result that exposure to air induces Mn 2+ within $La_{2/3}Ca_{1/3}MnO_3$ and $La_{2/3}Sr_{1/3}MnO_3$ films. Studies of highly granular $La_{2/3}Ca_{1/3}MnO_3$ films grown by magnetron sputtering indicated the development of a large (up to 15%) Mn 2+ component throughout the entire film over a time span of several weeks [210]. Further work examined several film thicknesses, substrates, and annealing conditions and demonstrated that smooth films were much less susceptible than highly granular films to Mn 2+ formation, indicating that it occurs primarily at exposed surfaces [211]. The exposure to air might be expected

to prevent oxygen vacancies within the film, but Valencia et al. proposed an alternate mechanism by which atmosphere can reduce the surface of manganites. Catalysis studies demonstrated that CO can bond with manganite surfaces and reduce manganese to the 2+ valence state [212]. Valencia et al. showed that this mechanism explains the formation of Mn 2+ in LCMO films; exposure to a pure CO atmosphere for three days generates a similar Mn 2+ content to three months of exposure to ambient air [211].

Our MBE grown films have smooth surfaces and do not have a granular structure, which is expected to preserve the manganese valence within the bulk of our films. Nevertheless, the surface of our films also shows susceptibility to the formation of Mn 2+ over a time span of several weeks, which we have observed in our own XPS and XAS studies. For this reason, manganite films are stored in vacuum conditions when awaiting additional measurements, which was found to effectively prevent Mn 2+ formation [210].

Valencia et al. [211] studied several substrates and found significant differences in Mn 2+ formation that they attributed to variations in granular structure of their films. Nevertheless, epitaxial strain may also play a key role in the stability of various manganese valences. In particular, stoichiometric $SrMnO_3$ has a pseudocubic lattice constant of a = 3.81 Å, but in bulk can accommodate large concentrations of oxygen vacancies up to $SrMnO_{2.5}$ with a corresponding 3% increase in the unit cell volume [97, 213]. Thus, one might expect that the stability of stoichiometric $SrMnO_3$ is highest under compressive strain, providing a potential method for preventing Mn 2+ formation in thin films. To investigate this possibility, we grew a series of five 10 nm thick $SrMnO_3$ films on the same growth day using several substrates with varying amounts of strain and oxygen rotation patterns (table A.1). Immediately after growth (< 1 hr exposure to air) we measured the manganese valence in each film using XPS spectra of the Mn 3s states (section 6.1). The films were then stored in ambient conditions (T = 22 ± 1 °C and relative humidity of 18 ± 5%) between a series of subsequent XPS measurements. As seen in Fig. A.1a, we do

Substrate	a_p (Å)	strain	rotations
(110) $YAlO_3$	3.70	-2.6%	yes
$(100)_p$ $LaAlO_3$	3.79	-0.21%	yes
(110) $NdGaO_3$	3.86	1.6%	yes
(100) $(LaAlO_3)_{0.3}$-$(SrAl_{1/2}Ta_{1/2}O_3)_{0.7}$ (LSAT)	3.87	1.8%	no
(100) $SrTiO_3$	3.91	2.7%	no

Table A.1: Substrates used for the growth of 10 nm thick $SrMnO_3$ films, listing the pseudocubic in-plane lattice constant (a_p), the epitaxial strain, and whether or not the substrate has oxygen rotations.

observe a significant change in the Mn 3*s* spectra over the span of several weeks, indicating the formation of Mn 2+ within our films. Figure A.1b shows the measured manganese valence for all films. The films show small within-error variations in manganese valence, but overall we observe no significant differences between the various substrates. Figure A.1c shows the Mn valence as a function of time for films under the most compressive and tensile strain ($SrTiO_3$ and $YAlO_3$), as well as the film on LSAT. All three show no significant differences from each other, and have a saturated Mn 2+ signal after the first month within error. Thus, we find that all films are equally susceptible to the formation of Mn 2+ with a time scale of several weeks, irrespective of strain.

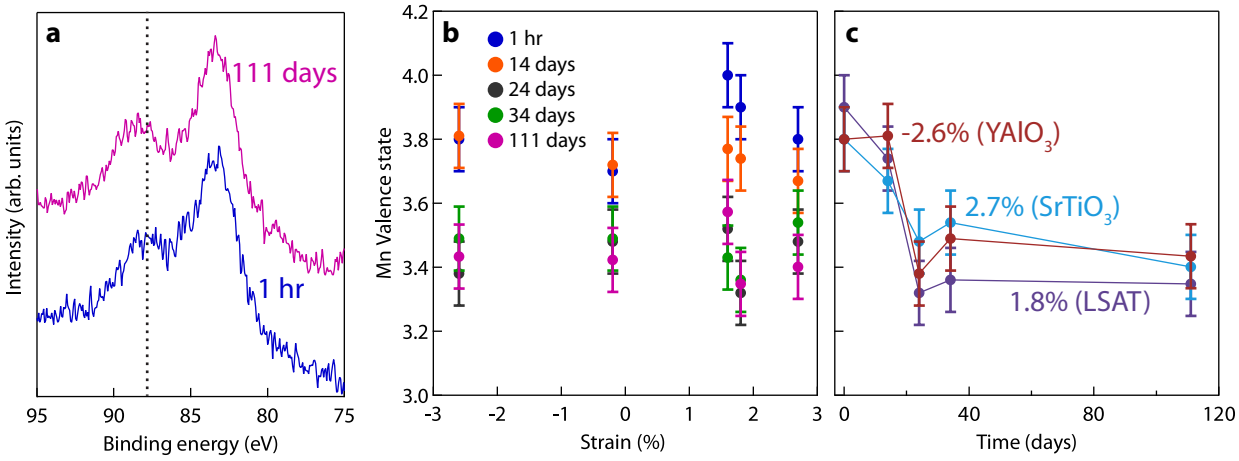

Figure A.1: (**a**) Example Mn 3*s* spectra from a $SrMnO_3$/LSAT film taken after 1 hour and after 111 days of air exposure. The spectra were shifted to align the peaks at 84 eV, and the dashed vertical line highlights the shift in the higher binding energy peak. (**b**) Extracted manganese valence for each film after the indicated amount of air exposure. Within error, no significant trends emerge. (**c**) Manganese valence vs. time for the indicated $SrMnO_3$ films, again no significant differences are apparent.

Appendix B

Electronic structure of polar surfaces in $La_{0.7}Sr_{0.3}MnO_3$ from DFT

$La_{1-x}Sr_xMnO_3$ is potentially susceptible to a number of surface reconstructions, including the possibility of a 'dead layer' where the electronic and magnetic properties at the surface show significant changes relative to the bulk [125, 214]. Both the $Mn^{(3+x)+}O_2^{2-}$ and $La^{3+}_{1-x}Sr^{2+}_xO^{2-}$ (001) surfaces are nominally polar, which drives a reconstruction to prevent the divergent electrostatic potential associated with a polar catastrophe [215, 137, 216]. This can be accomplished through a modification of the surface layer chemistry or structure as in conventional semiconductors [215], or through a purely electronic mechanism as seen in several oxide thin films [9, 217]. These effects could dramatically alter the doping estimates from ARPES away from the nominal bulk values and/or radically alter the measured electronic structure. Thus it might be expected that a surface sensitive probe like ARPES would not be able to observe an electronic structure representative of the bulk in $La_{1-x}Sr_xMnO_3$, contrary to what we have shown in this dissertation.

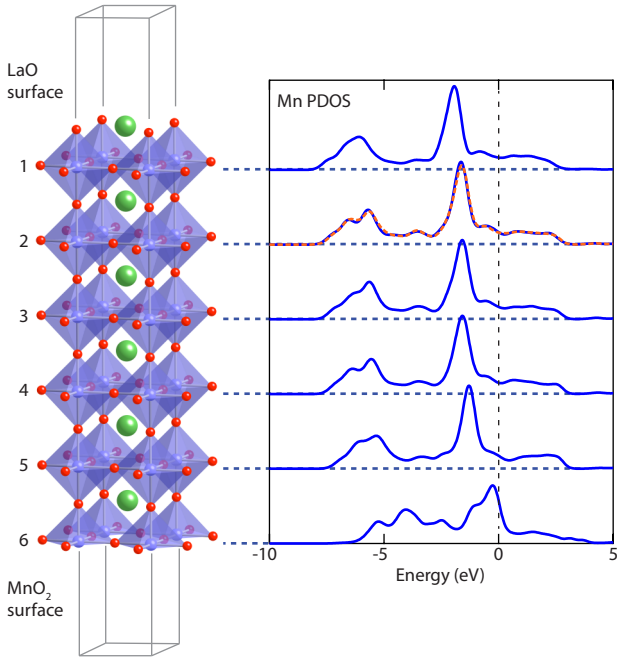

Figure B.1: Surface electronic structure of $La_{0.7}Sr_{0.3}MnO_3$ from DFT. Layer-resolved majority spin Mn partial density of states (PDOS, offset for clarity) for the illustrated slab. The top curve is at the (La,Sr)O surface; the bottom curve is at the MnO_2 surface. The Mn PDOS from an $La_{0.7}Sr_{0.3}MnO_3$ bulk calculation (dashed orange line) has been overlaid onto the second MnO_2 layer to demonstrate the recovery of a bulk-like electronic structure.

Although we do not have a complete understanding of the mechanism for reconstruction in our samples, we can consider the simplest case of a purely electronic reconstruction to prevent the polar catastrophe in $La_{0.7}Sr_{0.3}MnO_3$ as an example case. With this goal in mind, we have performed a DFT slab calculation for 6 unit cells of $La_{0.7}Sr_{0.3}MnO_3$ with 12 Å of vacuum [218] separating the MnO_2 and (La,Sr)O (001) surfaces, as shown in Fig. B.1. This configuration was chosen since a proper account of the effects of surface polarity requires a slab with the correct charge density that also contains both MnO_2 and LaO surfaces to preserve stoichiometry [219]. We used lattice constants a = b = 3.905 Å and c = 3.86 Å to simulate strain from a $SrTiO_3$ substrate. The interaction parameter (U) was fixed at zero to avoid the tendency of U to promote an ordered, insulating phase in large unit cells. For the comparison in Fig. B.1, a bulk $La_{0.7}Sr_{0.3}MnO_3$ calculation was performed

under the same conditions. The polarity of the surface is directly related to the charged La ions and their location throughout the enlarged unit cell. For this reason, accounting for the average charge on the La site becomes critical, and so these calculations were performed with the virtual crystal approximation (at $x = 0.3$) rather than a rigid shift of E_F.

Despite a reconstructed density of states at the topmost MnO_2 layer (6) and small energy shifts for layers 1 & 5, the Mn partial density of states for all other layers is nearly indistinguishable from bulk $La_{0.7}Sr_{0.3}MnO_3$. Since ARPES is sensitive to approximately 3-4 unit cells, the measured near-E_F spectral weight should primarily reflect the bulk-like inner layers of the calculation, consistent with our experimental observations.

Appendix C

Phase separation in $La_{2/3}Sr_{1/3}MnO_3$/$LaAlO_3$ films

$La_{2/3}Sr_{1/3}MnO_3$ films become insulating under very strong compressive strain [83, 127]. Early DFT studies suggested that the films enter a C-type AF state [163]. This phase is characterized by $d_{3z^2-r^2}$ orbital polarization and a quasi-one-dimensional bandstructure dispersing primarily along the *c*-axis. X-ray linear dichroism measurements verified a degree of $d_{3z^2-r^2}$ orbital polarization in $La_{2/3}Sr_{1/3}MnO_3$/LAO films, although it appears much weaker than that found in layered manganites [54]. Nevertheless, despite its expected presence in strained $La_{2/3}Sr_{1/3}MnO_3$ films, and its presence in the bulk phase diagram of the layered manganites [220], no detailed ARPES studies of the Mn e_g states in C-type AF manganites have been published. Toward this goal, strained $Pr_{0.6}Ca_{0.4}MnO_3$ films that are also expected to be in the C-AF phase were studied with variable photon energy ARPES [221]. Detailed measurements of the Mn t_{2g} and O_{2p} derived valence band were made, and the expected Mn e_g derived bands near E_F were found to be absent. It is important to note, though, that similar studies of metallic $La_{2/3}Sr_{1/3}MnO_3$ films were also unable to

resolve clearly dispersive features in the metallic phase [121, 119]; an anomaly that was resolved by our detailed measurements of MBE-grown films (chapter 5).

In this chapter, I present ARPES measurements of the electronic structure of 15 nm and 6 nm thick $La_{2/3}Sr_{1/3}MnO_3$/LAO films. Rather than the insulating bandstructure expected for the C-type phase, we find an unexpected two-component electronic structure consisting of a low-energy metallic band strongest in the thicker film, and a high-energy insulating band sharpest in the thinner film. AFM measurements demonstrate a thickness-dependent island morphology of our films due to relaxation of the strain imposed by the substrate. I argue that the observed high-energy insulating features in our ARPES spectra arise from coherently strained atomically smooth portions of our films, whereas partially relaxed islands give rise to metallic spectra.

C.1 ARPES results

We performed ARPES measurements on 6 nm and 15 nm thick $La_{2/3}Sr_{1/3}MnO_3$/LAO films grown by the procedure described in chapter 5. Measurements were performed with an energy resolution of 40 meV, and at T = 65-100 K to prevent charging of the insulating films.

The angle-integrated valence band spectra for both film thicknesses are shown in Fig. C.1b. Both were nominally (La,Sr)O terminated from growth, although the 15 nm film shows deeply bound Sr 4p and La 5p features characteristic of a mixed surface termination (section 5.3.1) and corresponding minor changes in the region within 10 eV of E_F. Variations in surface termination occasionally occur in our manganite films but do not appear to significantly affect the dispersive states near E_F (section 5.3.1). Nevertheless, the most significant difference between the two films is the clear metal-like Fermi step for

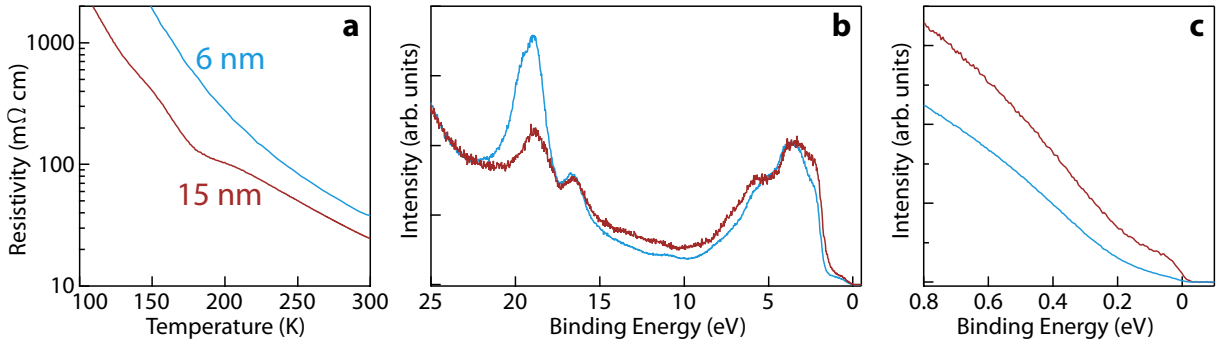

Figure C.1: (**a**) Resistivity from 6 nm and 15 nm thick $La_{2/3}Sr_{1/3}MnO_3$/LAO films measured by ARPES. (**b**) Angle-integrated valence band spectra from the same two films. (**c**) Spectra at the hole-pocket k_F for the same two films showing the much greater intensity at E_F for the 15 nm film.

the 15 nm film that is nearly absent for the 6 nm film (Fig. C.1c). This difference cannot be ascribed to a dead-layer [222] effect in the thinner film because its thickness of 15 unit cells remains much larger than typical dead layers. Furthermore, it is the *thicker* film that is anomalous: showing a metallic spectrum despite its insulating resistivity (Fig. C.1a).

The striking difference between the two films can be examined in more detail through the k-dependent electronic structure. The ARPES spectra in Fig. C.2a,c demonstrate two distinct energy scales characterizing the near-E_F electronic structure. This is most apparent in the 6 nm film. We see vertically dispersing features for $E < 0.5$ eV that fail to reach E_F due to the insulating 0.1 eV gap, and a deep parabolic feature at $E > 0.8$ eV. These unusual spectra were confirmed on an additional 6 nm film (Fig. C.3). The 15 nm thick film shows a low-energy feature as well, but it has now evolved into a well-defined parabolic band crossing E_F. In contrast, the high-energy parabolic feature from thinner films has become only weakly k-dependent but still spans a similar E and k range. The opposite evolution of these two features with thickness is strong evidence that we are imaging two distinct but related components of the electronic structure. This is in contrast to the

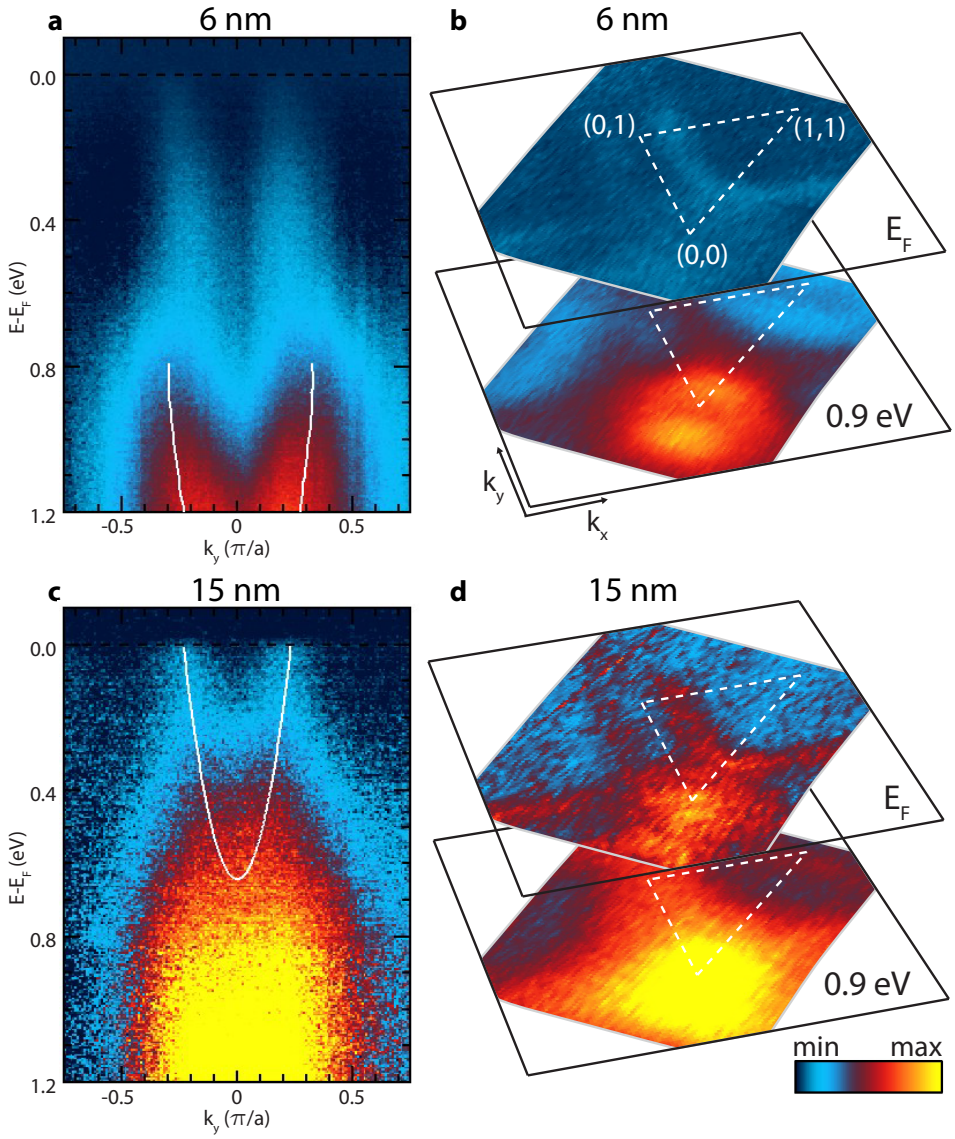

Figure C.2: (**a**) ARPES spectra from a 6 nm $La_{2/3}Sr_{1/3}MnO_3$/LAO film at $k_x = 0.58\pi/a$ after subtraction of a non-dispersive background. White lines show extracted dispersion from the high-energy parabolic feature. (**b**) Iso-energy maps of spectral intensity at E_F and $E = 0.9$ eV for the same 6 nm $La_{2/3}Sr_{1/3}MnO_3$/LAO. (**c,d**) Same as in panels a,b but for a 15 nm $La_{2/3}Sr_{1/3}MnO_3$/LAO film. White line in panel c shows a parabolic fit to the extracted low-energy metallic band. All data are normalized to the VB peak at 3.5 eV, but maps at E_F are enhanced by an additional factor of 15 to make the weak metallic dispersion more evident.

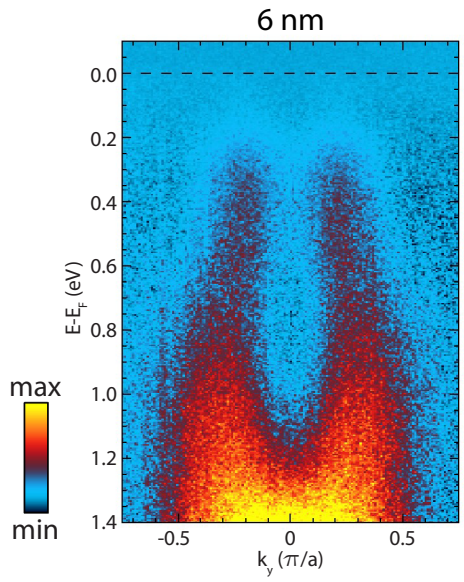

Figure C.3: ARPES measurement from a second 6 nm thick $La_{2/3}Sr_{1/3}MnO_3$/LAO film along the same **k**-space cut shown in Fig. C.2a,c, after subtraction of a non-dispersive background. Here again we see the apparent presence of a low energy and high energy feature, but the gap at E_F is more apparent.

waterfall feature in the cuprates [223], where a single band transits between a large and small energy scale due to many-body effects.

The iso-energy contours presented in Fig. C.2b,d demonstrate that a similar phenomenology holds true across *k*-space. At E_F, the 15 nm film shows a much more intense FS than the thinner film and has a dispersion reminiscent of the FS from the metallic $La_{2/3}Sr_{1/3}MnO_3$ films of chapter 5. On the other hand, at 0.8 eV the 15 nm film shows only weakly-*k*-resolved spectral weight that tracks the more sharply defined features of the 6 nm film.

Surprisingly, the low-energy feature seen in the 15 nm $La_{2/3}Sr_{1/3}MnO_3$/LAO film is quantitatively consistent with the bandstructure of the more weakly strained metallic $La_{2/3}Sr_{1/3}MnO_3$ films (chapter 6). The effective mass determined from MDC fits to

the low energy bandstructure is 0.22 ± 0.03 m_e, in close agreement with that found for metallic films and for our DFT calculation of cubic $La_{2/3}Sr_{1/3}MnO_3$. Furthermore, in $La_{2/3}Sr_{1/3}MnO_3$/NSAT we observed a decreased hole pocket size and occupied bandwidth due to compressive strain; both features are present in the $La_{2/3}Sr_{1/3}MnO_3$/LAO low-energy band, whose extrapolated band-bottom lies 0.1 eV closer to E_F than that found for the less-strained $La_{2/3}Sr_{1/3}MnO_3$/NSAT.

C.2 Film microstructure

To address the disparity between $La_{2/3}Sr_{1/3}MnO_3$/LAO films of varying thickness, additional film characterization tools are essential. X-ray diffraction measurements of 6 nm to 20 nm thick $La_{2/3}Sr_{1/3}MnO_3$/LAO films showed equal out-of-plane lattice constants (c = 4.00 ± 0.01 Å), and film rocking curves were unfortunately unable to provide insight into the quality of each film due to the broad rocking curves intrinsic to LAO substrates. Using XPS measurements of the Sr 3d and La 4d peaks from the films presented in Fig. C.2, I found x = 0.34 ± 0.02 and x = 0.33 ± 0.02 for the 6 nm and 15 nm films, respectively. This demonstrates that both have the expected Sr concentration and that differences in x cannot account for their differing electronic structure.

On the other hand, AFM measurements of $La_{2/3}Sr_{1/3}MnO_3$/LAO films reveal a significant roughness that evolves with film thickness. The 6 nm thick $La_{2/3}Sr_{1/3}MnO_3$/LAO film from Fig. C.2 has a surface consisting predominantly of a step-terrace morphology (Fig. C.4a). In addition, we can also resolve a low density of ≈ 5nm high islands that are not present in $La_{2/3}Sr_{1/3}MnO_3$ films on better lattice-matched substrates. As the film thickness increases to 15 nm, the surface becomes densely packed with islands of similar height (Fig. C.4b) and now lacks any appreciable atomically smooth regions.

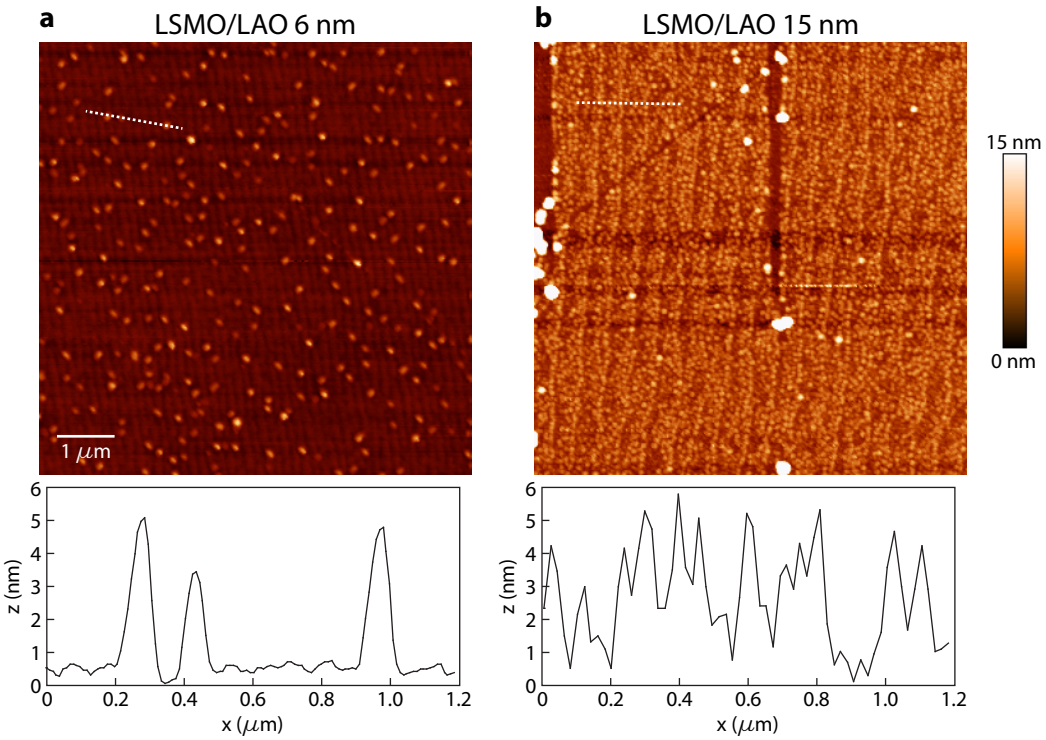

Figure C.4: (**a,b**) AFM images from 6 nm and 15 nm $La_{2/3}Sr_{1/3}MnO_3$/LAO films measured by ARPES. On increasing film thickness, the density of islands dramatically increases. Bottom panels show line cuts corresponding to the white dashed lines shown in the top panels.

Qualitatively similar thickness-dependent transitions have been studied in $La_{2/3}Sr_{1/3}MnO_3$ thin films grown on several substrates, and in many cases a transition from thin atomically-smooth surfaces to island formation in thicker films has been observed [224, 225, 226]. This phenomena is understood as a Stranski-Krastanov related growth mode, wherein the film grows coherently strained and atomically smooth up to a critical thickness, but subsequent layers form isolated islands that allow a sudden or gradual relaxation of the large substrate-induced strain [227]. In our case, island formation is expected to occur with the smallest critical thickness for $La_{2/3}Sr_{1/3}MnO_3$/LAO films due to the large biaxial strain (2.3%) in comparison to the other substrates we have used.

Film	Growth date	Haynes wafer	Thickness (nm)	RMS (nm)
CA2111	11/12/2012	ARPES	6	0.3
CA2116	11/12/2012	ARPES	6	0.2
CA2119	11/12/2012	ARPES	6	0.5
CA2166	1/9/2013	ARPES	6	1.2
CA2168	1/9/2013	ARPES	6	0.7
CA2112	11/12/2012	#3	6	0.3
CA2165	1/9/2013	#7	6	0.2
EJM004	8/29/2013	#7	9	0.1
EJM051	10/6/2013	#25	9	0.2
EJM005	8/29/2013	#30	12	0.1
EJM052	10/6/2013	#7	12	0.2
CA2048	8/10/2012	ARPES	15	2.2
CA2169	1/9/2013	#7	20	3.0

Table C.1: Root-mean-square (RMS) surface roughness for several films as measured by AFM. Also included are the film thicknesses, growth dates, and whether each film was grown on a numbered Haynes wafer used for standard MBE growths or a custom Haynes wafer used for ARPES measurements. ARPES data shown in Figs. C.1 and C.2 is from CA2168 and CA2048.

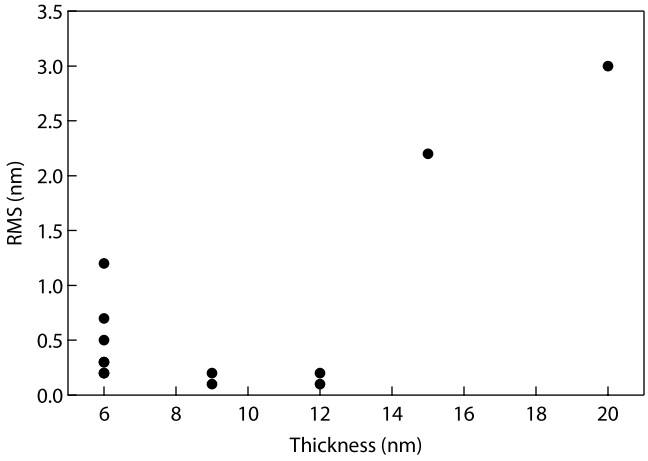

Figure C.5: RMS vs. film thickness, using the data of Table C.1.

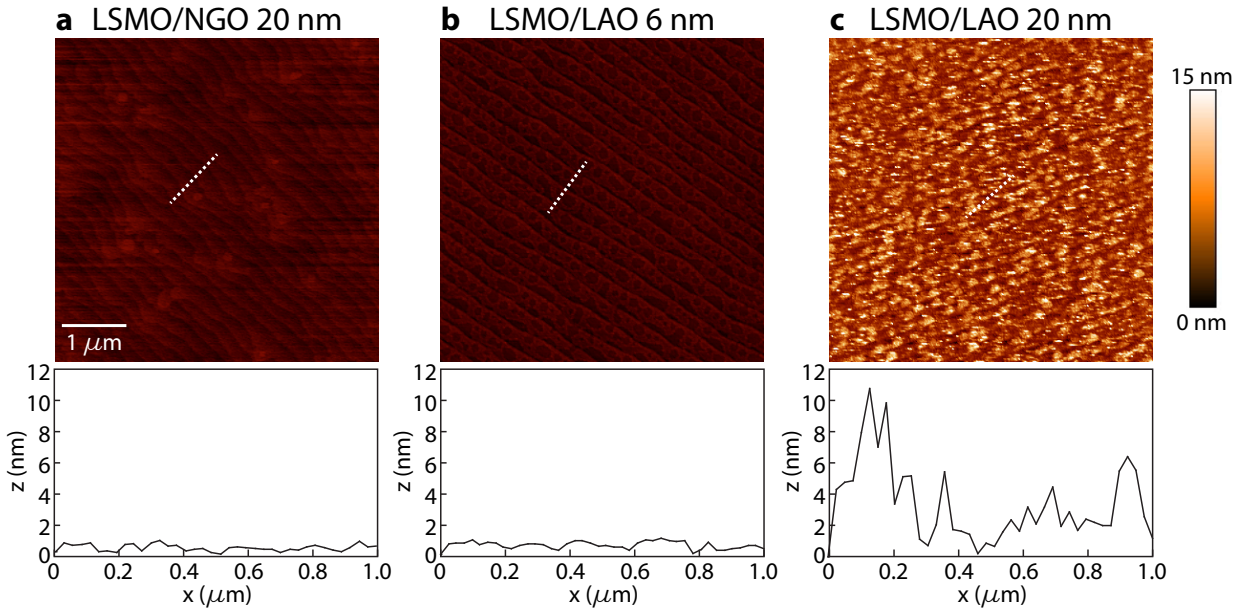

Figure C.6: AFM measurements for a 20 nm $La_{2/3}Sr_{1/3}MnO_3$/NGO film (**a**), a 6 nm $La_{2/3}Sr_{1/3}MnO_3$/LAO film (**b**), and a 20 nm $La_{2/3}Sr_{1/3}MnO_3$/LAO film (**c**) all grown on the same day using the same calibration. Bottom panels show line cuts corresponding to the white dashed lines shown in the top panels. Although the $La_{2/3}Sr_{1/3}MnO_3$/NGO and 6 nm $La_{2/3}Sr_{1/3}MnO_3$/LAO films show atomically smooth surfaces with unit-cell or half unit-cell steps, the 20 nm $La_{2/3}Sr_{1/3}MnO_3$/LAO film is very rough.

To explore the reproducibility and thickness dependence of island formation within our films, we grew several additional $La_{2/3}Sr_{1/3}MnO_3$ films and measured their microstructure with AFM. A summary of the measured root mean square surface roughness for each is provided in Table C.1 and displayed in Fig. C.5, which provides a measure for the degree of island formation. We also note that a total of nine $\leq$ 15 nm $La_{2/3}Sr_{1/3}MnO_3$/LAO films were measured by resistivity and found to be insulating, whereas the 20 nm film is metallic below 250 K, consistent with ref. [228]. Notably, we see a large variation in the degree of island formation for films of nominally the same thickness, and the more recently grown films with 9-12 nm thickness are smoother than nearly all 6 nm thick films.

One possible explanation for the variation in surface roughness between film growths is a variation in film stoichiometry. Warusawithana [229] found a transition from unit cell step-terrace surfaces to island formation as a function of the (La + Sr)/Mn ratio in 110 nm $La_{2/3}Sr_{1/3}MnO_3$/STO films. Island formation occurs for (La + Sr)/Mn < 1.000 ± 0.002. Similar phenomena were observed in films grown on other substrates including LAO. To address the possibility of stoichiometry alone giving rise to the island formation observed in our films, we grew three films using the same calibration on the same growth day: a 6 nm film on LAO, a 20 nm film on LAO, and a 20 nm film on nearly lattice-matched [110] $NdGaO_3$ (0.3% compressive strain). Fig. C.6 shows that the 6 nm film and weakly strained 20 nm film both provide smooth surfaces, whereas the 20 nm film on LAO shows severe islanding, providing strong evidence for the crucial roles played by epitaxial strain and film thickness in island formation. Furthermore, we note that the islands observed by Warusawithana [229] have much smaller heights (≈2 nm) than those found in our $La_{2/3}Sr_{1/3}MnO_3$/LAO films, which can be > 10nm.

Nevertheless, we cannot rule out the possibility that stoichiometry influences the critical thickness where island formation begins. In addition island formation can depend sensitively on other growth parameters. Several groups using different growth conditions find different critical thicknesses and island morphologies [225, 226, 228]. Our films were grown using multiple sample holders for which variations in the absolute temperature of the substrate surface can occur. It is clear that island formation in our films depends sensitively on growth parameters, and reproducing specific results in the transition region between flat and rough films remains a challenge.

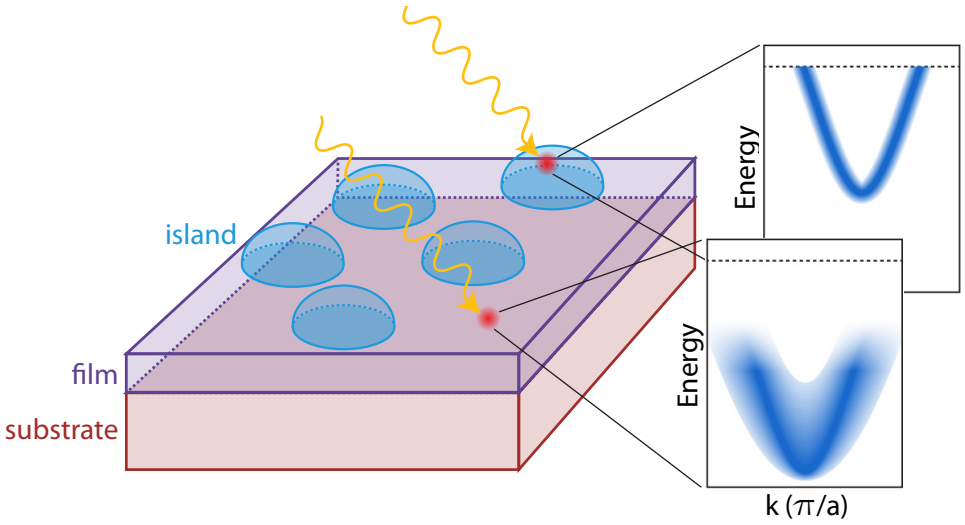

Figure C.7: Illustration of the proposed mechanism for inducing both metallic and insulating features in our ARPES spectra. Smooth, coherently strained parts of the film providing insulating spectra. Islands formed on the film surface are partially relaxed and thus metallic, accounting for the metal-like spectra seen in thicker films.

C.3 Relaxation induced metal-insulator transition

The impact of film microstructure on the strain-induced metal insulator transition was discussed in the context of $La_{0.67}Ca_{0.33}MnO_3$/LAO films by ref. [230]. Coherently strained $La_{0.67}Ca_{0.33}MnO_3$ shares a similar AF insulating phase to that of $La_{2/3}Sr_{1/3}MnO_3$/LAO, but resistivity and magnetization measurements indicated a significant fraction of each film assumed a FM metallic phase. Corresponding AFM and magnetic-force microscopy found locally inhomogeneous magnetism and island formation that occurred on the same length scale. It was thus inferred that the relaxed islands assume the FM metallic phase of bulk $La_{0.67}Ca_{0.33}MnO_3$, whereas coherently strained regions of the film remain AF and insulating. A more recent study of $La_{2/3}Sr_{1/3}MnO_3$/LAO films provides further support to this model [228]. Nuclear magnetic resonance measurements found locally FM components within $La_{2/3}Sr_{1/3}MnO_3$/LAO films that are absent for very thin films but rapidly

increase with thickness starting at 12 nm. At the same thickness, the film resistivity begins to drop, eventually becoming metallic for > 20 nm. This thickness dependent resistivity is in good agreement with films grown by our group, and was attributed to percolation of the FM metallic islands by Tebano et al. [228].

The observed microstructure provides a natural explanation for our ARPES data: thin films have smooth highly strained surfaces that are insulating. Thicker films have a larger degree of strain relaxation, giving rise to partially relaxed metallic islands. As we increase the film thickness, we see a low-energy metallic bandstructure from the islands that becomes stronger and more coherent as more and larger islands are formed (Fig. C.7). Simultaneously, the high-energy insulating bandstructure becomes less well-defined. Our ARPES results indicate that the metallic islands for 15 nm thick $La_{2/3}Sr_{1/3}MnO_3$/LAO still retain substantial residual strain, suggesting that the strain relief provided by island formation occurs primarily through gradual elastic deformation rather than defect formation at the interfaces [227].

In Fig. C.2, the evolution of the low energy and high energy features is more complex than a simple change in intensity for each, being accompanied by complex changes to the momentum-space structure as well. This likely indicates a crossover to incoherent or localized states for the low-energy band on making the film thinner, and for the high-energy band on making the film thicker. This will require a more detailed study of the complicated relaxation-induced microstructure and possible role of interfaces between metallic and insulating regions that is, however, beyond the scope of this thesis.

Future work to address the interplay between film microstructure and the electronic structure should pursue magnetic force microscopy and magnetic impedance microscopy [159] measurements on films that have also been measured by ARPES to circumvent film-to-film variability and directly correlate real-space and momentum space structure.

Bibliography

[1] Chesterton, G. K. *Orthodoxy* (Project Gutenberg, 1994). http://www.gutenberg.org/ebooks/130.

[2] Wigner, E. *Phys. Rev.* **46**, 1002–1011 (1934), http://link.aps.org/doi/10.1103/PhysRev.46.1002.

[3] Mott, N. F. *Proc. Phys. Soc. A* **62**, 416 (1949), http://iopscience.iop.org/0370-1298/62/7/303.

[4] Schilling, A., Cantoni, M., Guo, J. D. & Ott, H. R. *Nature* **363**, 56–58 (1993), http://www.nature.com.proxy.library.cornell.edu/nature/journal/v363/n6424/abs/363056a0.html.

[5] Maignan, A., Simon, C., Caignaert, V. & Raveau, B. *Solid State Communications* **96**, 623–625 (1995), http://www.sciencedirect.com/science/article/pii/0038109895005382.

[6] Imada, M., Fujimori, A. & Tokura, Y. *Rev. Mod. Phys.* **70**, 1039–1263 (1998), http://link.aps.org/doi/10.1103/RevModPhys.70.1039.

[7] Chakhalian, J., Millis, A. J. & Rondinelli, J. **11**, 92–94 (2012), http://www.nature.com/nmat/journal/v11/n2/full/nmat3225.html.

[8] Mannhart, J. & Schlom, D. G. **327**, 1607–1611 (2010), http://www.sciencemag.org/cgi/doi/10.1126/science.1181862.

[9] Ohtomo, A. & Hwang, H. Y. *Nature* **427**, 423–426 (2004), http://www.nature.com.proxy.library.cornell.edu/nature/journal/v427/n6973/abs/nature02308.html.

[10] Lee, J. H. *et al.* *Nature* **466**, 954–958 (2010), http://www.nature.com.proxy.library.cornell.edu/nature/journal/v466/n7309/full/nature09331.html.

[11] Dagotto, E., Hotta, T. & Moreo, A. *Physics Reports* **344**, 1–153 (2001), http://www.sciencedirect.com/science/article/pii/S0370157300001216.

[12] Hueso, L. E. *et al.* **445**, 410–413 (2007), http://www.nature.com/doifinder/10.1038/nature05507.

[13] Wu, S. M. *et al.* *Nat Mater* **9**, 756–761 (2010), http://www.nature.com/nmat/journal/v9/n9/full/nmat2803.html.

[14] Garcia, V. *et al.* *Science* **327**, 1106–1110 (2010), http://www.sciencemag.org/content/327/5969/1106.

[15] Yajima, T., Hikita, Y. & Hwang, H. Y. **10**, 198–201 (2011), http://www.nature.com/doifinder/10.1038/nmat2946.

[16] Damascelli, A., Hussain, Z. & Shen, Z.-X. *Rev. Mod. Phys.* **75**, 473–541 (2003), http://link.aps.org/doi/10.1103/RevModPhys.75.473.

[17] Sun, Z. *et al.* *Phys. Rev. B* **78**, 075101 (2008), http://link.aps.org/doi/10.1103/PhysRevB.78.075101.

[18] Schlom, D. G., Chen, L.-Q., Pan, X., Schmehl, A. & Zurbuchen, M. A. **91**, 2429–2454 (2008), http://doi.wiley.com/10.1111/j.1551-2916.2008.02556.x.

[19] Santos, T. S. *et al.* *Phys. Rev. Lett.* **107**, 167202 (2011), http://link.aps.org/doi/10.1103/PhysRevLett.107.167202.

[20] Logvenov, G., Gozar, A. & Bozovic, I. *Science* **326**, 699–702 (2009), http://www.sciencemag.org/content/326/5953/699.

[21] Okamoto, S. & Millis, A. J. *Nature* **428**, 630–633 (2004), http://www.nature.com.proxy.library.cornell.edu/nature/journal/v428/n6983/full/nature02450.html.

[22] Jang, H. W. *et al.* *Science* **331**, 886–889 (2011), http://www.sciencemag.org/content/331/6019/886.

[23] Hertz, H. *Annalen der Physik* **267**, 983–1000 (1887), http://onlinelibrary.wiley.com/doi/10.1002/andp.18872670827/abstract.

[24] Stoney, G. J. *Philos. Mag.* **38**, 418–420 (1894), http://www.tandfonline.com/doi/abs/10.1080/14786449408620653.

[25] Einstein, A. *Annalen der Physik* **322**, 132–148 (1905), http://onlinelibrary.wiley.com/doi/10.1002/andp.19053220607/abstract.

[26] Millikan, R. A. *Phys. Rev.* **7**, 355–388 (1916), http://link.aps.org/doi/10.1103/PhysRev.7.355.

[27] Gobeli, G. W., Allen, F. G. & Kane, E. O. *Phys. Rev. Lett.* **12**, 94–97 (1964), http://link.aps.org/doi/10.1103/PhysRevLett.12.94.

[28] Kane, E. O. *Phys. Rev. Lett.* **12**, 97–98 (1964), http://link.aps.org/doi/10.1103/PhysRevLett.12.97.

[29] Hufner, S. *Photoelectron Spectroscopy: Principles and Applications* (Springer, 2003), 3rd edn.

[30] Yeh, J. J. & Lindau, I. *Atomic Data and Nuclear Data Tables* **32**, 1–155 (1985), http://www.sciencedirect.com/science/article/pii/0092640X85900166.

[31] Seah, M. P. & Dench, W. A. *Sur. and inter. anal.* **1**, 2–11 (1979), http://onlinelibrary.wiley.com/doi/10.1002/sia.740010103/abstract.

[32] Fadley, C. S., Baird, R. J., Siekhaus, W., Novakov, T. & Bergstrom, S. . L. *Journal of Electron Spectroscopy and Related Phenomena* **4**, 93–137 (1974), http://www.sciencedirect.com/science/article/pii/0368204874900012.

[33] Yi, M. *et al. Phys. Rev. Lett.* **110**, 067003 (2013), http://link.aps.org/doi/10.1103/PhysRevLett.110.067003.

[34] Wang, Y. H. *et al. Phys. Rev. Lett.* **107**, 207602 (2011), http://link.aps.org/doi/10.1103/PhysRevLett.107.207602.

[35] Shen, K. M. *et al. Phys. Rev. Lett.* **93**, 267002 (2004), http://link.aps.org/doi/10.1103/PhysRevLett.93.267002.

[36] Mishchenko, A. & Nagaosa, N. *Phys. Rev. Lett.* **93**, 036402 (2004), http://link.aps.org/doi/10.1103/PhysRevLett.93.036402.

[37] Rosch, O. & Gunnarsson, O. *Eur. Phys. J. B* **43**, 11–18 (2005), http://link.springer.com/article/10.1140/epjb/e2005-00022-x.

[38] Ashcroft, N. W. & Mermin, N. D. *Solid state physics* (Saunders College, 1976).

[39] Veenstra, C. N., Goodvin, G. L., Berciu, M. & Damascelli, A. *Phys. Rev. B* **82**, 012504 (2010), http://link.aps.org/doi/10.1103/PhysRevB.82.012504.

[40] Strocov, V. N. *Journal of Electron Spectroscopy and Related Phenomena* **130**, 65–78 (2003), http://www.sciencedirect.com/science/article/pii/S0368204803000549.

[41] Heinz, K. *Rep. on Prog. in Phys.* **58**, 637 (1995), http://iopscience.iop.org/0034-4885/58/6/003.

[42] Koralek, J. D. *et al. Rev. Sci. Instr.* **78**, 053905 (2007), http://scitation.aip.org.proxy.library.cornell.edu/content/aip/journal/rsi/78/5/10.1063/1.2722413.

[43] Kiss, T. *et al. Rev. Sci. Instr.* **79**, 023106 (2008), http://scitation.aip.org.proxy.library.cornell.edu/content/aip/journal/rsi/79/2/10.1063/1.2839010.

[44] Harter, J. W. *et al. Rev. Sci. Instr.* **83**, 113103 (2012), http://scitation.aip.org.proxy.library.cornell.edu/content/aip/journal/rsi/83/11/10.1063/1.4766962.

[45] Umansky, V. *et al. Journal of Crystal Growth* **311**, 1658–1661 (2009), http://www.sciencedirect.com/science/article/pii/S0022024808009901.

[46] Cho, A. Y. & Arthur, J. R. *Progress in Solid State Chemistry* **10, Part 3**, 157–191 (1975), http://www.sciencedirect.com/science/article/pii/0079678675900059.

[47] Pfeiffer, L. & West, K. W. *Physica E: Low-dimensional Systems and Nanostructures* **20**, 57–64 (2003), http://www.sciencedirect.com/science/article/pii/S1386947703005174.

[48] Cho, A. *MRS Bulletin* **20**, 21–28 (1995).

[49] Tsui, D. C., Stormer, H. L. & Gossard, A. C. *Phys. Rev. Lett.* **48**, 1559–1562 (1982), http://link.aps.org/doi/10.1103/PhysRevLett.48.1559.

[50] Bednorz, J. G. & MÃijller, K. A. *Z. Physik B - Condensed Matter* **64**, 189–193 (1986), http://link.springer.com/article/10.1007/BF01303701.

[51] Martin, L. W. & Schlom, D. G. *Current Opinion in Solid State and Materials Science* **16**, 199–215 (2012), http://www.sciencedirect.com/science/article/pii/S1359028612000046.

[52] May, S. J. *et al. Nat. Mater.* **8**, 892–897 (2009), http://www.nature.com/doifinder/10.1038/nmat2557.

[53] Schlom, D. G. *et al. MRS Bulletin* **39**, 118–130 (2014).

[54] Aruta, C. *et al. Phys. Rev. B* **73**, 235121 (2006), http://link.aps.org/doi/10.1103/PhysRevB.73.235121.

[55] Chakhalian, J. *et al. Nat Phys* **2**, 244–248 (2006), http://www.nature.com.proxy.library.cornell.edu/nphys/journal/v2/n4/full/nphys272.html.

[56] King, P. D. C. *et al. Nature Nano. (AOP)* DOI: 10.1038/nnano.2014.59 (2014), http://www.nature.com/nnano/journal/vaop/ncurrent/full/nnano.2014.59.html.

[57] Sauerbrey, G. *Z. Physik* **155**, 206–222 (1959), http://link.springer.com/article/10.1007/BF01337937.

[58] Auciello, O. & Krauss, A. R. *In Situ Real-Time Characterization of Thin Films* (John Wiley & Sons, 2001).

[59] Haeni, J. H., Theis, C. D. & Schlom, D. G. *Journal of Electroceramics* **4**, 385–391 (2000), http://link.springer.com/article/10.1023/A%3A1009947517710.

[60] Chiang, T.-C. *Surf. Sci. Rep.* **39**, 181–235 (2000), http://www.sciencedirect.com/science/article/pii/S0167572900000066.

[61] Horiba, K. *et al. Rev. Sci. Instr.* **74**, 3406 (2003), http://link.aip.org/link/RSINAK/v74/i7/p3406/s1&Agg=doi.

[62] Shi, M. *et al. Phys. Rev. B* **70**, 140407 (2004), http://link.aps.org/doi/10.1103/PhysRevB.70.140407.

[63] Horiba, K., Kamakura, N., Yamamoto, K., Kobayashi, K. & Shin, S. *Journal of Electron Spectroscopy and Related Phenomena* **144-147**, 1027–1030 (2005), http://www.sciencedirect.com/science/article/pii/S0368204805002914.

[64] Shai, D. E. *et al. Phys. Rev. Lett.* **110**, 087004 (2013), http://link.aps.org/doi/10.1103/PhysRevLett.110.087004.

[65] Rondinelli, J. M. & May, S. J. *Nat Mater* **11**, 833–834 (2012), http://www.nature.com.proxy.library.cornell.edu/nmat/journal/v11/n10/full/nmat3425.html?WT.ec_id=NMAT-201210.

[66] Turchanin, M. A., Velikanova, T. Y., Agraval, P. G., Abdulov, A. R. & Dreval, L. A. *Powder Metall Met Ceram* **47**, 586–606 (2008), http://link.springer.com/article/10.1007/s11106-008-9062-y.

[67] Ho, C. Y., Powell, R. W. & Liley, P. E. *J. Phys. Chem. Ref. Data* **1**, 279–421 (1972).

[68] Wollan, E. O. & Koehler, W. C. *Phys. Rev.* **100**, 545–563 (1955), http://link.aps.org/doi/10.1103/PhysRev.100.545.

[69] Volger, J. *Physica* **20**, 49–66 (1954), http://www.sciencedirect.com/science/article/pii/S0031891454800152.

[70] Jin, S. *et al. Science* **264**, 413–415 (1994), http://www.sciencemag.org/content/264/5157/413.

[71] Millis, A. J., Littlewood, P. B. & Shraiman, B. I. *Phys. Rev. Lett.* **74**, 5144–5147 (1995), http://link.aps.org/doi/10.1103/PhysRevLett.74.5144.

[72] Hemberger, J. *et al. Phys. Rev. B* **66**, 094410 (2002), http://link.aps.org/doi/10.1103/PhysRevB.66.094410.

[73] Tomioka, Y., Asamitsu, A., Kuwahara, H., Moritomo, Y. & Tokura, Y. *Phys. Rev. B* **53**, R1689–R1692 (1996), http://link.aps.org/doi/10.1103/PhysRevB.53.R1689.

[74] Galakhov, V. *et al. Phys. Rev. B* **65**, 113102 (2002), http://link.aps.org/doi/10.1103/PhysRevB.65.113102.

[75] Ederer, C., Lin, C. & Millis, A. J. *Phys. Rev. B* **76**, 155105 (2007), http://link.aps.org/doi/10.1103/PhysRevB.76.155105.

[76] Chuang, Y.-D., Gromko, A. D., Dessau, D. S., Kimura, T. & Tokura, Y. *Science* **292**, 1509–1513 (2001), http://www.sciencemag.org/content/292/5521/1509.

[77] Zhang, F. C. & Rice, T. M. *Phys. Rev. B* **37**, 3759–3761 (1988), http://link.aps.org/doi/10.1103/PhysRevB.37.3759.

[78] Park, J.-H. *et al. Nature* **392**, 794–796 (1998), http://www.nature.com/nature/journal/v392/n6678/abs/392794a0.html.

[79] Bowen, M. *et al. Appl. Phys. Lett.* **82**, 233–235 (2003), http://scitation.aip.org.proxy.library.cornell.edu/content/aip/journal/apl/82/2/10.1063/1.1534619.

[80] Krempasky, J. *et al. Phys. Rev. B* **77**, 165120 (2008), http://link.aps.org/doi/10.1103/PhysRevB.77.165120.

[81] Slater, J. C. & Koster, G. F. *Phys. Rev.* **94**, 1498 (1954), http://prola.aps.org/abstract/PR/v94/i6/p1498_1.

[82] Koizumi, A. *et al. Phys. Rev. Lett.* **86**, 5589–5592 (2001), http://link.aps.org/doi/10.1103/PhysRevLett.86.5589.

[83] Konishi, Y. *et al. J. Phys. Soc. Jpn.* **68**, 3790 (1999), http://jpsj.ipap.jp/link?JPSJ/68/3790/pdf.

[84] Alexandrov, A. S. & Devreese, J. T. *Advances in polaron physics* (Springer, 2010). http://public.eblib.com/EBLPublic/PublicView.do?ptiID=510422.

[85] Alexandrov, A. S. & Bratkovsky, A. M. *Phys. Rev. Lett.* **82**, 141–144 (1999), http://link.aps.org/doi/10.1103/PhysRevLett.82.141.

[86] Vasiliu-Doloc, L. *et al. Phys. Rev. Lett.* **83**, 4393–4396 (1999), http://link.aps.org/doi/10.1103/PhysRevLett.83.4393.

[87] Zhao, G.-m., Smolyaninova, V., Prellier, W. & Keller, H. *Phys. Rev. Lett.* **84**, 6086–6089 (2000), http://link.aps.org/doi/10.1103/PhysRevLett.84.6086.

[88] Alexandrov, A. S. *et al. Phys. Rev. B* **64**, 140404 (2001), http://link.aps.org/doi/10.1103/PhysRevB.64.140404.

[89] Okimoto, Y., Katsufuji, T., Ishikawa, T., Arima, T. & Tokura, Y. *Phys. Rev. B* **55**, 4206–4214 (1997), http://link.aps.org/doi/10.1103/PhysRevB.55.4206.

[90] Kim, K. H., Jung, J. H. & Noh, T. W. *Phys. Rev. Lett.* **81**, 1517–1520 (1998), http://link.aps.org/doi/10.1103/PhysRevLett.81.1517.

[91] Dessau, D. S. *et al. Phys. Rev. Lett.* **81**, 192 (1998), http://prl.aps.org/abstract/PRL/v81/i1/p192_1.

[92] Mannella, N. *et al. Phys. Rev. B* **76**, 233102 (2007), http://link.aps.org/doi/10.1103/PhysRevB.76.233102.

[93] Zener, C. *Phys. Rev.* **81**, 440–444 (1951), http://link.aps.org/doi/10.1103/PhysRev.81.440.

[94] Anderson, P. W. & Hasegawa, H. *Phys. Rev.* **100**, 675–681 (1955), http://link.aps.org/doi/10.1103/PhysRev.100.675.

[95] Hwang, H. Y., Cheong, S.-W., Radaelli, P. G., Marezio, M. & Batlogg, B. *Phys. Rev. Lett.* **75**, 914–917 (1995), http://link.aps.org/doi/10.1103/PhysRevLett.75.914.

[96] Chen, Y. *et al. Phys. Rev. B* **78**, 212301 (2008), http://link.aps.org/doi/10.1103/PhysRevB.78.212301.

[97] Chmaissem, O. *et al. Phys. Rev. B* **64**, 134412 (2001), http://link.aps.org/doi/10.1103/PhysRevB.64.134412.

[98] Akimoto, T. *et al. Phys. Rev. B* **57**, R5594–R5597 (1998), http://link.aps.org/doi/10.1103/PhysRevB.57.R5594.

[99] Murakami, Y. *et al. Phys. Rev. Lett.* **81**, 582 (1998), http://prl.aps.org/abstract/PRL/v81/i3/p582_1.

[100] Rodriguez-Carvajal, J. *et al. Phys. Rev. B* **57**, R3189–R3192 (1998), http://link.aps.org/doi/10.1103/PhysRevB.57.R3189.

[101] Goodenough, J. B. *Phys. Rev.* **100**, 564–573 (1955), http://link.aps.org/doi/10.1103/PhysRev.100.564.

[102] Voit, J. *Rep. Prog. Phys.* **58**, 977 (1995), http://iopscience.iop.org/0034-4885/58/9/002.

[103] Zheng, H., Li, Q., Gray, K. E. & Mitchell, J. F. *Phys. Rev. B* **78**, 155103 (2008), http://link.aps.org/doi/10.1103/PhysRevB.78.155103.

[104] Evtushinsky, D. V. *et al. Phys. Rev. Lett.* **105**, 147201 (2010), http://link.aps.org/doi/10.1103/PhysRevLett.105.147201.

[105] Sun, Z. *et al. Phys. Rev. B* **86**, 201103 (2012), http://link.aps.org/doi/10.1103/PhysRevB.86.201103.

[106] Massee, F. *et al. Nat Phys* **7**, 978–982 (2011), http://www.nature.com/nphys/journal/v7/n12/full/nphys2089.html.

[107] Moritomo, Y., Asamitsu, A., Kuwahara, H. & Tokura, Y. *Nature* **380**, 141–144 (1996), http://www.nature.com.proxy.library.cornell.edu/nature/journal/v380/n6570/abs/380141a0.html.

[108] Reutler, P., Friedt, O., Buchner, B., Braden, M. & Revcolevschi, A. *Journal of Crystal Growth* **249**, 222–229 (2003), http://www.sciencedirect.com/science/article/pii/S0022024802021048.

[109] Urushibara, A. *et al. Phys. Rev. B* **51**, 14103–14109 (1995), http://link.aps.org/doi/10.1103/PhysRevB.51.14103.

[110] Burton, J. D. & Tsymbal, E. Y. *Phys. Rev. Lett.* **106**, 157203 (2011), http://link.aps.org/doi/10.1103/PhysRevLett.106.157203.

[111] Yunoki, S., Dagotto, E., Costamagna, S. & Riera, J. A. *Phys. Rev. B* **78**, 024405 (2008), http://link.aps.org/doi/10.1103/PhysRevB.78.024405.

[112] Salvador, P. A., Haghiri-Gosnet, A.-M., Mercey, B., Hervieu, M. & Raveau, B. *Appl. Phys. Lett.* **75**, 2638–2640 (1999), http://scitation.aip.org/content/aip/journal/apl/75/17/10.1063/1.125103.

[113] Adamo, C. *et al. Phys. Rev. B* **79**, 045125 (2009), http://link.aps.org/doi/10.1103/PhysRevB.79.045125.

[114] Nanda, B. R. K. & Satpathy, S. *Phys. Rev. Lett.* **101**, 127201 (2008), http://link.aps.org/doi/10.1103/PhysRevLett.101.127201.

[115] Lin, C. & Millis, A. J. *Phys. Rev. B* **78**, 174419 (2008), http://link.aps.org/doi/10.1103/PhysRevB.78.174419.

[116] Chikamatsu, A. *et al. Journal of Electron Spectroscopy and Related Phenomena* **144-147**, 511–514 (2005), http://www.sciencedirect.com/science/article/pii/S0368204805000654.

[117] Falub, M. *et al. Phys. Rev. B* **72**, 054444 (2005), http://link.aps.org/doi/10.1103/PhysRevB.72.054444.

[118] Chikamatsu, A. *et al. Phys. Rev. B* **73**, 195105 (2006), http://link.aps.org/doi/10.1103/PhysRevB.73.195105.

[119] Chikamatsu, A. *et al. Phys. Rev. B* **76**, 201103 (2007), http://link.aps.org/doi/10.1103/PhysRevB.76.201103.

[120] Chikamatsu, A. *et al. J. Magn. Magn. Mater.* **310**, 1030–1032 (2007), http://linkinghub.elsevier.com/retrieve/pii/S0304885306014119.

[121] Shi, M. *et al. J. Phys.: Condens. Matter* **20**, 222001 (2008), http://iopscience.iop.org/0953-8984/20/22/222001.

[122] Krempasky, J. *et al. Journal of Electron Spectroscopy and Related Phenomena* **181**, 63–69 (2010), http://www.sciencedirect.com/science/article/pii/S0368204810001271.

[123] Livesay, E. A., West, R. N., Dugdale, S. B., Santi, G. & Jarlborg, T. *J. Phys.: Condens. Matter* **11**, L279 (1999), http://iopscience.iop.org/0953-8984/11/25/104.

[124] Tebano, A. *et al. Phys. Rev. B* **82**, 214407 (2010), http://link.aps.org/doi/10.1103/PhysRevB.82.214407.

[125] Bertacco, R. *et al. Phys. Rev. B* **78**, 035448 (2008), http://link.aps.org/doi/10.1103/PhysRevB.78.035448.

[126] Koster, G., Kropman, B. L., Rijnders, G. J. H. M., Blank, D. H. A. & Rogalla, H. *Appl. Phys. Lett.* **73**, 2920–2922 (1998), http://scitation.aip.org/content/aip/journal/apl/73/20/10.1063/1.122630.

[127] Adamo, C. *et al. Appl. Phys. Lett.* **95**, 112504 (2009), http://link.aip.org/link/APPLAB/v95/i11/p112504/s1&Agg=doi.

[128] Hibble, S. J., Cooper, S. P., Hannon, A. C., Fawcett, I. D. & Greenblatt, M. *J. Phys.: Condens. Matter* **11**, 9221 (1999), http://iopscience.iop.org/0953-8984/11/47/308.

[129] Adamo, C. *et al. (pre print)* (2014).

[130] Tanuma, S., Powell, C. J. & Penn, D. R. *Surf. Interface Anal.* **21**, 165–176 (1994), http://onlinelibrary.wiley.com/doi/10.1002/sia.740210302/abstract.

[131] Bertacco, R., Contour, J. P., Barthelemy, A. & Olivier, J. *Surface Science* **511**, 366–372 (2002), http://www.sciencedirect.com/science/article/pii/S0039602802015467.

[132] Fister, T. T. *et al.* *Appl. Phys. Lett.* **93**, 151904 (2008), http://link.aip.org/link/APPLAB/v93/i15/p151904/s1&Agg=doi.

[133] Ferrari, V., Pruneda, J. M. & Artacho, E. *Phys. Status Solidi A* **203**, 1437–1441 (2006), http://onlinelibrary.wiley.com/doi/10.1002/pssa.200566183/abstract.

[134] Nanda, B. & Satpathy, S. *Phys. Rev. B* **79**, 054428 (2009), http://link.aps.org/doi/10.1103/PhysRevB.79.054428.

[135] Perdew, J. P., Burke, K. & Ernzerhof, M. *Phys. Rev. Lett.* **77**, 3865–3868 (1996), http://link.aps.org/doi/10.1103/PhysRevLett.77.3865.

[136] Blaha, P., Schwarz, K., Madsen, G. K. H., Kvasnicka, D. & Luitz, J. *WIEN2k, an augmented plane wave plus local orbitals program for calculating crystal properties* (Vienna University of Technology, 2009).

[137] Nakagawa, N., Hwang, H. Y. & Muller, D. A. *Nat Mater* **5**, 204–209 (2006), http://www.nature.com/doifinder/10.1038/nmat1569.

[138] Freeland, J. W. *et al.* *Nat Mater* **4**, 62–67 (2004), http://www.nature.com/doifinder/10.1038/nmat1280.

[139] Asamitsu, A. & Tokura, Y. *Phys. Rev. B* **58**, 47–50 (1998), http://link.aps.org/doi/10.1103/PhysRevB.58.47.

[140] Trinckauf, J. *et al.* *Phys. Rev. Lett.* **108**, 016403 (2012), http://link.aps.org/doi/10.1103/PhysRevLett.108.016403.

[141] Mannella, N. *et al.* *Nature* **438**, 474–478 (2005), http://www.nature.com/doifinder/10.1038/nature04273.

[142] Sun, Z. *et al.* *Phys. Rev. Lett.* **97**, 056401 (2006), http://link.aps.org/doi/10.1103/PhysRevLett.97.056401.

[143] Sun, Z. *et al.* *PNAS* **108**, 11799–11803 (2011), http://www.pnas.org/content/108/29/11799.short.

[144] Okuda, T. *et al.* *Phys. Rev. Lett.* **81**, 3203–3206 (1998), http://link.aps.org/doi/10.1103/PhysRevLett.81.3203.

[145] Maezono, R., Ishihara, S. & Nagaosa, N. *Phys. Rev. B* **57**, R13993 (1998), http://link.aps.org/doi/10.1103/PhysRevB.57.R13993.

[146] Dho, J., Chi, E., Kim, W., Hur, N. & Choi, Y. *Phys. Rev. B* **65**, 132414 (2002), http://link.aps.org/doi/10.1103/PhysRevB.65.132414.

[147] Kuwahara, H., Okuda, T., Tomioka, Y., Asamitsu, A. & Tokura, Y. *Phys. Rev. Lett.* **82**, 4316 (1999), http://link.aps.org/doi/10.1103/PhysRevLett.82.4316.

[148] Izumi, M., Manako, T., Konishi, Y., Kawasaki, M. & Tokura, Y. *Phys. Rev. B* **61**, 12187 (2000), http://link.aps.org/doi/10.1103/PhysRevB.61.12187.

[149] Muduli, P. K., Bose, S. K. & Budhani, R. C. *J. Phys.: Condens. Matter* **19**, 226204 (2007), http://stacks.iop.org/0953-8984/19/i=22/a=226204?key=crossref.8d6dc394dfc3252ae484db5e67994605.

[150] Matsuno, J., Fujimori, A., Takeda, Y. & Takano, M. *EPL* **59**, 252 (2002), http://iopscience.iop.org/0295-5075/59/2/252.

[151] Horiba, K. *et al. Phys. Rev. B* **71**, 155420 (2005), http://link.aps.org/doi/10.1103/PhysRevB.71.155420.

[152] Kovacik, R. & Ederer, C. *Phys. Rev. B* **81**, 245108 (2010), http://link.aps.org/doi/10.1103/PhysRevB.81.245108.

[153] Chen, X.-J. *et al. Nature* **466**, 950–953 (2010), http://www.nature.com/nature/journal/v466/n7309/full/nature09293.html.

[154] Kagawa, F., Miyagawa, K. & Kanoda, K. *Nature* **436**, 534–537 (2005), http://www.nature.com/nature/journal/v436/n7050/abs/nature03806.html.

[155] Gegenwart, P., Si, Q. & Steglich, F. *Nat Phys* **4**, 186–197 (2008), http://www.nature.com/nphys/journal/v4/n3/abs/nphys892.html.

[156] Hanaguri, T. *et al. Nature* **430**, 1001–1005 (2004), http://www.nature.com/nature/journal/v430/n7003/abs/nature02861.html.

[157] Hsieh, D. *et al. Nature* **452**, 970–974 (2008), http://www.nature.com/nature/journal/v452/n7190/abs/nature06843.html.

[158] Mii, Y. J. *et al. Appl. Phys. Lett.* **59**, 1611–1613 (1991), http://scitation.aip.org.proxy.library.cornell.edu/content/aip/journal/apl/59/13/10.1063/1.106246.

[159] Lai, K. *et al. Science* **329**, 190 (2010), http://www.sciencemag.org/content/329/5988/190.

[160] Locquet, J.-P. *et al.* *Nature* **394**, 453–456 (1998), http://www.nature.com.proxy.library.cornell.edu/nature/journal/v394/n6692/full/394453a0.html.

[161] Fuchs, D. *et al.* *Phys. Rev. B* **75**, 144402 (2007), http://link.aps.org/doi/10.1103/PhysRevB.75.144402.

[162] Ramesh, R. & Spaldin, N. A. *Nat Mater* **6**, 21–29 (2007), http://www.nature.com.proxy.library.cornell.edu/nmat/journal/v6/n1/full/nmat1805.html.

[163] Fang, Z., Solovyev, I. V. & Terakura, K. *Phys. Rev. Lett.* **84**, 3169 (2000), http://prl.aps.org/abstract/PRL/v84/i14/p3169_1.

[164] Ma, C., Yang, Z. & Picozzi, S. *J. Phys.: Condens. Matter* **18**, 7717–7728 (2006), http://stacks.iop.org/0953-8984/18/i=32/a=019?key=crossref.0b6559c1e6ed61027690d5c4b5834312.

[165] Colizzi, G., Filippetti, A., Cossu, F. & Fiorentini, V. *Phys. Rev. B* **78**, 235122 (2008), http://link.aps.org/doi/10.1103/PhysRevB.78.235122.

[166] Baena, A., Brey, L. & Calderon, M. J. *Phys. Rev. B* **83**, 064424 (2011), http://link.aps.org/doi/10.1103/PhysRevB.83.064424.

[167] Takamura, Y., Chopdekar, R. V., Arenholz, E. & Suzuki, Y. *Appl. Phys. Lett.* **92**, 162504 (2008), http://link.aip.org/link/APPLAB/v92/i16/p162504/s1&Agg=doi.

[168] Mateika, D., Kohler, H., Laudan, H. & Volkel, E. *Journal of Crystal Growth* **109**, 441–446 (1991), http://www.sciencedirect.com/science/article/pii/002202489190215Q.

[169] Nelson, J. B. & Riley, D. P. *Proc. Phys. Soc.* **57**, 160 (1945), http://iopscience.iop.org/0959-5309/57/3/302.

[170] Aschauer, U., Pfenninger, R., Selbach, S. M., Grande, T. & Spaldin, N. A. *Phys. Rev. B* **88**, 054111 (2013), http://link.aps.org/doi/10.1103/PhysRevB.88.054111.

[171] Pesquera, D. *et al.* *Nat Commun* **3**, 1189 (2012), http://www.nature.com/ncomms/journal/v3/n11/full/ncomms2189.html.

[172] Freeland, J. W. *et al.* *J. Phys.: Condens. Matter* **19**, 315210 (2007), http://stacks.iop.org/0953-8984/19/i=31/a=315210?key=crossref.b3835181771e056d45129f022d5b540c.

[173] Millis, A. J., Shraiman, B. I. & Mueller, R. *Phys. Rev. Lett.* **77**, 175–178 (1996), http://arxiv.org/abs/cond-mat/9507084.

[174] Gurvitch, M. *Phys. Rev. B* **28**, 544 (1983), http://prb.aps.org/abstract/PRB/v28/i2/p544_1.

[175] Chainani, A. *et al.* *Phys. Rev. B* **56**, R15513–R15516 (1997), http://link.aps.org/doi/10.1103/PhysRevB.56.R15513.

[176] Brouet, V. *et al.* *Phys. Rev. B* **77**, 235104 (2008), http://link.aps.org/doi/10.1103/PhysRevB.77.235104.

[177] Dagotto, E. *Nanoscale Phase Separation and Colossal Magnetoresistance - The Physics of Manganites and Related Compounds* (Springer, 2003). http://www.springer.com/materials/book/978-3-540-43245-6.

[178] Sen, C., Alvarez, G. & Dagotto, E. *Phys. Rev. Lett.* **98**, 127202 (2007), http://link.aps.org/doi/10.1103/PhysRevLett.98.127202.

[179] Mukherjee, A., Cole, W. S., Woodward, P., Randeria, M. & Trivedi, N. *Phys. Rev. Lett.* **110**, 157201 (2013), http://link.aps.org/doi/10.1103/PhysRevLett.110.157201.

[180] Yang, Z. Q., Zhang, Y. Q., Aarts, J., Wu, M.-Y. & Zandbergen, H. W. **88**, 072507 (2006), http://scitation.aip.org/content/aip/journal/apl/88/7/10.1063/1.2172715.

[181] Monkman, E. J. *et al.* *Nat Mater* **11**, 855–859 (2012), http://www.nature.com/nmat/journal/v11/n10/full/nmat3405.html?WT.ec_id=NMAT-201210.

[182] Kroemer, H. *Quasi-Electric Fields and Band Offsets: Teaching Electrons New Tricks* (Nobel Lecture, 2000).

[183] Dagotto, E. *Science* **318**, 1076–1077 (2007), http://www.sciencemag.org/content/318/5853/1076.

[184] Bhattacharya, A. *et al. Phys. Rev. Lett.* **100**, 257203 (2008), http://link.aps.org/doi/10.1103/PhysRevLett.100.257203.

[185] Adamo, C. *et al. Appl. Phys. Lett.* **92**, 112508 (2008), http://scitation.aip.org.proxy.library.cornell.edu/content/aip/journal/apl/92/11/10.1063/1.2842421.

[186] Dong, S. *et al. Phys. Rev. B* **78**, 201102 (2008), http://link.aps.org/doi/10.1103/PhysRevB.78.201102.

[187] May, S. J. *et al. Phys. Rev. B* **77**, 174409 (2008), http://link.aps.org/doi/10.1103/PhysRevB.77.174409.

[188] Hannon, J. P., Trammell, G. T., Blume, M. & Gibbs, D. *Phys. Rev. Lett.* **61**, 1245–1248 (1988), http://link.aps.org/doi/10.1103/PhysRevLett.61.1245.

[189] Materlik, G., Sparks, C. J. & Fischer, K. *Resonant anomalous X-ray scattering: theory and applications* (North-Holland, 1994).

[190] Freeland, J. W. *et al. Appl. Phys. Lett.* **71**, 276–278 (1997), http://scitation.aip.org/content/aip/journal/apl/71/2/10.1063/1.119518.

[191] Seve, L. *et al. Phys. Rev. B* **60**, 9662 (1999), http://prb.aps.org/abstract/PRB/v60/i13/p9662_1.

[192] Smadici, e. *et al. Phys. Rev. Lett.* **99**, 196404 (2007), http://link.aps.org/doi/10.1103/PhysRevLett.99.196404.

[193] Wadati, H. *et al. J. Appl. Phys.* **106**, 083705 (2009), http://scitation.aip.org/content/aip/journal/jap/106/8/10.1063/1.3246788.

[194] Benckiser, E. *et al. Nat Mater* **10**, 189–193 (2011), http://www.nature.com/doifinder/10.1038/nmat2958.

[195] Smadici, S. *et al. Phys. Rev. B* **85**, 094519 (2012), http://link.aps.org/doi/10.1103/PhysRevB.85.094519.

[196] Smadici, S., Nelson-Cheeseman, B. B., Bhattacharya, A. & Abbamonte, P. *Phys. Rev. B* **86**, 174427 (2012), http://link.aps.org/doi/10.1103/PhysRevB.86.174427.

[197] Aruta, C. *et al. Phys. Rev. B* **80**, 140405 (2009), http://link.aps.org/doi/10.1103/PhysRevB.80.140405.

[198] Hawthorn, D. G. *et al. Rev. Sci. Instr.* **82**, 073104 (2011), http://scitation.aip.

org.proxy.library.cornell.edu/content/aip/journal/rsi/82/7/10.1063/1.3607438.

[199] Macke, S. & Goering, E. ReMagX x-ray magnetic reflectivity tool (2009). www.mf.mpg.de/remagx.html.

[200] Shklovskii, B. I. & Efros, A. L. *Electronic Properties of Doped Semiconductors* (Springer, 1984). http://www.springer.com/materials/book/978-3-662-02405-8.

[201] Larochelle, S. *et al. Phys. Rev. B* **71**, 024435 (2005), http://link.aps.org/doi/10.1103/PhysRevB.71.024435.

[202] Lin, C. & Millis, A. *Phys. Rev. B* **78**, 184405 (2008), http://link.aps.org/doi/10.1103/PhysRevB.78.184405.

[203] Iorio, A., Perroni, C. A., Ramaglia, V. M. & Cataudella, V. *Phys. Rev. B* **83**, 085107 (2011), http://prb.aps.org/abstract/PRB/v83/i8/e085107.

[204] Pardo, V., Botana, A. S. & Baldomir, D. *Appl. Phys. Lett.* **104**, 081602 (2014), http://scitation.aip.org.proxy.library.cornell.edu/content/aip/journal/apl/104/8/10.1063/1.4866271.

[205] Salafranca, J., Alvarez, G. & Dagotto, E. *Phys. Rev. B* **80**, 155133 (2009), http://link.aps.org/doi/10.1103/PhysRevB.80.155133.

[206] Lee, J.-S. *et al. Phys. Rev. Lett.* **107**, 037206 (2011), http://link.aps.org/doi/10.1103/PhysRevLett.107.037206.

[207] Wakabayashi, Y. *et al. Phys. Rev. Lett.* **96**, 017202 (2006), http://link.aps.org/doi/10.1103/PhysRevLett.96.017202.

[208] de Jong, M. *et al. Phys. Rev. B* **71**, 014434 (2005), http://link.aps.org/doi/10.1103/PhysRevB.71.014434.

[209] de Jong, M. P. *et al. Phys. Rev. B* **73**, 052403 (2006), http://link.aps.org/doi/10.1103/PhysRevB.73.052403.

[210] Valencia, S. *et al. Phys. Rev. B* **73**, 104402 (2006), http://link.aps.org/doi/10.1103/PhysRevB.73.104402.

[211] Valencia, S. *et al. 184431* **75**, 184431 (2007), http://link.aps.org/doi/10.1103/PhysRevB.75.184431.

[212] Craciun, R., Nentwick, B., Hadjiivanov, K. & Knozinger, H. *Applied Catalysis A: General* **243**, 67–79 (2003), http://www.sciencedirect.com/science/article/pii/S0926860X02005380.

[213] Caignaert, V., Nguyen, N., Hervieu, M. & Raveau, B. *Materials Research Bulletin* **20**, 479–484 (1985), http://www.sciencedirect.com/science/article/pii/0025540885901011.

[214] Verna, A. *et al. Journal of Magnetism and Magnetic Materials* **322**, 1212–1216 (2010), http://www.sciencedirect.com/science/article/pii/S0304885309005393.

[215] Tasker, P. W. *Journal of Physics C: Solid State Physics* **12**, 4977 (1979), http://iopscience.iop.org/0022-3719/12/22/036.

[216] Nanda, B. R. K. & Satpathy, S. *Phys. Rev. B* **81**, 224408 (2010), http://link.aps.org/doi/10.1103/PhysRevB.81.224408.

[217] Moetakef, P. *et al. Appl. Phys. Lett.* **99**, 232116 (2011), http://scitation.aip.org.proxy.library.cornell.edu/content/aip/journal/apl/99/23/10.1063/1.3669402.

[218] Fang, Z. & Terakura, K. *J. Phys. Soc. Jpn* **70**, 3356–3361 (2001), http://journals.jps.jp/doi/abs/10.1143/JPSJ.70.3356.

[219] Gu, X., Elfimov, I. S. & Sawatzky, G. A. *arXiv:0911.4145* (2009), http://arxiv-web3.library.cornell.edu/abs/0911.4145.

[220] Ling, C. D. *et al. Phys. Rev. B* **62**, 15096 (2000), http://link.aps.org/doi/10.1103/PhysRevB.62.15096.

[221] Wadati, H. *et al. Phys. Rev. Lett.* **100**, 026402 (2008), http://link.aps.org/doi/10.1103/PhysRevLett.100.026402.

[222] Kourkoutis, L. F., Song, J. H., Hwang, H. Y. & Muller, D. A. *PNAS* **107**, 11682 (2010), http://www.pnas.org/content/107/26/11682.

[223] Graf, J. *et al. Phys. Rev. Lett.* **98**, 067004 (2007), http://link.aps.org/doi/10.1103/PhysRevLett.98.067004.

[224] Maurice, J.-L. *et al. Phil. Mag.* **83**, 3201 (2003).

[225] Lebedev, O. I., Tendeloo, G. V., Amelinckx, S., Ju, H. L. & Krishnan, K. M. *Phil. Mag. A* **80**, 673 (2000), http://www.tandfonline.com/doi/abs/10.1080/01418610008212075.

[226] Jiang, J. C., Meletis, E. I. & Gnanasekar, K. I. *Appl. Phys. Lett.* **80**, 4831 (2002), http://scitation.aip.org/content/aip/journal/apl/80/25/10.1063/1.1489078.

[227] Shchukin, V. A. & Bimberg, D. *Rev. Mod. Phys.* **71**, 1125 (1999), http://link.aps.org/doi/10.1103/RevModPhys.71.1125.

[228] Tebano, A. *et al. Phys. Rev. B* **74**, 245116 (2006), http://link.aps.org/doi/10.1103/PhysRevB.74.245116.

[229] Warusawithana, M. P. Heteroepitaxial interfaces modify collective states in complex oxides (2005). http://hdl.handle.net/2142/35201.

[230] Biswas, A. *et al. Phys. Rev. B* **63**, 184424 (2001), http://link.aps.org/doi/10.1103/PhysRevB.63.184424.